

Light extraction in organic light-emitting diodes

Dissertation

zur Erlangung des
Doktorgrades der Naturwissenschaften
(Dr. rer. nat.)

eingereicht an der
Mathematisch-Naturwissenschaftlichen Fakultät
der Universität Augsburg

vorgelegt von

Jörg Frischeisen

geb. am 07. Oktober 1979
in Schwabmünchen

Juni 2011

1. Gutachter: Prof. Dr. Wolfgang Brütting

2. Gutachter: Prof. Dr. Achim Wixforth

3. Gutachter: Prof. Dr. Paolo Lugli

Tag der mündlichen Prüfung: 26.07.2011

Contents

1. Motivation	1
2. Introduction to organic light-emitting diodes (OLEDs)	7
2.1 Organic semiconductors	7
2.2 Fluorescence and phosphorescence	9
2.3 OLED device structure and operation	11
2.4 External quantum efficiency	16
2.5 Optical loss channels	18
2.6 OLED preparation	21
2.7 Basic stack design	22
2.7.1 OLED materials	23
2.7.2 Blocking, injection and transport layers	24
2.7.3 Exemplary OLED stacks	26
2.7.4 Current-voltage-luminance characteristics	31
3. Interaction of electromagnetic radiation with matter	35
3.1 Maxwell's equations and electromagnetic waves	35
3.2 Complex refractive index	38
3.3 Reflection and refraction of electromagnetic waves	40
3.4 Transfer-matrix formulation	45
3.5 Waveguide and leaky modes	48
4. Surface plasmon polaritons	53
4.1 Surface plasmons, bulk plasmons and localized plasmons	53
4.2 Dispersion relation of surface plasmons	54
4.3 Coupling of surface plasmons and light	60
4.4 Attenuated total reflection	65
4.5 Surface plasmon resonance sensor utilizing an integrated OLED	67
5. Optical simulations of OLEDs	75
5.1 Optical simulations based on the dipole model	75
5.2 Power dissipation spectra	77
5.3 Angular dependent emission spectra	81

5.4	Integral power dissipation	86
5.5	Optimization of OLEDs by thickness variations	88
6.	Light extraction techniques in OLEDs	93
6.1	Extraction of substrate modes	93
6.2	Extraction of waveguide modes	96
6.3	Reduction of surface plasmon losses	97
6.4	Microcavity devices, top-emitting OLEDs and transparent OLEDs	98
6.5	High-index substrates	102
7.	Near-field coupling	105
7.1	Surface plasmon dispersion in thin films	105
7.2	Basic principle	109
7.3	Material requirements and experimental setup	110
7.4	Results	112
7.4.1	Variation of silver thickness	112
7.4.2	Measurement of excited state lifetime	115
7.4.3	Estimation of extraction efficiency	118
7.5	Conclusions	119
8.	Grating coupling	121
8.1	Basic principle	121
8.2	Nanoimprint fabrication of gratings and experimental setup	122
8.3	One-dimensional line gratings with 555 nm period	125
8.4	One-dimensional line gratings with 833 nm period	128
8.4.1	Extraction of surface plasmons	130
8.4.2	Extraction of waveguide modes	132
8.5	DVD gratings	135
8.6	Alternative fabrication methods for periodically structured films	137
8.7	Conclusions	138
9.	Prism coupling	141
9.1	Basic principle	141
9.2	Sample preparation and experimental setup	144
9.3	Extraction of surface plasmons	145
9.3.1	Influence of different metals	145
9.3.2	Variation of organic layer thickness	147
9.3.3	Variation of silver thickness	148
9.3.4	Comparison to optical simulations	152
9.4	Extraction of leaky modes	156
9.4.1	Variation of organic layer thickness	157

9.4.2	Variation of silver thickness	159
9.5	Conclusions	163
10.	High-index coupling	165
10.1	Basic principle	165
10.2	Sample preparation and experimental setup	168
10.3	Influence of prism material	170
10.4	Extraction of surface plasmons and waveguide modes	172
10.5	Application to OLEDs	178
10.6	Efficiency prediction by optical simulations	186
10.7	Technical implementation of high-index coupling	195
10.8	Conclusions	197
11.	Emitter orientation	199
11.1	Influence of dipole orientation on OLED efficiency	200
11.1.1	Power dissipation spectra	201
11.1.2	Influence of electron transport layer thickness	202
11.1.3	Potential of horizontally oriented emitters	206
11.2	Dipole emission pattern	207
11.3	Determination of molecular dipole orientation by PL measurements	209
11.3.1	Basic principle and experimental setup	210
11.3.2	Investigation of organic guest-host systems	212
11.3.3	Thickness control using s-polarized measurements	215
11.3.4	Optimization of device layout and discussion	216
11.4	Increased light extraction efficiency in dye-doped small molecule OLEDs with horizontally oriented emitters	221
11.4.1	Stack layout and sample preparation	221
11.4.2	Current-voltage characteristics and emission spectra	224
11.4.3	External quantum efficiency	225
11.5	Phosphorescent guest-host systems	227
11.6	Conclusions	229
12.	Summary and outlook	233
A.	Appendix	241
A.1	Abbreviations	241
A.2	Optical constants	243
A.3	Optical simulation program	249
	Bibliography	255

1. Motivation

Organic light-emitting diodes (OLEDs) are flat large-area light sources with a diffuse light emission. A typical OLED structure has a total thickness of only 100 to 500 nm and consists of several organic layers sandwiched between two electrodes. Light emission results from a process called electroluminescence, i.e. electrons and holes are injected into the device and recombine to generate photons¹.

Since the publication of the first low-voltage OLED based on small molecules by Tang and VanSlyke in 1987² and the first report on OLEDs based on polymers by Burroughes *et al.* in 1990³, intense research has resulted in a vast number of publications and patents in the area of OLEDs. Both their power conversion efficiency as well as lifetime have been continually improved through novel materials and device architectures.

Besides the implementation of OLEDs in displays due to their high contrast and excellent viewing angle characteristics, these light sources have a great potential for applications in general lighting, thus aiming at a market with a global size exceeding \$90 billion⁴. Keeping in mind that about one sixth of the total electricity is consumed for general lighting⁴, it is inevitable to use energy-efficient, long-living and environmentally friendly light sources. In fact, white OLEDs are now on the edge of being introduced as commercial light sources, cf. Fig. 1.1(a).

OLEDs can be produced not only on glass substrates, but also on flexible substrates such as plastic or metal foils, leading to many new innovative designs. Moreover, it is even possible to fabricate OLEDs that are almost completely transparent and, thus, could be used as windows during daytime while emitting diffuse light at night. The unique shape of OLEDs even allows for a combination with other modern light sources like inorganic LEDs, as can be seen in Fig. 1.1(b).

Regarding OLED efficacy, i.e. the fraction of emitted visible light relative to the electric power, a value of 66 lm/W has been demonstrated for a white OLED⁴. The device used a thin light extraction layer and it was based on a hybrid architecture, i.e. a combination of a blue fluorescent as well as yellow and red phosphorescent emission layers. Although this efficacy value is superior to incandescent lamps having an efficacy around 15 lm/W, at first glance OLEDs appear to be less efficient than LEDs with reported efficacies of more than 100 lm/W. However, LEDs require a fixture, which significantly reduces their efficacy by usually more than 60 % when sold as a luminaire⁴. The OLED by itself is almost a luminaire and just requires a driver, which reduces the efficiency by only 10–15 %.

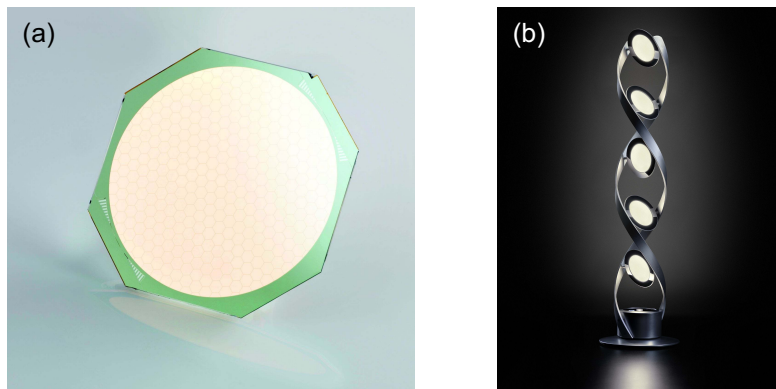


Figure 1.1: (a) Orbeos OLED panel from OSRAM⁵. The panel has an active area of 49 cm². (b) PirOLED, an OSRAM table light with a height of 88 cm, combining both OLEDs and LEDs⁶.

In terms of lifetime, inorganic LEDs are still superior to OLEDs. Nevertheless, OLED lifetimes well above 10.000 hours have been demonstrated before a 30 % reduction in light output is reached⁴. Certainly, the first OLED products on the market are too expensive compared to other light sources. However, a cost reduction with large-scale manufacturing is projected until 2015, aiming at costs below \$100 per square meter^{4,7}. Thus, it is expected that OLED luminaires will soon be competitive to other light sources in terms of efficacy, lifetime and costs.

Comparing reported efficacy values with the theoretical maximum of 184 lm/W for a typical hybrid stack or even 249 lm/W for an all-phosphorescent device, it is apparent that there is clearly a lot of room for improvement⁴. The main reason for this large discrepancy is a rather low light extraction (or outcoupling) efficiency η_{out} . As a result of the large difference in refractive index between air ($n = 1.0$), glass ($n \approx 1.5$), and organic layers ($n \approx 1.7 - 2.0$), only a small fraction of light can leave the device. In a typical OLED with optimized cavity structure, only about 20 % of the light is directly emitted into air, and roughly the same amount is trapped inside the glass substrate owing to total internal reflection at the interface between glass and air⁸. By applying outcoupling enhancement structures like prisms, microlense arrays or microstructured substrates, it is possible to extract a large fraction of substrate modes⁹⁻¹².

The remaining power is lost to waveguide modes, which propagate inside the organic layers, or lost to surface plasmons, i.e. guided electromagnetic surface waves traveling along the interface between the organic material and the metallic cathode. Coupling to waveguide modes and SPs causes losses of typically 50 % in conventional small molecule based OLEDs^{13,14}, thus representing the main limitation for highly efficient OLEDs in general lighting.

With improved light outcoupling, the same emission intensity could be obtained at a lower driving current, which would result in a substantial increase in device lifetime^{4,15}. Alternatively, a higher light outcoupling efficiency allows for obtaining more light for

the same amount of electrical power. Altogether, an enhanced light extraction makes OLEDs more energy-efficient and thus contributes to global energy saving.

Although the physics of an excited molecule inside a simple cavity has been investigated for a long time¹⁶⁻¹⁸, this topic experiences a completely new application in OLEDs. In this context, several modern fields of physics and optics like plasmonics and cavity physics need to be merged in order to completely understand OLEDs and to further improve their efficiency.

The scope of this thesis is to thoroughly analyze the most important aspects regarding light extraction in OLEDs. Besides a fundamental discussion of a variety of existing light extraction strategies and of the fundamental physics behind each approach, several novel techniques with high potential will be introduced and compared in terms of performance and applicability. The reduction of power dissipation to surface plasmons and waveguide modes as well as the recovery of lost power will be the major topics of this work, because they are promising ways to strongly enhance the outcoupling efficiency.

In detail, this thesis is organized in the following way:

- Chapter 2 gives a basic introduction to organic semiconductors and explains the principles of OLED operation. The factors that determine the efficiency of an OLED will be defined. In particular, all optical channels that influence the outcoupling efficiency will be discussed. Moreover, some well-known OLED materials and the preparation of OLEDs will be presented. Finally, several exemplary OLEDs will be demonstrated to explain some basic concepts of stack design.
- Chapter 3 explains the interaction of electromagnetic waves with matter. Since OLEDs inherently represent a planar multilayer stack, the reflection and refraction of electromagnetic waves will be reviewed, and a transfer-matrix formulation will be introduced. Moreover, a discussion of waveguide and leaky modes in thin film structures will be presented.
- Chapter 4 is devoted to surface plasmon polaritons (often simply called surface plasmons, SPs). The dispersion relation of SPs will be derived, and different methods for the excitation of SPs by incident light will be reviewed. The chapter closes with the demonstration of a novel surface plasmon resonance sensor which utilizes an OLED as integrated light source.
- Chapter 5 introduces the optical simulation program which is used to calculate the power dissipation spectrum of an exemplary OLED. In addition, the angular dependent emission spectrum of the OLED will be simulated and compared to measurements. The theoretical outcoupling efficiency will be derived and an optimization of the OLED device structure by varying the thickness of the transport layers will be presented.

- Chapter 6 contains an overview of existing light extraction techniques which are commonly used to extract substrate modes, waveguide modes, or surface plasmons. Special OLED geometries like microcavity devices as well as top-emitting OLEDs and transparent OLEDs will be discussed. Furthermore, the influence of high-index substrates will be addressed and analyzed by optical simulations.
- Chapter 7 is dedicated to the near-field coupling approach. In this technique, molecules with an appropriate absorption spectrum are placed close to a thin metallic layer in order to recover some of the energy which is usually lost to SPs. Optical simulations will be used to clarify the basic principle of this method. By measuring the excited state lifetime, the energy transfer process from SPs to molecules will be experimentally verified. To study the influence of the thickness of the metallic layer, a systematic thickness variation will be investigated. Finally, the efficiency of recovering energy dissipated to SPs by using this approach will be estimated.
- Chapter 8 introduces the grating coupling approach, which makes use of periodic grating structures in order to transform waveguide modes and SPs into free-space radiation by Bragg scattering. One-dimensional line gratings fabricated by nanoimprint will be used to extract bound modes and to clarify the influence of the grating period. Moreover, extraction of SPs using the periodic structure induced by a DVD stamp will be presented to demonstrate the low-cost, high-quality and large-area applicability of grating structures in optoelectronic devices.
- Chapter 9 explains the physical background of the prism coupling method. This approach is based on a reversed Kretschmann configuration, i.e. SPs propagating at a thin metallic layer can transform into free-space radiation on the opposite side of the metal if there is a medium with large enough refractive index. The influence of the thickness of both the metal and the organic layer will be studied by thickness variations and comparison of photoluminescence experiments to simulations. Furthermore, it will be demonstrated that this technique can also be applied to extract waveguide modes.
- Chapter 10 studies the high-index coupling technique, which has a physical background similar to prism coupling. By using layers with a particularly high refractive index next to a thin metallic layer, it is possible to extract SPs and waveguides from organic layers with an arbitrary thickness. The basic principle will be illustrated by varying the material of the high-index layer. It will be presented that this technique even allows for extracting SPs and waveguide modes from real OLED devices. To demonstrate the high potential of this novel method, optical simulations will be performed to predict the extraction efficiency. The chapter closes with a discussion of the technical implementation of high-index coupling.

- Chapter 11 investigates the effects of a non-isotropic emitter orientation. A predominantly horizontal orientation strongly reduces the initial coupling to SPs, thus rendering a recovery almost unnecessary. Optical simulations will be used to demonstrate the impact of emitter orientation on OLED efficiency. Subsequently, a novel method will be presented, which allows for a straightforward and quantitative determination of the orientation in fluorescent thin films even in the case of doped layers. In contrast to the general opinion that small molecules deposited by evaporation are isotropically oriented, evidence of a considerable non-isotropic orientation will be provided. The huge potential of horizontally oriented emitters in small molecule OLEDs will be demonstrated for the first time by comparing the efficiency of OLEDs based on two emitters which have comparable properties except for their degree of orientation. The chapter closes with experimental results which indicate that even phosphorescent emitters can exhibit an explicit non-isotropic orientation, thus opening up new prospects for extremely high OLED efficiencies.
- The thesis concludes with a summary of the main results and gives an outlook on promising future investigations.

2. Introduction to organic light-emitting diodes (OLEDs)

This chapter discusses the basic properties of organic semiconductors. In addition, light emission by fluorescence and phosphorescence will be explained in order to understand the operation principle of organic light-emitting diodes (OLEDs). The different factors which determine the efficiency of an OLED will be defined. In particular, the importance of the outcoupling efficiency will be illustrated by discussing all optical loss channels which occur in an OLED under operation. Next, typical organic materials will be introduced and the preparation of OLEDs will be explained. Several rules for optimizing an OLED stack will be presented on the basis of four OLEDs with different device structures. Finally, the current-voltage-luminance characteristics and efficiencies will be compared for two green-emitting OLEDs based on fluorescent and phosphorescent emitter materials, respectively.

2.1. Organic semiconductors

The field of organic electronics has attracted great interest in academic and industrial research due to many promising applications like organic light-emitting diodes, organic field-effect transistors (OFETs) and organic photovoltaic cells (OPVCs). All areas of organic electronics have in common that they use organic compounds which include conjugated π -electron systems in their structures¹. These materials are mainly constructed of carbon and hydrogen atoms but often contain other elements like nitrogen, oxygen or sulfur and even metals like aluminum, platinum or iridium. In general, two types of organic semiconductors can be distinguished: the class of small molecule materials and the class of polymers, i.e. long chain like molecules composed of repeating structural units. While small molecules have a specific and rather low molecular weight (up to about 1000 u), polymeric materials usually have a higher molecular weight. Since polymers show a distribution of chain length, it is common to specify the average molecular weight. Concerning device fabrication, small molecular materials are usually deposited from the gas phase by thermal evaporation while polymers are processed from solution by methods like spin coating or printing.

Both material classes have in common that the basic molecular structure contains covalent σ -bonds and conjugated π -bonds as exemplarily shown in Fig. 2.1 for the

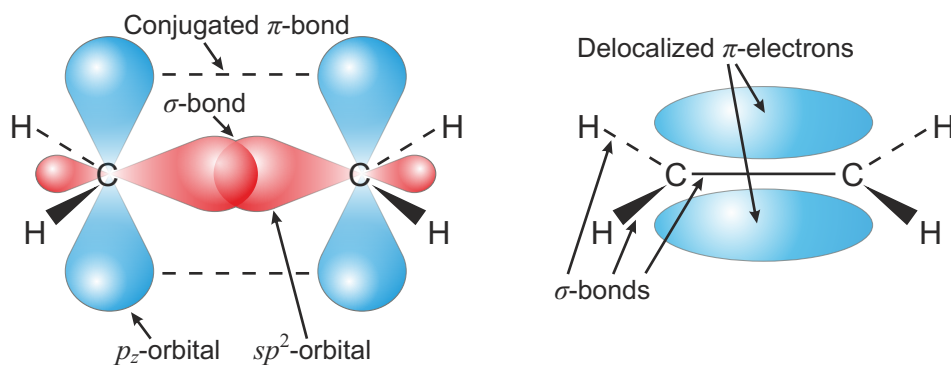


Figure 2.1: Two representations of ethene illustrating the σ -bonds and the conjugated π -bonds which are delocalized between both carbon atoms. The σ -bond between each C–H bonding is not shown for reasons of clarity.

hydrocarbon ethene (C_2H_4). Besides ethyne (C_2H_2), this is one of the simplest molecules containing a conjugated π -electron system. The carbon atoms in this coplanar molecule are sp^2 -hybridized, i.e. three degenerate orbitals are constructed out of one s - and two p -orbitals, with a σ -bond between each C–H and C–C bond¹⁹. The remaining p_z -orbitals are oriented perpendicular with respect to the plane of the sp^2 -orbitals. The p_z -orbitals of the two neighboring carbon atoms overlap above and below the plane of the molecule and form a delocalized π -system.

Organic compounds usually are neutral molecules with closed electron shells. The covalent σ -bonds are stronger than the π -bonds and thus account for the main intramolecular stability. In contrast, the π -bonds are responsible for the weak intermolecular bonding. The molecules may have a permanent or induced dipole moment so that the intermolecular stability is determined by van der Waals forces¹. Due to the weak interaction, the molecules remain intact within the solid and directly determine the physical properties of the material. Thus, for example, the size of a molecule in a film is only slightly changed compared to free molecules. Organic semiconductors usually have a low electronic conductivity compared to their inorganic counterparts and they are relatively soft solids with a comparatively low melting point.

Besides the intermolecular bonding, the π -electron system also determines the electrical and optical properties of organic semiconductors. The π -bonds possess electronic excitation energies in the range of only a few electron volts (eV) and hence absorb and emit in the visible, near infrared and the near ultraviolet spectral regions. The lowest electronic excitation is a π - π^* -transition between the highest occupied molecular orbital (HOMO) and the lowest unoccupied molecular orbital (LUMO)¹⁹. The excited state is a coulombically bound electron-hole pair and is termed an exciton, i.e. a neutral electronic state with an excitation energy which is smaller than the energy required for the formation of a free electron-hole pair¹. The exciton binding energy is typically around 0.5 to 1 eV.

Concerning charge transport, the carriers must be thermally activated in order to hop from molecule to molecule and the process of electrical conduction is referred to as hopping conduction¹. Due to the required thermal activation, the mobility in disordered molecular solids increases with rising temperature.

2.2. Fluorescence and phosphorescence

The basic optical processes in an organic semiconductor are illustrated in the energy level scheme in Fig. 2.2. Here, S_n ($n \geq 0$) denotes an electronic singlet state in which the two outermost electrons are coupled pairwise to a total spin quantum number of zero. If both electrons have a parallel spin orientation, resulting in a total spin quantum number of one, the electronic levels are called triplet levels T_n ($n \geq 1$). As a rule, the electronic ground state of a molecule with an even number of electrons is a singlet state and is denoted S_0 . By absorption of an incident photon, one of the electrons can be lifted to a higher electronic state S_n . All excited states S_n or T_n , except for the two lowest terms S_1 and T_1 , are very short-lived. They release their excess energy very rapidly and relax nonradiatively to the first excited state S_1 or T_1 , respectively. This process of conversion of electronic excitation energy into heat is called internal conversion. The process of a radiative transition from the S_1 to the S_0 state is called fluorescence. This transition is allowed by symmetry and it is often very efficient. The decay is fast with an excited state lifetime of the order of a few nanoseconds. The radiative transition from the T_1 state to the ground state is called phosphorescence. In contrast to the fluorescent decay, this transition is usually not allowed by symmetry. Therefore, the decay is inefficient and usually slow with a lifetime of typically milliseconds. Transitions between the singlet and the triplet systems, so called intersystem crossings (ISC), are normally forbidden.

It should be noted that the classification of states according to their total spin quantum numbers assumes a vanishing spin-orbit coupling. For materials with a small number of nuclear charges, e.g. for carbon and hydrogen, the spin-orbit coupling is very weak¹. Therefore, the lifetime of the T_1 state is long but not infinite. The intersystem crossing from triplet to singlet states and vice versa is partially allowed by the very weak spin-orbit coupling. When the molecules contain atoms heavier than carbon and hydrogen, for example bromine, iodine or especially heavy metal atoms like platinum or iridium, the intersystem crossing rate between the singlet and the triplet systems increases significantly due to the stronger spin-orbit interaction. In that case, the phosphorescent decay of excited triplet states can be very efficient. An example for phosphorescent emission will be discussed in Sec. 2.7.3.

In addition to the electronic energy levels, there are a number of superimposed vibrational sublevels which describe excited molecular vibrations within the molecule. A higher excited vibrational level rapidly relaxes back to the vibrational ground state of

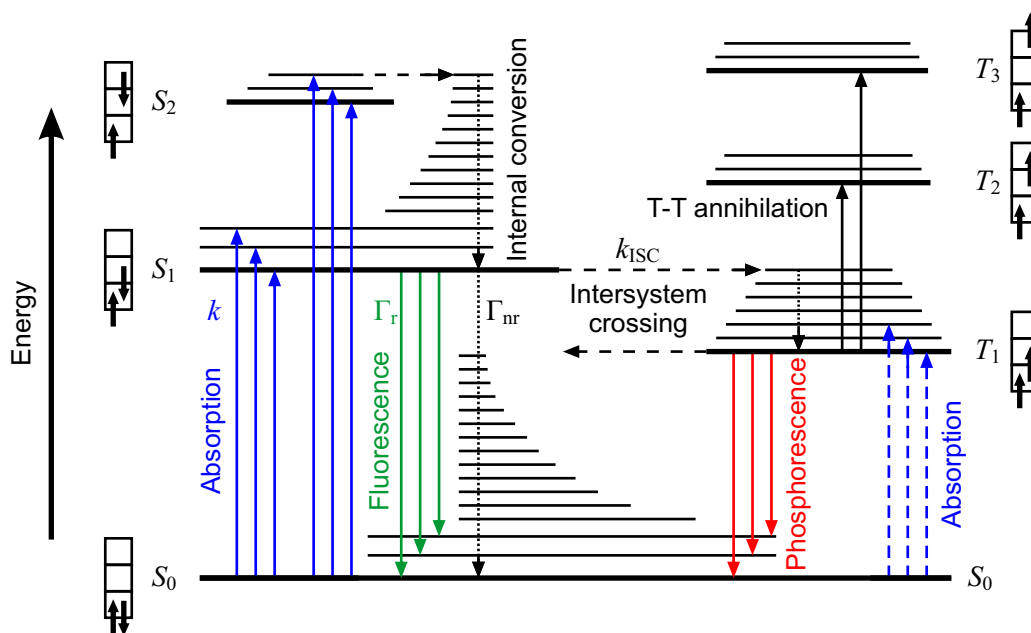


Figure 2.2: Energy level scheme of an organic molecule showing the most important transitions between various singlet levels (S_n) and triplet levels (T_n)^{1,19}. The orientation of the spins of the two outermost electrons is indicated for each electronic state. S_0 denotes the electronic ground state. The levels above each electronic state correspond to vibronic sublevels. Arrows with solid lines denote radiative transitions, those with broken lines refer to either nonradiative or normally forbidden transitions. The rate constant for absorption is indicated by k , the fluorescent decay rate by Γ_r , nonradiative transitions from singlet levels by Γ_{nr} and the intersystem crossing rate by k_{ISC} . Nonradiative transitions from triplet levels are not indicated. Strictly speaking, the discrete levels are only valid for free molecules whereas in disordered molecular films the states are more accurately described by broader excitonic bands, which are omitted for reasons of clarity.

the respective electronic state. According to the Franck-Condon principle, an electronic transition is more likely to happen if the vibrational wave functions of the initial and final state overlap more significantly. Generally, excited electronic states are spatially more extended and therefore the atoms in the molecule possibly have a different equilibrium distance in comparison to the ground state. Since electronic transitions are essentially instantaneous compared with the time scale of nuclear motion, it is likely that the transition from the lowest vibrational level of the S_0 state ends in a higher vibrational level of the S_1 state and vice versa. Thus, the absorption and emission spectra of organic molecules have mirror symmetry. Since the energy of an absorbed photon required to excite an electron from the S_0 state to a vibrational level of the S_1 state is larger than the energy of the reverse process of photon emission during a transition from the S_1 state back to a vibrational level of the S_0 state, the emission spectrum is red-shifted in comparison to the absorption spectrum. This effect is known as Stokes-shift and it is apparent in Fig. 2.3 which shows the absorption and fluorescence of tris-(8-hydroxyquinoline)aluminum (Alq_3). In addition, it can be seen that the

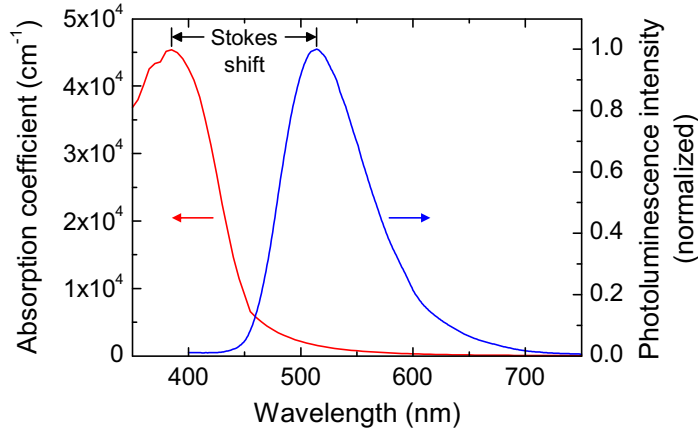


Figure 2.3: Absorption and fluorescence of Alq₃. The absorption coefficient α was calculated from the optical constants of Alq₃ (cf. appendix Sec. A.2) according to $\alpha = 4\pi \cdot \kappa/\lambda$, where λ is the wavelength and κ describes the extinction coefficient, i.e. the imaginary part of the complex index of refraction. The fluorescence spectrum represents the photoluminescence spectrum of a 50 nm thick Alq₃ film on a glass substrate under excitation with a 375 nm laser diode.

absorption coefficient of organic semiconductors for the allowed singlet-singlet transition is very large, for instance about $\alpha = 4 \times 10^4 \text{ cm}^{-1}$ in the case of Alq₃.

In addition to fluorescence and phosphorescence which describe transitions within one molecule, there are a number of less probable bimolecular excitonic processes many of which eventually lead to quenching, i.e. a nonradiative reduction of available excited states¹. For instance, two triplet excitons can combine according to the scheme $T_1 + T_1 \rightarrow S_0 + T_n \rightarrow T_1$. This process is called triplet-triplet annihilation and reduces the number of excited triplet states. On the other hand, two triplet excitons can also combine their energy and form a singlet exciton: $T_1 + T_1 \rightarrow S_0 + S_n \rightarrow S_1$. In this process, which is called delayed fluorescence^{20,21}, the excited state lifetime is determined by the triplet exciton lifetime whereas the quantum energy of the emitted radiation corresponds to singlet excitons. Additionally, singlet-triplet as well as singlet-singlet annihilation may occur. These quenching processes become stronger with increasing excitation intensity, i.e. with an increasing steady-state concentration of S_1 and T_1 excitons. Finally, excitons can also be quenched by charge carriers or at interfaces²²⁻²⁴. Especially an emitter position close to one of the electrodes results in significant quenching of excitons²⁵⁻²⁸.

2.3. OLED device structure and operation

In this section, the basic process of light emission through electrical excitation in an OLED will be discussed. In general, this effect is called electroluminescence (EL), whereas luminescence under excitation with light is termed photoluminescence (PL). From a historical point of view, the phenomenon of electroluminescence in organic

solids has been known for almost 50 years. Pope *et al.* as well as Helfrich and Schneider discovered and investigated the electroluminescence of anthracene single crystals between two electrodes^{29,30}. They used highly-purified crystal platelets with a thickness between 10 μm and 5 mm, hence a high voltage of several hundred to more than thousand volts was required in order to create electroluminescence from the thick crystals. In 1970, Williams and Schadt used laterally-structured electrodes to define the area of emission³¹. In addition, they encapsulated their device in order to protect it against air, in a manner that is basically still used today.

The major breakthrough occurred in 1987 when Tang and VanSlyke published their results about "Organic electroluminescent diodes"². They were the first to build a heterostructure OLED using low molecular weight evaporated organic thin films with a thickness of around 100 nm. This approach reduced the required voltage significantly, and an external quantum efficiency of 1 photon per 100 injected electrons was obtained. Three years later, Burroughes and co-workers produced the first OLED using polymers deposited from solution by spin coating³. These results were the beginning of a worldwide research and development in the field of OLEDs, both based on small molecules and polymers.

In principle, the simplest possible OLED consists of only one organic layer sandwiched between two electrodes, i.e. the anode and the cathode³². However, a multilayer OLED made of at least two organic layers is superior in terms of efficiency and lifetime because the properties of the OLED can be defined depending on the choice of materials. A typical stack layout of such an OLED is displayed in Fig. 2.4. The positively biased anode is required in order to inject holes into the hole transport layer (HTL), as will be explained below. Similarly, electrons are injected from the cathode into the electron transport layer (ETL). In some cases, the ETL is simultaneously the emission layer (EML)^{2,33}. In other cases, a separate layer is used as EML. High-efficiency OLEDs often employ many additional layers like separate blocking and injection layers. The individual functions and benefits of these layers will be discussed in Sec. 2.7.2.

The most common substrate material is glass, but also other materials can be used. For bottom-emitting OLEDs which emit light through the substrate, it is also possible to use transparent polymer foils. Moreover, top-emitting OLEDs may also be produced on metal foils or silicon wafers.

One of the two electrodes must be semitransparent so that the produced light can leave the device. Frequently, the anode of an OLED consists of indium-tin oxide (ITO), which is highly transparent and shows a good electrical conductivity. In general, anode materials need a high work function which makes also metals like gold a suitable choice. For the cathode, low work function metals like calcium or magnesium are often used in combination with a highly reflective and less reactive metal like aluminum or silver.

Since many organic materials and low work function metals are not stable under ambient conditions³⁴, i.e. they often react with oxygen and moisture, it is necessary

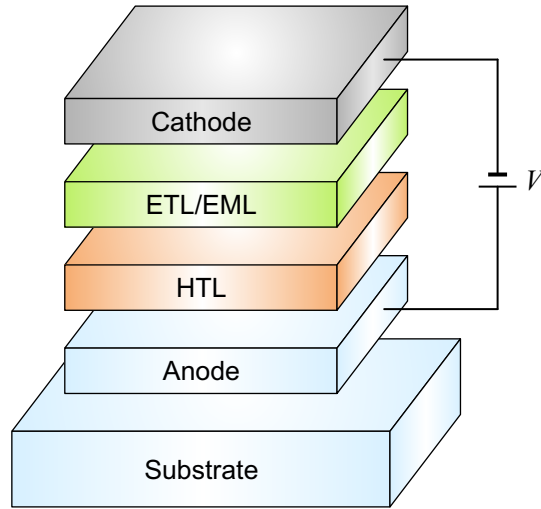


Figure 2.4: Simplified illustration of a two-layer OLED stack. ETL, EML and HTL denote the electron transport layer, the emission layer and the hole transport layer, respectively. In order to obtain light emission, a negative voltage must be applied to the cathode.

to protect the materials with an air-tight encapsulation. The most common method utilizes a cover glass that is glued to the substrate, thus creating a cavity filled with inert gas when the process is carried out in a glovebox system. In addition, a getter can be used in this cavity to absorb small amounts of oxygen and water that penetrate through the encapsulation in the course of time.

The active area of the OLED is defined as the overlap of the two electrodes. Hence, OLEDs can in principle have any shape and size and they are therefore suited for a wide range of applications, cf. Fig. 2.5. Laboratory OLEDs have a typical size of a few mm^2 . In commercial products the active area of the OLEDs has already been scaled-up to around 50 cm^2 and beyond. The thickness of the organic layers is typically in the range between 10 and a few 100 nanometers. Altogether, OLEDs are very thin, large-area light sources in contrast to other products which are usually either point sources, e.g. incandescent light bulbs or light-emitting diodes (LEDs), or linear light sources, e.g. fluorescent tubes.

The basic processes under operation are illustrated in Fig. 2.6 for an OLED with two organic layers¹. An external voltage source of typically a few volts is applied to the device so that the two types of charge carriers are injected from the opposite electrodes, i.e. electrons from the cathode and holes from the anode, and drift towards each other. When the initially free electrons and holes meet, they can create coulombically bound excitons in the organic layer by a diffusive process called Langevin recombination. Subsequently, these excitons may decay radiatively. In detail, the whole process can be separated into four fundamental steps as denominated in Fig. 2.6:

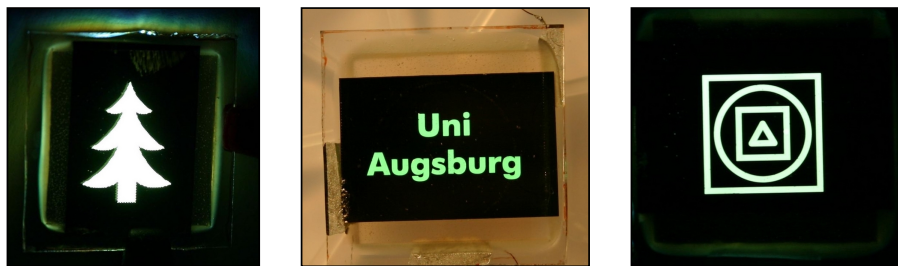


Figure 2.5: Different OLEDs demonstrating the facile manufacturing of arbitrary shapes. The photograph in the middle was recorded with some background illumination. The black area is the metallic cathode. The shape in all OLEDs was defined by a photolithography structuring step of a photoresist between two extensive electrodes. The left picture also shows some light emission through the edges of the device.

- (1) Injection of electrons and holes
- (2) Transport of charge carriers
- (3) Recombination of electrons and holes to form excitons
- (4) Radiative exciton decay and emission of light

As mentioned above, the anode should have a high work function Φ_A whereas the cathode ideally has a low work function Φ_C , so that the barriers for the injection of holes into the HOMO and for the injection of electrons into the LUMO are as small as possible. For this to occur, the respective energy barriers $\Phi_{B,h}$ and $\Phi_{B,e}$ must be overcome. The contact of the two electrodes across the organic layers produces an internal electric field with the built-in voltage Φ_{BI} . This prevents the transport of injected electrons and holes when no external voltage is applied. Current can only flow if a negative voltage is applied to the cathode and if the external voltage is larger in magnitude than the built-in contact potential. When electrons and holes meet in the device, they can form excitons which finally can decay radiatively and contribute to the electroluminescence. With a suitable choice of layer thicknesses, recombination occurs only in the neighborhood of the HTL/ETL interface. This is favorable because recombination near the electrodes usually causes quenching and therefore a reduction in efficiency. Both the energy gap and the exciton energy, and thus the wavelength of the emitted light, depend on the utilized materials. With the great variety of applicable organic semiconductors to choose from, it is possible to fabricate OLEDs with emission colors in the whole visible spectral range. Examples for different types of OLEDs with a variety of emission colors will be presented in Sec. 2.7.3.

One of the peculiarities of organic emitters is their intrinsic broad spectrum which can also be seen in Fig. 2.3. By the combination of several organic emitters with different emission spectra it is possible to create a very broad white emission spectrum with an excellent color rendering index (CRI), i.e. the ability to reproduce the color of

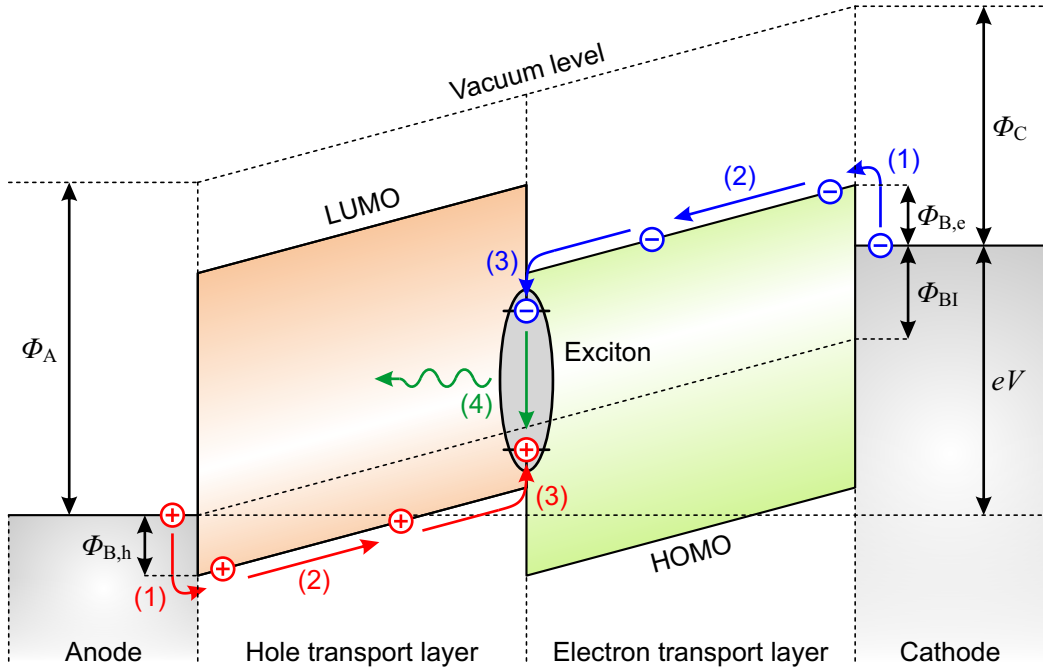


Figure 2.6: Schematic energy diagram and charge carrier processes in a two-layer OLED illustrating the basic processes of electroluminescence. (1) Injection of electrons from the cathode into the LUMO and of holes from the anode into the HOMO, (2) transport of charge carriers, (3) recombination of electrons and holes to form excitons, and (4) radiative exciton decay and emission of light. $\Phi_{B,h}$ describes the injection barrier for holes whereas $\Phi_{B,e}$ is the barrier for electrons. Since the anode and cathode have different work functions Φ_A and Φ_C , respectively, a built-in voltage Φ_{BI} exists in the device. Therefore, an external voltage V is applied with its polarity chosen to allow the current to flow in the pass direction through the diode, thus lifting the cathode level by eV with e describing the elementary charge. If the polarity is reversed, neither electrons nor holes can be transported³³. Under forward bias, charge carriers are blocked by the barrier at the interface between both organic materials which results from the differences in HOMO and LUMO levels. Thus, recombination occurs close to the interface in the ETL which is also the emission layer. It should be noted that HOMO and LUMO levels are not sharp in these noncrystalline layers, but are drawn as sharp levels for clarity.

illuminated objects. This is a clear advantage in comparison to fluorescent tubes and LEDs which intrinsically have narrow emission bands and thus require additional color conversion.

There are several methods in order to create OLEDs with a white emission spectrum^{35,36}. For example, three separate OLEDs with blue, green and red emission color may be placed next to each other. This is common in displays but it is not appropriate for applications in general lighting which requires a large, homogeneous emission area. For this purpose, it is more suitable to stack three emission layers on top of each other within one OLED or to stack three complete monochromatic OLEDs. In addition, white light from OLEDs may be produced similar to inorganic LEDs, i.e. by combining a blue OLED with either red and green or yellow external color converters^{35,37}. Depending on

the method and the choice of materials it is possible to cover a large variety of colors and color temperatures within the CIE 1931 color space (*Commission internationale de l'éclairage*).

2.4. External quantum efficiency

Apart from its spectral characteristics, the most important parameter characterizing an OLED is the external electroluminescence quantum efficiency (EQE) that describes the ratio between the number of emitted photons and injected charge carriers³⁸:

$$\eta_{\text{EQE}} = \gamma \cdot \eta_{\text{ST}} \cdot q_{\text{eff}} \cdot \eta_{\text{out}}. \quad (2.1)$$

Here, γ describes the charge carrier balance, η_{ST} is the fraction of spin-allowed excitons (sometimes called singlet/triplet factor), q_{eff} represents the effective radiative quantum efficiency of the emitting material, and η_{out} is the outcoupling efficiency.

The charge carrier balance γ depends on the number of electrons and holes that are injected and transported per unit of time. If all injected electrons and holes are consumed by recombination, then $\gamma = 1$. If the numbers of electrons and holes are different, then the excess part of the charge carriers does not contribute to the production of light, and the efficiency of the OLED is reduced. The charge carrier balance can be brought close to unity by using multilayer stacks with doped transport layers and additional blocking layers, cf. Sec. 2.7.2.

The fraction of spin-allowed excitons η_{ST} describes the probability of formation of an exciton that is allowed to decay radiatively according to the spin selection rules. Under electrical operation, singlet and triplet excitons are formed by recombination of electrons and holes. However, the probability of forming a triplet exciton is statistically three times higher than the probability of forming a singlet exciton, since the distribution of spin orientations of the injected electrons and holes is isotropic and every triplet state is threefold degenerate. Therefore, η_{ST} is believed to have a value of 25% for fluorescent emitters which only make use of singlet excitons^{39,40}. However, this value might be enhanced by triplet-triplet annihilation^{20,21}. In the context of conjugated polymer systems, there has been a debate whether the value might even be larger than 25%^{41–45}. A significant efficiency enhancement can be obtained by using phosphorescent materials which harvest both singlet and triplet excitons, hence η_{ST} can be raised to 100%^{46–48}.

The effective radiative quantum efficiency q_{eff} corresponds to the radiative (also PL or intrinsic) quantum efficiency q , i.e. the ratio of the number of emitted photons to the number of absorbed photons under PL excitation, modified by the cavity of the OLED

device^{8,26,49}. The intrinsic radiative quantum efficiency q of an emitter is defined as

$$q = \frac{\Gamma_r}{\Gamma_r + \Gamma_{nr}}, \quad (2.2)$$

where Γ_r is the radiative decay rate and Γ_{nr} is the sum of all competing nonradiative decay rates. It is apparent that every nonradiative contribution to the decay reduces the radiative quantum efficiency. Certainly, q should be close to 1 and fortunately there is a wide range of materials with a value of q between 0.5 and 1.

In an infinite homogeneous medium, q_{eff} and q are identical. However, due to the many layers with different optical properties in an OLED, interference effects modify the radiative rate $\Gamma_r \rightarrow \Gamma_r^* = F \cdot \Gamma_r$. Here, F describes the Purcell factor^{50,51}. By contrast, the nonradiative decays like dissipation of excitation energy into heat are not influenced by the cavity environment⁵². Thus, the effective radiative quantum efficiency q_{eff} can be defined as

$$q_{\text{eff}} = \frac{\Gamma_r^*}{\Gamma_r^* + \Gamma_{nr}} = \frac{F \cdot \Gamma_r}{F \cdot \Gamma_r + \Gamma_{nr}}. \quad (2.3)$$

The cavity effect can either increase or reduce the effective radiative quantum efficiency. Consequently, the optimization of the OLED cavity is very important in terms of efficiency as will be discussed in Secs. 5.1 and 5.5.

The product of the factors γ , η_{ST} and q_{eff} represents the internal quantum efficiency η_{int} which describes the number of photons produced within a device divided by the number of injected charges. Thus, Eq. (2.1) can be written as

$$\eta_{\text{EQE}} = \eta_{\text{int}} \cdot \eta_{\text{out}}. \quad (2.4)$$

By the utilization of phosphorescent emitters with high radiative quantum efficiency, η_{int} can approach values close to one^{53–55}.

The outcoupling or light extraction efficiency η_{out} describes the amount of generated photons that can be extracted from the device. Unfortunately, there are several optical loss channels besides the desired direct emission, hence η_{out} is the main factor in Eq. (2.1) that still strongly limits the EQE. Since light extraction is the major subject of this thesis, the characteristics of η_{out} and all optical loss channels will be explained in detail in the next section.

In order to quantify the amount of visible light reaching the observer, one has to consider the sensitivity of the human eye. The luminous flux Φ_v is obtained by multiplying the radiant flux per wavelength $\Phi_{R\lambda}$ with the response curve of the eye $V(\lambda)$ (also known as luminosity function) and integrating over the whole visible spectral range⁵⁶:

$$\Phi_v = K_m \int_{380 \text{ nm}}^{780 \text{ nm}} V(\lambda) \cdot \Phi_{R\lambda} d\lambda, \quad (2.5)$$

with the photopic constant $K_m = 683 \text{ lm/W}$. The units of Φ_v and $\Phi_{R\lambda}$ are $[\Phi_v] = 1 \text{ lm}$

(lm = lumen) and $[\Phi_{R\lambda}] = 1 \text{ W/nm}$, respectively.

Besides the external quantum efficiency, the luminous efficacy η_P (often called luminous power efficiency) is an important parameter which describes the ratio of the luminous flux Φ_V to the electrical input power as^{1,57,58}

$$\eta_P = \frac{\Phi_V}{I \cdot V}, \quad (2.6)$$

where V is the operating voltage and I describes the current. The unit of η_P is $[\eta_P] = 1 \text{ lm/W}$.

For a Lambertian light source, the luminous intensity $I_V(\theta)$ at an angle θ to the surface normal is $I_V(\theta) = I_0 \cdot \cos \theta$ with I_0 being the luminous intensity emitted perpendicular to the surface. For such a light source, the luminance L_V is constant for all viewing angles and the luminous efficacy simplifies to

$$\eta_P = \frac{\pi \cdot \text{sr} \cdot L_V}{j \cdot V}, \quad (2.7)$$

with j describing the current density^{1,59}. The units of I_V , L_V and j are $[I_V] = 1 \text{ cd}$, $[L_V] = 1 \text{ cd/m}^2$ and $[j] = 1 \text{ mA/cm}^2$, respectively. In Eq. (2.7), sr (steradian) represents the unit of solid angle ($1 \text{ sr} = 1 \text{ m}^2/\text{m}^2 = 1$), which is strictly speaking required to convert candela into lumen ($1 \text{ lm} = 1 \text{ sr} \cdot \text{cd}$). All factors on the right hand side of Eqs. (2.6) and (2.7) can be measured, hence η_P is an observable.

Another quantity that basically characterizes an OLED is the current efficiency η_L . It is defined as the ratio between luminance and current density⁵⁷:

$$\eta_L = \frac{L_V}{j}. \quad (2.8)$$

The unit of η_L is $[\eta_L] = 1 \text{ cd/A}$. Since both luminance and current density are directly measurable, the current efficiency can be determined rather easily.

Although the applied voltage has no immediate effect on η_{EQE} and η_L , it directly influences the luminous efficacy η_P . Consequently, it is important to keep voltage losses due to charge injection barriers and charge transport resistance as low as possible in order to produce a sustainable OLED with low power consumption.

2.5. Optical loss channels

As mentioned above, the outcoupling efficiency η_{out} still is a strongly limiting factor for high-efficiency OLEDs. The main problems arise from total internal reflection due to the high refractive index of the organic layers ($n_{\text{organic}} = 1.7 - 2.2$ depending on wavelength and material) in comparison to air ($n_{\text{air}} = 1.0$) and glass ($n_{\text{glass}} \approx 1.5$) as well as from coupling to the metallic cathode, as will be explained on the basis of Fig. 2.7.

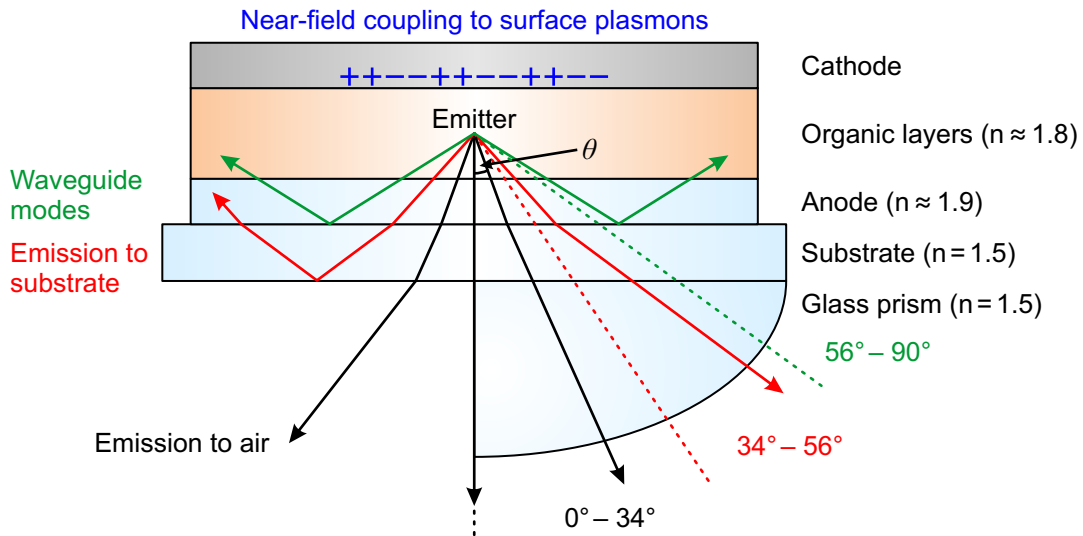


Figure 2.7: Schematic illustration of an OLED showing all optical loss channels. Without outcoupling enhancement, only a small fraction of light is directly emitted to air as shown in the left part of the figure. By applying e.g. an index-matched glass hemisphere, also the substrate emission can be extracted, cf. the right part of the figure.

Since nonradiative transitions, e.g. dissipation of excited energy into heat, are already included in the effective radiative quantum efficiency q_{eff} , the following discussion about the outcoupling efficiency only treats radiative transitions. Generally, an excited state can radiatively couple to one of the following four optical channels:

- **Direct emission:**

The direct emission to air is the only desired optical channel in a standard planar device that generates radiation which may be used for e.g. illumination purposes if no outcoupling structure is applied to the OLED, cf. left part of Fig. 2.7. Due to the refraction at the interfaces, radiation can only leave the device if the emission angle θ in the organic layers is smaller than around 34° with respect to the surface normal (assuming $n_{\text{organic}} = 1.8$).

- **Substrate emission:**

For larger emission angles between 34° and 56° , total internal reflection occurs at the interface between air and glass, so that the radiation is trapped within the glass substrate. This optical channel is often referred to as substrate modes. By applying an outcoupling enhancement structure, e.g. an index-matched glass hemisphere, total internal reflection at the air/glass interface is circumvented and the substrate emission can leave the device, thus contributing to the useful radiation as depicted in the right part of Fig. 2.7.

- **Waveguide modes:**

If the light is emitted under angles larger than 56° , the light is totally reflected

at the interface between glass and the anode, which in the case of ITO has a comparable refractive index ($n_{\text{ITO}} = 1.7 - 2.1$) as the organic layers. Thus, the light is waveguided between the glass/anode interface and the reflecting cathode, and may finally leave the device through the edges.

- **Surface plasmons:**

The main optical loss channel besides waveguide modes is coupling to surface plasmon polaritons (or simply surface plasmons, SPs), i.e. guided electromagnetic surface waves traveling along the interface between a dielectric and a metal. The properties of SPs will be explained in detail in Chapter 4. Since the emitting molecules in OLEDs usually are located in close proximity to a metallic interface, it is possible to excite SPs via the optical near-field of the excited molecule. The SPs travel along the organic/metal interface and are eventually dissipated into heat.

In addition to these optical decay channels, light can also be absorbed by the organic layers or the electrodes before it is emitted into air or the substrate. Naturally, this effect is more pronounced in OLEDs comprising very thick organic layers but it also depends on the absorption coefficient of the used materials.

Apparently, a large fraction of the produced radiation cannot leave the device but instead is either trapped as substrate and waveguide modes or coupled to SPs. Therefore, the light extraction efficiency and, as a consequence, the external quantum efficiency are significantly limited. A rough estimation under the assumption of isotropic molecular orientation and Lambertian emission yields an outcoupling efficiency of

$$\eta_{\text{out}} \approx \frac{1}{2n^2}, \quad (2.9)$$

where n is the refractive index of the emitting material^{38,59}. For a refractive index of $n_{\text{organic}} = 1.8$ this yields a rough limit for the outcoupling efficiency of $\eta_{\text{out}} = 15\%$. In other words, 85% of the generated radiation is dissipated to unfavorable optical channels. This estimate is also supported by optical simulations of a typical OLED with optimized cavity structure where only about 20% of the light is emitted directly into air and around 20% to 30% is trapped inside the glass substrate^{8,13,14,60}. Coupling to waveguide modes and SPs causes losses of typically 50% in conventional small molecule based OLEDs.

Therefore, it is of crucial importance to enhance the outcoupling efficiency by either reducing coupling to waveguide modes and SPs or by recovering some of these losses. Chapter 6 will give an overview of different techniques for increased light extraction that have been published in literature in the previous two decades. Subsequent chapters will present detailed experimental results and extensions for some of these methods as well as novel approaches that have been developed during the work for this thesis.

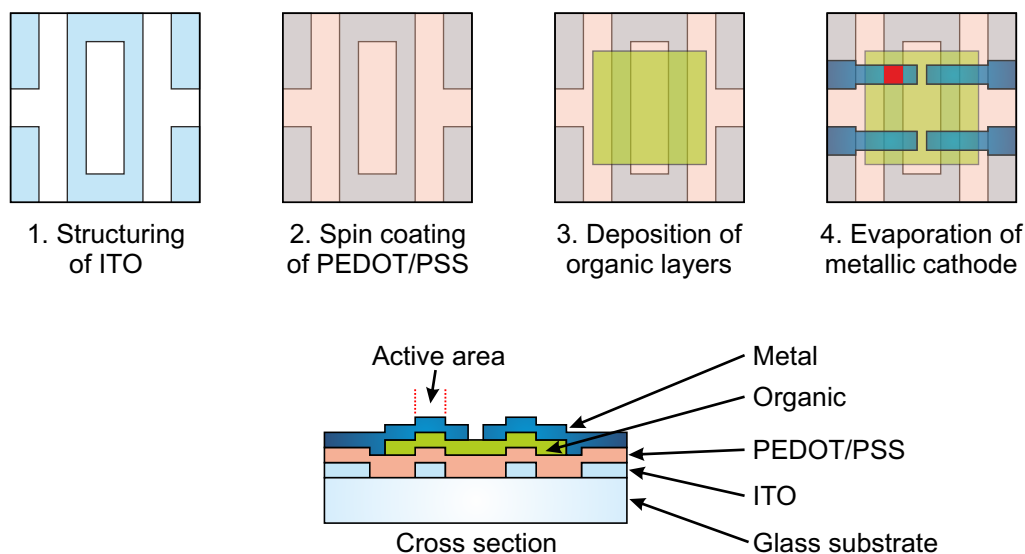


Figure 2.8: Main steps of the OLED preparation process illustrating the shadow masks used for the deposition of each layer. The active area is defined by the overlap of the cathode and the anode as depicted by the red area and in the cross section. It should be noted that the thicknesses are not true to scale. The four corners in the ITO structure overlap with the cathode and thus simplify the application of electrical contacts to the OLED. The corners are separated from the active area by several millimeters so that negligible conduction occurs through the PEDOT/PSS layer which covers the whole sample.

2.6. OLED preparation

This section explains the basic steps for fabricating typical small molecule OLEDs as illustrated in Fig. 2.8. All OLEDs were fabricated on commercial glass substrates with a size of $20 \times 20 \text{ mm}^2$ covered with 140 nm thick ITO as anode material. The ITO layer is structured in a photolithography process in a cleanroom. A photoresist is spin coated on the substrates, then dried by baking and finally exposed to UV light through a shadow mask. After developing, the uncovered ITO areas are etched in hydrochloric acid. Finally, the remaining photoresist is lifted-off, yielding the ITO structure as shown in Fig. 2.8. After cleaning in ultrasonic baths with acetone, isopropyl alcohol and high purity water, the substrates are exposed to an oxygen plasma to remove any residues and to increase the work function of ITO⁶¹. Then, an approximately 30 nm thick layer of poly(3,4-ethylenedioxythiophene) poly(styrenesulfonate) (PEDOT/PSS, AI 4083, H.C. Starck) is deposited onto the whole substrate by spin coating and subsequently dried on a hot plate. This polymer layer helps to smooth the ITO surface and improves the injection of holes into the organic layers. The chemical structure of PEDOT/PSS is shown in Fig. 2.9.

Afterwards, the samples are transferred from the cleanroom to an evaporation chamber which is attached to a nitrogen filled glovebox. The chamber has a base pressure of typically 3×10^{-7} mbar. It contains six effusion cells for the thermal evaporation

of organic materials and three places for the deposition of metals by resistive heating using boats (e.g. for silver) or baskets (e.g. for aluminum). The deposition rates are monitored using quartz crystal microbalances. Two of the effusion cells for organic materials have a separate microbalance in order to independently control small rates during the co-evaporation of two organic materials, which is required for doping of a guest material into a host matrix. Typical deposition rates for organic materials and metals are 1.2 \AA/s and 1.5 \AA/s , respectively.

The evaporation chamber has a rotary mask and sample holder system. Four samples are placed in one holder, which in turn may be positioned at four different places, each equipped with selectable shadow masks. Organic layers are usually deposited through a square mask as shown in Fig. 2.8. The metallic cathode is evaporated using a shadow mask with four separate openings. The active area of $2 \times 2 \text{ mm}^2$ is defined by the overlap of the ITO anode and the cathode. Finally, the samples are encapsulated in the glovebox using a cover glass and either a two-component glue or a UV-curing epoxy with small spacers to form an inert gas cavity.

Comparing the fabrication of OLEDs based on small molecules and polymers, a clear advantage of small molecules is the possibility to fabricate OLEDs with many different and even doped layers, allowing for an optimization of the optical and electrical properties. Small molecule OLEDs are further compatible with commercial in-line deposition processes. Although polymers usually are decomposed by evaporation, they are well suited for cost-efficient printing and roll-to-roll processes. However, it is much more complicated to fabricate multilayer polymer OLEDs because orthogonal solvents are required so that the previously deposited layers are not redissolved. Frequently, PEDOT/PSS is used in polymer OLEDs because it can be spin coated from an aqueous dispersion and therefore is compatible to polymers which are deposited from organic solvents. It should also be noted that it is possible to produce multilayer polymer OLEDs by crosslinking which renders a polymer layer almost insoluble⁶². However, small molecule OLEDs typically have a higher efficiency and lifetime in comparison to polymer OLEDs.

2.7. Basic stack design

The external quantum efficiency of an OLED with a singlet emitter remains small even if the electron and hole currents are equal ($\gamma = 1$), and even if the organic layer has a large radiative quantum efficiency, e.g. $q = 50 \%$. In detail, according to Eq. (2.1) this yields an EQE of only $\eta_{ext} \approx 1 \cdot 25 \% \cdot 50 \% \cdot 15 \% \approx 2 \%$. From this estimate, it becomes clear which measures must be taken to optimize OLEDs in order to achieve a high efficiency: a radiative decay from triplet states needs to be obtained, the balance between electron and hole currents must be maintained, emission layers with high radiative quantum efficiency must be used and the light extraction must be improved.

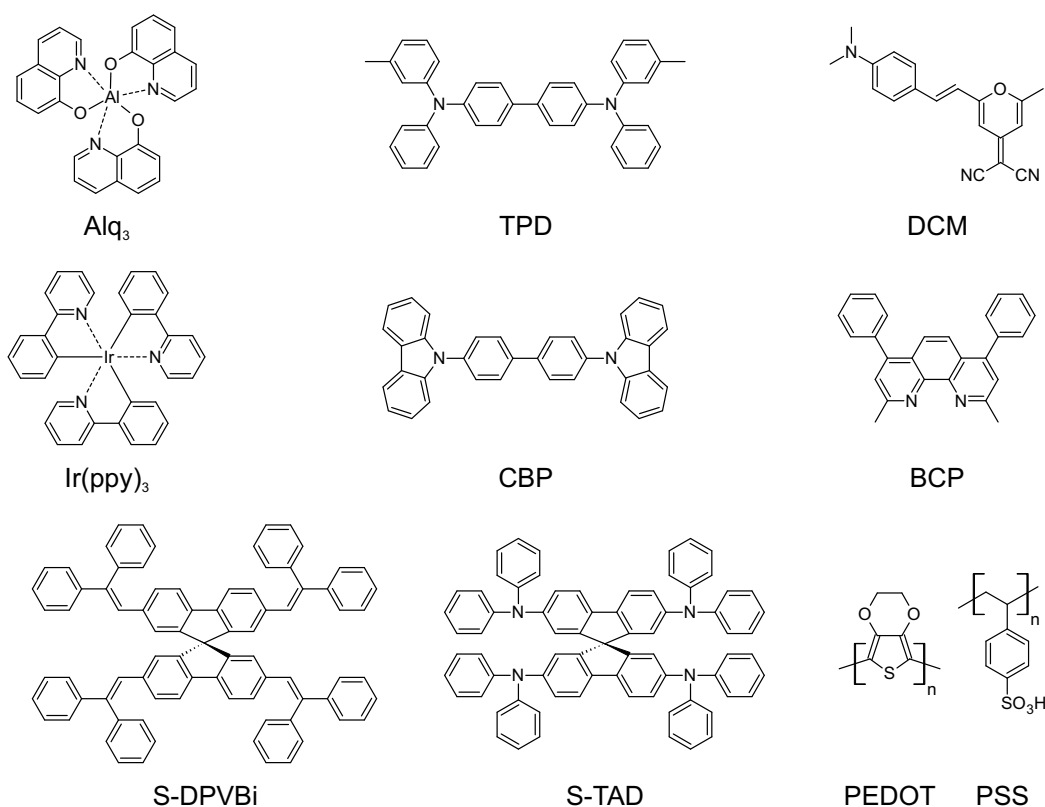


Figure 2.9: Organic materials used for fabricating OLEDs in this section. In the displayed skeletal formulas, carbon atoms are located at all vertices and termini of line segments without being indicated with the atomic symbol C. Hydrogen atoms attached to carbon atoms are not shown in this notation. Since each carbon atom has four bonds, the correct number of hydrogen atoms is well-defined. The chemical formula for each material as well as its function in an OLED is explained in the text.

This section shows examples of bottom-emitting OLED devices in order to demonstrate some basic rules for stack design. At the beginning, the organic materials used in the devices are explained. The first presented OLED uses a green fluorescent emitter with only moderate efficiency, next a higher efficiency three-layer blue OLED will be shown. Then, the effect of doped emitting layers is introduced using an exemplary red fluorescent OLED. Finally, a very efficient green phosphorescent OLED with additional blocking layer is presented. Almost the same stack layouts as shown in Sec. 2.7.3 are also used for OLEDs in Sec. 4.5 where they are applied as light sources for a surface plasmon resonance sensor. Although this section explains several basic ideas about efficient OLED stack design, particular strategies for increasing the light outcoupling efficiency will be explained separately in Chapter 6.

2.7.1. OLED materials

A selection of common organic materials that were used for fabricating OLEDs in the course of this thesis are displayed in Fig. 2.9. A well-known fluorescent emit-

ting material is tris-(8-hydroxyquinoline) aluminum (Alq_3), which was already used by Tang and VanSlyke². It emits in the green wavelength range and is widely used as an exemplary material despite its rather low radiative quantum efficiency of $q \approx 20 - 25\%$ ⁶³⁻⁶⁶. It also has good electron conducting properties and is often combined with N,N'-diphenyl-N,N'-bis(3-methylphenyl)-1,1'-biphenyl-4,4'-diamine (TPD), which is used as hole transporting material even though it has a low melting point and crystallizes at temperatures around 80 °C, which then destroys the OLED. As an alternative to TPD, it is possible to use 2,2',7,7'-tetrakis-(N,N-diphenylamino)-9,9'-spiro-bifluoren (S-TAD), which has a significantly higher melting point⁶⁷. Other fluorescent emitters are 4-(dicyanomethylene)-2-methyl-6-(4-dimethylaminostyryl)-4H-pyran (DCM) with red emission and 4,4'-bis(2,2'-diphenylvinyl)-1,1'-spirobiphenyl (S-DPVBi) with an emission in the blue spectral region.

As mentioned before, the efficiency of an OLED can be considerably enhanced by the utilization of phosphorescent emitters which are usually used as a guest-host system. A very famous example is the green phosphorescent emitter tris(2-phenylpyridine) iridium ($\text{Ir}(\text{ppy})_3$), which is often doped into 4,4'-N,N'-dicarbazole-biphenyl (CBP). It may also be beneficial to use blocking layers, for instance 2,9-dimethyl-4,7-diphenyl-1,10-phenanthroline (BCP), as will be explained in the next section.

2.7.2. Blocking, injection and transport layers

In small molecule based OLEDs which are deposited from the vapor phase, it is possible to use many layers with different properties. The optimization of the efficiency using multilayer OLEDs may in principle be achieved by optimizing each layer for an individual process, provided it is neutral for the other processes. For instance, it is possible to implement a hole blocking layer (HBL) that prevents holes from passing into the ETL and thus not contributing to the emission. In addition, electron blocking layers (EBL) can be used to further improve the charge carrier balance⁶⁸. Blocking layers can also inhibit exciton diffusion into adjacent layers²³. Hence, it is possible to clearly confine the recombination zone within the emission layer.

In addition, hole and electron injection layers (HIL and EIL) can be used. These layers feature a HOMO and LUMO, respectively, that lies between the level of the electrode and the corresponding transport layer, thus reducing the barrier for injection of charge carriers. In principle, calcium and PEDOT/PSS may be used as injection layers which improve the charge carrier injection from the metallic electrode and ITO, respectively. Besides calcium and other low work function metals, LiF in combination with aluminum is also often used as EIL^{34,69}.

The mobilities μ of the charge carriers vary strongly in the different materials: there are some materials in which predominantly electrons are transported ($\mu_e \gg \mu_h$), and some in which mainly holes participate in the transport ($\mu_h \gg \mu_e$). The transport layers may also be doped in order to improve the transport of charge carriers. For

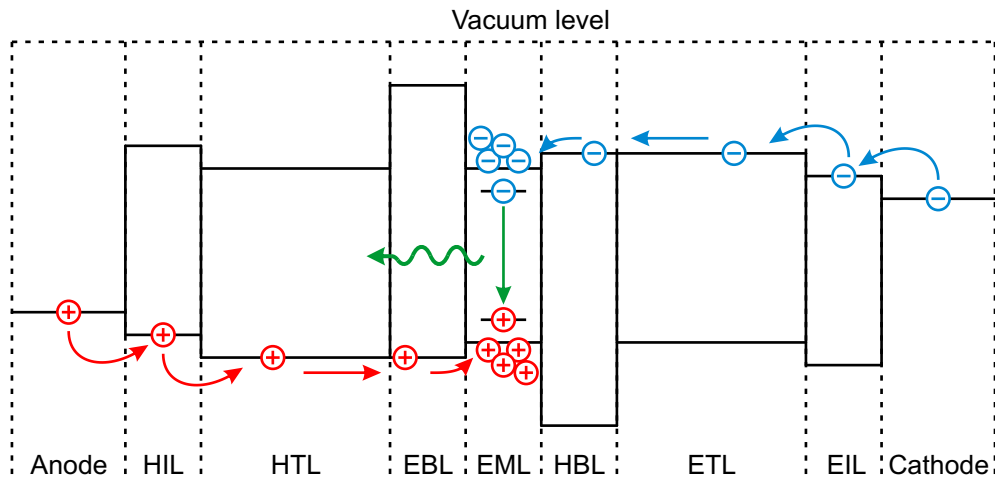


Figure 2.10: Schematic HOMO and LUMO levels of a highly efficient OLED comprising injection, transport and blocking layers for both holes and electrons in case of no applied external voltage. The emission layer typically consists of an efficient guest-host system in which the HOMO level of the dopant lies above and the LUMO level below the respective levels of the matrix so that excitons are trapped on the dopant. Therefore, recombination takes place on guest molecules which results in a corresponding emission of radiation.

example, tetrafluoro-tetracyanoquinodimethane (F_4 -TCNQ) and LiF can be used as p- and n-dopants, respectively^{70–72}. Since doped transport layers have a very low resistance, the thickness can be adjusted in order to obtain optimal interference for the emission layer within the cavity resonator^{49,73,74}. The cavity optimization will be discussed separately in Sec. 5.5. In addition, doping of the transport layers causes strong band bending at the electrodes and thus enables tunneling of charge carriers into the organic layers, thus allowing for injection from a wide range of cathode materials with different energy levels^{49,70,75}.

A schematic band diagram of a multilayer OLED stack incorporating all discussed layers is shown in Fig. 2.10. In addition, several emitting layers in order to create white OLEDs can be used as discussed in Sec. 2.3. Furthermore, two or more emission layers in stacked OLEDs may be connected by using charge generation layers, thus usually creating OLEDs with considerably more than ten layers⁷⁵.

In the following, four exemplary OLEDs will be introduced in order to discuss some basic stack design rules. Each OLED stack will be accompanied by an energy level diagram, as well as by a photograph of the OLED under electrical operation and by a measured emission spectrum.

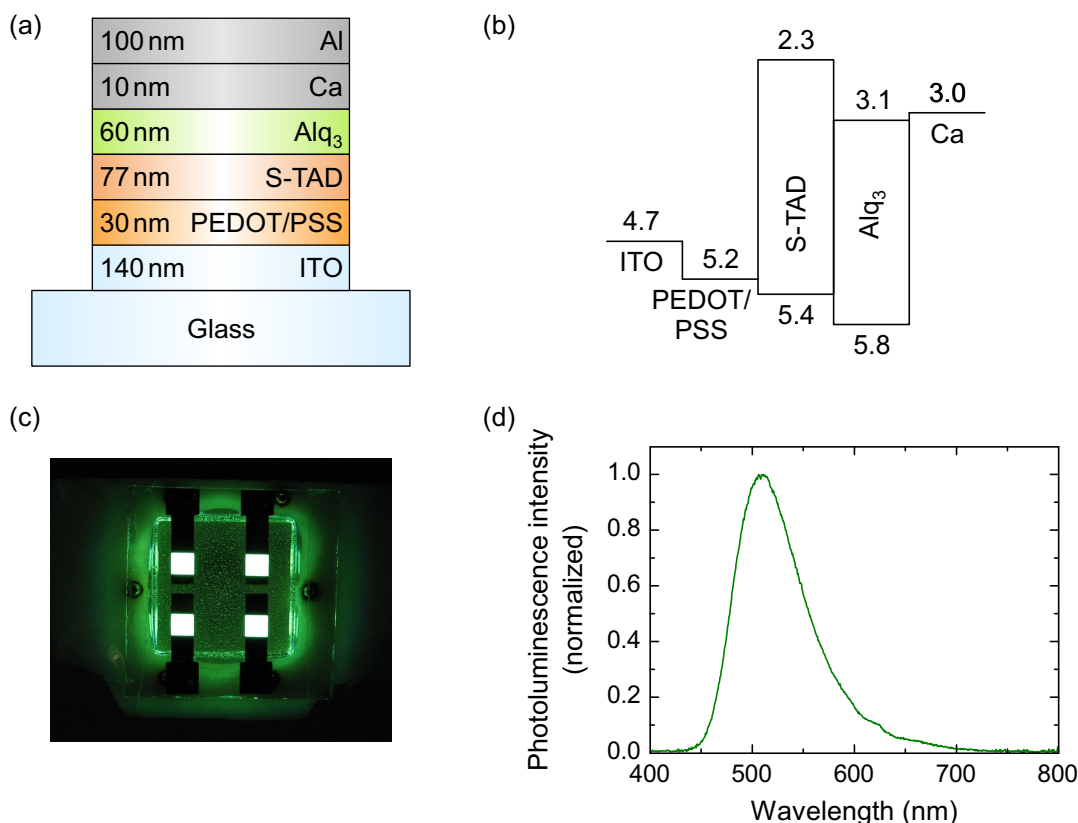


Figure 2.11: (a) Stack layout of the two-layer green OLED. The thickness of the Alq₃ and S-TAD layers were determined by comparison to simulations, cf. Sec. 5.3. Actually, a thickness of 80 nm Alq₃ was intended. The deviation probably results from a wrong tooling factor or from a much too high or low filling level of the effusion cell. Concerning the S-TAD thickness, 80 nm were planned which agrees perfectly with the control by simulations. (b) Schematic energy level diagram of the OLED. It is important to note that HOMO and LUMO levels are not sharp in these noncrystalline layers, but are drawn as sharp levels for clarity. The energy levels for a certain material often differ by several tenth of an electron volt depending on the reference. Therefore, most energy levels in this section were averaged based on several references^{24, 76–83}. Strictly speaking, all energy levels should be negative to represent the difference with respect to the vacuum level. However, the minus sign was omitted for reasons of clarity. (c) Photograph showing light emitted through the bottom side. For the photograph, the device is mounted on a sample holder that includes six contact pins. Apparently, a certain fraction of light is guided in the organic layers or the substrate and is then scattered by the epoxy or emitted through the edges. Camera settings for comparison to other pictures: f-number f/2.8; exposure time 0.6 s. (d) EL emission spectrum in bottom direction measured normal to the substrate.

2.7.3. Exemplary OLED stacks

Two-layer green OLED

The stack layout of an exemplary green fluorescent two-layer OLED, i.e. two organic layers in addition to the electrodes and PEDOT/PSS, is shown in Fig. 2.11(a). The well-known material Alq₃ is used as both electron transport layer and emission layer in

this OLED stack. The cathode comprises a thin layer of the low work function metal calcium in combination with the more stable aluminum. This reduces the work function from about 4.2 eV (Al) to 3.0 eV (Ca)^{76,78,83}.

Alq₃ and S-TAD are good electron and hole transport materials, respectively, but they do not have good transport properties for the opposite charge carrier type. Therefore, charge carriers are partly blocked at the interface between Alq₃ and S-TAD, as can also be seen in Fig. 2.11(b). The recombination and thus the light emission occurs in the Alq₃ layer, to the most part in a thin region near the interface. Hence, nonradiative recombination in the neighborhood of the cathode is minimized. The emission maximum of Alq₃ is usually located between 510 nm and 530 nm as can be seen by the photograph and emission spectrum in Figs. 2.11(c) and (d), respectively. It is apparent that organic emitters typically have broad emission spectra, which makes them ideally suited for lighting applications that require a high color rendering index.

Although the radiative quantum efficiency of Alq₃ is rather low, this OLED stack with its well-known materials will be used as exemplary device throughout this thesis. Current-voltage-luminance characteristics will be shown in Sec. 2.7.4. This OLED will also be used in order to discuss different light extraction approaches as well as to study the results of optical simulations which will be presented in Chapter 5. Angular dependent emission spectra will be discussed in Sec. 5.3.

Three-layer blue OLED

A further improvement can be obtained by using three organic layers as depicted for a blue fluorescent OLED in Fig. 2.12(a). By choosing the HOMO and LUMO levels of the organic layers appropriately, a three-layer OLED basically offers the advantage that the recombination zone can be completely confined if electrons are blocked at the interface to the HTL and holes are blocked at the ETL interface²³, cf. Fig. 2.12(b). It should be noted, however, that the three organic layers have not been optimized according to their energy levels but the OLED is rather used to introduce the basic concept. The emitting layer consists of S-DPVBi which has a blue emission around 465 nm, cf. Figs. 2.12(c) and (d). In comparison to Alq₃, S-DPVBi has a very high radiative quantum efficiency. For example, $q = 82\%$ was reported for S-DPVBi in a C₆H₁₂ solution⁶⁷. The devices are very stable because the spiro compounds S-DPVBi and S-TAD have a rather high glass transition temperature of around 130 °C.

Red OLED with fluorescent guest-host system

An approach for high-efficiency OLEDs is doping, i.e. the implementation of a small amount of guest molecules in a host matrix. Doping in order to improve the electrical properties was already discussed in Sec. 2.7.2. Here, the effect of doping an emitter into a matrix in order to improve the optical properties and recombination efficiency

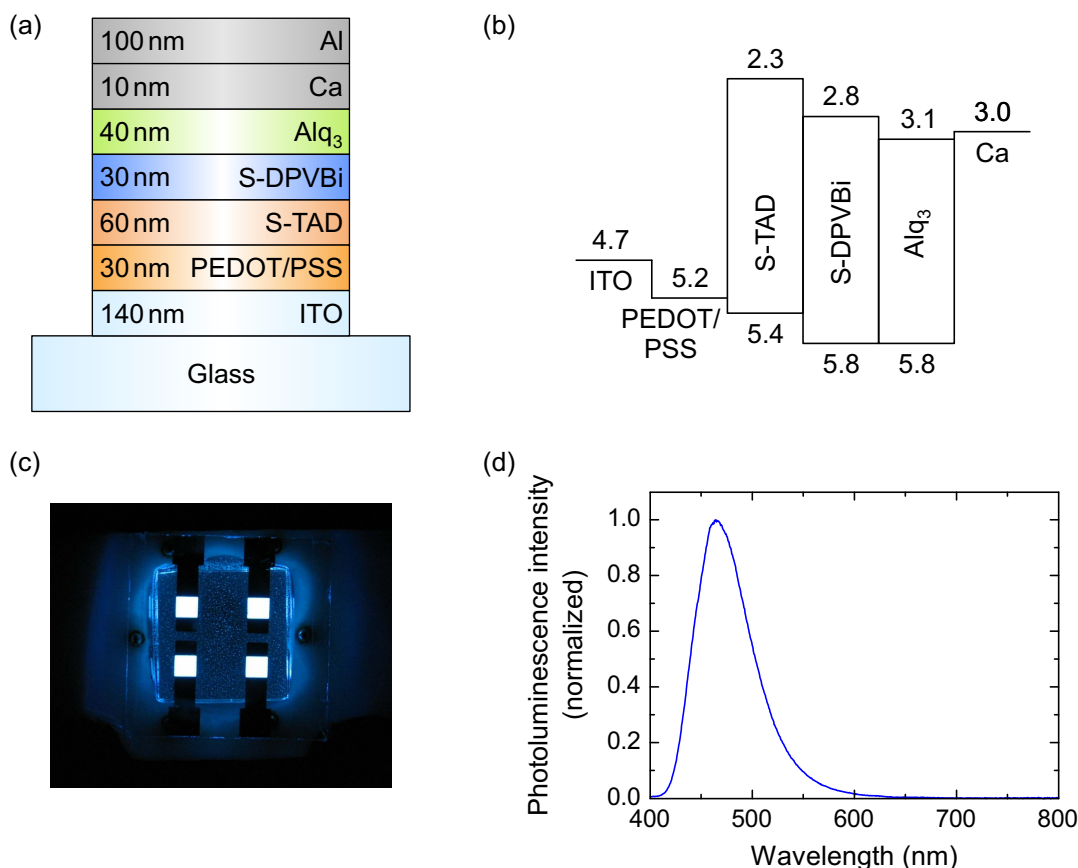


Figure 2.12: (a) Illustration of the three-layer blue OLED. (b) Schematic energy level diagram. Details are explained in Fig. 2.11. (c) Photograph of the OLED under operation. Camera settings: f-number $f/2.8$; exposure time 0.25 s. (d) Measured EL emission spectrum.

is explained. The basic stack layout is illustrated in Fig. 2.13(a) and the energy level diagram is presented in Fig. 2.13(b).

In this case, the host Alq₃ contains 5 wt% of the fluorescent red emitter DCM. If an excited singlet exciton is formed on an Alq₃ molecule, it diffuses through the layer. When the exciton reaches a guest molecule within its lifetime, it is trapped there because the electronic energy states of DCM are lower and light from the guest molecules is emitted¹. Thus, the fluorescence contains mainly emission from DCM as can be seen in the photograph in Fig. 2.13(c) and in the emission spectrum in Fig. 2.13(d).

It should be noted that the concentration of DCM is rather high in this stack so that DCM molecules partially quench each other's emission. The low efficiency is also apparent from the large exposure time that was necessary to obtain a photograph of approximately equal brightness compared to the other OLED pictures. Probably a more efficient OLED could be fabricated by choosing a lower DCM concentration of only around 0.5% as explained in Ref. [84]. Then, a radiative quantum efficiency of the guest-host system of almost unity is possible. That is the reason why this material

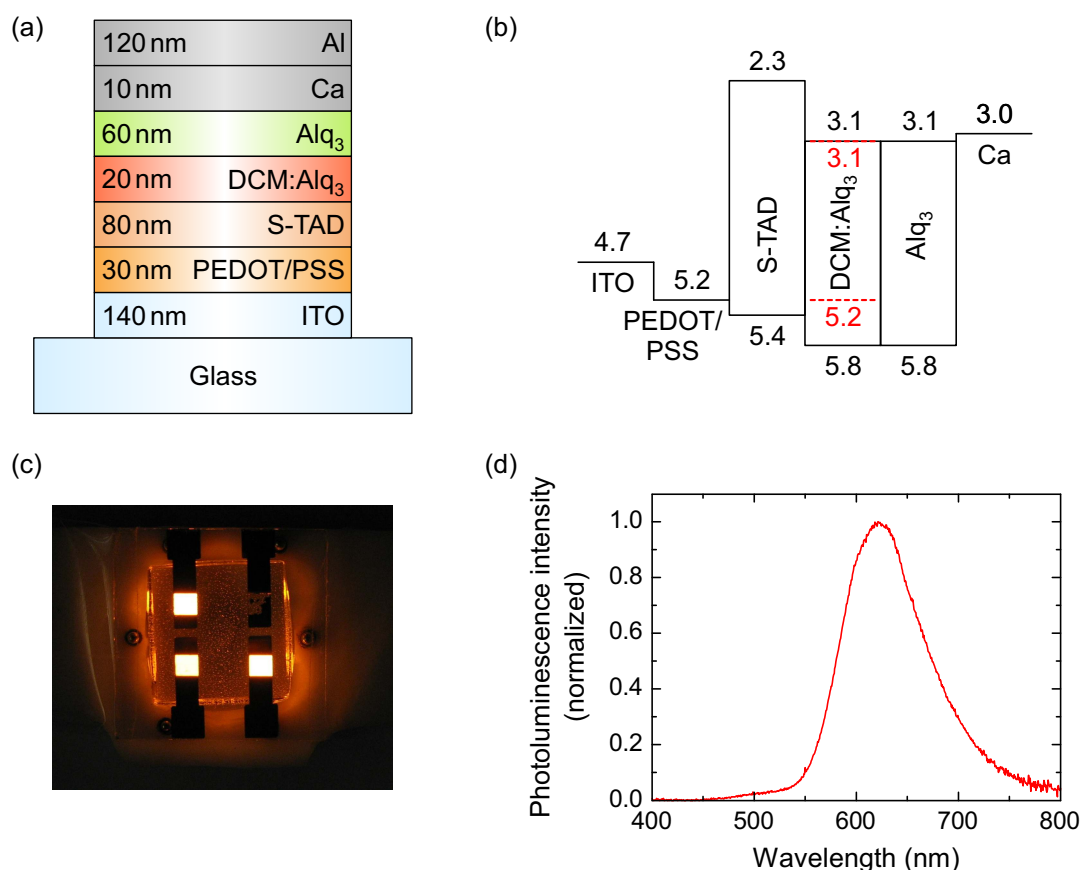


Figure 2.13: (a) Layout of the fluorescent red doped OLED. The doping ratio in the DCM:Alq₃ layer is 5 wt%. After depositing the doped layer, the DCM deposition rate was linearly decreased during the deposition of the first half of the 60 nm thick Alq₃ layer. (b) Schematic energy level diagram. The energy levels of the DCM dopant are depicted as dashed red lines. Further details are explained in Fig. 2.11. (c) Photograph of the OLED under operation. One of the four pixels was damaged prior to encapsulation. Camera settings: f-number f/2.8; exposure time 1.6 s. (d) Measured EL emission spectrum.

combination is frequently used as a laser system⁸⁵. Despite the high DCM concentration, there is still a small Alq₃ emission observable in Fig. 2.13(d). This can be explained by exciton diffusion from the ETL/HTL interface into the undoped Alq₃ region where green light is emitted from Alq₃ molecules. Such a diffusion can be inhibited by utilizing a blocking layer as will be demonstrated in the following section.

Green OLED with phosphorescent guest-host system

In contrast to all fluorescent OLEDs discussed above, this section introduces a phosphorescent OLED. The basic idea is to use guest molecules that contain a heavy metal atom, because spin-orbit coupling strongly increases for higher atomic numbers. Thus, S_1 and T_1 energetic states are mixed and radiative decay from both singlet and triplet states is allowed. With a suitable guest-host combination, also the triplet excitations of the

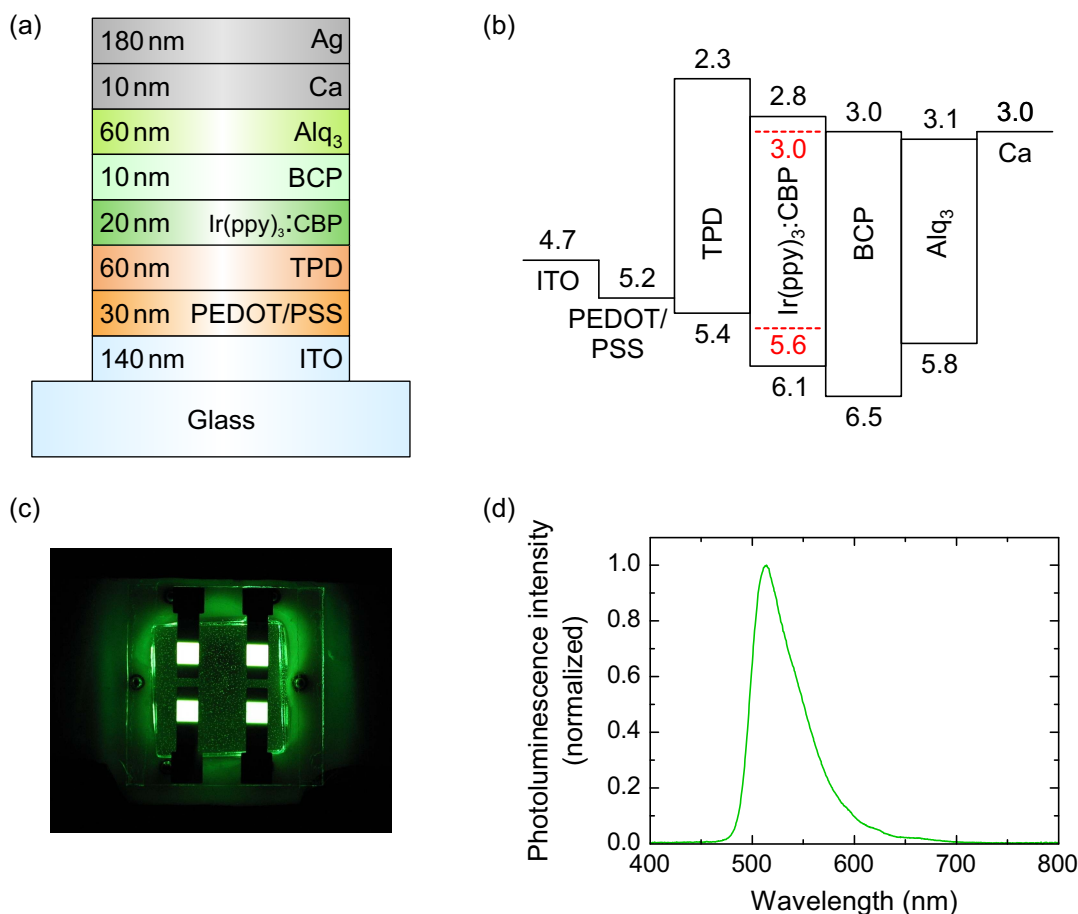


Figure 2.14: (a) Stack layout of the phosphorescent green doped OLED. The concentration of Ir(ppy)₃ in CBP is 6 wt%. (b) Schematic energy level diagram. The energy levels of the Ir(ppy)₃ dopant are depicted as dashed red lines. BCP acts as a hole blocking layer. Further details are explained in Fig. 2.11. (c) Photograph of the OLED under operation. Camera settings: f-number f/2.8; exposure time 0.067 s. (d) Measured EL emission spectrum.

matrix material can be harvested by an energy transfer to the phosphorescent dopant and all singlet and triplet levels can be used, thus allowing for internal quantum efficiencies up to 100%. This concept was first introduced for OLEDs by Baldo *et al.* with 2,3,7,8,12,13,17,18-octaethyl-21H,23H-porphine platinum (PtOEP) doped into an Alq₃ layer⁴⁶. This material still had a too long excited state lifetime and therefore a rather low efficiency⁸¹. A breakthrough for phosphorescent emitters was the introduction of Ir(ppy)₃, containing the heavy metal atom iridium, with a lifetime of its T_1 state of less than 1 μ s. A radiative quantum efficiency of more than 60% was published^{73,81,86}, sometimes even values close to 100% were reported⁸⁷.

In the OLED stack shown in Fig. 2.14(a), Ir(ppy)₃ is doped into CBP at a concentration of 6 wt%. In the case of the phosphorescent Ir(ppy)₃, this concentration does not cause strong quenching but rather corresponds to the optimal doping ratio^{86,87}. The matrix CBP is an ambipolar material, i.e. it transports both electrons and holes, although

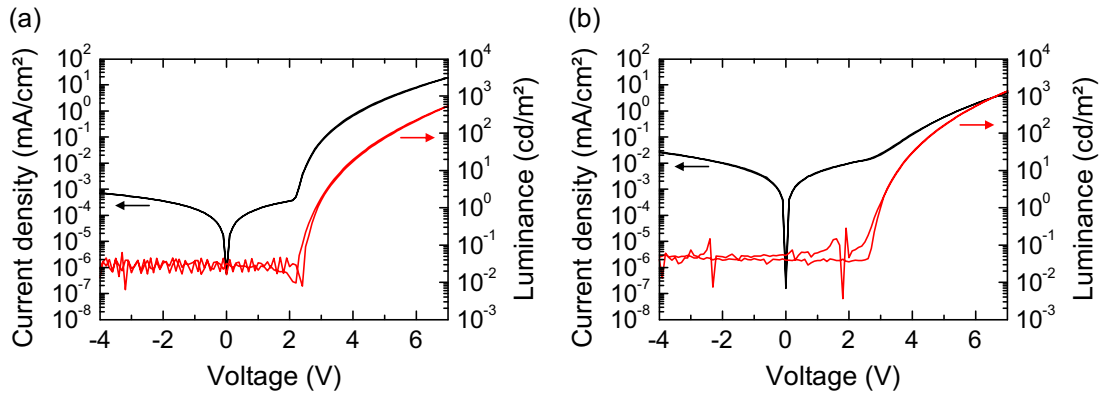


Figure 2.15: (a) Current-voltage-luminance characteristics of the fluorescent Alq_3 OLED. (b) Characteristics of the phosphorescent $\text{Ir}(\text{ppy})_3$ OLED. The measurement of current and luminance was performed simultaneously inside the glove box in a cube that blocks ambient light. The photodiode for the luminance measurement was calibrated by comparison to a radiance measuring head. All measurements were performed from negative to positive voltages as well as in the opposite direction.

the hole mobility is slightly larger^{88,89}. Regarding the energy levels in Fig. 2.14(b), it can be seen that the LUMO of $\text{Ir}(\text{ppy})_3$ lies below and the HOMO is located above the corresponding levels of the CBP matrix, thus enabling efficient charge carrier trapping on the dopant.

The OLED emits light in the green spectral region as illustrated in Figs. 2.14(c) and (d). Current-voltage-luminance characteristics will be presented in Sec. 2.7.4. The cathode of this OLED is made of a combination of calcium (work function 3.0 eV^{76,83}) and silver (work function approximately 4.5 eV^{90,91}) and thus offers good electron injection as well as an excellent reflectivity. Here, a thin hole blocking layer made of BCP is used between the EML and ETL. This prevents holes and excitons from entering the ETL, which would result in emission from Alq_3 and thus a reduced efficiency^{65,70,86,92}.

2.7.4. Current-voltage-luminance characteristics

Some basic electrical and optical properties of OLEDs can be derived from current-voltage-luminance characteristics as shown exemplarily in Fig. 2.15 for the green fluorescent Alq_3 and the phosphorescent $\text{Ir}(\text{ppy})_3$ OLEDs. In these graphs, the current density and the luminance are shown in a semilogarithmic plot as a function of the applied voltage which typically has a value of a few volts. The OLED based on Alq_3 shows a pronounced diode behavior. While there is only a small current flow under reverse bias, the current density strongly increases under forward bias starting at the built-in voltage of slightly above 2V. At this point, both electrons and holes are effectively injected into the device. Therefore, the increase of current is accompanied by the onset of light emission which results from the recombination of both charge carrier types.

The characteristics of the OLED based on $\text{Ir}(\text{ppy})_3$ clearly shows higher leakage cur-

rents and thus a less pronounced diode behavior. The higher leakage currents are probably caused by the employment of other materials or by small differences in fabrication conditions. However, the phosphorescent Ir(ppy)₃ OLED still has a significantly higher light emission at a certain current density compared to the Alq₃ OLED, although both OLEDs have a rather similar emission spectrum.

A detailed comparison of both OLEDs at a current density of 4 mA/cm² yields a luminance for the fluorescent Alq₃ OLED of 112 cd/m² while the phosphorescent Ir(ppy)₃ OLED has a luminance of 1100 cd/m². From these values, a current efficiency of 2.8 cd/A and 27.7 cd/A is obtained for the Alq₃ and Ir(ppy)₃ OLEDs, respectively. There are two reasons for the enormous difference in efficiency. First, the phosphorescent Ir(ppy)₃:CBP system can use both singlets and triplets for radiative transitions. Therefore, the number of excited energy states that contribute to the emission is four times larger compared to the fluorescent Alq₃. Secondly, the radiative quantum efficiency of Ir(ppy)₃:CBP is significantly higher than that of Alq₃. Altogether, the phosphorescent Ir(ppy)₃ OLED is approximately ten times more efficient.

The determination of luminous efficacy also involves the applied voltage. For a current density of 4 mA/cm² the required voltage is 5.3 V and 6.8 V for the Alq₃ and Ir(ppy)₃ OLEDs, respectively. If a Lambertian emission is assumed, the luminous efficacy of both OLEDs can be estimated to 1.6 lm/W and 13 lm/W, respectively. Here, the higher leakage current and consequently larger required voltage in the OLED based on Ir(ppy)₃ clearly reduce the luminous efficacy, even though it is still far better than the fluorescent Alq₃ OLED. Altogether, the determined current efficiencies and luminous efficacies agree very well with published values for these emitter systems^{86,93}.

The current efficiency and luminous efficacy as a function of the applied voltage are presented in Figs. 2.16(a) and (b), respectively. It is apparent that the OLED based on Ir(ppy)₃ is much more efficient over the whole voltage range in comparison to the Alq₃ OLED. Both the current efficiency as well as the luminous efficacy strongly depend on the actual voltage. This is especially obvious in the case of the Ir(ppy)₃ OLED. For small voltages, it is likely that the charge balance is not optimal⁷¹, while for higher voltages, i.e. higher current densities, quenching processes reduce the OLED efficiency^{74,89}.

Steps to be taken in order to further improve OLEDs include the exploitation of the substrate emission by using outcoupling enhancement structures. In addition, injection layers and doped transport layers can significantly reduce the driving voltage and thus increase the luminous flux per electric power. Furthermore, appropriate blocking layers can optimize the charge balance within the device. Of course, better phosphorescent guest-host systems with improved radiative quantum efficiency also account for a higher overall efficiency.

However, the most important aspect for high-efficiency OLEDs is an enhanced light outcoupling. As mentioned above, typically half of the light is trapped in waveguide modes and surface plasmons. Of course, access to these modes could considerably

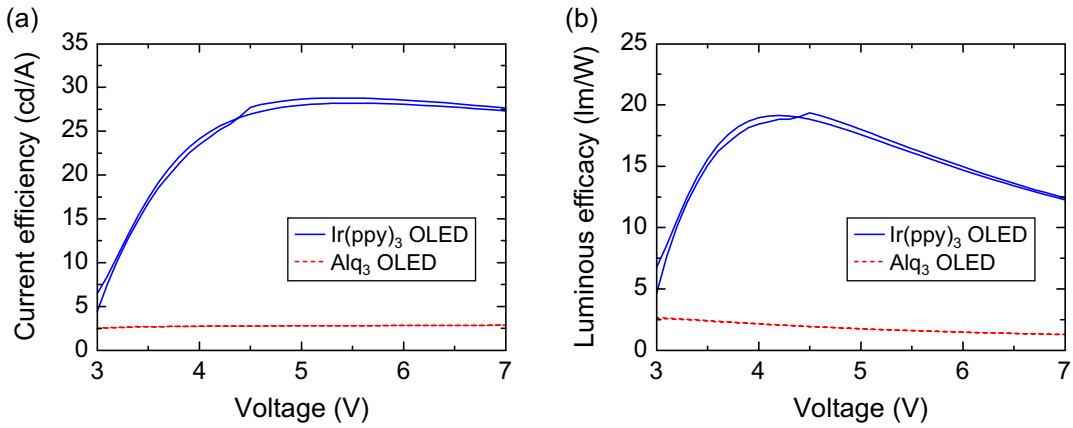


Figure 2.16: (a) Current efficiency and (b) luminous efficacy as a function of the applied voltage for the OLEDs based on Alq_3 and $\text{Ir}(\text{ppy})_3$.

boost the efficiency. By improving the light extraction, the same emission intensity could be obtained at a lower driving current, which would result in a reduced energy consumption and in an increase in device lifetime^{4,15}. Moreover, a smaller current density leads to a higher internal quantum efficiency due to a reduced roll-off, which is normally caused by nonradiative decay channels like triplet-triplet annihilation at high current densities^{74,94}.

It is not the aim of this thesis to fabricate an OLED with record efficiency by combining efficient emitters and optimized devices with doped transport and blocking layers as demonstrated by Mladenovski *et al.* and Reineke and co-workers^{9,73}. Instead, this thesis will fundamentally discuss a variety of existing light extraction strategies and, in particular, several novel techniques with high potential will be introduced and compared in terms of performance and applicability.

3. Interaction of electromagnetic radiation with matter

This chapter explains the theory of optical phenomena which are required for understanding the properties of OLEDs. Starting with Maxwell's equation and plane waves, the chapter continues with the explanation of the complex refractive index as well as absorption, reflection and transmission. Subsequently, the transfer-matrix formalism will be introduced which allows for calculating the reflectance and transmittance of multilayer stacks. Finally, the existence of waveguide modes in layered media will be discussed.

3.1. Maxwell's equations and electromagnetic waves

In order to derive the wave equations for electromagnetic waves it is necessary to start with Maxwell's equations which are the most fundamental equations in electrodynamics^{95,96}. Here, Maxwell's equations are given for regions where both the charge density and current density vanish, which is often the case in the propagation of electromagnetic radiation:

$$\vec{\nabla} \times \vec{E} = -\frac{\partial \vec{B}}{\partial t}, \quad (3.1)$$

$$\vec{\nabla} \times \vec{H} = \frac{\partial \vec{D}}{\partial t}, \quad (3.2)$$

$$\vec{\nabla} \cdot \vec{D} = 0, \quad (3.3)$$

$$\vec{\nabla} \cdot \vec{B} = 0. \quad (3.4)$$

In these equations, $\vec{E} = \vec{E}(\vec{r}, t)$ describes the electric field vector and $\vec{H} = \vec{H}(\vec{r}, t)$ is the magnetic field vector. The quantities $\vec{D} = \vec{D}(\vec{r}, t)$ and $\vec{B} = \vec{B}(\vec{r}, t)$ are used to include the effects of the field on matter and are called electric displacement and magnetic induction, respectively.

The quantities \vec{E} , \vec{H} , \vec{D} and \vec{B} are related by the material equations^{95,96}:

$$\vec{D} = \varepsilon \cdot \vec{E} = \varepsilon_0 \cdot \vec{E} + \vec{P}, \quad (3.5)$$

$$\vec{B} = \mu \cdot \vec{H} = \mu_0 \cdot (\vec{H} + \vec{M}). \quad (3.6)$$

In these equations, $\varepsilon = \varepsilon_r \cdot \varepsilon_0$ describes the permittivity with ε_r being the relative permittivity or dielectric function and $\varepsilon_0 \approx 8.854 \times 10^{-12}$ F/m the vacuum permittivity. Accordingly, $\mu = \mu_r \cdot \mu_0$ is the permeability with μ_r indicating the relative permeability and $\mu_0 = 4\pi \times 10^{-7}$ H/m being the vacuum permeability. \vec{P} and \vec{M} are the electric polarization and magnetization, respectively. An electromagnetic field present in matter can perturb the motion of electrons and produce a dipole polarization \vec{P} per unit volume. Similarly, a magnetic field can induce a magnetization \vec{M} in materials having a permeability that differs from μ_0 .

By combining Maxwell's equations and assuming an isotropic medium so that ε and μ are scalars, the electromagnetic wave equations can be obtained:

$$\vec{\nabla}^2 \vec{E} - \mu \cdot \varepsilon \cdot \frac{\partial^2 \vec{E}}{\partial t^2} = 0, \quad (3.7)$$

$$\vec{\nabla}^2 \vec{B} - \mu \cdot \varepsilon \cdot \frac{\partial^2 \vec{B}}{\partial t^2} = 0. \quad (3.8)$$

A detailed derivation is found for example in Ref. [95]. These equations are satisfied by the well-known monochromatic sinusoidal plane waves which may be written as⁹⁶

$$\vec{E} = \vec{E}_0 \cdot e^{i(\vec{k} \cdot \vec{r} - \omega \cdot t)}, \quad (3.9)$$

$$\vec{B} = \vec{B}_0 \cdot e^{i(\vec{k} \cdot \vec{r} - \omega \cdot t)}. \quad (3.10)$$

Here, \vec{E}_0 and \vec{B}_0 denote the complex amplitudes of the corresponding fields, \vec{k} describes the wave vector and thus the direction of propagation and ω is the angular frequency. Strictly speaking, no electromagnetic field in physics is complex. However, complex representations lead to great mathematical simplification and therefore the complex quantity described in Eq. (3.9) will be termed a "field", keeping in mind that the actual field is the real part of the expression. It should be noted that a definition of plane waves as in Refs. [96–98] is used. Other textbooks use a solution with the exponent $i(\omega \cdot t - \vec{k} \cdot \vec{r})$ as in Refs. [95, 99].

The triad \vec{E}_0 , \vec{B}_0 and \vec{k} forms a set of orthogonal vectors, hence \vec{E} and \vec{B} are perpendicular to the direction of propagation. For this reason, electromagnetic waves are said to be transverse waves. Since the complex amplitudes of \vec{E} and \vec{B} are related^{95, 96}, only the electric field vector \vec{E} will be considered in the following.

In vacuum with $\varepsilon_r = 1$ and $\mu_r = 1$, the angular frequency ω and the absolute value of the vacuum wave vector $k_0 = |\vec{k}_0|$ are related by⁹⁵

$$\omega = c_0 \cdot k_0, \quad (3.11)$$

with the speed of light in vacuum $c_0 = 1/\sqrt{\mu_0 \cdot \varepsilon_0} \approx 2.998 \times 10^8$ m/s. Equation (3.11) is also called dispersion relation of light in vacuum. The surfaces of constant phase travel

in the direction of \vec{k} with phase velocity c_0 . The separation between two neighboring field peaks is termed wavelength of light in vacuum and it is given by

$$\lambda_0 = \frac{2\pi}{k_0} = \frac{2\pi \cdot c_0}{\omega}. \quad (3.12)$$

Besides the properties of electromagnetic waves in vacuum, it is essential to study the influence of a transparent medium. Media with absorption will be discussed later in this chapter. Most transparent media are nonmagnetic and have a relative permeability of $\mu_r = 1$ so that $\mu = \mu_0$. In the following, all media will be assumed to be nonmagnetic. However, the relative permittivity usually deviates considerably from unity. In such a medium, the absolute value of the wave vector k , wavelength λ' and phase velocity v are given by^{95,96,98,100}

$$k = n \cdot k_0 = \frac{2\pi \cdot n}{\lambda_0}, \quad (3.13)$$

$$\lambda' = \frac{\lambda_0}{n}, \quad (3.14)$$

$$v = \frac{c_0}{n}, \quad (3.15)$$

with

$$n = \sqrt{\epsilon_r} \quad (3.16)$$

being the refractive index of the medium. It is apparent that the wavelength and phase velocity of the plane wave in a medium with $n > 1$ are smaller than the corresponding quantity in vacuum whereas the wave vector is larger than the vacuum wave vector. It is necessary to distinguish between λ' in a medium and λ_0 in vacuum.

The best way to describe the energy of a photon is its angular frequency ω or its frequency $\nu = \omega/(2\pi)$ because the frequency is independent of the medium in which the photon propagates as can be seen by the dispersion relation of light in a medium:

$$\omega = v \cdot k = \frac{c_0}{n} \cdot k = c_0 \cdot k_0. \quad (3.17)$$

However, it is more convenient to describe e.g. green light by its vacuum wavelength of $\lambda_0 = 550 \text{ nm}$ than by its frequency of $\nu \approx 5.45 \times 10^{14} \text{ Hz}$. Therefore, the wavelength will be used in the following to describe the energy and color of a photon even if the photon travels in a medium. To keep it simple, the vacuum wavelength will be abbreviated with λ from now on.

The refractive index n is usually a function of frequency, i.e. $n(\nu)$ or $n(\omega)$. In most transparent media the refractive index increases with ω . Therefore, the refractive index for blue light is typically higher than for red light. Generally, the dependence of the refractive index on frequency is called dispersion. Frequently, the dispersion is expressed in terms of wavelength, i.e. $n(\lambda)$. Examples for the dispersion in different materials can be seen in the optical constants in the appendix, cf. Sec. A.2.

3.2. Complex refractive index

In order to account for optical absorption in nontransparent media, the refractive index n is replaced by a complex refractive index \tilde{n} :

$$\tilde{n} = n + i\kappa, \quad (3.18)$$

with the refractive index n and the extinction coefficient κ being the real and imaginary part of the complex refractive index \tilde{n} , respectively. The extinction coefficient represents an attenuation of electromagnetic waves.

An estimation of the complex refractive index can be obtained within the classical electron model. Since electrons have a much smaller mass compared to the atomic nucleus, they will be displaced from their equilibrium positions under the influence of an electric field $\vec{E} = \vec{E}_0 \cdot e^{-i\omega \cdot t}$, thus inducing a dipole moment which is proportional to the atomic polarizability of a given material^{95,98,99}. Solving the equation of motion for the electrons yields the following expression for the index of refraction in a medium with N atoms per unit volume^{95,98}:

$$\tilde{n}^2 = 1 + \frac{N \cdot e^2}{\varepsilon_0 \cdot m_e \cdot (\omega_0^2 - \omega^2 - i\gamma \cdot \omega)}. \quad (3.19)$$

In this equation, m_e and $-e$ are the mass and charge of the electron, respectively, γ is the damping coefficient which gives rise to the phenomenon of optical absorption and ω_0 is the resonant frequency of the electron motion.

If the second term in Eq. (3.19) is small compared to 1, the complex index of refraction is approximately

$$\tilde{n} = 1 + \frac{N \cdot e^2}{2\varepsilon_0 \cdot m_e \cdot (\omega_0^2 - \omega^2 - i\gamma \cdot \omega)}. \quad (3.20)$$

By working out the real and imaginary parts, the complex refractive index is found to be^{95,98}

$$\tilde{n} = n + i\kappa = 1 + \frac{N \cdot e^2 \cdot (\omega_0^2 - \omega^2)}{2\varepsilon_0 \cdot m_e \cdot [(\omega_0^2 - \omega^2)^2 + \gamma^2 \cdot \omega^2]} + i \frac{N \cdot e^2 \cdot \gamma \cdot \omega}{2\varepsilon_0 \cdot m_e \cdot [(\omega_0^2 - \omega^2)^2 + \gamma^2 \cdot \omega^2]}. \quad (3.21)$$

Depending on the definition of the driving electric field, the complex refractive index is $\tilde{n} = n - i\kappa$ in some text books^{95,99}.

Usually, n increases with ω for low frequencies ($\omega < \omega_0$). This behavior is called normal dispersion. However, in nontransparent media with $\kappa > 0$, light can be absorbed and couple to electronic states at the resonant frequencies ω_0 . In this case, the refractive index may also decrease with frequency if the resonant frequency is approached. Such a negative slope is referred to as anomalous dispersion.

To see the effect of κ , we consider the propagation of a monochromatic plane wave in

a medium with a complex refractive index. In this case, the magnitude of the complex wave vector is given by

$$k = \frac{2\pi}{\lambda} \cdot (n + i\kappa). \quad (3.22)$$

Inserting this equation into Eq. (3.9) and considering propagation in the z direction yields

$$E(z, t) = E_0 \cdot \exp \left[i \left(\frac{2\pi \cdot n}{\lambda} \cdot z - \omega \cdot t \right) \right] \cdot \exp \left[\left(-\frac{2\pi \cdot \kappa}{\lambda} \cdot z \right) \right]. \quad (3.23)$$

Obviously, the imaginary part of the refractive index leads to an attenuation of electromagnetic radiation along its direction of propagation. The intensity is proportional to $|\vec{E}|^2$ and described by

$$I(z) = I_0 \cdot e^{-\alpha \cdot z}, \quad (3.24)$$

where I_0 is the intensity at $z = 0$ and α is the absorption or attenuation coefficient which is related to κ by

$$\alpha = \frac{4\pi \cdot \kappa}{\lambda}. \quad (3.25)$$

Typical OLED devices contain several organic layers which can be well described as dielectric media having an absorption in certain spectral regions. In addition, an OLED usually has a metallic cathode. There are free electrons in a metal that do not oscillate but are free to move under the influence of an applied electric field⁹⁵. Thus, there is no restoring force, hence $\omega_0 = 0$. Consequently, in the case of metals Eq. (3.19) simplifies to

$$\tilde{n}^2 = 1 - \frac{N \cdot e^2}{\varepsilon_0 \cdot m_e \cdot (\omega^2 + i\gamma \cdot \omega)}, \quad (3.26)$$

with N being the electron density. The damping coefficient γ results for instance from collisions of electrons. If $\gamma \ll \omega$ is assumed, the complex index of refraction of a metal can be written as

$$\tilde{n}^2 = \varepsilon(\omega) \simeq 1 - \frac{\omega_p^2}{\omega^2}, \quad (3.27)$$

with $\varepsilon(\omega)$ being the frequency dependent permittivity and ω_p describing the plasma angular frequency, which is given by

$$\omega_p^2 = \frac{N \cdot e^2}{\varepsilon_0 \cdot m_e}. \quad (3.28)$$

For high-frequency radiation ($\omega > \omega_p$), the refractive index is real. The free electrons of the metal are no more able to respond to the imposed oscillating fields and hence the metal behaves like a transparent dielectric medium in which the waves propagate freely. For frequencies lower than the plasma frequency, the refractive index is purely imaginary. Therefore, the fields within the metal fall off exponentially with distance from the surface. As a consequence, electromagnetic radiation with $\omega < \omega_p$ incident

on a metal will be mostly reflected from the surface. In general, the index of refraction of a metal is complex, when γ is finite, and thus some fraction of the incident light is absorbed. However, some metals like silver have a reflectivity in the visible spectral region which is well above 90%. The optical constants, i.e. the refractive indices and extinction coefficients, for several metals are shown in the appendix, cf. Sec. A.2.

3.3. Reflection and refraction of electromagnetic waves

A plane wave incident from a medium (refractive index n_1) on the interface to a second medium (refractive index n_2) will in general be split into two waves: a transmitted wave that is refracted at the interface and that enters the second medium, and a reflected wave propagating back into the first medium, cf. Fig. 3.1. This is a consequence of the boundary conditions of the field vectors between two media which result from Maxwell's equations. A detailed derivation can be found in Refs. [95,96,101]. For simplicity, both media are assumed to be nonmagnetic, isotropic and transparent, so that ε_1 and ε_2 are real and scalars and $\mu_1 = \mu_2 = \mu_0$. In this case, the boundary conditions in regions with vanishing charge and current density are given by:

$$\vec{E}_{2t} = \vec{E}_{1t}, \quad (3.29)$$

$$\varepsilon_2 \cdot \vec{E}_{2n} = \varepsilon_1 \cdot \vec{E}_{1n}, \quad (3.30)$$

$$\vec{H}_{2t} = \vec{H}_{1t}, \quad (3.31)$$

$$\vec{B}_{2n} = \vec{B}_{1n} \quad \text{and for } \mu_1 = \mu_2 = \mu_0 \text{ also } \vec{H}_{2n} = \vec{H}_{1n}. \quad (3.32)$$

In these equations, subscript t denotes the component tangential to the interface and subscript n describes the normal component.

The incident electromagnetic wave can be described by an electric field vector of the form $\vec{E}_i \cdot \exp[i(\vec{k}_i \cdot \vec{r} - \omega_i \cdot t)]$, where \vec{k}_i is the incident wave vector, cf. Fig. 3.1. Similarly, the reflected plane wave is described by $\vec{E}_r \cdot \exp[i(\vec{k}_r \cdot \vec{r} - \omega_r \cdot t)]$ with wave vector \vec{k}_r , and the transmitted wave is represented by $\vec{E}_t \cdot \exp[i(\vec{k}_t \cdot \vec{r} - \omega_t \cdot t)]$ with wave vector \vec{k}_t .

Any boundary condition that relates these three fields at the interface $z = 0$ requires that the temporal variation must be similar for all times⁹⁶, hence it directly follows that the angular frequency is constant for all fields, i.e. $\omega_i = \omega_r = \omega_t \equiv \omega$. In addition, the spatial variation implies that⁹⁵

$$\left(\vec{k}_i \cdot \vec{r}\right)_{z=0} = \left(\vec{k}_r \cdot \vec{r}\right)_{z=0} = \left(\vec{k}_t \cdot \vec{r}\right)_{z=0}. \quad (3.33)$$

It follows from this equation that all three wave propagation vectors \vec{k}_i , \vec{k}_r and \vec{k}_t must lie in the same plane which is called the plane of incidence. In Fig. 3.1, it is the x - z -plane. Furthermore, the tangential component remains constant so that $k_{i,x}$, $k_{r,x}$

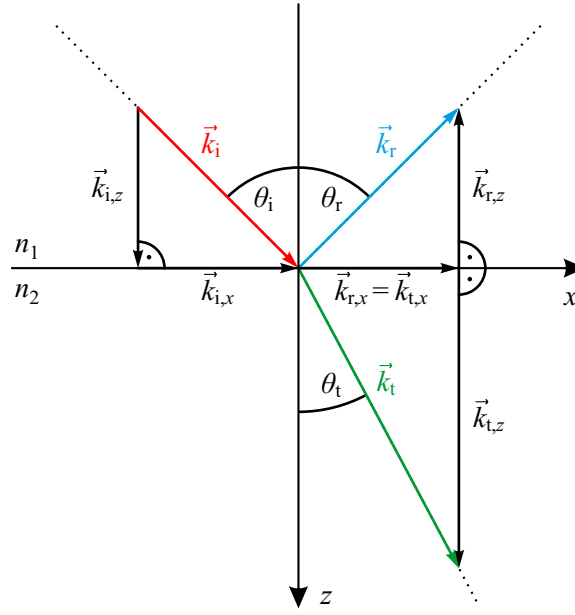


Figure 3.1: Reflection and refraction at an interface between two dielectric media. The electromagnetic wave is incident from medium 1 with refractive index n_1 . The transmitted wave is refracted at the interface ($z = 0$) and propagates in medium 2 (refractive index n_2). The wave vectors for incident, reflected and transmitted waves are denoted by \vec{k}_i , \vec{k}_r and \vec{k}_t , respectively. The same indication applies to all angles θ . The index x describes the projected component of the wave vectors onto the x -axis, i.e. the component tangential to the interface, while the index z refers to the normal component along the z -axis.

and $k_{t,x}$ must be equal. The absolute value of the wave vectors is given by

$$|\vec{k}_i| = k_i = |\vec{k}_r| = k_r = \frac{\omega}{c_0} \cdot n_1 \quad \text{and} \quad |\vec{k}_t| = k_t = \frac{\omega}{c_0} \cdot n_2. \quad (3.34)$$

If θ_i , θ_r and θ_t describe the angles with respect to the normal of the interface for the incident, reflected and transmitted waves, respectively, the following relation must be satisfied:

$$n_1 \cdot \sin \theta_i = n_1 \cdot \sin \theta_r = n_2 \cdot \sin \theta_t. \quad (3.35)$$

Thus, it follows that the angle of reflection must be equal to the angle of incidence, i.e. $\theta_r = \theta_i$. In addition, a relation between θ_i and θ_t is obtained:

$$\frac{\sin \theta_i}{\sin \theta_t} = \frac{n_2}{n_1}. \quad (3.36)$$

This equation is known as Snell's law.

In order to derive an expression for the intensity of the reflected and transmitted waves, it is convenient to decompose each field vector into two linearly polarized components parallel and perpendicular to the plane of incidence. The parallel and perpendicular components are called p-polarized or TM (transverse magnetic) wave and

s-polarized or TE (transverse electric) wave, respectively. As long as both media are homogeneous and isotropic, the s- and p-polarized waves are independent of each other and maintain their s- and p-character in reflection and refraction⁹⁵.

The following relations can be derived between the s- and p-polarized components of the electric field amplitude E_i of the incident wave and the amplitudes E_r and E_t of the reflected and transmitted waves, respectively^{95,96}:

$$r_s = \frac{E_{r,s}}{E_{i,s}} = \frac{n_1 \cdot \cos \theta_i - n_2 \cdot \cos \theta_t}{n_1 \cdot \cos \theta_i + n_2 \cdot \cos \theta_t}, \quad (3.37)$$

$$r_p = \frac{E_{r,p}}{E_{i,p}} = \frac{n_2 \cdot \cos \theta_i - n_1 \cdot \cos \theta_t}{n_2 \cdot \cos \theta_i + n_1 \cdot \cos \theta_t}, \quad (3.38)$$

$$t_s = \frac{E_{t,s}}{E_{i,s}} = \frac{2n_1 \cdot \cos \theta_i}{n_1 \cdot \cos \theta_i + n_2 \cdot \cos \theta_t}, \quad (3.39)$$

$$t_p = \frac{E_{t,p}}{E_{i,p}} = \frac{2n_1 \cdot \cos \theta_i}{n_2 \cdot \cos \theta_i + n_1 \cdot \cos \theta_t}. \quad (3.40)$$

These relations are known as Fresnel equations. r_s , r_p are called Fresnel reflection coefficients and t_s , t_p are the Fresnel transmission coefficients. These formulas are general and apply to any two media, thus including reflection from the surface of absorbing media. The reflection coefficient r_p for p-polarized light becomes zero at Brewster's angle¹⁰² $\theta_B = \arctan(n_2/n_1)$. At this angle, the propagation vectors of the transmitted and reflected wave are mutually orthogonal⁹⁵.

For normal incidence, i.e. $\theta_i = 0$, there is no difference between s- and p-polarized waves and the Fresnel formulas become

$$r_s = -r_p = \frac{n_1 - n_2}{n_1 + n_2}, \quad (3.41)$$

$$t_s = t_p = \frac{2n_1}{n_1 + n_2}. \quad (3.42)$$

It is noteworthy that some text books obtain a different sign in the numerator in the right part of Eq. (3.38), thus yielding $r_s = r_p$ for normal incidence. This depends on the definition of the electric field directions of the incident and reflected p-polarized waves^{95,96,102}. Here, a similar definition as in Refs. [96, 102] is used.

Since the power flow is proportional to the square of the electric field amplitude, the reflectance and transmittance are related to the Fresnel coefficients by

$$R_s = |r_s|^2, \quad (3.43)$$

$$R_p = |r_p|^2, \quad (3.44)$$

$$T_s = \frac{n_2 \cdot \cos \theta_t}{n_1 \cdot \cos \theta_i} \cdot |t_s|^2, \quad (3.45)$$

$$T_p = \frac{n_2 \cdot \cos \theta_t}{n_1 \cdot \cos \theta_i} \cdot |t_p|^2. \quad (3.46)$$

In contrast to the general Eqs. (3.37)–(3.40), the formulas for the transmittance are only valid for pure dielectric media with real n_1 , n_2 and θ_i , θ_t .

An example for the reflection coefficients between two interfaces with refractive indices $n_1 = 1.0$ and $n_2 = 1.5$ is illustrated in Fig. 3.2(a). The reverse case with $n_1 = 1.5$ and $n_2 = 1.0$ is plotted in Fig. 3.2(b). The corresponding reflectances are shown in Figs. 3.3(a) and (b), respectively. The transmittances can be calculated from $R_{s,p} + T_{s,p} = 1$ which is required in order to fulfill the conservation of energy in media without absorption. The reflectance at normal incidence is 4%. For an s-polarized wave, it rises with incidence angle until it reaches 100% at an angle of incidence of 90° . For a p-polarized wave, the reflectance first decreases until it reaches $R_p = 0$ at Brewster's angle.

In case of incidence through the medium with higher refractive index, i.e. $n_1 > n_2$, a critical angle of incidence θ_c exists where $\theta_t = 90^\circ$ and $\sin \theta_t = 1$. It is defined by

$$\sin \theta_c = \frac{n_2}{n_1}. \quad (3.47)$$

For larger angles of incidence ($\theta_i > \theta_c$), Snell's law yields $\sin \theta_t = (\sin \theta_i / \sin \theta_c) > 1$. This implies a purely imaginary cosine in order to fulfill $\sin^2 \theta_t + \cos^2 \theta_t = 1$ ^{95,96}:

$$\cos \theta_t = i \cdot \sqrt{\left(\frac{\sin \theta_i}{\sin \theta_c}\right)^2 - 1}. \quad (3.48)$$

Thus, the Fresnel reflection coefficients become complex. However, $|r_s| = |r_p| = 1$ so that the reflectances R_s and R_p are unity, cf. Fig. 3.3(b). This phenomenon is called total internal reflection, i.e. all the light is totally reflected from the surface. The amplitude of the reflected wave is only different from the incident amplitude by a phase shift $\Delta \Phi_{s,p}$.

In general, the phase shift $\Delta \Phi_{s,p} = 0$ for real $r_{s,p} > 0$ and $\Delta \Phi_{s,p} = \pi$ for real $r_{s,p} < 0$. In case of total internal reflection with complex $r_{s,p}$, the phase shift can be calculated by using Eq. (3.48) to rewrite Eqs. (3.37) and (3.38) in the form $r_{s,p} = |r_{s,p}| \cdot \exp(-i \Delta \Phi_{s,p})$, thus yielding^{96,102}

$$\tan(\Delta \Phi_s/2) = \frac{1}{\cos \theta_i} \sqrt{\sin^2 \theta_i - \left(\frac{n_2}{n_1}\right)^2} \quad (3.49)$$

for an s-polarized wave and

$$\tan(\Delta \Phi_p/2) = \frac{n_1^2}{n_2^2 \cos \theta_i} \sqrt{\sin^2 \theta_i - \left(\frac{n_2}{n_1}\right)^2} \quad (3.50)$$

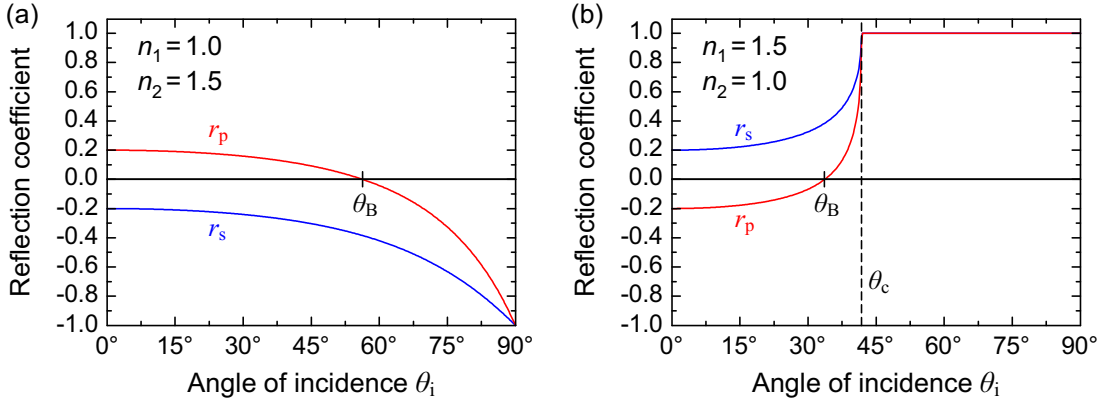


Figure 3.2: (a) Reflection coefficients of s- and p-polarized waves at the interface between two dielectric media with $n_1 = 1.0$ and $n_2 = 1.5$, i.e. air and glass, respectively. $\theta_B \approx 56.3^\circ$ represents Brewster's angle. (b) Opposite case for incidence from a medium with $n_1 = 1.5$ to a medium with $n_2 = 1.0$, where $\theta_c \approx 41.8^\circ$ describes the critical angle and $\theta_B \approx 33.7^\circ$ corresponds to Brewster's angle.

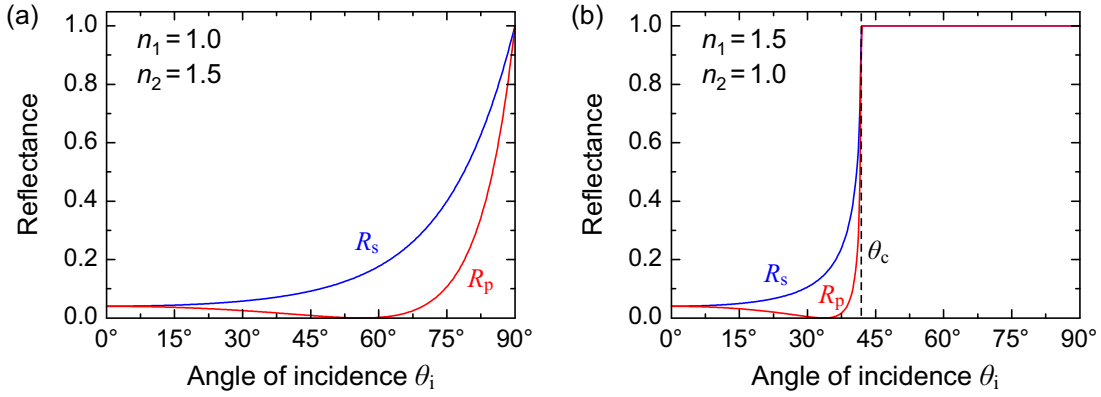


Figure 3.3: (a) Reflectance of s- and p-polarized waves at the interface between two dielectric media with $n_1 = 1.0$ and $n_2 = 1.5$. (b) Opposite case for incidence from a medium with $n_1 = 1.5$ to a medium with $n_2 = 1.0$. $\theta_c \approx 41.8^\circ$ describes the critical angle. In both graphs, the p-polarized reflectance becomes zero at Brewster's angle.

for a p-polarized wave. The dependence of $\Delta\Phi_{s,p}$ on the angle of incidence is plotted in Figs. 3.4(a) and (b) for an air/glass and a glass/air interface, respectively.

Although the transmittances T_s and T_p become zero under total internal reflection, the Fresnel transmission coefficients t_s and t_p are not vanishing, i.e. $t_{s,p} \neq 0$. This means that even though the light is totally internally reflected, the electromagnetic field still penetrates into the second medium^{95,96}. This is obvious from the calculation of the transmitted electric field which is proportional to the real part of $\exp(i\vec{k}_t \cdot \vec{r}) = \exp[ik_t \cdot (x \cdot \sin\theta_t + z \cdot \cos\theta_t)]$. By using Snell's Law and Eq. (3.48), this expression takes the form

$$\exp\left(i k_t \cdot x \cdot \frac{\sin\theta_i}{\sin\theta_c}\right) \cdot \exp(-q \cdot z), \quad (3.51)$$

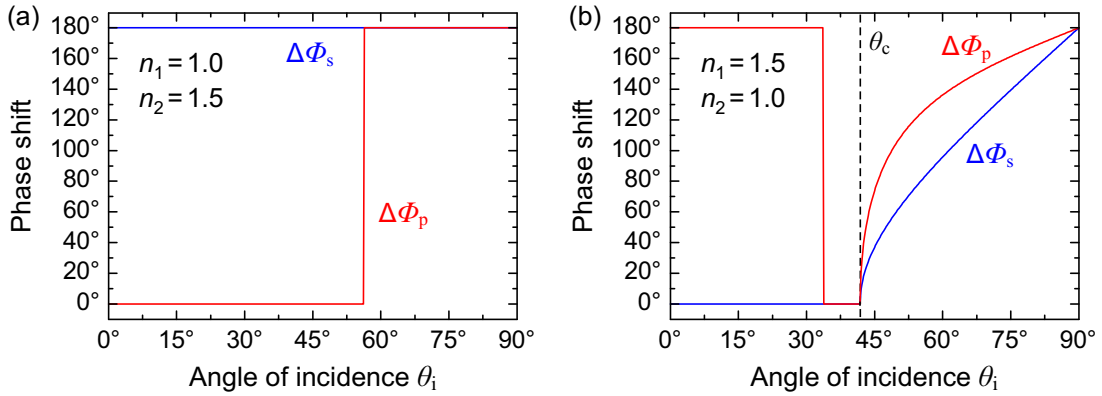


Figure 3.4: (a) Phase shift of s- and p-polarized waves at the interface between two dielectric media with $n_1 = 1.0$ and $n_2 = 1.5$. (b) Opposite case for incidence from a medium with $n_1 = 1.5$ to a medium with $n_2 = 1.0$. $\theta_c \approx 41.8^\circ$ describes the critical angle.

with

$$q = k_t \cdot \sqrt{\left(\frac{\sin \theta_i}{\sin \theta_c}\right)^2 - 1}. \quad (3.52)$$

Since $\theta_i > \theta_c$, q is a positive number and hence the electric field vector decreases exponentially as z increases, i.e. as the distance from the surface increases. Besides the penetration into medium 2, the wave also propagates parallel to the interface as can be seen from Eq. (3.51). Such a wave is called an evanescent wave. The penetration depth inside medium 2 is q^{-1} , which is only several wavelengths except for incident angles near the critical angle⁹⁵. If medium 2 has a finite thickness, some fraction of the light can penetrate through the layer as will be discussed in Secs. 3.5, 4.2 and 4.3.

3.4. Transfer-matrix formulation

The reflectance and transmittance of a single interface can be calculated by the Fresnel equations. An OLED usually contains several layers of organic or metallic materials. Therefore, multiple reflections as well as constructive or destructive interference effects must be taken into account. This is possible by using a transfer-matrix formulation as depicted in detail in Ref. [95]. This systematic approach is based on the fact that continuity conditions exist for the electric field across interfaces from one medium to the next. The main results will be discussed in the following.

Figure 3.5 displays the multilayer stack under consideration. The stack is bounded by two semi-infinite layers. Let A_i and B_i be the amplitudes of the electric field vectors traveling in the i -th layer in the positive and negative z -direction, respectively. A relation between the amplitudes at the interface between layer i and layer $i - 1$ are

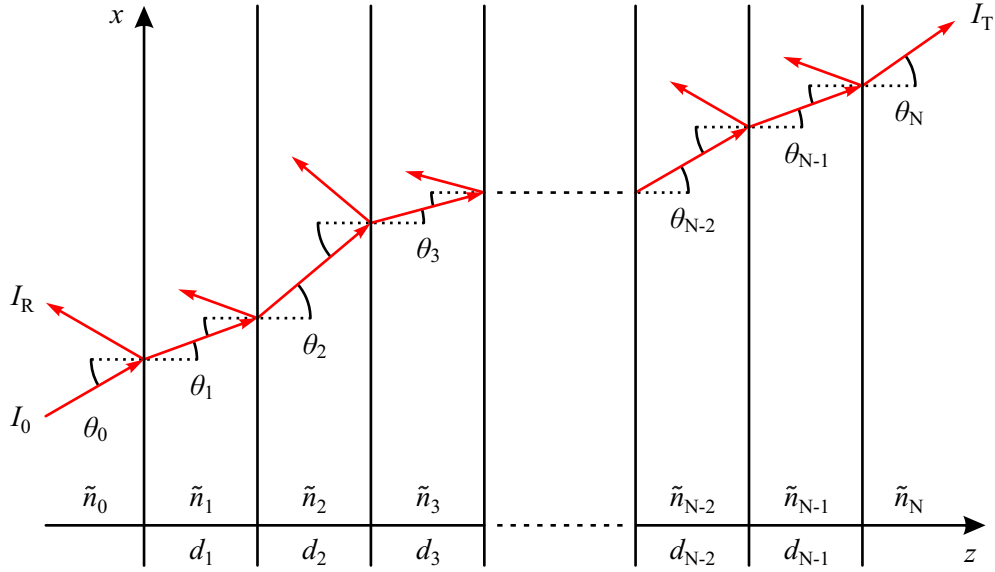


Figure 3.5: Propagation of electromagnetic radiation through a multilayer stack which is bounded by two semi-infinite layers on the left (subscript 0) and right side (subscript N) with refractive indices \tilde{n}_0 and \tilde{n}_N and propagation angles with respect to the z -direction of θ_0 and θ_N , respectively. The refractive indices, layer thicknesses and propagation angles for all other layers are denoted by \tilde{n}_i , d_i and θ_i , respectively, with $i = 1, 2, \dots, N - 1$. The intensities of the incident, reflected and transmitted light are described by I_0 , I_R and I_T , respectively.

given by the transmission matrix $D_{i-1,i}$:

$$\begin{pmatrix} A_{i-1} \\ B_{i-1} \end{pmatrix} = D_{i-1,i} \begin{pmatrix} A_i \\ B_i \end{pmatrix}. \quad (3.53)$$

The transmission matrix can be calculated using the Fresnel reflection and transmission coefficients at this interface:

$$D_{i-1,i} = \frac{1}{t_{i-1,i}} \cdot \begin{pmatrix} 1 & r_{i-1,i} \\ r_{i-1,i} & 1 \end{pmatrix}. \quad (3.54)$$

It should be kept in mind that Fresnel coefficients are different for s- and p-polarized waves and thus Eq. (3.54) is polarization dependent.

Since the transfer-matrix formulation also considers absorbing layers, the propagation through each layer must be taken into account. This is accomplished by the propagation matrix P_i of an electromagnetic wave which travels through the i -th layer:

$$P_i = \begin{pmatrix} e^{i\phi_i} & 0 \\ 0 & e^{-i\phi_i} \end{pmatrix}. \quad (3.55)$$

In this equation, ϕ_i is defined by

$$\phi_i = \frac{2\pi}{\lambda} \cdot \tilde{n}_i \cdot d_i \cdot \cos \theta_i, \quad (3.56)$$

where $\tilde{n}_i = n_i + i\kappa_i$ is the complex refractive index and d_i and θ_i describe the thickness and propagation angle in the i -th layer, respectively. The imaginary part of the refractive index directly results in an attenuation of the wave depending on the thickness of the layer.

Multiple reflections are accounted for by multiplying the transmission matrices for each interface and the propagation matrices for each layer. This yields the transfer-matrix for the whole multilayer stack:

$$M = \begin{pmatrix} M_{11} & M_{12} \\ M_{21} & M_{22} \end{pmatrix} = \left[\prod_{i=1}^{N-1} D_{i-1,i} P_i \right] D_{N-1,N}. \quad (3.57)$$

The matrix M relates the electric field amplitudes A_0 and B_0 of the incident and reflected waves in medium 0 with the amplitudes A_N and B_N of the transmitted and incident waves in medium N:

$$\begin{pmatrix} A_0 \\ B_0 \end{pmatrix} = \begin{pmatrix} M_{11} & M_{12} \\ M_{21} & M_{22} \end{pmatrix} \begin{pmatrix} A_N \\ B_N \end{pmatrix}. \quad (3.58)$$

Assuming incidence only from medium 0 and thus setting $B_N = 0$, the reflection and transmission coefficients of the whole multilayer stack can be obtained as

$$r = \frac{B_0}{A_0} = \frac{M_{21}}{M_{11}} \quad (3.59)$$

and

$$t = \frac{A_N}{A_0} = \frac{1}{M_{11}}. \quad (3.60)$$

The reflectance $R(\lambda, \theta_0)$ of the multilayer system is determined from the square of the reflection coefficient, assuming that medium 0 is lossless, i.e. n_0 is real:

$$R(\lambda, \theta_0) = \left| \frac{M_{21}}{M_{11}} \right|^2. \quad (3.61)$$

Under the assumption of real refractive indices n_0 and n_N as well as angles θ_0 and θ_N , the transmittance $T(\lambda, \theta_0)$ of the system is

$$T(\lambda, \theta_0) = \frac{n_N \cdot \cos \theta_N}{n_0 \cdot \cos \theta_0} \cdot |t|^2 = \frac{n_N \cdot \cos \theta_N}{n_0 \cdot \cos \theta_0} \cdot \left| \frac{1}{M_{11}} \right|^2. \quad (3.62)$$

The requirement of energy conservation allows for calculating the absorption of the

multilayer stack:

$$A(\lambda, \theta_0) = 1 - R(\lambda, \theta_0) - T(\lambda, \theta_0). \quad (3.63)$$

3.5. Waveguide and leaky modes

A very important effect based on total internal reflection is the occurrence of guided waves if a layered material with high refractive index is surrounded by lower index materials. Since waveguide modes account for significant losses in OLEDs, the basic properties of these modes will be explained in the following. More details and a derivation of the formulas can be found in Refs. [95, 101].

A typical example of a planar optical waveguide structure is displayed in Fig. 3.6. A thin dielectric film, i.e. the guiding layer (“core”), is sandwiched between a substrate and a cover or cladding layer. The film has a finite thickness d in the z -direction and is expanded infinitely in both other dimensions. Substrate and cover are assumed semi-infinite in the z -direction. The refractive indices for film, substrate and cover are denoted by n_F , n_S and n_C , respectively. For the sake of simplicity, all layers are assumed to be transparent (i.e. nonabsorbing) and nonmagnetic. An asymmetric waveguide structure is investigated, i.e. substrate and cover have different refractive indices.

Total internal reflection at both interfaces requires that the index of refraction of the core must be larger than those of the surrounding media⁹⁵, i.e. $n_F > n_S, n_C$. Without loss of generality, the following relation can be assumed¹⁰¹:

$$n_F > n_S \geq n_C. \quad (3.64)$$

The critical angle θ_S for total internal reflection between film and substrate and the corresponding critical angle θ_C at the cover layer are given by

$$\theta_S = \arcsin \frac{n_S}{n_F} \quad \text{and} \quad \theta_C = \arcsin \frac{n_C}{n_F}. \quad (3.65)$$

If the propagation angle θ is larger than θ_S and θ_C , the wave is totally internally reflected and thus zigzag guided along the x -direction inside the film layer. The electric field decays exponentially in the adjacent media as described in Sec. 3.3. Therefore, the wave propagates without energy dissipation, if the media have no absorption.

It is convenient to describe the propagation of modes by the tangential component of the wave vector, k_x , also called in-plane wave vector or propagation constant which is often denoted by β , or by the effective refractive index n_{eff} of the mode. These characteristic values are defined by¹⁰¹

$$k_x = n_F \cdot k_0 \cdot \sin \theta = n_{\text{eff}} \cdot k_0, \quad (3.66)$$

where k_0 is the wave vector in vacuum. From the necessary condition $\theta \geq \theta_S \geq \theta_C$ for

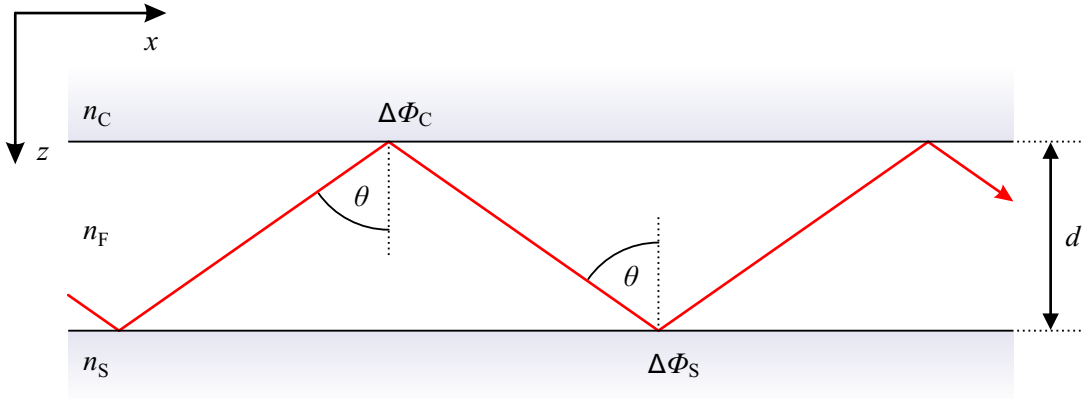


Figure 3.6: Schematic illustration of a planar waveguide structure. The guiding film layer with thickness d has a refractive index n_F and is bounded by a substrate and a cover layer with refractive indices n_S and n_C , respectively. The guided wave propagates at an angle θ , and total internal reflection occurs at the interfaces to the cover and substrate. This changes the phase by $\Delta\Phi_C$ and $\Delta\Phi_S$, respectively.

guided waves and because $\sin\theta \leq 1$, it is possible to derive constraints for the in-plane wave vector and the effective refractive index:

$$k_0 \cdot n_S \leq k_x \leq k_0 \cdot n_F \quad (3.67)$$

and

$$n_S \leq n_{\text{eff}} \leq n_F. \quad (3.68)$$

The number of possible modes within a film of given thickness d is further constrained by the mode condition in z -direction (transverse resonance condition). According to Ref. [101], this condition can be written as:

$$2k_0 \cdot n_F \cdot d \cdot \cos\theta_m - \Delta\Phi_C - \Delta\Phi_S = 2\pi \cdot m. \quad (3.69)$$

In this equation, $m = 0, 1, 2, \dots$ is the mode number, θ_m describes the propagation angle of mode m , and $\Delta\Phi_C$ and $\Delta\Phi_S$ are the phase shifts upon reflection at the interface to the cover and substrate, respectively, which can be expressed as^{95,101}

$$\tan(\Delta\Phi_{C,S}^{\text{TE}}/2) = \sqrt{\frac{n_{\text{eff}}^2 - n_{C,S}^2}{n_F^2 - n_{\text{eff}}^2}} \quad (3.70)$$

for an s-polarized wave and

$$\tan(\Delta\Phi_{C,S}^{\text{TM}}/2) = \frac{n_F^2}{n_{C,S}^2} \cdot \sqrt{\frac{n_{\text{eff}}^2 - n_{C,S}^2}{n_F^2 - n_{\text{eff}}^2}} \quad (3.71)$$

for a p-polarized wave. For constructive interference, it is required that the phase

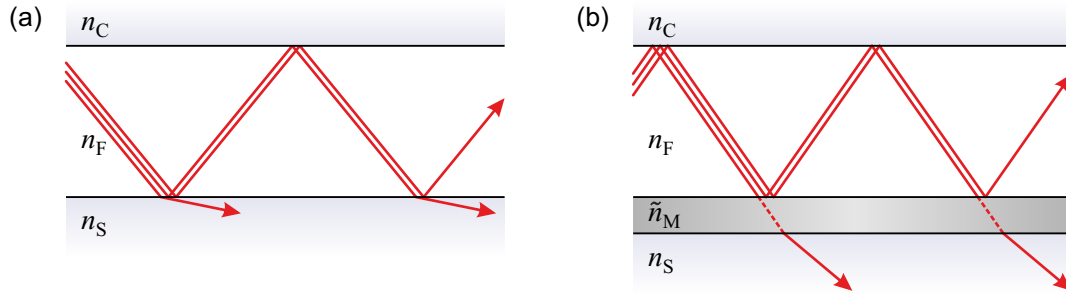


Figure 3.7: (a) Illustration of a leaky mode structure. Light is incident on the film/substrate interface under an angle slightly below the critical value and can thus partially escape into the substrate and propagate there under a large angle. (b) Artificial leaky mode structure. One side of the film layer is bounded by a semitransparent metallic layer with complex refractive index \tilde{n}_M , hence even for angles well below the critical angle it is possible to create modes that are to some extent guided in the film.

difference during one cycle of the guided mode is an integer multiple of 2π .

The number of confined modes is discrete and depends on the thickness, the frequency, and the indices of refraction n_F , n_S and n_C . In the case of an asymmetric waveguide, a certain minimal thickness d is required for the existence of guided modes. This value is called cut-off thickness and is always larger for TM-polarized waves than for TE-polarized radiation. At a given wavelength, the number of confined modes increases with increasing thickness, starting with the TE_0 and TM_0 modes, then the TE_1 and TM_1 modes and so on. For a given thickness d , a maximal wavelength exists for the propagation of guided modes. In other words, a certain waveguide mode m may exist at a smaller thickness in the blue wavelength region in comparison to the red spectral region.

Since an OLED contains several organic layers with higher refractive index than glass and air, and because light emission occurs within the organic layers, such a stack naturally represents a waveguide structure. However, the reflection at one of the interfaces typically occurs at a metallic electrode so that absorption losses occur. In addition, organic layers and ITO have noticeable absorption so that a guided wave gets damped during propagation through the layers and is finally dissipated as heat.

By nature, true waveguide modes are totally internally reflected and confined to a high-index layer and thus are not directly measurable. However, it is also interesting to study light propagating under an angle slightly below the critical angle. From the reflectance shown in Fig. 3.3(b) for light incident from a medium with higher refractive index, it is obvious that the reflectance smoothly decreases for angles below the critical angle. Thus the light wave can partially escape into the lower index medium, while some fraction of the light is reflected. If this picture is transferred to light traveling in a waveguide structure as shown in Fig. 3.7(a), the radiation will be partially emitted into the substrate upon each reflection and propagate there under an angle close to 90° . These modes are called weakly guided modes or leaky modes because they leak from

the waveguide layer to an adjacent medium¹⁰³.

In order to study the properties of usually inaccessible guided modes even for angles well below the critical angle, it is possible to create artificial guided modes in a layer that is bounded on one side by a semitransparent mirror as depicted in Fig. 3.7(b), e.g. a thin film of silver or aluminum. Although the evanescent wave inside the metallic film decays exponentially with thickness, the field can penetrate through this layer if it is thin enough. Consequently, a small fraction of the intensity of the guided mode is transmitted through the metallic layer upon each reflection if the propagation angle is smaller than the critical angle θ_S , i.e. if the mode is allowed to propagate in the substrate as well. Thus, the mode leaks from the guiding layer into the substrate. The concept of leaky modes will be used to extract and investigate guided modes in Chapters 9 and 10.

4. Surface plasmon polaritons

Surface plasmon polaritons are electromagnetic surface waves propagating along the interface between a conductor and a dielectric^{97,104}. Taking Maxwell's equations as a starting point, this chapter describes the fundamentals of surface plasmon polaritons at flat interfaces. First, the dispersion relation will be derived, and properties like the propagation length and skin depth will be discussed. Subsequently, the excitation of surface plasmon polaritons will be investigated and both the grating and prism coupling methods will be explained. Finally, a surface plasmon resonance sensor will be presented which uses an integrated OLED light source and thus offers several advantages compared to other sensing systems.

4.1. Surface plasmons, bulk plasmons and localized plasmons

Besides the term surface plasmon polariton (SPP) which directly indicates the coupling of surface waves and the free electromagnetic field, these surface waves are often described by the shorter expression surface plasmon (SP)^{104,105}. Hence, the term SP will be used in the following. Basically, SPs can be understood as quasiparticles which describe longitudinal fluctuations of the electron density at a metal/dielectric interface. These confined p- (TM-)polarized waves have their intensity maximum at the surface and exponentially decaying fields perpendicular to the interface. The dispersion of SPs strongly depends on the refractive indices of the metal and the adjacent dielectric, which makes them particularly interesting for sensing applications. SPs are usually nonradiative because they have a larger wave vector in comparison to light of similar frequency, hence special coupling methods are required to overcome the mismatch in momentum.

Besides surface plasmons, also excitations of the electrons in the bulk of a metal exist. These volume plasmons can be excited by electron impact at energies above the plasma frequency^{97,104}. In addition, metallic nanostructures support localized plasmons. These plasmons are non-propagating excitations of the conduction electrons of nanoparticles and can be excited by direct light illumination⁹⁷. Localized plasmons have found many applications, even hundreds of years ago they were incidentally used in staining of glass for windows or in ornamental cups, e.g. the Lycurgus Cup^{106,107}.

However, since OLEDs in this work comprise flat layers without nanoparticles and since light in the visible spectral region lies below the plasma frequency of those metals

commonly used for electrodes, both volume and localized plasmons are not relevant and therefore the discussion in the next sections exclusively focuses on surface plasmons.

4.2. Dispersion relation of surface plasmons

The derivation of the surface plasmon dispersion follows the approach of Sambles *et al.* as in Ref. [100]. Other descriptions are found for example in the textbooks about surface plasmons by Raether¹⁰⁴ and Maier⁹⁷.

Basically, a propagating wave solution confined to a flat interface between a nonabsorbing dielectric medium 1 and a conducting metallic medium 2 is requested. Confinement implies that the fields are evanescent perpendicular to the interface, i.e. they decay exponentially with increasing distance from the surface. Let the x - y -plane be the interface plane and medium 1 expand into the negative z -direction while medium 2 is located in the half space in positive z -direction, as shown in Fig. 4.1(a). Both media are assumed nonmagnetic and isotropic. The dielectric is assumed transparent, i.e. the relative permittivity ε_1 is a positive real number. For frequencies below the plasma frequency, the relative permittivity ε_2 of the metal is largely real and negative¹⁰⁰, cf. Eq. (3.27). In the beginning, a purely real permittivity ε_2 is assumed for the metal, i.e. a purely imaginary refractive index. The effect of an imaginary component of ε_2 will be discussed later.

A surface wave must satisfy the wave equation in both media. In the case of a p-polarized wave, the electric field vector lies in the x - z -plane, i.e. the plane of incidence, while the magnetic field vector only has a y -component. Consequently, the y -component of the electric field as well as the x - and z -components of the magnetic field are zero. Thus, the propagation of a p-polarized wave in x -direction is described by the following fields where subscript 1 and 2 denote the first and second medium, respectively:

$$\vec{E}_1 = \begin{pmatrix} E_{x1} \\ 0 \\ E_{z1} \end{pmatrix} e^{i(k_x \cdot x - \omega \cdot t)} \cdot e^{ik_{z1} \cdot z} \quad \text{and} \quad \vec{H}_1 = \begin{pmatrix} 0 \\ H_{y1} \\ 0 \end{pmatrix} e^{i(k_x \cdot x - \omega \cdot t)} \cdot e^{ik_{z1} \cdot z}, \quad (4.1)$$

$$\vec{E}_2 = \begin{pmatrix} E_{x2} \\ 0 \\ E_{z2} \end{pmatrix} e^{i(k_x \cdot x - \omega \cdot t)} \cdot e^{ik_{z2} \cdot z} \quad \text{and} \quad \vec{H}_2 = \begin{pmatrix} 0 \\ H_{y2} \\ 0 \end{pmatrix} e^{i(k_x \cdot x - \omega \cdot t)} \cdot e^{ik_{z2} \cdot z}. \quad (4.2)$$

In these equations, the continuity of the tangential component of the wave vector was used, i.e. $k_{x1} = k_{x2} \equiv k_x$. The x - and z -components of the wave vector are related by

$$k_x^2 + k_{zi}^2 = \varepsilon_i \cdot k_0^2 \quad \text{with } i = 1 \text{ or } 2, \quad (4.3)$$

where $k_0 = \omega/c_0$ is the vacuum wave vector with angular frequency ω and the speed of

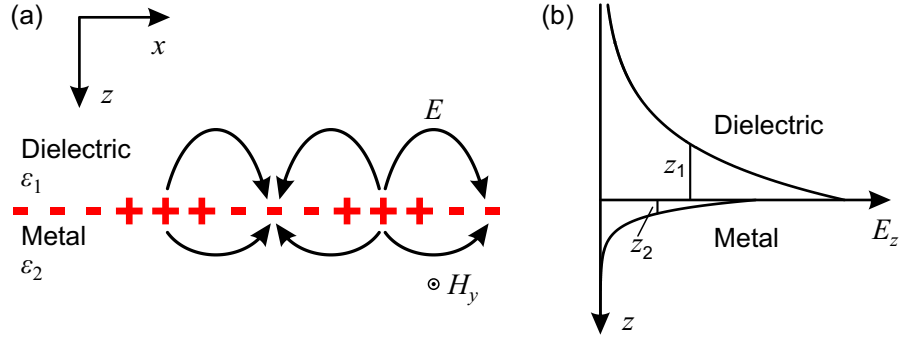


Figure 4.1: (a) Schematic illustration of a confined surface plasmon wave which results from fluctuations of the electron density at a metal/dielectric interface. The wave is propagating in the x -direction. (b) Distribution of the electric fields of a surface plasmon wave. The maximum is located at the interface and the evanescent fields decay exponentially with increasing distance from the interface. Typically, the decay in the metal is significantly faster in comparison to the dielectric. z_1 and z_2 describe the skin depth of the dielectric and metal, respectively. These values correspond to the depth at which the electric field falls to $1/e$.

light c_0 in vacuum.

For a confined surface mode, the electric field must be evanescent and thus decay exponentially into both media, therefore the following requirements must be fulfilled:

$$(ik_{z1}) > 0, \quad (4.4)$$

$$(ik_{z2}) < 0. \quad (4.5)$$

This condition can only be fulfilled by assuming a p-polarized wave as will be shown later.

By applying Maxwell's equations $\vec{\nabla} \cdot \vec{E} = 0$ and $\vec{\nabla} \times \vec{E} = -\mu_0 \cdot \frac{\partial \vec{H}}{\partial t}$ for isotropic and nonmagnetic media, the following relations between the electric field components are found:

$$E_{z1} = -E_{x1} \cdot \frac{k_x}{k_{z1}}, \quad (4.6)$$

$$E_{z2} = -E_{x2} \cdot \frac{k_x}{k_{z2}}, \quad (4.7)$$

$$\mu_0 \cdot \omega \cdot H_{y1} = E_{x1} \cdot k_{z1} - E_{z1} \cdot k_x, \quad (4.8)$$

$$\mu_0 \cdot \omega \cdot H_{y2} = E_{x2} \cdot k_{z2} - E_{z2} \cdot k_x. \quad (4.9)$$

Using these results as well as Eqs. (3.11) and (4.3), the following relationship between H_y and E_x is obtained:

$$H_{y1} = \varepsilon_0 \cdot \varepsilon_1 \cdot \omega \cdot E_{x1} / k_{z1}, \quad (4.10)$$

$$H_{y2} = \varepsilon_0 \cdot \varepsilon_2 \cdot \omega \cdot E_{x2} / k_{z2}. \quad (4.11)$$

According to the boundary conditions in Eqs. (3.29) and (3.31), the tangential compo-

nents of the electric and magnetic field are continuous across the interface, i.e. $E_{x1} = E_{x2}$ and $H_{y1} = H_{y2}$. This leads to the following relationship between the relative permittivities and the normal components of the wave vectors:

$$\frac{\varepsilon_1}{k_{z1}} = \frac{\varepsilon_2}{k_{z2}}. \quad (4.12)$$

This relation can only satisfy requirements (4.4) and (4.5) if ε_1 and ε_2 have opposite sign, which is possible if the media are dielectric and metallic, respectively. Equation (4.3) can thus be rewritten as

$$k_{z1} = -i (k_x^2 - \varepsilon_1 \cdot k_0^2)^{1/2}, \text{ requiring } k_x^2 > \varepsilon_1 \cdot k_0^2, \quad (4.13)$$

and

$$k_{z2} = i (k_x^2 - \varepsilon_2 \cdot k_0^2)^{1/2}, \text{ requiring } k_x^2 > \varepsilon_2 \cdot k_0^2, \quad (4.14)$$

thus fulfilling the requirements for exponentially decaying fields in both media. Equation (4.13) demands that the surface plasmon wave vector is larger than the maximum photon wave vector available in the dielectric, which causes a fundamental problem for the excitation of SPs by light as will be discussed in Sec. 4.3. Condition (4.14) for the metal is automatically satisfied with negative ε_2 . It is obvious from Eqs. (4.12)–(4.14) that the evanescent electric field decays much faster in the metal than in the dielectric. A typical surface plasmon wave and the dependence of the electric fields on the distance from the interface is illustrated in Figs. 4.1(a) and (b), respectively.

By substituting expressions (4.13) and (4.14) into Eq. (4.12), the dispersion relation of surface plasmons is found:

$$k_x(\omega) = k_0 \cdot \left(\frac{\varepsilon_1 \cdot \varepsilon_2}{\varepsilon_1 + \varepsilon_2} \right)^{1/2} = \frac{\omega}{c_0} \cdot \left(\frac{\varepsilon_1(\omega) \cdot \varepsilon_2(\omega)}{\varepsilon_1(\omega) + \varepsilon_2(\omega)} \right)^{1/2}. \quad (4.15)$$

It should be emphasized that the permittivities depend on frequency, i.e. $\varepsilon_1(\omega)$ and $\varepsilon_2(\omega)$. Thus, Eq. (4.15) cannot be easily resolved into $\omega(k_x)$. Moreover, it is important to note that Eq. (4.15) is strictly valid only for semi-infinite metal and dielectric layers. The influence of finite thicknesses will be discussed in Sec. 7.1.

With negative ε_2 , it is necessary that $|\varepsilon_2| > \varepsilon_1$ in order to obtain a real k_x , which is the requirement for a propagating mode. Altogether, Maxwell's equations and the boundary conditions are satisfied and the result is a confined surface wave having real k_x with $k_x > \sqrt{\varepsilon_1} \cdot k_0 = n_1 \cdot k_0$ and imaginary k_{z1} and k_{z2} , provided $\varepsilon_2 < 0$ and $|\varepsilon_2| > \varepsilon_1$. Examples of calculated SP dispersion curves are displayed in Fig. 4.2. For low frequencies, i.e. small k_x , the dispersion relation of SPs approaches the light line, which is given by $\omega = c_0 \cdot k_x$, but it always remains larger so that SPs cannot transform into light at smooth interfaces. At large k_x or $\varepsilon_2 \rightarrow -\varepsilon_1$, the value of ω approaches the

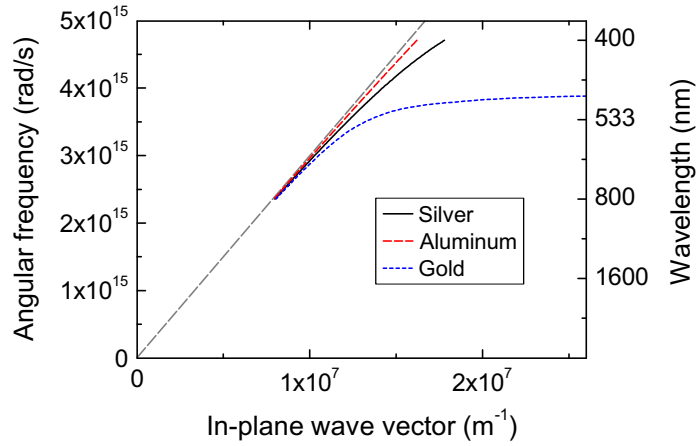


Figure 4.2: Dispersion relation of surface plasmons at the interface between air and several metals according to Eq. (4.15). The dispersion is shown for silver, aluminum and gold in the range between 400 nm and 800 nm. All values were calculated from the optical constants shown in the appendix, cf. Sec. A.2. The dashed gray line describes the light line in air for grazing incidence which is given by $\omega = c_0 \cdot k_x$.

surface plasmon frequency ω_{sp} which is given by^{97,104}

$$\omega_{\text{sp}} = \frac{\omega_{\text{p}}}{(1 + \varepsilon_1)^{1/2}}, \quad (4.16)$$

where ω_{p} is the plasma frequency, cf. Eq. (3.28).

It should be noted that gold approaches its plasma frequency for short wavelengths and thus becomes partially transparent (cf. optical constants of gold in the appendix in Sec. A.2). This does not only give gold its typical color because blue light is reflected less, but also results in a loss of its metallic character. Therefore, surface plasmons are not supported at the interface to a gold film for short wavelengths, i.e. high frequencies. This causes the strong bending towards large k_x values in the dispersion in Fig. 4.2.

It is important to keep in mind that the term wavelength is used as a descriptive parameter for the energy throughout this work, assuming the relation of $\omega = (2\pi \cdot c_0/\lambda)$. For instance, SPs with a wavelength of 500 nm correspond to SPs having an angular frequency of $\omega \approx 3.77 \times 10^{15}$ Hz. The true wavelength of SPs is smaller because the wave vector is larger compared to free-space radiation.

As mentioned above, surface plasmons are p-polarized. This can be proven by considering an s-polarized wave of the form

$$\vec{E}_i = \begin{pmatrix} 0 \\ E_{yi} \\ 0 \end{pmatrix} e^{i(k_x \cdot x - \omega \cdot t)} \cdot e^{ik_{zi} \cdot z} \quad \text{and} \quad \vec{H}_i = \begin{pmatrix} H_{xi} \\ 0 \\ H_{zi} \end{pmatrix} e^{i(k_x \cdot x - \omega \cdot t)} \cdot e^{ik_{zi} \cdot z}, \quad (4.17)$$

with $i = 1$ or 2 . Applying Maxwell's equation $\vec{\nabla} \cdot \vec{B} = \mu_0 \vec{\nabla} \cdot \vec{H} = 0$ gives

$$H_{x1} \cdot k_x + H_{z1} \cdot k_{z1} = 0, \quad (4.18)$$

$$H_{x2} \cdot k_x + H_{z2} \cdot k_{z2} = 0. \quad (4.19)$$

From the boundary conditions for nonmagnetic materials it is known that $H_{x1} = H_{x2}$ and $H_{z1} = H_{z2}$, cf. Eqs. (3.31) and (3.32). Consequently, for an s-polarized wave it is necessary that

$$k_{z1} = k_{z2}. \quad (4.20)$$

However, this result is inconsistent with the requirement that the electric fields decay exponentially into both media, cf. Eqs. (4.4) and (4.5). In addition, there is a simple descriptive argument why SPs must not be s-polarized: waves propagating along the interface between two media must necessarily have electric field components normal to the surface¹⁰⁸. Since s-polarized waves only have an electric field component parallel to the interface, this requirement cannot be fulfilled. Hence, no confined s-polarized surface wave can exist at the interface between two homogeneous media⁹⁵. In other words, surface plasmon waves are always p- (TM-)polarized.

So far, it was assumed that the permittivities are purely real. In this case the surface plasmon resonance is infinitely sharp and has an infinite propagation length¹⁰⁰. In reality, the free electrons in a metal suffer scattering with lattice vibrations, defects and the surface, which leads to damping of the oscillations created by the electric field. This causes an imaginary component of the relative permittivity:

$$\varepsilon_2 = (n_2 + i\kappa_2)^2 = n_2^2 - \kappa_2^2 + 2in_2 \cdot \kappa_2 = \varepsilon_{2r} + i\varepsilon_{2i}, \quad (4.21)$$

where ε_{2r} and ε_{2i} describe the real and imaginary component of the relative permittivity of the metal, respectively. Hence, the dispersion relation is modified:

$$k_x = k_0 \cdot \left(\frac{\varepsilon_1 \cdot (\varepsilon_{2r} + i\varepsilon_{2i})}{\varepsilon_1 + \varepsilon_{2r} + i\varepsilon_{2i}} \right)^{1/2}. \quad (4.22)$$

Thus, the wave vector in x -direction becomes complex, i.e. $k_x = k_{xr} + i k_{xi}$. By working out the real and imaginary parts and assuming $\varepsilon_{2i} \ll \varepsilon_{2r}$, the components of the complex wave vector are found to be^{97,104}

$$k_{xr} = k_0 \cdot \left(\frac{\varepsilon_1 \cdot \varepsilon_{2r}}{\varepsilon_1 + \varepsilon_{2r}} \right)^{1/2}, \quad (4.23)$$

$$k_{xi} = k_0 \cdot \left(\frac{\varepsilon_1 \cdot \varepsilon_{2r}}{\varepsilon_1 + \varepsilon_{2r}} \right)^{3/2} \cdot \frac{\varepsilon_{2i}}{2(\varepsilon_{2r})^2}. \quad (4.24)$$

Obviously, the equation for the real component of k_x corresponds to Eq. (4.15) if ε_2 is

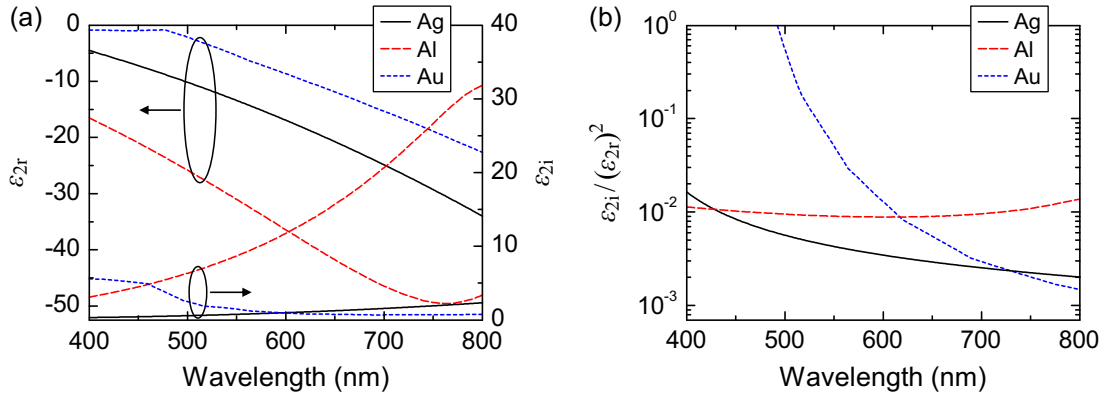


Figure 4.3: (a) Real (ϵ_{2r}) and imaginary (ϵ_{2i}) parts of the permittivity of silver, aluminum and gold calculated from the optical constants in the appendix, cf. Sec. A.2. (b) Ratio $\epsilon_{2i}/(\epsilon_{2r})^2$ which determines the width and thus the observability of SP resonance.

replaced by ϵ_{2r} . Therefore, the dispersion relation only depends on the real component of the permittivity of the metal. The result for the imaginary component can be further simplified if $\epsilon_1 \ll \epsilon_{2r}$ is assumed¹⁰⁰:

$$k_{xi} = \frac{1}{2}k_0 \cdot \frac{\epsilon_{2i} \cdot (\epsilon_1)^{3/2}}{(\epsilon_{2r})^2}. \quad (4.25)$$

Hence, the attenuation of surface plasmon waves is governed by both the real and imaginary component of the metal. The width of the SP resonance is proportional to k_{xi} . Therefore, metals with small ϵ_{2i} and large negative ϵ_{2r} are required in order to obtain a sharp resonance and thus an increase in observability¹⁰⁰. Although many metals support a sharp resonance in the near infrared, only a few materials are suitable in the visible spectral region. Especially silver, gold and aluminum are good candidates, and the real and imaginary parts of their complex permittivity are shown in Fig. 4.3(a). The ratio $\epsilon_{2i}/(\epsilon_{2r})^2$, which determines the internal damping, is plotted in Fig. 4.3(b). It is obvious that silver is the optimal metal for a sharp SP resonance in the visible spectrum¹⁰⁴. This will also be confirmed by measurements in Sec. 9.3.1. Therefore, silver is the material of choice for studying the properties of SPs and it will be used throughout this work in order to investigate ways of extracting energy which was dissipated to SPs.

The spatial extension of an SP wave may be described by the wave vectors in x - and z -direction, but it is more convenient to use the propagation length and the skin depth¹⁰⁴. As the wave propagates along a planar interface, it loses energy to the metal due to finite damping, which causes heating of the metal. The intensity of SPs is proportional to the square of the electric field and decreases as $\exp(-2k_{xi} \cdot x)$. The propagation length L after which the intensity decreases to $1/e$ is thus given by¹⁰⁴

$$L = \frac{1}{2k_{xi}}. \quad (4.26)$$

The skin depth $z_i \propto 1/k_{zi}$ in medium i is defined as the depth at which the electric field falls to $1/e$ (cf. Fig. 4.1(b)) and is thus given by^{104,108}:

$$z_1 = \frac{\lambda}{2\pi} \cdot \left(\frac{\varepsilon_1 + \varepsilon_{2r}}{-(\varepsilon_1)^2} \right)^{1/2} \quad \text{and} \quad z_2 = \frac{\lambda}{2\pi} \cdot \left(\frac{\varepsilon_1 + \varepsilon_{2r}}{-(\varepsilon_{2r})^2} \right)^{1/2}. \quad (4.27)$$

It should be noted that the values in Eq. (4.27) must be actually multiplied with the imaginary unit and the correct sign in order to obtain an exponential decay of the fields defined in Eqs. (4.1) and (4.2). However, the skin depth is written in this form to obtain a descriptive (i.e. real and positive) value which can be expressed in nanometers.

It is instructive to calculate examples of the characteristic values which describe an SP wave. For an interface between air and silver and a wavelength of $\lambda = 550$ nm, the refractive indices are given by $n_1 = 1$ and $n_2 = 0.105 + i3.66$, and thus the permittivities are $\varepsilon_1 = 1$ and $\varepsilon_2 = -13.4 + i0.769$. Hence, the real part of the in-plane wave vector is $k_{xr} = 1.188 \times 10^7 \text{ m}^{-1}$, which is larger than $k_0 = 1.142 \times 10^7 \text{ m}^{-1}$ in air. According to Eq. (4.24), the imaginary part of k_x has a value of $k_{xi} = 2.75 \times 10^4 \text{ m}^{-1}$. This corresponds to a propagation length of $18.2 \mu\text{m}$. The skin depth in air is 308 nm, while the skin depth in silver is only 23 nm.

If the interface between a typical organic material with a permittivity of $\varepsilon_1 = n_1^2 = (1.8)^2 = 3.24$ and silver is examined, most of the above values change significantly. The real part of the wave vector then increases to $k_{xr} = 2.36 \times 10^7 \text{ m}^{-1}$, while the propagation length decreases to $2.3 \mu\text{m}$. The skin depth in the organic medium is reduced to 86 nm, whereas the skin depth in the metal is 21 nm and thus almost similar to the first example.

Considering the interaction of SPs with light as discussed in the next section, only the real part of the complex wave vector is relevant. In the following, the real component will be denoted by k_x , keeping in mind that it actually refers to k_{xr} .

4.3. Coupling of surface plasmons and light

As discussed in the previous section, surface plasmons on a flat metal/dielectric interface cannot be directly excited by light incident from the dielectric because the projection of the photon momentum along the interface is always smaller than the SP wave vector, even at grazing incidence. Nevertheless, excitation of SPs by light is possible by using special coupling methods (prism or grating coupling) or via the near-field of e.g. a fluorescent dye which is in proximity to a metal surface^{97,104}. In addition, SPs can be excited by electron bombardment and highly focused optical beams⁹⁷. However, the latter approaches will not be treated in this work because they are not relevant for OLEDs.

Apparently, the excitation by light must circumvent the fundamental problem that the wave vector of an SP wave for a given frequency is larger than the wave vector of light, cf. Eq. (4.13). Figure 4.4 illustrates this problem and shows the schematic dispersion of

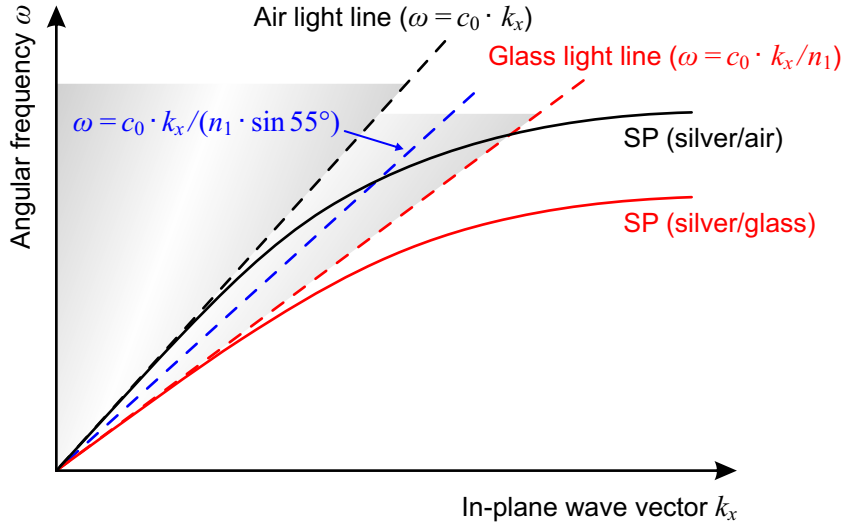


Figure 4.4: Schematic illustration of the SP dispersion at a silver/air and a silver/glass interface (solid lines). The dashed black and red lines represent the light line in air and glass (refractive index n_1), respectively. The air and glass light cones are indicated as gray areas. By changing the angle of incidence, the slope of the light dispersion increases as depicted by the dashed blue line.

SPs and the light line for both a silver/air as well as a silver/glass interface.

In general, the wave vector of light (i.e. its momentum) is increased by a factor n_1 in comparison to the vacuum wave vector, if the light wave propagates in a medium with refractive index n_1 . Therefore, the in-plane wave vector of light in such a medium at an angle of incidence θ is given by

$$k_x = n_1 \cdot k_0 \cdot \sin \theta, \quad (4.28)$$

with k_0 being the wave vector in vacuum. Thus, the dispersion in terms of the in-plane wave vector at this angle is

$$\omega = c_0 \cdot k_0 = \frac{c_0 \cdot k_x}{(n_1 \cdot \sin \theta)}. \quad (4.29)$$

The maximum in-plane wave vector is obtained at grazing incidence, i.e. the angle of incidence is $\theta = 90^\circ$. In this case, $k_x = n_1 \cdot k_0 \cdot \sin 90^\circ = n_1 \cdot k_0$, and the dispersion relation is given by $\omega = c_0 \cdot k_x / n_1$. This determines the light line of the medium. For a given frequency, the wave vector of light in a medium with $n_1 > 1$ is larger than the corresponding wave vector in air. Hence, the slope of the glass light line is reduced by a factor $(1/n_1)$ and the light line in glass is bent to the right in comparison to the light line in air, cf. Fig. 4.4.

It is apparent from Eq. (4.28) that the in-plane wave vector of light can take any value between zero and $(n_1 \cdot k_0)$ if the angle is varied between $0 \leq \theta \leq 90^\circ$. This defines the light cone as the area between the axis $k_x = 0$ and the light line. An exemplary

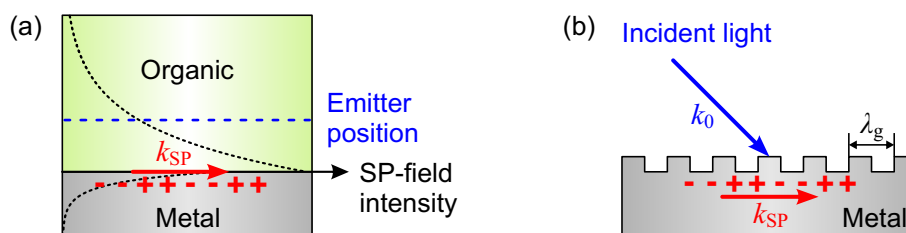


Figure 4.5: (a) Illustration of near-field coupling of an excited molecule to SPs. The emitting molecule must be positioned close to the metal so that its dipole field overlaps with the evanescent SP field. (b) SP excitation by grating coupling. The wave vector mismatch between incident light and SPs is compensated by Bragg scattering at the grating, thus changing the wave vector by integer multiples of the grating wave vector $k_g = 2\pi/\lambda_g$, with λ_g being the period of the grating.

dispersion of light propagating in glass at an angle of $\theta = 55^\circ$ is indicated as dashed blue line in Fig. 4.4.

However, it is obvious that the SP dispersion at a silver/air interface lies to the right of the air light cone, and similarly the SPs at a glass/air interface have a larger wave vector than the corresponding light line in glass. In other words, the excitation of SPs at a planar interface by light incident from the adjacent dielectric medium is not possible because energy ($\hbar\omega$) and momentum ($\hbar k_x$) conservation for the coupling of light and SPs cannot be fulfilled as SPs have a too large in-plane wave vector. Hence, special coupling methods are required in order to excite SPs.

As a matter of fact, the reverse process is also prohibited, i.e. SPs propagating at a planar interface are normally nonradiative and cannot transform into free-space radiation. However, if SPs can be excited by a certain coupling technique, it should also be possible to make SPs radiative and thus extract energy from SPs and transform them back to visible light by the reverse method. These approaches represent interesting concepts for enhancing the light extraction of OLEDs and hence will be treated in detail in Chapters 7, 8, and 9. Therefore, this section only briefly explains the basic idea of each of the coupling techniques, i.e. near-field coupling, grating coupling and prism coupling.

Near-field coupling

This coupling method was already mentioned in the context of optical loss channels of OLEDs in Sec. 2.5. If an excited organic molecule is in close proximity to a metallic surface, i.e. within a distance of about one hundred nanometers, the field of the molecular dipole oscillator and the evanescent SP field overlap, as illustrated in Fig. 4.5(a). Energy and momentum conservation can be fulfilled because an excited dye is not restricted to small wave vectors²⁵. Therefore, the molecule can dissipate its energy via its optical near-field into a confined SP wave instead of emitting a freely propagating photon into the organic layer.

The coupling of excited molecules to SPs strongly depends on the distance of the

molecule to the metallic surface and the orientation of the transition dipole moment as will be discussed in Secs. 5.5 and 11.1.2, respectively¹⁰⁹. In Chapter 7, this coupling method will be used in a reverse way in order to excite acceptor molecules by the SP field and thus recover some of the energy lost to SPs.

Grating coupling

In order to excite SPs at a metallic surface with light incident through the adjacent dielectric medium, it is necessary to match the in-plane wave vector k_{light} of the incident photons with the SP wave vector k_{SP} for a given frequency.

One of the methods to achieve this is grating coupling^{97,104,110}. In this approach, the interface between the metal and the dielectric is not planar but periodically corrugated, as shown in Fig. 4.5(b). The grating has a period λ_g and a corresponding wave vector $k_g = 2\pi/\lambda_g$. The incident light can Bragg scatter at the grating, thus shifting the in-plane wave vector by a multiple of the grating wave vector. Hence, the mismatch in k_x between light and SPs is compensated by an additional wave vector component k_g . Consequently, energy and momentum conservation can be fulfilled and coupling between radiation and SPs is allowed.

Besides coupling of light to SPs, the reverse process is also possible, i.e. SPs can Bragg scatter at the grating and transform into propagating light. Extraction of SPs by means of a periodically structured grating and the accompanying theoretical description will be studied in detail in Chapter 8.

Prism coupling

Even without a grating, SPs can be excited by incident light using the prism coupling approach¹⁰⁴. This method makes use of the evanescent field which occurs in the case of total internal reflection of light as discussed in Sec. 3.3. One of the configurations used to excite SPs is depicted in Fig. 4.6(a). This setup is commonly called Kretschmann- (or Kretschmann-Raether-) configuration¹¹¹. Light is incident through a prism with refractive index n_p which must be larger than the refractive index of the environment at the bottom side of the metal, e.g. air. It should be noted that p-polarized light is required for coupling between light and SPs. Typically, the prism is made of glass and frequently silver is used as metallic layer. Hence, the light line in the prism corresponds to the glass light line in Fig. 4.4. Upon reflection at the silver/glass interface, an evanescent field emerges which penetrates through the silver layer if the thickness is small enough, i.e. a few tens of nanometers. The SP dispersion on the bottom silver surface is mainly determined by the air environment and thus represented by the silver/air dispersion in Fig. 4.4. Depending on the angle of incidence, the in-plane wave vector of light in the prism can take any value between zero and the glass light line, cf. Eq. (4.28). Thus, coupling between radiation in the prism and SP waves at the silver/air interface

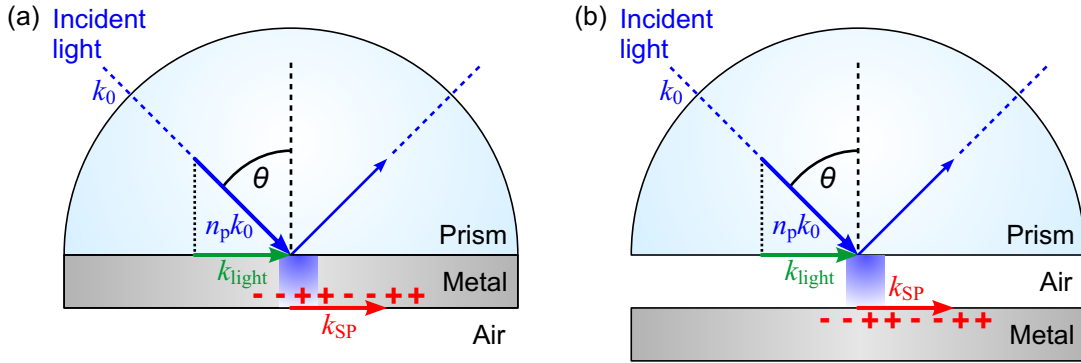


Figure 4.6: Illustration of the prism coupling technique. (a) Kretschmann configuration. Light incident through a glass prism can couple to SPs at the metal/air interface via the evanescent field that occurs upon total reflection at the metal/glass interface. (b) Otto configuration. Coupling takes place via the evanescent field through a thin air gap.

can be realized by adjusting the angle of incidence for a given frequency. In other words, varying the angle of incidence of the radiation allows for tuning through the resonance¹⁰⁰. Coupling is possible up to a maximum frequency which is determined by the crossing point of the glass light line and the SP dispersion at the silver/air interface. It should be noted that excitation of SPs at the silver/glass interface cannot be achieved because the SP dispersion at this interface lies outside the glass light cone.

Another possible configuration is displayed in Fig. 4.6(b). In the so-called Otto configuration, the prism and metal are separated by a thin air gap^{100,112}. Here, the evanescent field that occurs upon total internal reflection at the glass/air interface penetrates through the air gap and can couple to SPs at the top silver/air interface. This configuration has less practical importance nowadays, which is mainly due to the problematic realization of the thin air gap. Therefore, this gap is sometimes replaced by a thin dielectric spacer which must have a lower refractive index in comparison to the prism¹⁰⁰.

The prism coupling approach based on the Kretschmann geometry will be widely used throughout this work. The following section discusses the influence of various parameters in detail. Section 4.5 introduces a surface plasmon resonance sensor which makes use of the prism coupling approach.

As in the case of grating coupling, the reversed prism coupling approach may be utilized for transforming SPs into free-space radiation. Chapter 9 investigates the commonly used configuration with a glass prism and studies the influence of the metal and its thickness as well as the role of an adjacent dielectric medium. In order to apply the reversed method for increasing light extraction in OLEDs, it is necessary to modify the configuration so that the refractive index of the prism is significantly increased. This “high-index coupling” technique is subject of Chapter 10.

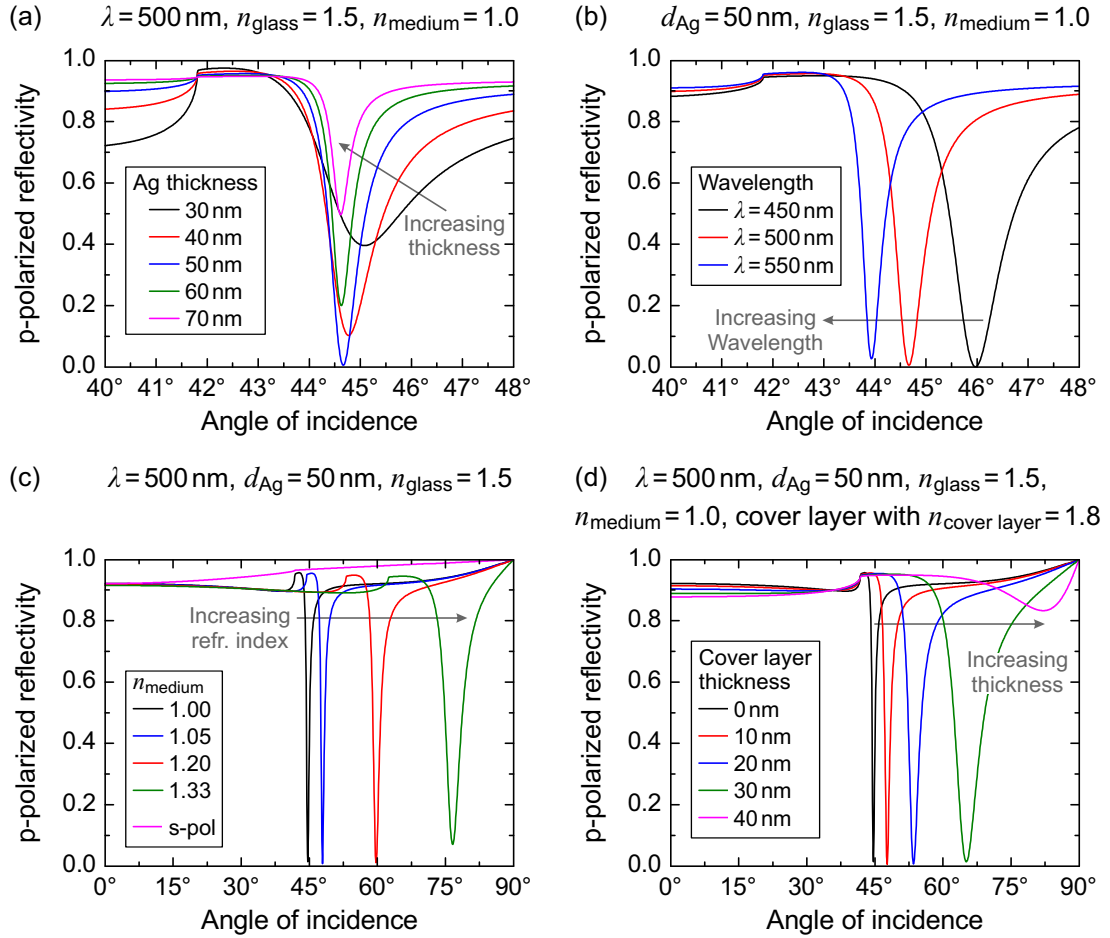


Figure 4.7: Simulated p-polarized reflectivity in a Kretschmann configuration as shown in Fig. 4.6(a) with variation of (a) silver thickness d_{Ag} , (b) wavelength λ of the incident light, (c) refractive index n_{medium} of the adjacent medium and (d) thickness $d_{\text{cover layer}}$ of a dielectric cover layer ($n = 1.8$). Light is incident through a prism with $n_{\text{glass}} = 1.5$. For comparison, the s-polarized reflectivity is plotted in (c) for $n_{\text{medium}} = 1$. Optical constants of silver: $n = 0.081 + i2.69$ (450 nm), $n = 0.092 + i3.19$ (500 nm) and $n = 0.105 + i3.66$ (550 nm). Simulations were performed using the program RSim from Markus Leitz¹¹⁴.

4.4. Attenuated total reflection

The prism coupling approach is also called frustrated or attenuated total (internal) reflection (ATR) because the incident light resonantly couples to SPs and therefore the intensity of the reflected light is attenuated^{111,113}. The basic setup was already presented in Fig. 4.6(a). Since the excitation occurs under an angle of incidence larger than the critical angle of total internal reflection, the transmission naturally vanishes. Hence, due to conservation of energy, a minimum in the reflectivity corresponds to a maximum in the absorption and thus strong coupling of light to SPs. Figure 4.7 illustrates the dependence of the p-polarized reflectivity on several parameters of the setup^{104,111}.

The thickness of the metal is probably the most important parameter as can be seen in Fig. 4.7(a). The depth of the surface plasmon resonance (SPR) strongly depends on the thickness. In fact, the reflectivity can even reach a value of zero for a certain thickness. A further increase reduces the depth of the SPR again. Moreover, the width of the SPR is reduced with increasing thickness. In contrast, the angular position of the SPR is only slightly influenced. For a small metal thickness, the evanescent SP field partially penetrates through the metal and senses the higher refractive index of the prism. Hence, the dispersion is not only determined by the adjacent medium on the bottom metal side but also slightly by the prism material. Therefore, the dispersion is shifted to higher wave vectors and thus the angle of the SPR is increased. This effect will be discussed in more detail in Sec. 7.1.

The influence of the wavelength is displayed in Fig. 4.7(b). It is obvious that a smaller wavelength primarily shifts the SPR to larger angles whereas the depth remains almost unchanged. In addition, the width increases slightly because the internal damping is larger at smaller wavelengths¹¹¹, cf. Fig. 4.3(b).

Another very important parameter is the refractive index of the adjacent medium as shown in Fig. 4.7(c). Even small changes in the refractive index cause a significant shift of the SPR position and thus are easily detectable. For the purpose of comparison, this graph also shows the s-polarized reflectivity. In this case, the reflectivity is very high over the whole angular range because SPs cannot be excited by s-polarized radiation.

Figure 4.7(d) illustrates the influence of a thin dielectric cover layer ($n = 1.8$) on the bottom side of the Ag film. Due to the higher refractive index compared to air, the SPR shifts to higher angles. Depending on the thickness of this layer, the evanescent SP field penetrates through the dielectric layer into air and thus the SPR position is determined by both media as will be explained in detail in Sec. 7.1. If the thickness of the dielectric layer gets too large, i.e. above around 50 nm, a large fraction of the SP field is located in the dielectric layer and thus the SP dispersion is governed by this layer. Since the refractive index is larger in the dielectric layer than in the prism, the Kretschmann configuration is no more fulfilled and no coupling to SPs is possible. It should also be noted that the width of the SPR will increase if the cover layer is absorbing.

It should be stressed that SPs excited by the prism coupling method are inherently leaky waves, i.e. they lose energy not only due to internal damping but also due to leakage of radiation into the prism⁹⁷. The minimum in the intensity of the reflected beam arises from destructive interference between leakage radiation and directly reflected light. As displayed in Fig. 4.7(a), the destructive interference can be perfect for a specific metal thickness, thus providing a vanishing intensity of the reflected radiation.

The findings above are in general also valid in the case of the reversed Kretschmann configuration which will be used for extracting light from SPs in Chapters 9 and 10. In this case, SPs are excited by near-field coupling of an adjacent dye. Hence, there is no destructive interference in the prism, and leakage radiation can be coupled out.

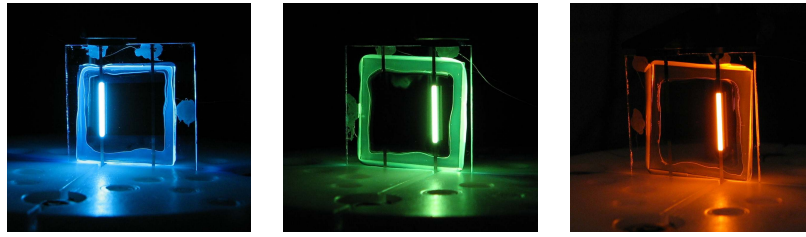


Figure 4.8: Photographs of the blue, green and red OLEDs used as light source for the SPR sensor. The active area of all OLED pixels is $10\text{ mm} \times 0.5\text{ mm}$, so that the OLED can be regarded as a linear light source in this case.

4.5. Surface plasmon resonance sensor utilizing an integrated OLED

Due to their unique properties, surface plasmons are utilized for instance in plasmonic waveguides⁹⁷ or in surface enhanced Raman scattering due to the enhanced field near the surface^{97,104}. In fact, a new field called plasmonics has emerged with numerous applications, see e.g. Refs. [97, 106, 108, 115] for a detailed list. This section briefly introduces a novel SPR sensor on the basis of an integrated OLED light source. A detailed description can be found in Refs. [116–119].

Since surface plasmons are extremely sensitive to slight perturbations within their skin depth, surface plasmon resonance sensors are ideally suited for sensing applications^{111,120–123}. The sensor presented in this section includes a metallic sensing layer and an OLED which are located on opposite sides of one common prism. The light emitted by the OLED leaves the prism after reflection at the sensing layer. Using an OLED as a light source has the considerable advantage that light is inherently emitted into a glass substrate. Therefore, OLEDs are perfect candidates for a combination with the prism coupling approach whereas the radiation from other light sources, e.g. lasers or halogen lamps, has to be coupled into the prism using special optical components.

First, an analysis of the spectral and angular dependent intensity of the reflected light will be shown for sensing layers consisting of silver and gold. Moreover, the sensor function will be illustrated by real-time monitoring of the dissolving process of sodium chloride (NaCl) in water. Finally, the monolithic integration of both the OLED and the metallic sensing layer will be presented.

Experimental setup

Three OLEDs with different emission spectra were used as light source in the experiments, cf. Fig. 4.8. The OLEDs are based on the same emitter materials as the OLEDs described in Sec. 2.7.3. By combining a blue, green and red OLED, almost the whole visible spectrum can be covered.

The experimental arrangement is shown in Fig. 4.9. As metallic sensor films, silver

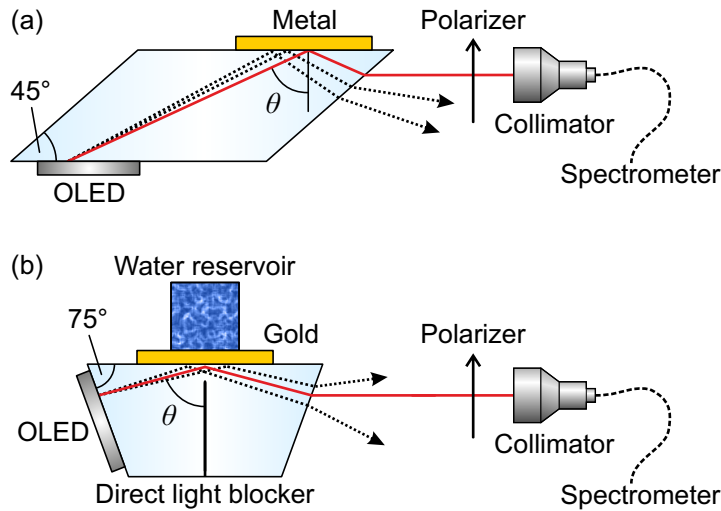


Figure 4.9: (a) Top view of the experimental setup for measurements in air: An OLED and a metallic sensor film are located on opposite sides of a glass prism which was mounted on a motorized rotation stage. Light was incident under an angle θ on the metallic sensing film. (b) For measurements in aqueous environment, the OLED and the metal film were attached to the edges of a trapezoidal plexiglass prism forming an angle of about 75° towards the prism base.

and gold were thermally evaporated on pre-cleaned glass substrates. For SPR measurements at a metal/air interface, two right-angle prisms were connected by index-matching gel to form a parallelepiped and the OLED and the metallic sensing layer were attached to opposite sides of the prism by index-matching gel, cf. Fig. 4.9(a). For SPR measurements in aqueous environment, the OLED was attached to the left edge of a custom-made trapezoidal plexiglass prism, and the metallic sensing layer was located at the base of the prism, as shown in Fig. 4.9(b). Inside the glass prism, the OLED irradiated the metallic sensing layer with polychromatic light under various angles of incidence. The reflected light left through the edge of the prism and passed a linear polarizing filter so that only the p-polarized fraction was detected. A collimating lens focused the light onto an optical fiber guiding it to a calibrated CCD spectrometer.

For the measurement of the plasmon dispersion relation, the prism was mounted on a motorized computer-controlled rotation stage in such a way that the illuminated metal film was located on the axis of rotation. A spectrum of the reflected light was recorded after each angle step. Additionally, the refraction of the light at the prism/air interface must be taken into account in order to determine the angle of incidence under which the light of the OLED impinges on the metal film. In order to obtain the p-polarized reflectivity, a reference measurement without metallic layer was performed for each experiment.

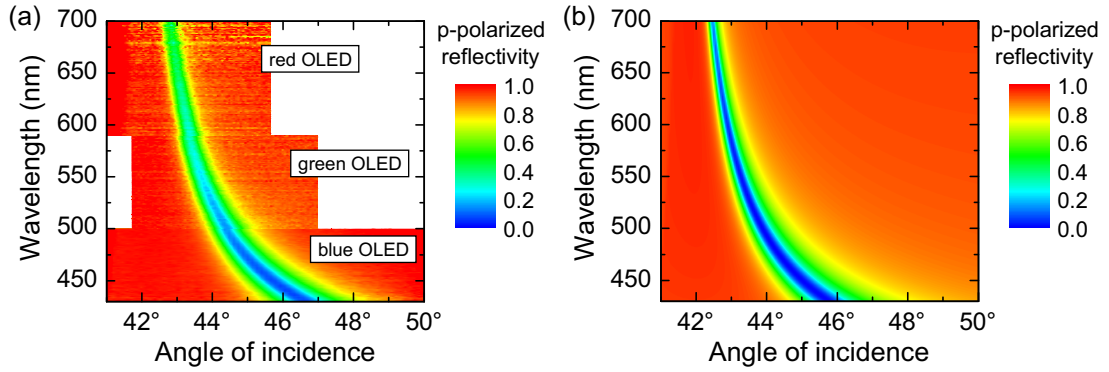


Figure 4.10: (a) Measurement and (b) simulation of the spectrally resolved angular dependent p-polarized reflectivity of a 49 nm thick silver film exposed to air. Light is incident through a BK7 glass prism. Regions of low reflectivity indicate resonant coupling to SPs. The simulation was carried out with the commercial software ETFOS (Fluxim AG, Switzerland) using optical constants from ellipsometric measurements, cf. appendix Sec. A.2.

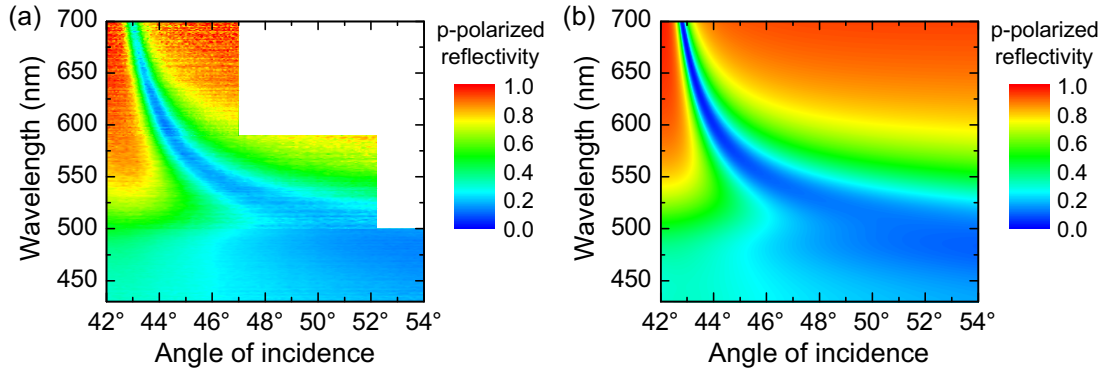


Figure 4.11: (a) Measurement and (b) simulation of the spectrally resolved angular dependent p-polarized reflectivity of a 49 nm thick gold film exposed to air.

Surface plasmon resonance at metal/air interfaces

Figure 4.10 displays the measured and simulated p-polarized reflectivity at the interface of a 49 nm thick silver film to air obtained over a spectral range from 430 nm to 700 nm using three different OLEDs (cf. Fig. 4.8). It should be noted that the measured SP dispersion is plotted in terms of wavelength versus angle of incidence whereas the dispersion relations in Figs. 4.2 and 4.4 were plotted as angular frequency versus in-plane wave vector.

At the chosen silver thickness it is expected that the resonance condition for the excitation of SPs is ideal and the reflectivity should drop to almost zero over a broad wavelength range as can be seen in the simulation. The observed angular dependence of the reflectivity minimum is in very good agreement with the simulated result.

The measurement at a gold/air interface in Fig. 4.11(a) illustrates the influence of the material that is used as sensing layer. The overall agreement between experiment

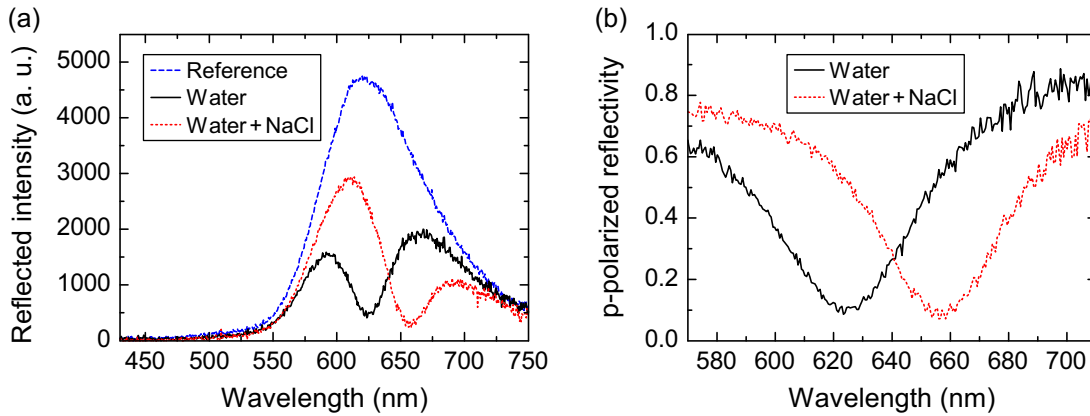


Figure 4.12: (a) Measured intensity of the p-polarized light of a red OLED reflected at a 48 nm gold film adjacent to a reservoir with either pure water or water with 10 wt% NaCl. The reference measurement was performed by replacing the gold film with a bare glass substrate. (b) Reflectivity obtained by dividing the measured spectra in (a) by the reference spectrum.

and simulation is again very good. The dispersion relation of the SPs has a smaller slope and is located at higher angles compared to silver. In addition, the SPR feature is much broader in the case of gold due to stronger internal damping. The SPR feature completely disappears for small wavelengths, and the reflectivity at the gold/air interface is low over the whole range of angles because the frequency of light approaches the plasma frequency of gold.

Real-time monitoring of the dissolving process of sodium chloride

SPR sensors are widely used to monitor biospecific interactions or to determine concentrations of biomolecules in a solvent. To illustrate the feasibility of the presented sensor to detect changes in concentration in real-time, this section demonstrates the dissolving process of NaCl in a water reservoir adjacent to the metallic sensing layer, cf. Fig. 4.9(b). For this purpose, 48 nm Au were evaporated on an approximately 1 nm thick Ti adhesion layer to increase the sticking of gold on the glass substrate in contact with the aqueous environment. Gold is frequently used for sensing in aqueous environment because it is chemically more stable than silver. A red OLED was used as light source in these experiments. Similar to the case of silver shown in Fig. 4.7(c), simulations predict that the SPR feature shifts to larger angles of about 70–80 degrees if the gold layer is in contact with water. Thus, a custom-made trapezoidal plexiglass prism was fabricated so that the light from the OLED was incident on the metal film under an angle in this range.

By increasing the NaCl concentration in water, the refractive index increases¹²⁴. Since the angle of incidence is kept constant in these measurements, the spectral position of the minimum is expected to shift to higher wavelengths depending on the concentration

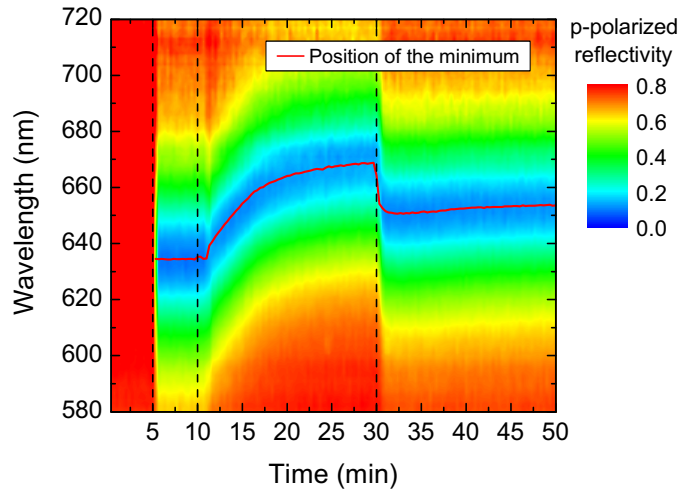


Figure 4.13: Wavelength and time dependent reflectivity of a gold/water interface at an incidence angle in the plexiglass prism of approximately 76° . The water reservoir was empty in the beginning. After five minutes, 4.5 ml water was filled into the reservoir adjacent to the gold film. Five minutes later, an amount of 0.5 g NaCl was added. The salt slowly dissolved, causing a shift of the spectral position of the minimum to higher wavelengths. After 30 minutes, the amount of water was increased by 5 ml which caused a dilution and the minimum shifted back to lower wavelengths.

of NaCl. Two exemplary measurements for pure water and water with a NaCl concentration of 10 wt% are displayed in Fig. 4.12(a). In addition, a reference measurement without metallic sensing layer is shown. It is obvious that coupling of incident light to SPs strongly reduces the reflected intensity. By dividing the measured spectra by the reference, the p-polarized reflectivity can be calculated, which yields a reflectivity of roughly 0.1 in the minimum as shown in Fig. 4.12(b). This verifies that the thickness of the gold film is close to the optimal value. It can be seen that the spectral position of the minimum significantly shifts by more than 30 nm due to the addition of 10 wt% NaCl to water.

In order to demonstrate the suitability of the presented SPR sensor for real-time monitoring, i.e. the detection of changes over time, Fig. 4.13 shows the reflectivity of a gold/water interface as a function of wavelength and time at a fixed angle of incidence. The water reservoir next to the gold film was empty for the first five minutes. Hence, the reflectivity is measured at an angle of incidence which is far away from the resonance position. Therefore, no minimum can be observed and the reflectivity of the gold film is very high over the whole wavelength range. After adding 4.5 ml of water, which was sufficient to cover the gold film completely with water, a pronounced minimum appears due to coupling of incident light to SPs. After ten minutes, an amount of 0.5 g NaCl was added, and after one more minute stirring of the water reservoir was started. The salt slowly dissolved and the minimum position shifts to higher wavelengths with increasing salt concentration. After 30 minutes, another 5 ml of pure water was added

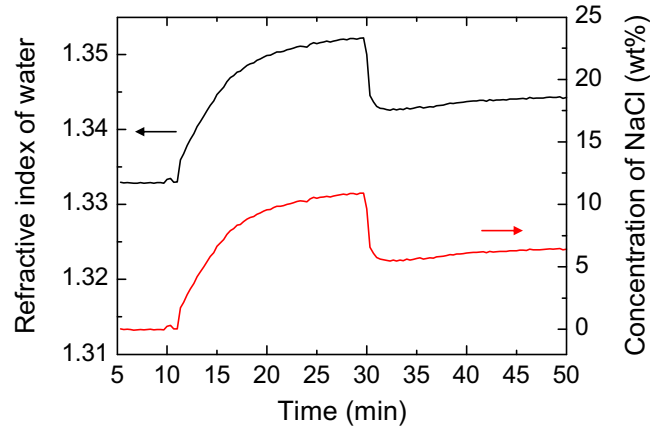


Figure 4.14: Refractive index of water and concentration of NaCl derived from the spectral position of the minimum in Fig. 4.13.

to the reservoir. This dilution instantaneously reduced the concentration of NaCl and the minimum position shifted back to lower wavelengths.

The concentration of NaCl can be computed from the refractive index of the solution, which in turn can be determined from the position of the minimum, as described in detail in Ref. [116]. The result is depicted in Fig. 4.14. The maximum measured NaCl concentration is 10.9 wt% and it drops to 5.5 wt% after dilution. The theoretical concentration that is derived from the amount of inserted water and salt should be 10 wt% before and 5 wt% after dilution, respectively. The difference between the measurement and the expected value possibly results from evaporation of water due to stirring.

This experiment demonstrates that the sensor is capable of monitoring the concentration of dissolved NaCl in water in real-time, thus the sensor also has the potential of measuring concentrations of other materials or biomolecules within a solvent. In addition, other parameters like changes of the temperature of a water reservoir can be detected because this directly influences the refractive index of water^{125,126}. Such a measurement and additional information about the presented SPR sensor like its sensitivity and detection limit as well as a discussion of the benefits of an OLED based sensor can be found in Refs. [116–118].

Monolithic integration of light source and sensing layer

Although the SPR sensor based on an integrated OLED light source is an important step for realizing a miniaturized sensing system, the large prism geometry still limits the size. Clearly, the next step in miniaturization is to monolithically integrate the OLED light source and the metallic sensing layer on one common substrate as depicted in Fig. 4.15(a). This approach demonstrates that the presented SPR sensor is particularly compatible with the planar glass light pipe platform¹²⁷.

The spectrally resolved angular dependent measurement of the reflected light using

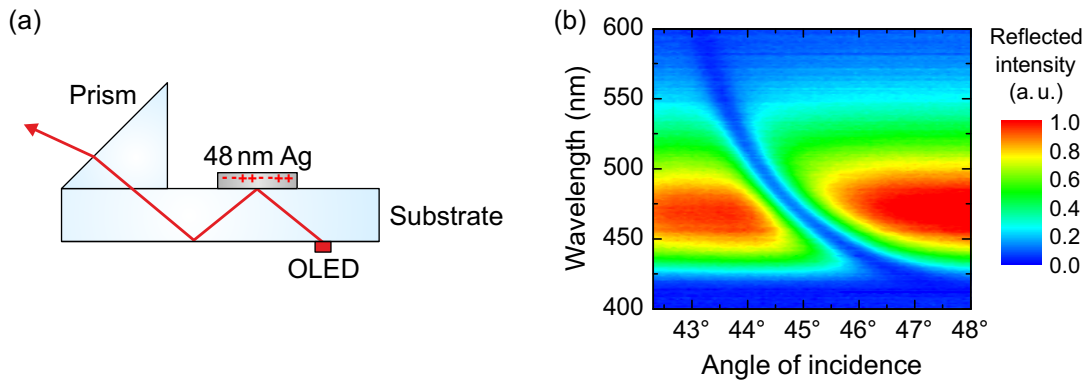


Figure 4.15: (a) Monolithic integration of OLED light source and metallic sensing film on one common substrate. A prism is used to extract the light which is waveguided along the substrate. (b) Measured angular and spectrally resolved intensity of p-polarized light extracted from the setup shown in (a).

this configuration is displayed in Fig. 4.15(b). It was not possible to determine a reference measurement in this case because the metallic layer was directly evaporated onto the substrate and could not be removed. Thus, the graph does not display the reflectivity but the intensity of the reflected light. Nevertheless, resonant coupling to SPs at the 48 nm thick silver film is clearly observable and the position of the minimum coincides excellently with the result shown in Fig. 4.10 which was measured with the larger prism setup using separated OLED and sensing layer.

Naturally, the application of a prism to extract light from the device shown in Fig. 4.15(a) as well as detection by an external spectrometer still significantly limit the size of the sensor. However, it should be stressed that the presented SPR sensor can easily be combined with an integrated detector, e.g. an organic photodiode. Hence, the sensor can be completely monolithically integrated on one substrate, which may even be a plastic foil. Thus, this sensor approach offers enormous potential for miniaturization and the possibility to fabricate low-cost disposable SPR sensors for a wide range of applications.

5. Optical simulations of OLEDs

This chapter discusses optical simulations based on the dipole model, in which an excited molecule is treated as a forced damped harmonic dipole oscillator. First, the basic physics behind this model will be explained with special emphasis on cavity effects, which influence the efficiency and the emission characteristics. Then, the simulations will be applied to an exemplary green Alq₃ OLED stack in order to obtain the total optical power dissipation spectrum. Subsequently, angular dependent emission spectra will be simulated and compared to measurements in order to provide evidence for the accuracy of the simulation tool. In addition, the integral coupling to different optical channels will be analyzed for this particular OLED. Finally, an optimization of the outcoupling efficiency in terms of a thickness variation will be performed and discussed.

5.1. Optical simulations based on the dipole model

The calculation of the reflectivities shown in the previous chapter is rather straightforward by using a transfer-matrix method as introduced in Sec. 3.4. In contrast, the optical model required to describe the behavior of an excited molecule in a multilayer OLED stack is far more complicated and must include optical near-field effects and the coupling to the photonic modes of the OLED cavity. Due to the multilayer structure of an OLED with different thin layers typically having thicknesses of less than a wavelength, it is necessary to take multiple reflections and interference effects into account⁵⁰.

Frequently, a dipole model is used that originally dates back to 1909 when Sommerfeld described the propagation of radio waves above the earth's conducting surface¹²⁸. According to this theory, an oscillating radio antenna can emit both propagating waves as well as bound surface waves. This model has been adapted for oscillating dipoles with frequencies in the visible spectral range, i.e. around nine orders of magnitude difference in frequency and wavelength^{17,18,25,28,129}. However, such a dipole similarly couples to freely propagating radiation, i.e. photons, as well as to bound surface waves, i.e. surface plasmons.

In this model, an excited molecule is treated as a forced damped harmonic oscillator inside the cavity environment of an OLED. The dipole is damped because the oscillator radiates power and it is forced in that the field reflected by interfaces provides a driving term, i.e. the cavity interacts with the dipole^{25,28}. This causes modifications in the decay

rate, the luminescence intensity and the radiation pattern of the molecular dipole. The equation of motion for the electronic dipole moment p is given by

$$\frac{d^2 p}{dt^2} + \omega_0^2 \cdot p = \frac{e^2}{m} \cdot E_r - \Gamma_0 \cdot \frac{dp}{dt}, \quad (5.1)$$

where ω_0 is the resonant angular frequency in the absence of all damping, m is the effective mass of the dipole, e is the electric charge, E_r is the reflected field at the dipole position, and Γ_0 is the decay rate in the absence of any interfaces. The decay rate is given by $\Gamma_0 = \Gamma_r + \Gamma_{nr}$ and it is also known as damping constant or inverse lifetime of the dipole oscillator and is composed of a radiative contribution Γ_r and a nonradiative contribution Γ_{nr} . These values are associated with the radiative quantum efficiency of the emitter as described in Sec. 2.4. It should be noted that coupling to waveguide modes and surface plasmons is also strongly influenced by the cavity and therefore attributed as a radiative decay channel even though each of these modes itself is normally trapped within the OLED and therefore non-emissive in a way that they cannot be easily extracted from the stack. Therefore, the truly nonradiative decay rate Γ_{nr} includes only intrinsic losses like thermal deactivation of the excited state. Hence, Γ_{nr} can be assumed to be constant, i.e. not influenced by the cavity environment⁵². In contrast, the radiative decay rate Γ_r can be enhanced or reduced by the cavity, resulting in a modified radiative decay rate $\Gamma_r^* = F \cdot \Gamma_r$, with F being the Purcell factor^{50,51}. This has an important effect on the radiative quantum efficiency q of an emitter and may lead to an increased effective radiative quantum efficiency q_{eff} as will be discussed in Sec. 5.4.

The derivation of the model is described in detail e.g. in Refs. [25,28,130]. Therefore, only a short summary about the main steps will be given in this section. The basic assumptions of the model are for instance layers which have a certain thickness in one dimension while extending infinitely in both other dimensions. All interfaces are assumed to be perfectly flat. In addition, the point dipole approximation is used, i.e. the size of the dipole is small compared to both the wavelength and the separation between dipole and interfaces.

As a first step, the Fresnel coefficients for s- and p-polarized radiation are calculated for the hemisphere above and below the emitting layer by means of a transfer-matrix method as introduced in Sec. 3.4, thus taking account of the thicknesses and complex permittivities of all layers as well as the emitter position which is assumed to be infinitely narrow. The dipole field is expanded as a sum of plane waves which are characterized by different in-plane wave vectors k_x , i.e. momenta in the plane of the surface. Then, the interaction of the dipole field with the cavity is considered by combining the reflected field with the source field to deduce the modified decay rate of the multilayer system.

Using the in-plane wave vector as a variable is advantageous, because this value is constant in each layer in contrast to the propagation angle. Furthermore, it allows the

incorporation of coupling to evanescent modes such as SPs, which have in-plane wave vectors larger than the radiation in the far-field.

The calculations are performed for a set of three orthogonal dipole orientations, two of them oriented in the plane of the interfaces whereas the third is perpendicular to the interfaces, as will be explained in detail in Chapter 11. Any particular dipole orientation can be represented as a weighted sum of these three cases. For small molecule based OLEDs, in many cases an isotropic dipole orientation is justified, i.e. each dipole orientation receives one third of the available power. However, some small molecular materials exhibit significant orientation effects as will be demonstrated in Chapter 11.

Since an excited dipole has a broad emission spectrum, the computation is performed for a wide range of wavelengths, each weighted according to the spectrum of the emitter, cf. Sec. 5.2. Finally, the extraction of radiation from the stack into air or into the substrate can be calculated by using the Fresnel transmission coefficients. For a comparison to experiments, it is also necessary to transform the in-plane wave vector into an emission angle as will be discussed in Sec. 5.3.

The simulation routine used for most optical simulations in the present work is implemented in a Maple program called Power Dissipation Calculator (PDCalc) which was for the most part developed by Nils Reinke¹³⁰ under collaboration with OSRAM Opto Semiconductors GmbH in Regensburg, Germany, within the project “OPAL 2008” funded by the German Federal ministry of Education and Research (BMBF). Afterwards, the program was checked intensively by Stefan Nowy in the course of his PhD thesis, and several additions like a batch mode for layer thickness variations have been included¹³¹.

During the work for this thesis, an additional program for the conversion of wave vector to angle was developed in order to compare the simulated results to measurements. Furthermore, the program was modified so that the results for each dipole orientation can be analyzed separately. The benefits of an anisotropic dipole orientation in OLEDs will be discussed in detail in Chapter 11.

An explanation of the input parameters and step sizes as well as some basic application guide lines for the simulation program will be given in the appendix, cf. Sec. A.3. Exemplary simulation results and a comparison to experiments will be demonstrated in the following sections.

5.2. Power dissipation spectra

The simulations are based on the exemplary green Alq₃ OLED, which was introduced in Sec. 2.7.3. The stack layout and the measured EL spectrum are once more shown in Figs. 5.1(a) and (b), respectively.

The basic result of the simulation is the optical power dissipation calculated for a given in-plane wave vector at a certain wavelength. By performing the simulation for a range of in-plane wave vectors and wavelengths, a power dissipation spectrum is

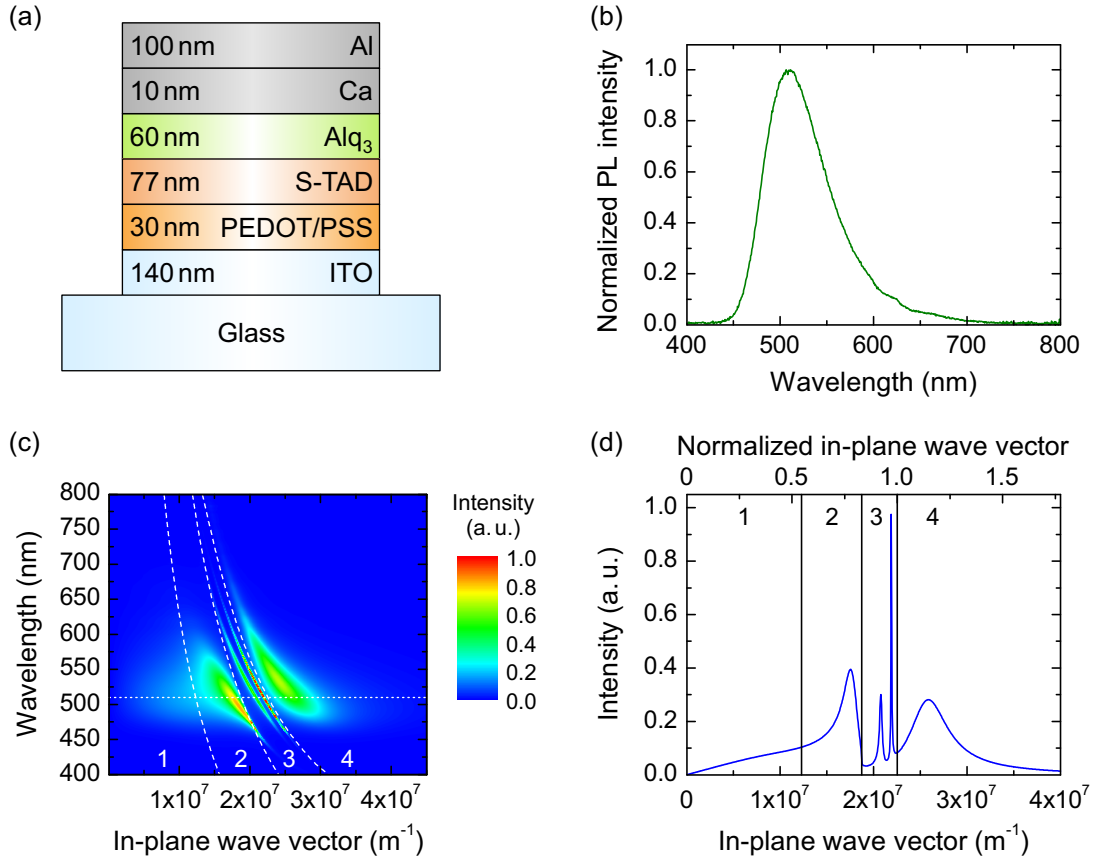


Figure 5.1: (a) Stack layout of the two-layer green OLED. (b) EL emission spectrum in bottom direction measured normal to the substrate. (c) Simulation of the total dissipated optical power of the OLED in part (a). The emitter position is assumed at the interface between Alq₃ and S-TAD. The result is shown for an isotropic dipole orientation. Red and yellow areas indicate a high amount of dissipated power. The dashed white lines divide the graph into four regions: (1) emission into air, (2) emission into substrate, (3) waveguide modes and (4) coupling to surface plasmons. (d) Cross section of (c) at a wavelength of 510 nm, i.e. at the emission maximum. The vertical lines divide the graph into four regions similar to (c). The upper axis shows the normalized in-plane wave vector u with respect to propagation in the organic layers and ITO at a wavelength of 510 nm.

obtained, as presented in Fig. 5.1(c). The graph shows the power radiated from an oscillating dipole within the OLED plotted in terms of wavelength (i.e. energy) versus in-plane wave vector k_x (i.e. momentum).

Depending on the k_x values, the power dissipation spectrum in Fig. 5.1(c) can be divided into four regions indicating coupling to different optical channels. The coupling to each channel can also be seen by the cross section at 510 nm displayed in Fig. 5.1(d).

Region (1) corresponds to light that can be emitted directly into air. The line dividing region (1) and (2) is equal to the air light line which indicates the maximum possible in-plane wave vector for light traveling in air under 90°. Hence, the in-plane wave vector of light in region (1) must satisfy the condition $0 \leq k_x \leq (n_{\text{air}} \cdot k_0)$ with $k_0 = 2\pi/\lambda$

being the vacuum wave vector at a certain wavelength λ .

The emission into the substrate is located in region (2) and it occurs for higher in-plane wave vectors $(n_{\text{air}} \cdot k_0) < k_x \leq (n_{\text{substrate}} \cdot k_0)$. Here, light is totally internally reflected at the substrate/air interface and thus trapped in the substrate unless it is extracted by means of an outcoupling structure like a prism or scattering foil.

Similarly, total internal reflection at the interface between ITO and the substrate leads to trapping of light in region (3). This corresponds to sharp waveguide modes which are bound to the organic layers and ITO. Generally, more waveguide modes are supported if the organic layers and ITO have a larger thickness or if layers with a higher refractive index are implemented. The condition for light in this region is given by $(n_{\text{substrate}} \cdot k_0) < k_x \leq (n_{\text{ITO+organic}} \cdot k_0)$. It is important to note that the maximum k_x for region (3) is usually not simply defined by the refractive index of the emitting layer. The reason for this is the small thickness of the layers, hence the near-field of the emitting dipole will sample the dielectric properties of several adjacent layers²⁵. Therefore, an “effective” refractive index $n_{\text{ITO+organic}}$ of the organic layers and ITO is determined similarly to calculating the capacitance of a plate capacitor with several dielectric media¹³¹.

Finally, region (4) corresponds to light fulfilling $k_x > (n_{\text{ITO+organic}} \cdot k_0)$. This condition implies coupling to evanescent modes, i.e. surface plasmons traveling at the Alq₃/cathode interface. It is obvious that a significant fraction of power is lost to this region as will be discussed in detail in Sec. 5.4. It should be noted that the surface plasmon dispersion depends on the optical constants of the adjacent organic layers and shifts to larger k_x values if layers with high refractive index are present.

The borders of each region can also be distinguished in terms of a normalized in-plane wave vector $u = k_x / (n_{\text{ITO+organic}} \cdot k_0)$. Then the condition for the occurrence of evanescent modes simplifies to $u > 1$. Since $n_{\text{ITO+organic}}$ and k_0 are wavelength dependent, the maximum u for e.g. direct emission changes with wavelength. The critical value of u above which radiation cannot propagate into air at e.g. 510 nm wavelength is $u = 1/n_{\text{ITO+organic}} \approx 0.546$ with $n_{\text{ITO+organic}} \approx 1.83$ (cf. Fig. 5.1(d)).

It is instructive to have a closer look at the waveguide modes in region (3). In the green and red spectral region two waveguide modes exist, in particular the TE₀ mode at higher k_x and the TM₀ mode at slightly lower k_x . In the wavelength region below about 460 nm, the TE₁ mode emerges as a third waveguide mode. For higher wavelengths, the in-plane wave vector of this mode is more and more reduced, hence the propagation angle decreases until it finally drops below the critical angle of total internal reflection between ITO and the glass substrate. Since the reflectance below the critical angle gradually decreases from 1 to lower values, the waveguide mode smoothly transforms into a leaky mode and thus partially propagates into the substrate as explained in Sec. 3.5. It can be seen that the mode gets broader and less confined with higher wavelengths, i.e. decreasing reflectance²⁵. In general, the occurrence of p-polarized substrate modes is

less probable because the reflectance below the critical angle drops much more rapidly and approaches zero at Brewster's angle.

In order to determine the influence of the OLED cavity, the power dissipation spectrum can be used to calculate the total relative decay rate P_{tot} by integrating over all in-plane wave vectors and wavelengths²⁸:

$$P_{\text{tot}} = \frac{\Gamma}{\Gamma_0} = (1 - q) + q \cdot \int_{\lambda_1}^{\lambda_2} S(\lambda) \int_0^\infty P(k_x, \lambda, z) dk_x d\lambda \equiv (1 - q) + q \cdot F. \quad (5.2)$$

In this equation, $\Gamma_0 = \Gamma_r + \Gamma_{\text{nr}}$ describes the total decay rate in free-space, while $\Gamma = \Gamma_r^* + \Gamma_{\text{nr}}$ represents the modified total decay rate inside the OLED cavity, which takes into account that the radiative decay rate is changed by the Purcell factor F according to $\Gamma_r^* = F \cdot \Gamma_r$. Thus, the integral of the spectrally weighted power dissipation directly yields the Purcell factor F . The borders for the integration over wavelengths are denoted by λ_1 and λ_2 . Typically, the integration is performed from $\lambda_1 = 400$ nm to $\lambda_2 = 800$ nm. $S(\lambda)$ describes the spectrum used for weighting the power dissipation. Usually, the photoluminescence spectrum of the emitter is used for $S(\lambda)$. For the simulations in Fig. 5.1, the power emitted at each wavelength is weighted with a specific spectrum in a way that the simulated unpolarized emission in normal direction resembles the measured spectrum of the OLED. However, this particular spectrum used for the simulations agrees very well with the photoluminescence spectrum of the emitter. Finally, $P(k_x, \lambda, z)$ is the layer specific power dissipation function depending on the in-plane wave vector k_x , the wavelength λ and the emitter position in the OLED stack which is denoted by z . In practice, the integral over k_x is only carried out up to a finite cut-off value where the contribution of surface plasmons has decayed to sufficiently small values (typically $4 \times 10^7 \text{ m}^{-1}$ or $4.5 \times 10^7 \text{ m}^{-1}$).

By using Eq. (5.2) as well as the definitions of the radiative quantum efficiency q and the effective radiative quantum efficiency q_{eff} in Eqs. (2.2) and (2.3), respectively, it is possible to calculate the effective radiative quantum efficiency q_{eff} of the emitter in the OLED cavity:

$$q_{\text{eff}} = \frac{F \cdot \Gamma_r}{F \cdot \Gamma_r + \Gamma_{\text{nr}}} = \frac{q \cdot F \cdot \Gamma_0}{\Gamma} = \frac{q \cdot F}{P_{\text{tot}}} = \frac{q \cdot F}{(1 - q) + q \cdot F}. \quad (5.3)$$

For $F > 1$, the cavity has a positive effect on the radiative decay rate. This corresponds to $P_{\text{tot}} > 1$ and $q_{\text{eff}} > q$ (or $q_{\text{eff}} = q$ for $q = 100\%$). Thus, the radiative decay rate of the emitter in the cavity is larger in comparison to the decay rate in free-space. On the contrary, for $F < 1$ (i.e. $P_{\text{tot}} < 1$ and $q_{\text{eff}} < q$), the cavity has a negative effect on the radiative decay.

It is noteworthy that Fig. 5.1(c) displays the power which the emitting dipole couples to different optical channels within the OLED stack. However, not all of the light emitted in region (1) or (2) can ultimately escape from the OLED due to absorption in

the organic layers as well as due to reflection losses at the interfaces (reflection losses at the glass/air interface are not taken into account). Therefore, the emitted power that actually leaves the device in either top or bottom direction is calculated by using the Fresnel reflection and transmission coefficients. This step is necessary for the comparison of the angular dependent emission pattern with experimental results, as will be shown in the next section.

5.3. Angular dependent emission spectra

In the context of an application in displays and general lighting, the angular dependent emission of an OLED plays an important role. In many cases, an approximately Lambertian emission pattern with a maximum emission in normal direction is desired. This section shows both the simulated and measured angular emission of the exemplary fluorescent Alq₃ OLED, cf. Fig. 5.1(a). First, the direct emission will be presented. Afterwards, the effect of an attached outcoupling prism in order to access the substrate modes will be discussed.

In order to compare the simulation results to angular dependent measurements of the emission pattern of an OLED, it is necessary to account for the transmission of light from the organic layers into the substrate and to transform the in-plane wave vector k_x to an emission angle θ in either air or glass. The relation between θ and k_x is given by

$$\theta = \arcsin\left(\frac{k_x}{n \cdot k_0}\right) = \arcsin\left(\frac{k_x \cdot \lambda}{2\pi \cdot n}\right), \quad (5.4)$$

where $n = n(\lambda)$ denotes the refractive index of the medium in which the light is extracted, e.g. air or glass depending on whether the emission with applied macro extractor or not is investigated. Details concerning the conversion from in-plane wave vector to angles can be found in the appendix, cf. Sec. A.3.

The simulated angular dependent emission characteristics without applied outcoupling structure for s- and p-polarized light are displayed in Figs. 5.2(a) and (b), respectively. The corresponding measurements are displayed in parts (c) and (d) of the figure. It can be seen that the simulated spectra agree excellently with the measurements.

For both polarizations, the emission has a maximum in normal direction, i.e. at an angle of 0° to the substrate normal. The angular dependent emission intensity decreases with increasing angle. The reduction corresponds very well to a Lambertian emission. The spectral shape is almost constant at each angular step, hence the color of the OLED is virtually independent of the viewing angle.

A rather simple but nevertheless extremely efficient method to increase the amount of extracted radiation is the application of an outcoupling structure like a prism or a scattering foil, thus eliminating the total internal reflection at the air/glass interface. Consequently, the substrate emission can be extracted and the light emission of the

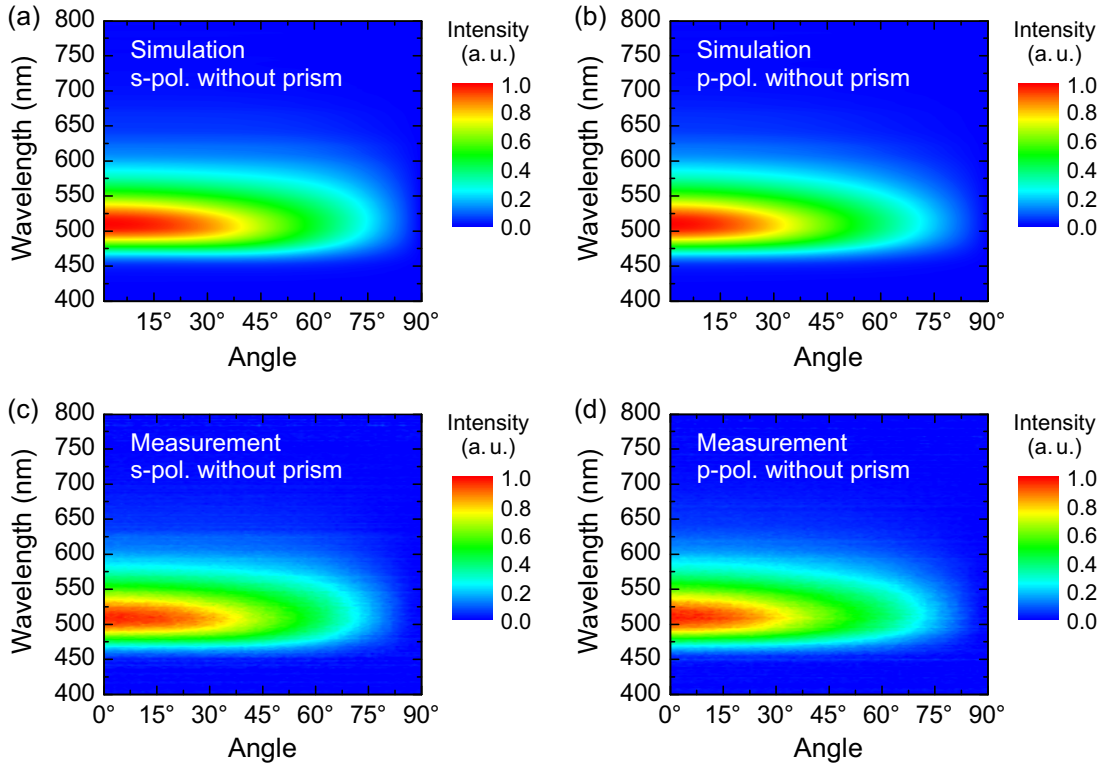


Figure 5.2: Simulation and measurement of the spectrally resolved angular dependent emission of the Alq₃ OLED. The graphs show the directly emitted light with no outcoupling structure attached to the OLED. (a) and (b) show the s- and p-polarized simulations, while (c) and (d) present the s- and p-polarized measurements, respectively. For the measurement, the OLED was mounted on a computer-controlled motorized rotation stage. The emitted light passed through a linear polarizing filter before it was focused by a collimating lens onto an optical fiber guiding it to a spectrometer. A spectrum was recorded from 0° to 90° with a step size of 1°. The edges of the substrate and encapsulation glass were blackened in order to prevent emission of guided modes through the edges. The OLED was driven at a constant current of 0.5 mA and the required voltage was controlled during the measurement to rule out degradation effects. At normal emission, the s- and p-polarized emission intensities are, by definition, equal. Therefore, the measured graphs are normalized to the same value at 0°. The simulation does not include emission for zero in-plane wave vector, i.e. at an emission angle of 0°. Hence, both simulated graphs are normalized to the same value at 1°, i.e. almost normal direction. The difference between emission at 0° and 1° is usually very small, e.g. below 0.02% in the case of Lambertian emission.

OLED is roughly doubled. Additional details about this technique will be discussed in Chapter 6.

Figure 5.3 shows the simulated and measured emission for both s- and p-polarization with a fused silica half cylinder prism attached to the OLED substrate by index-matching gel. Again, the agreement between simulation and measurement is excellent. While the p-polarized emission basically looks rather similar to the direct emission in Fig. 5.2, the s-polarized emission shows a significant contribution of an s-polarized substrate mode with a peak intensity around 70°. At this angle, the substrate emission

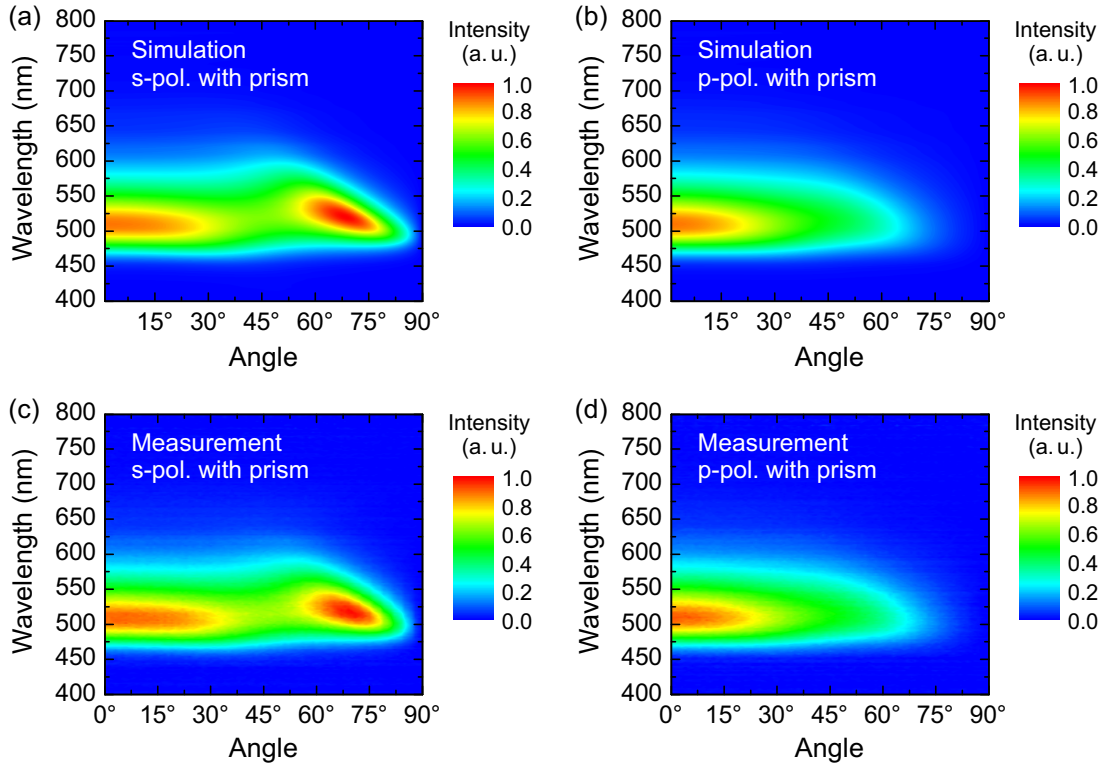


Figure 5.3: Simulation and measurement of the spectrally resolved angular dependent emission of the Alq_3 OLED with an attached index-matched fused silica half cylinder prism. (a) and (b) show the s- and p-polarized simulations, while (c) and (d) present the s- and p-polarized measurements, respectively. The measured graphs are normalized to the same value at 0° , where s- and p-polarized emissions are equal. The simulated graphs are normalized to the same value at 1° , because the emission at 0° is not calculated.

even has a higher intensity than the direct emission at 0° . As explained above, this substrate mode results from the TE_1 mode which propagates below the critical angle and leaks into the substrate.

Although fused silica has a slightly lower refractive index than the BK7 glass substrate and thus is not perfectly matched, the basic principle of substrate mode outcoupling is clearly observable. However, an even larger fraction of the substrate emission could be extracted by choosing a prism made of the same material as the substrate.

It should be kept in mind that the angle measured in an experiment with an applied outcoupling prism is equal to the angle inside the glass substrate because substrate and prism are index-matched and no refraction takes place at the prism/air interface since the light always hits the interface at a right incidence angle. In other words, the angular range from 0° to 90° without attached prism (Fig. 5.2) corresponds to a maximum of only $\arcsin(1/n_{\text{fused silica}}) \approx 43^\circ$ with attached prism (Fig. 5.3) using $n_{\text{fused silica}} \approx 1.46$. Therefore, also the p-polarized emission is larger if an outcoupling structure is applied, even though the increase is considerably lower compared to the s-polarized emission.

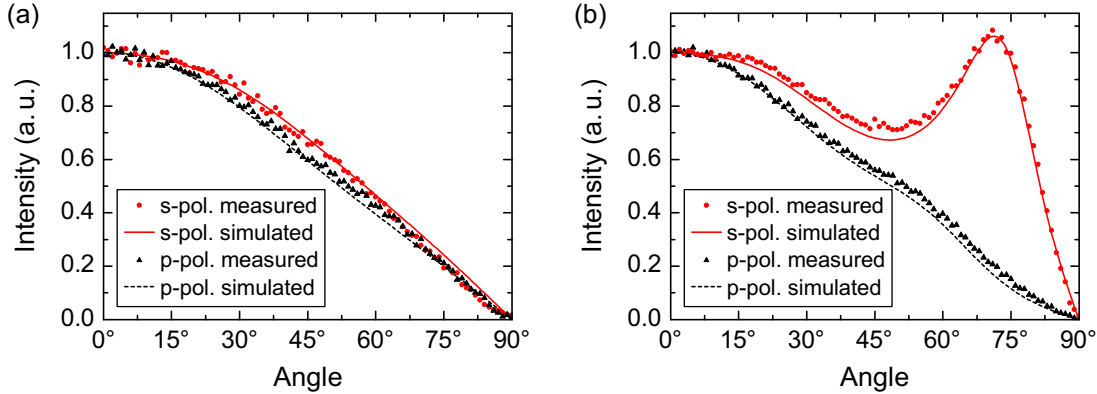


Figure 5.4: Cross section at a wavelength of 510 nm of the s- and p-polarized angular dependent measurement and simulation of Figs. 5.2 and 5.3. (a) Direct emission into air. (b) Emission with attached fused silica half cylinder prism.

By applying an outcoupling structure, the emission becomes clearly non-Lambertian. In addition, it is unfeasible to use large prism extractors for commercial products. Although the utilization of rather flat large-area scattering foils with microlenses would solve this problem, the scattering foil prohibits a mirror-like off-state appearance of the OLED device which is desired for certain applications. Nevertheless, the outcoupling of substrate emission can be realized rather straightforward, thereby leading to a significant improvement of efficiency.

For a detailed comparison of experiment and simulation, Fig. 5.4 shows a cross section at the peak emission wavelength of 510 nm. The agreement in all cases is excellent, i.e. the measured angular dependent characteristics can be well reproduced by optical simulations based on the dipole model.

As mentioned previously, the thickness of the Alq₃ and S-TAD layers were determined by comparison to simulations. For this purpose, both layer thicknesses were varied until the simulated result compared well with the s-polarized measurement with attached prism because this represents the most characteristic curve. Therefore, it is not surprising that the s-polarized measurement and simulation with attached prism agree well for the optimal case of 60 nm Alq₃ and 77 nm S-TAD. However, by choosing these values, excellent agreement is found also for all other combinations of measured and simulated spectra, i.e. for both polarizations as well as for direct emission or emission with outcoupling structure.

In order to demonstrate that the thicknesses of the organic layers have a significant influence on the emission characteristics and that they can be determined precisely by comparison between simulation and measurement, the s-polarized measurement with attached prism as well as simulations with varying Alq₃ and S-TAD thicknesses are shown in Fig. 5.5. In both cases, an increase of the thickness shifts the peak of the substrate emission to larger angles. This can be explained by the fact that a waveguide mode shifts to a higher k_x value, i.e. propagation angle, with increasing thickness of the

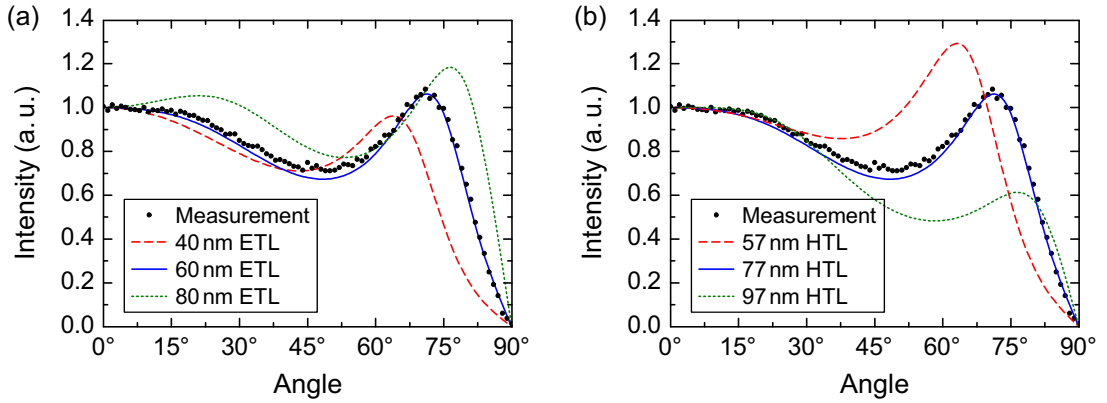


Figure 5.5: (a) Cross section of the s-polarized measurement with attached prism at a wavelength of 510 nm in comparison to simulations with varying electron transport layer (Alq_3) thickness. The hole transport layer has a constant thickness of 77 nm. (b) Similar to (a) except for a variation of the hole transport layer (S-TAD) thickness. Here, the electron transport layer has a fixed thickness of 60 nm.

waveguide structure. Consequently, also the leaky substrate mode is shifted to higher angles if either the thickness of Alq_3 or S-TAD is increased. Considering the magnitude of the peak at higher angles, a larger Alq_3 thickness causes an enhancement whereas increasing the S-TAD thickness results in a reduction of the peak value. Therefore, only the combination of 60 nm Alq_3 and 77 nm S-TAD can satisfactorily reproduce the measurement.

The strong influence of a nearby interface, especially of a metallic mirror, can also be understood in the simple picture that radiation into a particular direction may now occur via two different paths, i.e. either direct or by reflection from the interface. The radiation pattern in the far-field is given by the superposition of the fields from both paths, thereby accounting for their relative phase and amplitude. Thus, this is a classical interference situation, and the two paths may interfere constructively or destructively depending on the distance to the mirror^{25,26}. This effect on the emission characteristics is also important in terms of applications. Sometimes a rather Lambertian emission might be favorable, whereas a strongly dispersive emission into a certain angular range could be interesting for other purposes.

Besides changes of the angular dependent emission, also the spectral emission maximum can shift by several tens of nanometers due to interference arising from cavity effects, which are different for each wavelength²⁶. As an additional verification that the simulation tool works correctly, the spectrum used in the simulation in order to reproduce the measured zero degree spectrum was compared to an independently measured spectrum using a 50 nm thick Alq_3 film on glass. The agreement between both spectra is very good, i.e. they differ by a few nanometers at the most. This also implies that the measured values of the optical constants are reliable, which is an important requirement because they have a similar impact on the simulation as the layer thicknesses.

Further comparisons between other measurements and simulations as well as to data from literature^{16, 18, 53, 132} have also validated the accuracy of the program, cf. Refs. [13, 130, 131]. Consequently, it is reasonable to use the simulation program in order to compute the outcoupling efficiency by integrating the power dissipation spectrum as well as to optimize the device structure, as will be demonstrated in the following sections.

5.4. Integral power dissipation

For the purpose of optimizing OLEDs by optical simulations it is frequently necessary to calculate the integral amount of power which is emitted into air or the substrate or which is coupled to waveguide modes or SPs. This can be achieved by calculating the fraction of power that is dissipated into different optical modes, as discussed in Sec. 5.2:

$$P_{\text{mode}} = q \cdot \int_{\lambda_1}^{\lambda_2} S(\lambda) \int_{k_1}^{k_2} P(k_x, \lambda, z) dk_x d\lambda. \quad (5.5)$$

Here, k_1 and k_2 describe the limits for the integration over the in-plane wave vector. For instance, in the case of direct emission into air (P_{air}) the limits are set to $k_1 = 0$ (or equal to the lowest k_x value since $k_x = 0$ is not taken into account in the simulations) and $k_2 = n_{\text{air}} \cdot k_0$, with $n_{\text{air}} = 1$ being the refractive index of air and k_0 describing the vacuum wave vector at a given wavelength. It should be noted that k_1 and k_2 have to be individually determined for each wavelength. In addition, the transmission through the OLED stack has to be taken into account by using the Fresnel coefficients for the hemisphere above and below the emitting layer.

By comparing Eq. (5.5) with Eq. (5.2), it is found that the ratio of P_{air} to P_{tot} represents the combination of the effective radiative quantum efficiency q_{eff} and the outcoupling factor η_{out} , i.e.

$$\frac{P_{\text{air}}}{P_{\text{tot}}} = q_{\text{eff}} \cdot \eta_{\text{out}}. \quad (5.6)$$

Neglecting the influence of the cavity on the radiative quantum efficiency of the emitter by setting $q = q_{\text{eff}} = 100\%$, the outcoupling factor for direct emission into air can be calculated by

$$\eta_{\text{out}} = \frac{P_{\text{air}}}{P_{\text{tot}}}. \quad (5.7)$$

The fraction of power coupled to other optical modes can be calculated in a similar manner by choosing integration limits in Eq. (5.5) that correspond to a certain mode.

Figure 5.6 shows the simulated result for the green Alq₃ OLED obtained by integrating over all wavelengths and in-plane wave vectors in each of the regions in Fig. 5.1(c). Additionally, the losses during the transition from the organic layers into the glass substrate and into air are determined and denoted as absorption losses.

The direct emission amounts to 15.3% of the internally emitted power and thus agrees with the rough estimation of η_{out} presented in Sec. 2.5. The other optical modes

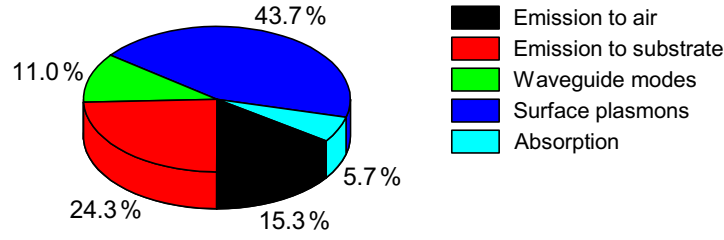


Figure 5.6: Fraction of power coupled to different optical channels obtained by integrating each region in the power dissipation spectrum in Fig. 5.1(c). In this diagram, a radiative quantum efficiency of $q = 100\%$ is assumed. The influence of values of q below unity are discussed in the text.

amount to 24.3% for the substrate emission, 11.0% for the waveguide modes and 43.7% of the power is coupled to SPs. The remaining 5.7% are lost due to absorption. It is noteworthy that the dipole couples significantly more power into the substrate compared to direct emission for this particular OLED stack. However, since a large fraction of the substrate emission occurs close to the glass light line, cf. Figs. 5.1(c) and (d), it is unlikely that all of this power can be extracted even by applying outcoupling structures. Hence, the detailed distribution of power within each of the regions is also important. This should be kept in mind if an optimization of OLEDs by means of optical simulations is desired.

As mentioned above, the cavity also alters the radiative decay rate. Therefore, the radiative quantum efficiency changes from its intrinsic value q to an effective radiative quantum efficiency q_{eff} , cf. Eq. (2.3). In reality, Alq_3 has a radiative quantum efficiency of around $q = 20\%$ ^{64,66}. Assuming this value in the simulation yields a result of $q_{\text{eff}} = 28.8\%$, hence an increase by a factor of 1.44 in comparison to the intrinsic radiative quantum efficiency. Apparently, the radiative rate is significantly enhanced by the cavity. In other words, the nonradiative losses are reduced from 80% without cavity effects to only 71.1% in this OLED stack. It is noteworthy that the increase of quantum efficiency is more rigorous for low values of the radiative quantum efficiency. If q was close to one anyway, i.e. the nonradiative decay rate was inherently very small, then the cavity environment could not strongly alter the ratio between radiative and nonradiative decay, hence the increase in efficiency would be marginal²⁶.

The influence of the cavity on the radiative quantum efficiency is often neglected in literature, which might lead to wrong conclusions, e.g. in the determination of the singlet fraction by the analysis of EQE measurements. However, in order to investigate fundamental changes of the outcoupling efficiency resulting from modifications in the stack layout, it is reasonable to set $q = 100\%$ for reasons of clarity. Nevertheless, if a comparison to measurements of a particular emitter system with known $q < 100\%$ is intended, the actual value of q can be included in the simulation to consider changes of the radiative quantum efficiency due to specific cavity effects in this system.

Taking into account a radiative quantum efficiency of $q = 20\%$ for Alq_3 yields a

value of $q_{\text{eff}} \cdot \eta_{\text{out}} \approx 4.4\%$ for directly emitted light. Assuming perfect charge carrier balance and remembering that Alq_3 is a fluorescent emitter, i.e. $\eta_{\text{ST}} = 25\%$, a total external quantum efficiency of around $\eta_{\text{EQE}} \approx 1.1\%$ is obtained, which is in agreement with typical values from literature^{2,133}. Clearly, the efficiency could be substantially increased if losses to waveguide modes and especially SPs could be reduced or if some of the lost power could be recovered. This will be the major topic of this work and different strategies as well as the fundamental physics behind each approach will be investigated in detail.

Because the impact of the cavity environment is particularly influenced by the distance to the metallic cathode, it should be noted that the emitter position has a dramatic effect on the efficiency and emission characteristics. This will be demonstrated by a variation of the distance to the electrodes in the next section. In the case of the exemplary OLED studied in this chapter, the emitter position was assumed to be at the interface between Alq_3 and S-TAD because Alq_3 is a good electron conductor whereas S-TAD transports holes very well. Therefore, it is expected that electrons and holes recombine close to the interface between both materials. Since the exciton diffusion length is rather small in most amorphous small molecular organic materials, the emitter position will be located close to the interface as well. Certainly, the real emission zone will not be infinitely small as assumed for the simulation. However, this assumption reproduces the angular dependent emission patterns very well, as was demonstrated in the previous section.

5.5. Optimization of OLEDs by thickness variations

The real benefit of an optical simulation tool is to study and optimize OLED stacks without the need for elaborate and time-consuming experiments. In this section, the exemplary OLED introduced in Sec. 2.7.3 will be investigated in terms of a simultaneous thickness variation of the electron transport layer (ETL) and hole transport layer (HTL). This basically corresponds to a variation of the distance between the emitter position and the interfaces to the metallic mirror and the glass substrate. Thus, the cavity will be strongly modified, which results in changes of the outcoupling efficiency into air and into the substrate.

The result in view of the direct emission into air is displayed in Fig. 5.7, which was simulated monochromatically at a wavelength of 510 nm. It is apparent that the variation of both the ETL and HTL thicknesses causes an oscillation of the outcoupling efficiency into air. The explanation for this behavior is similar to the discussion of the lifetime of an oscillating dipole in dependence of the distance to a mirror^{16,18,25,26,134}, i.e. there are certain combinations that cause constructive or destructive interference, respectively. Hence, the distance between adjacent maxima and minima is around 70 nm, i.e. one quarter of $(510 \text{ nm}/n)$ with $n \approx 1.8$. It is important to point out

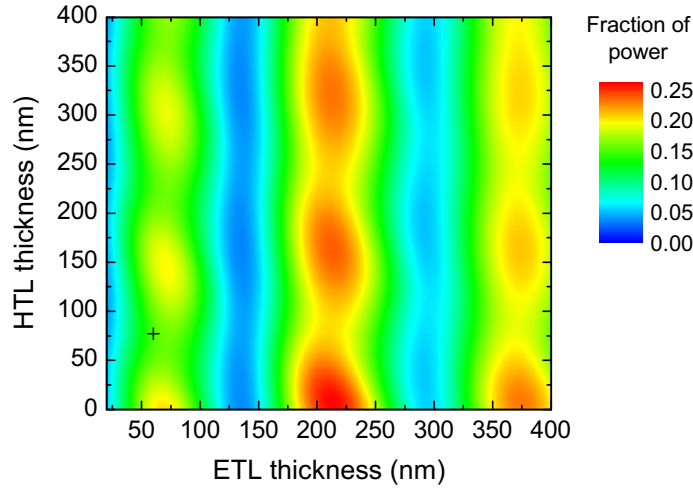


Figure 5.7: Fraction of optical power coupled into air in dependence of the electron and hole transport layer thicknesses. The stack consists of a glass substrate, 140 nm ITO, 30 nm PEDOT/PSS, varying thicknesses of S-TAD (HTL) and Alq₃ (ETL), 10 nm Ca and 100 nm Al. The position of the exemplary OLED stack used in this work (cf. Fig. 5.1(a)) is marked by a cross in the diagram. The plotted fraction of power is directly related to the outcoupling efficiency for direct emission into air. The simulations are performed at a single wavelength of 510 nm, i.e. close to the emission maximum of Alq₃. The ETL and HTL thicknesses are varied in steps of 5 nm and 10 nm, respectively. A radiative quantum efficiency of $q = 100\%$ is assumed.

that the location of the emitter position within the ETL also influences the distance to the metal and hence has a similar effect on the outcoupling efficiency^{8,37,60,74,135}. Therefore, a shift of the emission zone, resulting for instance from a different charge balance depending on the applied voltage, may cause changes in efficiency and emission characteristics due to the modified cavity environment¹³⁶.

Obviously, the distance to the metallic cathode causes a stronger oscillation in comparison to the distance to the glass substrate. This is a consequence of the fact that the metal causes a reflection of all incident light, whereas the interface to glass mainly reflects the fraction of radiation which propagates at an angle above the critical angle of total internal reflection and thus has a smaller influence on the directly emitted light.

The power emitted into both air and substrate is plotted in Fig. 5.8. Here, the oscillations are less pronounced and highest coupling occurs for smaller ETL thicknesses. The reason for this is that the number of waveguide modes increases with higher thickness of the organic layers. This optical loss channel competes with substrate emission and therefore reduces the total emission for larger ETL and HTL thicknesses.

It should be stressed that the simulations in Figs. 5.7 and 5.8 were performed for only one wavelength. Remembering that OLEDs have a broad emission spectrum, the maximum values in these graphs will definitely be reduced because they correspond to the optimal cavity for 510 nm, whereas other wavelengths do not receive best interference conditions. For instance, considering an optimization of the OLED in terms of out-

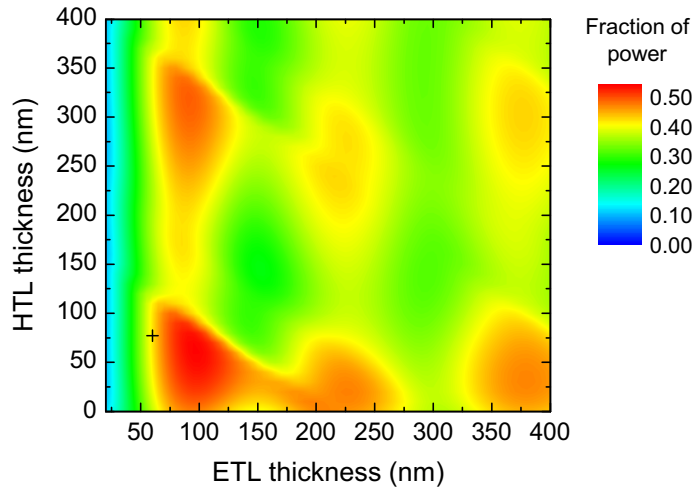


Figure 5.8: Fraction of optical power coupled into air and substrate in dependence of the electron and hole transport layer thicknesses simulated monochromatically at a wavelength of 510 nm for the same stack as in Fig. 5.7. The intensity is related to the outcoupling efficiency for total emission into air and substrate, provided that the power in the substrate can be completely extracted. The marker indicates the position of the exemplary OLED stack. In this diagram, again a radiative quantum efficiency of $q = 100\%$ is used.

coupling efficiency, a maximum direct emission of 26.3% is obtained at ETL and HTL thicknesses of 210 nm and 10 nm, respectively, if the simulation is performed monochromatically. However, if the broad Alq₃ emission spectrum is taken into account, this value is reduced to around 22.4%. Considering the total emission, it is additionally not possible to extract the substrate emission completely. Hence, the highest value of 53.5% in Fig. 5.8 at ETL and HTL thicknesses of 95 nm and 60 nm, respectively, cannot be reached in a real device.

Certainly, the simultaneous ETL and HTL thickness variation clearly demonstrates that the exemplary OLED stack could be further optimized, e.g. by increasing the ETL thickness so that the emitter is positioned precisely in the first or even second cavity maximum with respect to the distance to the metallic mirror^{74,132}. Although the simulation was performed for a particular stack layout, roughly the same behavior for direct and total emission was shown by Mladenovski *et al.* for a different OLED system⁷³.

In addition, an enhancement of η_{out} could be obtained by varying for instance the thickness of ITO or by choosing different materials, though this is beyond the scope of this work. Anyway, it should be kept in mind that changes in the layer thickness also modify the transport characteristics, and that a balancing of optical and electrical optimization is required. Moreover, it is unfavorable to use thick layers of materials having a rather low mobility (for instance Alq₃), because this would result in a higher required voltage and, thus, a lower luminous efficacy.

Aside from the examination of the outcoupling efficiency into air or substrate, it is

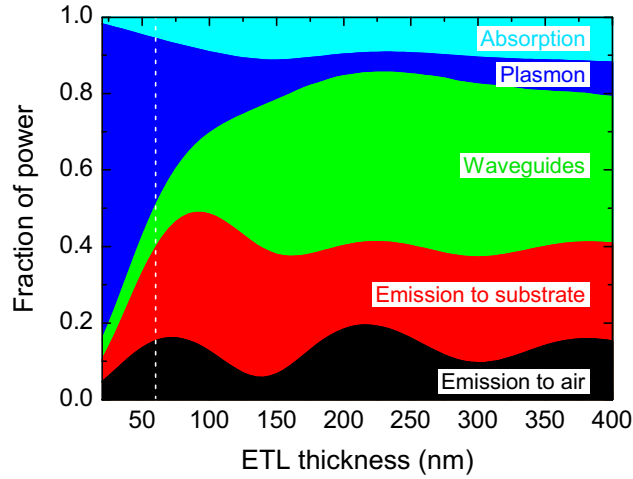


Figure 5.9: Fraction of power coupled to different optical channels for an OLED as depicted in Fig. 5.1(a) as a function of the electron transport layer (Alq_3) thickness assuming a radiative quantum efficiency of $q = 100\%$. The dashed white line indicates an ETL thickness of 60 nm which corresponds to the exemplary OLED, hence the intensity values are similar to Fig. 5.6. The simulation is performed polychromatically according to the emission spectrum of Alq_3 .

also instructive to study the coupling to other optical decay channels like waveguide modes and surface plasmons as this is important for the discussion of light extraction techniques. Therefore, Fig. 5.9 shows a polychromatic simulation of the fraction of power coupled to different optical channels for varying ETL thickness at a fixed HTL thickness of 77 nm.

The trend for directly emitted light and substrate emission is similar to Figs. 5.7 and 5.8. The thickness of 60 nm in the exemplary Alq_3 OLED is close to the first cavity maximum for direct emission. The oscillations in dependence of the ETL thickness are clearly observable^{74,132}. As the distance increases, the strength of the oscillations decreases because the intensity of the dipole radiation field weakens with increasing distance from the dipole, thus the strength of the reflected field will also be decreased²⁵.

In contrast, power dissipation to waveguide modes and surface plasmons shows a completely different progression. Coupling to waveguides is very low for small ETL thicknesses but it is strongly enhanced with increasing thickness. This can be explained by the increasing number of modes that are supported for larger thicknesses. On the contrary, coupling to SPs is strongest for a small ETL thickness, i.e. if the emitter is positioned close to the metallic cathode. This is obvious because SPs are evanescent waves. Therefore, coupling of the near-field of a dipole to SPs is reduced with increasing distance of the dipole to the metal. It should be noted that the simulation does not differentiate between coupling to surface plasmons and nonradiative energy transfer to lossy surface waves, i.e. luminescence quenching at the metal, which especially dominates for small distances below about 20 nm and significantly reduces the

efficiency^{25,26,109}.

In conclusion, modifying the cavity environment of the emitting molecules allows for optimizing the optical properties of an OLED and thus maximizing the outcoupling efficiency. Nevertheless, coupling to both surface plasmons and waveguide modes causes combined losses of about 50% of the total available power. Therefore, it is inevitable to either reduce coupling to these unfavorable loss channels or at least to partially recover some of the dissipated energy in order to develop highly efficient OLEDs. For this reason, the next chapter will introduce several promising approaches. Subsequently, some of these established methods as well as newly developed techniques will be investigated in detail in the following chapters.

6. Light extraction techniques in OLEDs

The strong influence of the cavity environment on the outcoupling efficiency was demonstrated in the previous chapter. In fact, the rule of thumb for the outcoupling efficiency into air of $\eta_{\text{out}} = 0.5 \cdot n^{-2}$, cf. Eq. (2.9), can be approximated as $\eta_{\text{out}} = 0.75 \cdot n^{-2}$ in case of an optimized cavity¹³⁷. This yields a value of $\eta_{\text{out}} \approx 23\%$ assuming a refractive index $n = 1.8$ for the organic, and thus agrees well with the simulations shown in Fig. 5.7.

Nevertheless, around 75% of the available power are still lost in a typical OLED device. Certainly, it is desirable to find ways to further increase the efficiency of OLEDs in order to facilitate a widespread and energy efficient application. Therefore, this chapter briefly reviews various reported techniques for enhanced light extraction from OLEDs in order to provide a background for the following chapters. First, rather established methods for extracting substrate and waveguide modes as well as for reducing surface plasmon losses will be presented. Afterwards, microcavity stacks, top-emitting devices and transparent OLEDs will be introduced as special stack designs which influence light extraction. Finally, the implementation of high-index substrates will be explained which – despite being uneconomic due to its high costs – is an excellent approach for high-efficiency OLEDs.

It should be noted that the particular enhancement factor of η_{out} reported for each method will not be specified because the values strongly depend on the detailed stack architecture, hence the reader is referred to the original literature for more details. An overview over various methods and the corresponding references can also be found in Ref. [138].

Furthermore, it is noteworthy that substrate and waveguide modes as well as surface plasmons show a strong dispersion, therefore most of the methods which extract some of the power lost into these optical channels will cause a non-Lambertian and polarized emission as well as color changes with varying viewing angle¹³⁹. This has to be kept in mind because these side-effects are often undesired for applications. Hence, it might be necessary to make further modifications to improve the emission characteristics again.

6.1. Extraction of substrate modes

Probably the most obvious way to enhance the amount of extracted light from an OLED device is to attach an index-matched outcoupling structure to the bottom side of the substrate in order to circumvent the total internal reflection at the glass/air interface,

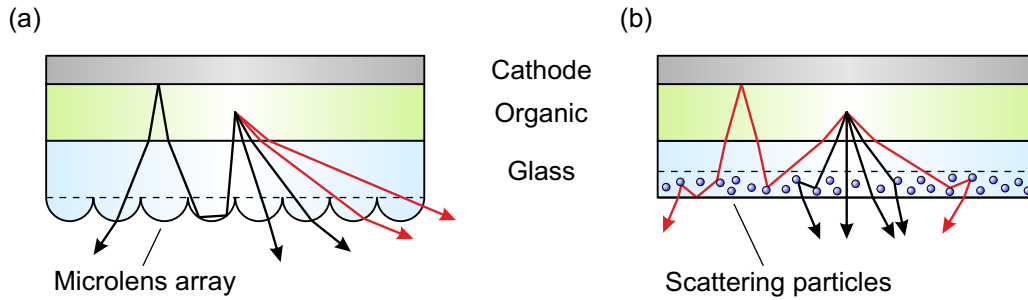


Figure 6.1: (a) Schematic illustration of substrate mode extraction by a microlens array. Light paths indicated in red correspond to radiation that would normally not be able to leave the device due to total internal reflection at the glass/air interface. Multiple reflections inside the stack reduce the efficiency due to absorption in the organic layers and in ITO as well as due to reflection losses at the cathode. (b) Concept of light outcoupling by scattering particles in a film attached to the substrate.

hence getting access to the substrate modes, cf. Fig. 2.7. This method was already demonstrated in Sec. 5.3 by means of a fused silica half cylinder prism attached to the glass substrate. Other examples for outcoupling structures include for instance acrylic truncated pyramids¹⁴⁰, glass lenses¹⁴¹ or epoxy lenses¹³⁵. Although these macro extractors are frequently used in research reports and have an excellent extraction efficiency, their size and weight contradict the flatness and low weight of OLED light sources which are key properties concerning their commercialization.

Therefore, it is desirable to use many small structures next to each other instead of one macro extractor, as shown in Fig. 6.1(a). Normally, these structures are arranged in an array and consist for instance of microlenses^{142–144}, micropyramids^{145,146} or microspheres^{147,148}. A wide variety of transparent materials like plastics, polymers or glass may be used and the size ranges from a few hundred nanometers^{147,148} to several hundred micrometers¹⁴². The influence of size, shape and refractive index of microlenses has been studied in detail by Sun and Forrest, cf. Ref. [94]. It should be emphasized that microstructures can never extract all the light in the substrate because radiation gets partially reflected at the glass/air interface, cf. Fig. 6.1(a). Besides a certain absorption arising from propagation through ITO and the organic layers, the reflectance of the cathode is a limiting factor¹⁴⁵. Therefore, highly reflective metals like aluminum or silver should be used as cathode materials in this case. Especially silver shows an excellent reflectivity throughout the whole visible spectrum, combined with a high conductivity and low absorption.

As an alternative method, flat layers containing scattering particles may be applied to the bottom side of the substrate as illustrated in Fig. 6.1(b). For example, particles like microspheres or inorganic powder may be dispersed in a polymer matrix and can be attached to the glass substrate^{149,150}. In addition, the scattering particles may be composed of a phosphor that is additionally used for down-conversion of blue light to yellow in order to create a white emission spectrum^{35,37}. Moreover, commercial diffuser

6.2. Extraction of waveguide modes

By extracting substrate modes, the outcoupling efficiency η_{out} can probably be raised to values above 30 % or even beyond 40 %. Nonetheless, in typical OLEDs a significant fraction of light is still trapped in either waveguide modes or surface plasmons, thus still representing a major limitation for high external quantum efficiencies. As a matter of fact, it is highly desirable to reduce dissipation into these loss channels or to recover some fraction of the lost power.

Substrate modes discussed in the previous section mainly travel through a thick and usually transparent substrate and only a short distance through absorbing layers, hence they can even escape through the edges of the OLED¹⁵⁵. In contrast, waveguide modes are bound inside the organic layers and ITO due to total internal reflection at the interface to glass. This means that they are subject to absorption inside the organic layers and upon reflection at the cathode. Hence, they have a typical propagation length of the order of 10 μm due to significant damping^{156,157}. As a consequence, extraction of waveguide modes has to occur on a much smaller length scale, and it is not possible to use structures with dimensions of several hundred micrometers.

A very common approach to extract waveguide modes is the use of grating structures between the substrate and the cathode. These periodic modulations allow for Bragg scattering of the guided modes, hence changing their propagation direction so that they might be extracted to air where they give rise to sharp polarized peaks in the emission spectrum. It should be stressed that the grating must be located in regions with a large electric field intensity of the waveguide mode¹⁵⁷. This issue as well as the basic principle will be discussed in detail together with experimental results on grating coupling in Chapter 8.

In general, the grating may be incorporated either directly into the organic layers¹⁵⁷ or into a separate photoresist film on the glass substrate^{156,158}. Frequently, these structures are either stamped or processed by photolithography. However, it has also been demonstrated that periodic gratings with a period of around 500 nm can be manufactured in a roll-to-roll process¹⁵⁹. Furthermore, periodic modulations may be etched directly into ITO^{135,160}. Yet another approach uses two-dimensional photonic crystal patterns between glass and ITO^{161,162}. If the period of the modulation could be further reduced, it is also possible to use self-assembled microarrays on ITO as reported by Park *et al.*¹⁶³.

It is worth mentioning that scattering at gratings causes strong deviations from Lambertian emission. Therefore, Sun and Forrest proposed to use an embedded low index grid between ITO and organic layers with a period of several μm , which only refracts the waveguided light without spectral distortion¹¹. Moreover, it is possible to utilize random gratings with many different periods and no preferred orientation in order to maintain Lambertian emission without sharp peaks. This was demonstrated by Koo *et*

al. using spontaneously formed buckles by deposition of 10 nm aluminum on preheated substrates and subsequent cooling¹⁰.

Similar to the extraction of substrate modes, waveguided light can also be coupled out by scattering layers incorporated close to the organic layers. Neyts and Nieto analyzed the influence of such an internal extraction layer by means of optical simulations¹⁶⁴. It was found once again that a highly reflecting cathode is important for the optimization of the extraction efficiency. Concerning an experimental verification of this technique, Nakamura and co-workers included a special scattering layer comprising a matrix made of high-index glass between the substrate and the anode in order to extract waveguide modes¹⁶⁵. In general, high-index materials can be used as a substrate material to completely inhibit coupling to waveguide modes. This topic will be separately discussed in Sec. 6.5. Finally, it should be mentioned that also an aerogel layer can reduce waveguide losses if the thickness of the organic layers and ITO is small enough so that the number of waveguide modes supported by the stack is reduced^{152,153}. In general, many described methods are not exclusively limited to a certain optical decay channel. In contrast, the extraction of waveguide modes also influences the substrate emission in many cases. Similarly, outcoupling of surface plasmon losses as described in the following section frequently affects substrate and waveguide modes as well.

6.3. Reduction of surface plasmon losses

In the context of surface plasmons, there are several approaches to either reduce coupling to SPs or to recover a fraction of the lost power. The easiest method to reduce the power dissipated into SPs is to simply increase the distance between the emitter and the cathode, since the coupling takes place via the optical near-field. The increased total thickness has the drawback that additional waveguide modes are excited so that in many cases only a shift of plasmon losses to waveguide losses happens without significantly increasing the overall efficiency, cf. Fig. 5.9 and Ref. [8]. It is also possible to fabricate completely transparent OLEDs without metallic cathodes so that no SPs are excited at all. This idea as well as the accompanying advantages and drawbacks are topics of Sec. 6.4.

Another promising approach to strongly reduce the coupling to SPs is the implementation of oriented emitters which have their transition dipole moment parallel to the substrate plane. In this case, the outcoupling efficiency can be enhanced because the coupling to SPs is significantly reduced. The importance of orientation has long been known in the context of polymer OLEDs^{14,135,137}. However, there are only few reports about orientation effects in thin films of small molecular materials measured by spectroscopic ellipsometry^{166,167}. Only recently, orientation effects have also been discovered in doped organic thin films¹⁶⁸.

In the present thesis the intentional utilization of horizontally oriented emitters in

small molecule based OLED devices will be presented for the first time. It will be demonstrated that an outcoupling enhancement of almost 50 % is achievable without any complicated or expensive modifications of the OLED. Moreover, a straightforward method for the determination of orientation in luminescent organic thin films has been developed and intensively studied. The results regarding effects of orientation will be presented in Chapter 11.

Concerning the recovery of SPs, three general methods exist which are based on the reversed processes of coupling light into SPs, cf. Sec. 4.3. First, near-field coupling used for extracting SPs utilizes a thin cathode of a few tens of nanometers and an additional dye-doped index coupled capping layer on the backside of the cathode¹⁶⁹. This method will be explained and studied in detail in Chapter 7.

Second, prism coupling requires a thin metal and an additional capping layer with higher refractive index than the organic layer¹⁷⁰. So far, this method has only been demonstrated in photoluminescence experiments using thin organic films that fulfill the Kretschmann configuration, cf. Fig. 4.6(a). It should be noted that all published reports on the employment of a high-index capping layer did not intend to extract SPs. Instead, only the modified reflectance and transmittance of a thin metallic cathode by the capping layer was investigated in order to enhance the emission of top-emitting OLEDs^{171–176}. In this work, it will be demonstrated by using high-index capping layers and appropriate outcoupling structures that “high-index coupling” is a very efficient way of recovering surface plasmons and also waveguide modes. Moreover, this approach is especially compatible with modern OLED fabrication processes as will be explained in Chapter 10.

Finally, grating coupling may also be used in order to transform surface plasmons into free-space radiation similar to the discussion of the outcoupling of waveguide modes. However, for the extraction of surface plasmons, which are usually bound to the interface between the organic electron transport layer and the metallic cathode, the grating structure should be located at this particular interface. The principle of this coupling approach as well as several grating fabrication methods will be discussed in Chapter 8.

6.4. Microcavity devices, top-emitting OLEDs and transparent OLEDs

It was already mentioned in Chapter 5 that an optical cavity environment has a considerable influence on the radiative decay rate and on the emission characteristics of emitting molecules placed within the cavity¹⁷⁷. A normal bottom-emitting OLED with an ITO anode already exhibits weak cavity effects¹⁷⁴, which was demonstrated by the thickness variation of the electron and hole transport layers, cf. Fig. 5.7. However, this effect may be intentionally utilized by inserting a second partially reflecting layer which causes strong multiple-beam interference effects¹⁷¹. Such a device will be called a mi-

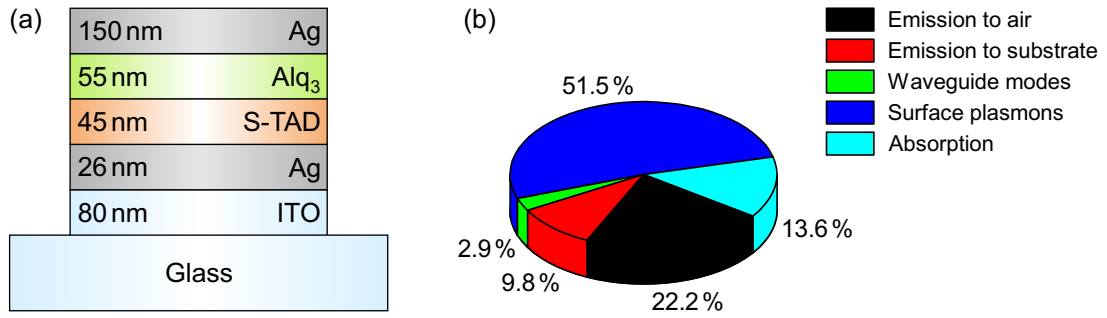


Figure 6.3: (a) Stack layout of an optical microcavity device consisting of a thick silver cathode and an additional 26 nm thick silver layer on ITO. The thicknesses of all layers except the thick silver cathode were varied within a few tens of nanometers and optimized monochromatically at a wavelength of 510 nm. (b) Fraction of power coupled to different optical channels assuming a radiative quantum efficiency of $q = 100\%$ and an isotropic emitter orientation.

microcavity OLED. This effect may for instance be used to enhance the direct emission into air.

An exemplary microcavity stack is depicted in Fig. 6.3(a). Here, the 26 nm thick silver layer between ITO and S-TAD reflects a certain fraction of the radiation, thus creating a strong cavity effect. It is important to note that injection layers or doped transport layers are required in order to use silver for both electrodes. The thin silver layer also supports surface plasmons traveling at larger in-plane wave vectors. Hence, the simulation has to be performed for a larger wave vector range. More details about the simulation of microcavities can be found in the appendix, cf. Sec. A.3.

Figure 6.3(b) clearly demonstrates that the direct emission can be significantly enhanced in comparison to Fig. 5.6 owing to a strongly reduced emission into the substrate. In other words, the presented microcavity redistributes the optical power from one channel to another. In fact, it was demonstrated by Meerheim *et al.* that monochromatic blue, green and red OLEDs using an additional silver layer with a thickness between 18 nm and 23 nm have enhanced light outcoupling in comparison to normal OLEDs¹⁷⁸.

The microcavity environment also has an influence on the angular and spectral emission pattern as depicted in Figs. 6.4(a) and (b) for emission without and with attached fused silica prism, respectively. Obviously, the emission characteristics significantly differ from the OLED with normal cavity, cf. Figs. 5.2 and 5.3.

First, it can be observed that the emission is concentrated in an angular cone at small angles with a maximum in forward direction. This is a result of multiple-beam interference which enhances the radiation emitted under small angles to the surface normal for this particular cavity.

Second, the emission spectrum is narrowed in comparison to an OLED with a bare ITO anode¹⁷⁹. This also results from interference effects because the emission into normal direction was optimized for the peak wavelength which gains constructive interfer-

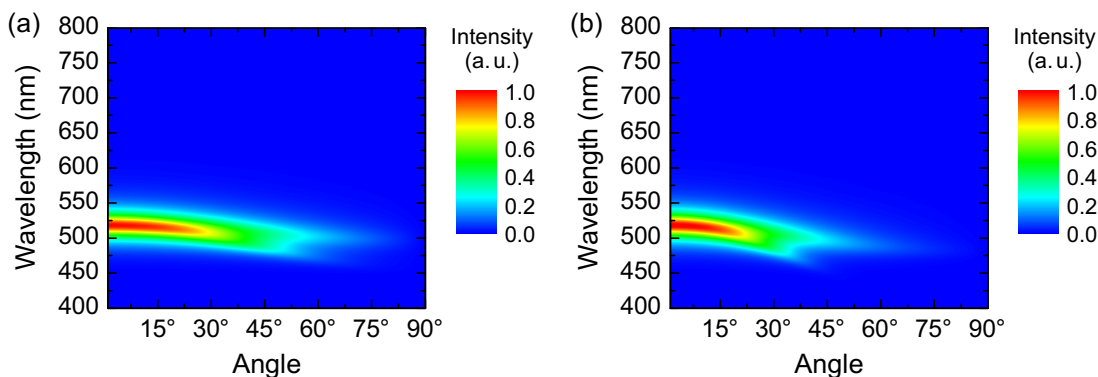


Figure 6.4: (a) Simulation of the angularly and spectrally resolved unpolarized direct emission into air from the microcavity OLED shown in Fig. 6.3(a). (b) Unpolarized emission into an attached fused silica prism. Both graphs are normalized to the maximum value in each case. The splitting into two branches for higher angles results from a different angular dependent behavior for s- and p-polarized emission, the former changing more with angle in this case.

ence in this direction. Consequently, other wavelengths do not gain optimal interference or even experience destructive interference, which causes a narrowing of the spectrum.

Finally, the angular dependent emission pattern becomes dispersive, i.e. the emission peak noticeably shifts to shorter wavelengths with increasing angle, thus causing substantial deviations from a Lambertian emission profile^{178–180}. In other words, the color of the OLED changes with viewing angle. This can be understood taking into account that the optical path length inside the cavity changes with propagation angle. Hence, the wavelength which gains optimal interference is changed as well, cf. Sec. 3.5. This is also obvious from the transverse resonance condition in Eq. (3.69) remembering that $k_0 = 2\pi/\lambda$. Hence, an increase of the angle, i.e. smaller $\cos\theta_m$, must be compensated by a lower wavelength of the mode¹⁷⁹. By using dispersive gratings, microlens outcoupling foils or sandblasted substrates, the viewing angle properties of microcavity OLEDs can be improved again^{151,178,181}. In general, microcavity devices can also exhibit a high degree of polarization depending on the actual stack layout¹⁸⁰.

The microcavity effects have several consequences for their applicability. First of all, it is rather inefficient to use a microcavity for white OLEDs because certain regions of the broad emission spectrum will suffer from destructive interference¹⁷⁴. In addition, the angular dispersive and thus non-Lambertian emission might be undesired for certain light sources. In contrast, microcavities might be particularly suited for specific applications in signage, e.g. for traffic lights. Here, a narrow emission spectrum and strong forward emission are clearly welcome. Of course, the emission pattern can also be optimized e.g. for maximum substrate emission or for emission into a certain angular range, which might be interesting for applications like the surface plasmon resonance sensor presented in Sec. 4.5.

It should be pointed out that all mentioned cavity effects significantly depend on

the reflectivities of both mirrors and thus generally become stronger with increasing thickness of the additional metal film. On the other hand, a larger metal thickness decreases the transmission through the layer and thus a smaller fraction of the generated radiation is able to leave the device. Furthermore, the emission enhancement is reduced or even becomes negative, if the device shows high absorption losses as demonstrated for example by Lin *et al.*, who modeled microcavities in dependence of the absorption of the semitransparent mirror¹⁷⁴.

Moreover, the cavity strongly influences the radiative decay rate as discussed in Secs. 5.1 and 5.4. In particular, the cavity can have a positive effect on rather small values of the radiative quantum efficiency. Assuming for instance a value of $q = 20\%$ in the example shown in Fig. 6.3, the effective radiative quantum efficiency becomes $q_{\text{eff}} = 39\%$ and thus is almost doubled.

The concept of optical microcavities is especially important for top-emitting OLEDs. These devices often comprise a highly reflecting anode and a semitransparent metallic cathode which is frequently made of silver or a combination of silver and aluminum. Such a cathode often has a thickness between about 15 nm and 25 nm^{173–176, 182}. Inherently, such a stack represents a strong microcavity¹⁷¹. By using a capping layer, the reflectance and transmittance of the semitransparent mirror can be modified in order to optimize the outcoupling efficiency or the direction of emission. Such a capping layer can be made for instance of C₆₀ and other transparent organic materials^{173, 182}, or by using ZnSe, TeO₂ and other inorganic materials^{76, 171, 172, 174–176}.

If the thick metallic anode is for instance replaced by a combination of ITO and a thin metallic film, it is possible to create a microcavity structure with two semitransparent electrodes⁹¹. Thus, radiation is emitted through both sides of the OLED, and the ratio between bottom and top emission can be tuned by an adjustment of the thicknesses of the metals used for the anode and the cathode side⁹¹.

Moreover, an almost completely transparent OLED may be designed by employing ITO both on the anode and the cathode side¹⁸³. However, the organic layers are usually damaged upon sputter deposition of ITO on top of the device⁹³. Hence, a buffer layer is required as protection. For example, it was demonstrated by Meyer *et al.* that tungsten oxide may be used as buffer layer¹⁸³. Depending on the thickness of this layer, the ratio between top and bottom emission changes^{13, 131}. Certainly, transparent OLEDs are particularly interesting for some applications like windows, room dividers or certain signage applications. However, an OLED light source intended for the use in general lighting will most probably be attached to a wall or to the ceiling. In this case, a device with one reflecting electrode might be the best choice.

It is noteworthy that a transparent OLED without metallic cathodes by nature represents an optimal method for significantly reducing power dissipation into surface plasmons. Nevertheless, the coupling to waveguide modes usually is much stronger because a device with two ITO electrodes is thicker and thus supports more guided modes.

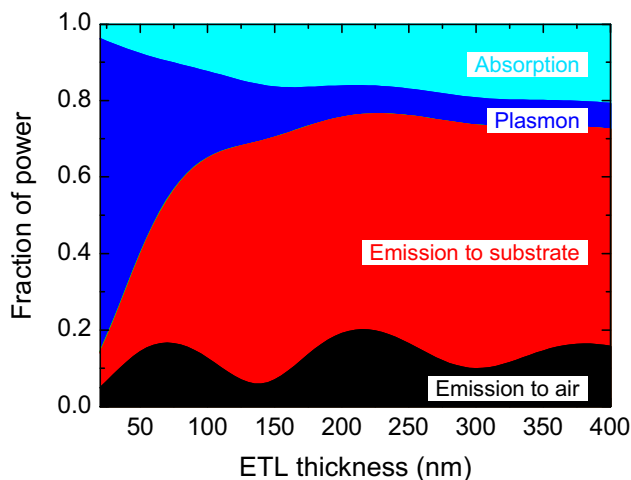


Figure 6.5: Fraction of power coupled to different optical channels in dependence of the electron transport layer (Alq_3) thickness for an OLED as depicted in Fig. 2.11(a) but with a high-index substrate (NSF6). The simulation is performed polychromatically according to the emission spectrum of Alq_3 , and a radiative quantum efficiency of $q = 100\%$ as well as an isotropic emitter orientation are assumed.

Therefore, often only a redistribution from surface plasmons to waveguided modes occurs without remarkably changing the overall efficiency^{13,131}.

6.5. High-index substrates

One of the most efficient methods regarding the outcoupling enhancement is the application of high-index substrates combined with appropriate outcoupling structures. By using high-index substrates with a refractive index of around 1.8, total internal reflection between the substrate and the organic layers and ITO can be eliminated almost completely, hence preventing any coupling to waveguide modes^{135,141,145,155}. The basic idea dates back to the year 2000 when Madigan and co-workers used polycarbonate substrates with a refractive index of $n = 1.59$ and a molded epoxy outcoupling lens to reduce the radiation which is waveguided in the organic layers and ITO¹⁴¹. Clearly, a refractive index of 1.59 is not high enough to prohibit all waveguides, nevertheless the outcoupling efficiency was considerably enhanced.

In order to study the influence of high-index substrates, the variation of the electron transport layer which was shown in Fig. 5.9 is repeated with just one modification. Instead of a substrate made of BK7 glass, it is assumed that the substrate is made of NSF6 (or similarly SF6). This glass has a refractive index around 1.8 and therefore is quite comparable to typical refractive indices of organic layers and ITO, cf. the optical constants in the appendix. The result of the ETL variation is depicted in Fig. 6.5.

It can be seen that absorption is slightly higher in comparison to the same stack on BK7 glass, cf. Fig. 5.9, but absorption could be reduced for instance by employing

a thinner ITO layer¹⁴⁵. The contribution to direct emission and surface plasmons is almost unchanged in comparison to the variation with normal BK7 glass substrate. On the other hand, there is hardly any power dissipated into sharp waveguide modes when a high-index substrate is utilized. Instead, the power is redistributed and emitted into the high-index substrate. In addition, by increasing the distance to the cathode, the power dissipation to surface plasmons can be considerably decreased¹⁴⁵. Normally, this power would to a large extent be reallocated to waveguide modes. Since this optical channel is circumvented owing to the high-index glass, the power is redistributed into substrate emission. From there the radiation may be extracted by using one of the methods described in Sec. 6.1 for the outcoupling of substrate modes. Alternatively, it is possible to include scattering particles into the high-index material¹⁶⁵. Altogether, highly efficient OLEDs with almost no power dissipation into undesired optical channels and hence an outcoupling efficiency η_{out} well above 50 % can be achieved.

It has already been reported that OLEDs can reach record efficiencies by means of high-index substrates. Mladenovski *et al.* demonstrated an external quantum efficiency of 42 % and a luminous efficacy of 183 lm/W for green phosphorescent OLEDs with thick doped ETL on sapphire substrates ($n = 1.8$) using an index-matched half-sphere lens⁷³. Moreover, white OLEDs reaching fluorescent tube efficiencies on a high-index glass ($n = 1.78$) were presented by Reineke and co-workers⁹, though the color is shifted somewhat into the green part of the color space. By using periodic outcoupling structures, they obtained values of 34 % and 90 lm/W for the external quantum efficiency and luminous efficacy, respectively.

Despite the rather easy application of high-index substrates to OLEDs and the enormous efficiency demonstrated in different laboratories, this method significantly increases production costs. Not only sapphire substrates but also other presently available materials with a refractive index of about 1.8 are too expensive in order to be applied for large area OLED light sources, so that this approach will probably not be economically advantageous for applications in general lighting⁴.

To summarize, many interesting approaches have been demonstrated in literature in order to enhance light extraction and to increase the overall efficiency of OLEDs. Nevertheless, none of the described techniques can solve all challenges from an optical point of view. Either a method is inapplicable for white OLEDs (microcavities), undesired for many common applications (transparent OLEDs) or simply economically unfeasible (high-index substrates). Thus, the following chapters will introduce several interesting novel approaches for enhanced outcoupling that are in particular compatible with common fabrication methods and applicable to a wide range of OLEDs. Moreover, some existing methods will be investigated in detail in order to gain a deeper understanding of the underlying fundamental physics, which is a key requirement in order to improve these techniques and to create completely new ways for enhancing light extraction and for realizing energy efficient OLEDs.

7. Near-field coupling

This chapter describes the near-field coupling (or index coupling) approach, which utilizes a thin metal film and adjacent media with comparable refractive indices as well as appropriate dye doping on both sides of the metal¹⁶⁹. By using such a stack layout, it is possible to utilize the power, which was dissipated by donor molecules to SPs, in order to excite an acceptor dye and hence to recover some of the SP losses^{184,185}.

First, modifications of the dispersion of SPs propagating at the interface to films having a finite thickness will be discussed by means of optical simulations. An effective SP index will be introduced to simplify the picture. Afterwards, the basic principle of near-field coupling will be explained along with the material requirements. Subsequently, PL experiments with a variation of the metal film thickness will be presented and the energy transfer will be verified by measurements of the excited state lifetime of the investigated dyes. Finally, an estimation of the extraction efficiency will be given and ideas for further improvements will be discussed.

7.1. Surface plasmon dispersion in thin films

The surface plasmon dispersion in Eq. (4.15) is strictly valid only for semi-infinite layers. In order to study coupling to SPs and a possible recovery of SP losses it is necessary to understand the modifications that arise from layers with a finite thickness.

The simplest modification is a combination of a semi-infinite silver layer and a finite Alq₃ or polymethylmethacrylate (PMMA) film bounded by air, cf. Fig. 7.1(a). In this case, the evanescent SP field penetrates through the dielectric film into air. Hence, the SP dispersion depends on the actual thickness of the dielectric layer¹⁰⁴ and cannot be correctly computed by Eq. (4.15), which is only valid for semi-infinite layers. On the other hand, by using optical simulations based on the dipole model, the SP dispersion can be accurately calculated for finite Alq₃ or PMMA layers. An example of the total power dissipation for a 43 nm thick Alq₃ film is depicted in Fig. 7.1(b), demonstrating strong coupling to SPs due to the small distance between the emitter and the Ag layer.

From the cross sections in Fig. 7.1(c) it is obvious that the SP dispersion is close to the case of a silver/air interface if the Alq₃ layer is very thin. On the other hand, the peak of the SP dispersion shifts to larger in-plane wave vectors with increasing Alq₃ thickness because a smaller part of the SP field penetrates into air. For an Alq₃ thickness of 100 nm, the dispersion is already close to that of a semi-infinite Alq₃ layer.

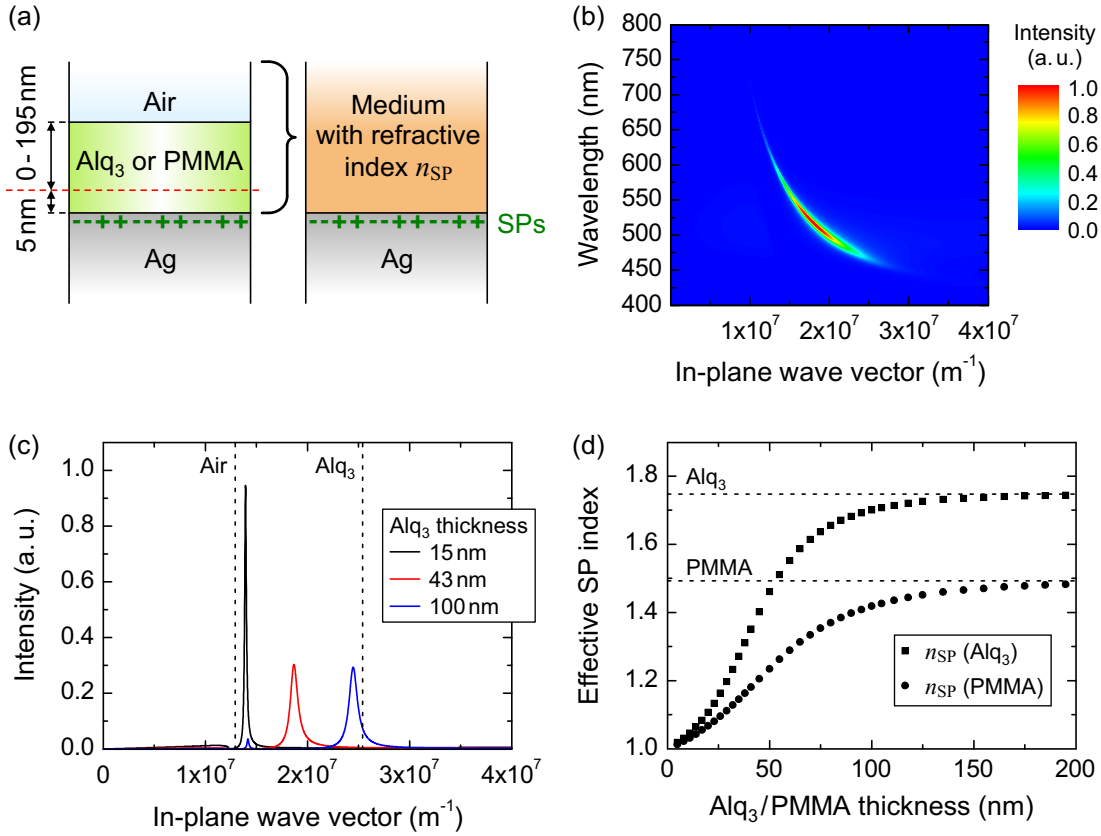


Figure 7.1: (a) Device layout for the investigation of the SP dispersion as a function of the thickness of a finite Alq₃ or PMMA film adjacent to a semi-infinite silver layer. The total thickness of Alq₃ or PMMA is varied between 5 nm and 200 nm. The red dashed line represents the emitter position which is located at a distance of 5 nm from the interface to silver. Instead of a finite Alq₃/PMMA layer surrounded by air, an almost similar SP dispersion may be obtained by assuming a homogeneous semi-infinite layer with a refractive index n_{SP} (“effective SP index”). (b) Total optical power dissipation for a 43 nm thick Alq₃ film. (c) Cross section of the power dissipation at a wavelength of 510 nm for three Alq₃ film thicknesses. Each cross section is normalized taking into account the appropriate cavity effects. For a 100 nm thick Alq₃ film a waveguide mode emerges at $k_x \approx 1.4 \times 10^7 \text{ m}^{-1}$. The dashed lines indicate the maximum of the SP dispersion at a bulk silver film adjacent to semi-infinite air and Alq₃, respectively. (d) Effective SP index n_{SP} derived from the k_x peak position as a function of the Alq₃ and PMMA thickness. The dashed lines correspond to the refractive indices of bulk Alq₃ and PMMA, respectively.

In order to simplify the further discussion, an effective SP index n_{SP} is introduced by assuming a homogeneous semi-infinite medium with refractive index n_{SP} instead of the combination of a finite Alq₃ or PMMA film bounded by air, cf. Fig. 7.1(a). In other words, n_{SP} can be understood as a combined refractive index of Alq₃ and air. The effective SP index is calculated by inserting the simulated k_x peak position of the SP dispersion for each Alq₃ or PMMA thickness at a wavelength of 510 nm into Eq. (4.15). Since the permittivity of bulk silver is known, it is possible to compute $n_{\text{SP}} = (\varepsilon_{\text{SP}})^{1/2}$. The result is plotted in Fig. 7.1(d). Again, it is apparent that n_{SP} is close to unity for

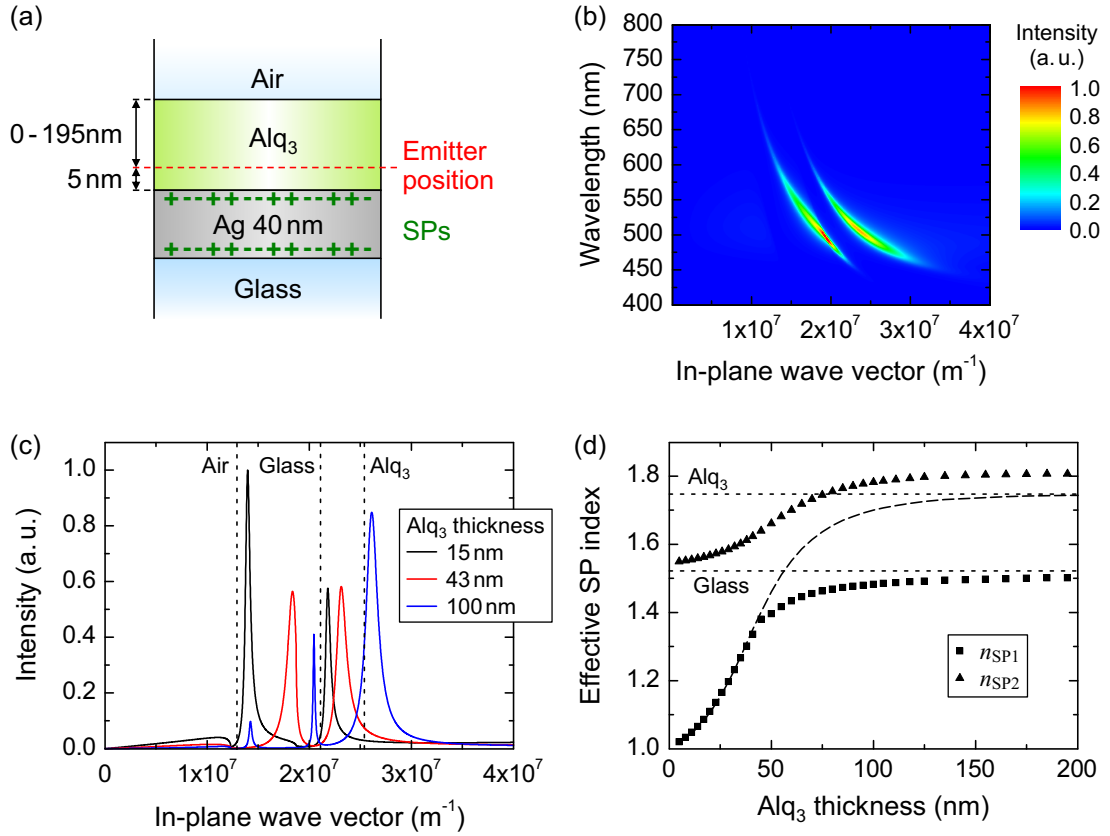


Figure 7.2: (a) Stack structure for the analysis of the SP dispersion as a function of the thickness of a finite Alq₃ film similar to Fig. 7.1(a), except that the silver layer has a finite thickness of 40 nm in this case, hence allowing for coupling to SPs at both silver interfaces. (b) Total optical power dissipation showing two SP branches for a 43 nm thick Alq₃ film. (c) Cross section of the power dissipation at a wavelength of 510 nm for three Alq₃ film thicknesses. The dashed lines indicate the maximum of the SP dispersion at a bulk silver film adjacent to semi-infinite air, glass and Alq₃, respectively. (d) Effective SP indices n_{SP1} and n_{SP2} calculated for the k_x values of the two SP peaks at a wavelength of 510 nm using Eq. (4.15), assuming a homogeneous semi-infinite medium instead of a finite Alq₃ film bounded by air. The dashed plot represents the curve from Fig. 7.1(d) in the case of Alq₃.

small Alq₃ or PMMA thicknesses because the SPs mainly sense the air environment. For larger thicknesses, n_{SP} approaches the corresponding value of a bulk film. It is noteworthy that the curve for the Alq₃ film converges slightly faster than in the case of PMMA. This can be explained by the fact that the SP skin depth is smaller for a dielectric medium with higher refractive index, cf. Eq. (4.27). Therefore, the SP field penetrates to a larger extent into air in case of a PMMA film of a certain thickness in comparison to Alq₃.

If also the silver thickness is finite and bounded by a glass substrate as illustrated in Fig. 7.2(a), the situation becomes more complicated because there are two silver interfaces that can basically sustain a bound SP mode⁹⁷. Consequently, two distinct SP branches can be seen in the power dissipation shown in Fig. 7.2(b) for the case of a

43 nm thick Alq₃ film.

For varying Alq₃ thicknesses, one could expect that the glass/silver SPs have a rather fixed k_x position because this side of the Ag is unchanged. In contrast, the SP on the silver/Alq₃ side should depend on the actual Alq₃ thickness as discussed above. However, this picture is only partially true as illustrated by the cross sections in Fig. 7.2(c). For small and large Alq₃ thicknesses, respectively, the two SP branches have a k_x value as expected, and it is reasonable to assign each branch to a certain interface. Interestingly, coupling to the SPs at the bottom Ag side is significantly stronger compared to SPs at the top side because the field of the emitting dipole has to penetrate through the silver in order to excite SPs at the top Ag side^{186,187}.

However, for an intermediate Alq₃ thickness, it is no more obvious to relate each SP dispersion to a specific Ag side¹⁸⁸. It is also noteworthy that no overlap or intersection of the two branches occurs, i.e. the two SP branches show an anti-crossing behavior. The reason for this is that interactions between SPs on both Ag sides give rise to coupled modes^{97,188}. This phenomenon can be understood by analyzing the effective SP index shown in Fig. 7.2(d). For small Alq₃ thicknesses, one SP branch originates at $n_{\text{SP1}} \approx n_{\text{air}}$ while the other is located at $n_{\text{SP2}} \approx n_{\text{glass}}$ with n_{air} and n_{glass} being the refractive indices of air and glass, respectively. With increasing Alq₃ thickness, both n_{SP1} and n_{SP2} increase until they reach a value of $n_{\text{SP1}} \approx n_{\text{glass}}$ and $n_{\text{SP2}} \approx n_{\text{Alq}_3}$ for an Alq₃ thickness larger than approximately 100 nm, with n_{Alq_3} corresponding to the refractive index of bulk Alq₃. Thus, it seems that the two SP branches changed their position on the two sides of the Ag layer.

In fact, it is no more possible to distinguish between both SP branches for intermediate Alq₃ thicknesses. The combined refractive index of Alq₃ and air on the top side becomes almost identical to that of glass, hence both SPs have a similar dispersion. Since their fields penetrate through the finite silver layer¹⁰⁶, the SPs interact and exchange energy so that the coupling strength to SPs on both Ag sides is comparable, which can be seen in Fig. 7.2(c). This effect is known as surface plasmon coupling.

In detail, the dispersion relation of SPs splits into two modes of opposite parity in the case of a thin metal film which is bounded by two layers having equal optical constants^{97,104,106,169}. The odd mode has an asymmetric distribution of the electric field component in the propagation direction and a higher frequency (or smaller k_x value) in comparison to the even mode. The former is also known as long range surface plasmon mode because the confinement to the metal film is reduced and, consequently, the propagation length is increased. A detailed discussion of coupled SP modes is given in Ref. [97].

It should be pointed out that it is not required to have exactly the same optical constants on both sides of the metal because the SPs have a finite width and thus coupling is allowed even for small differences in their dispersion.

Naturally, also the Ag thickness has a strong influence on the coupled modes, as will

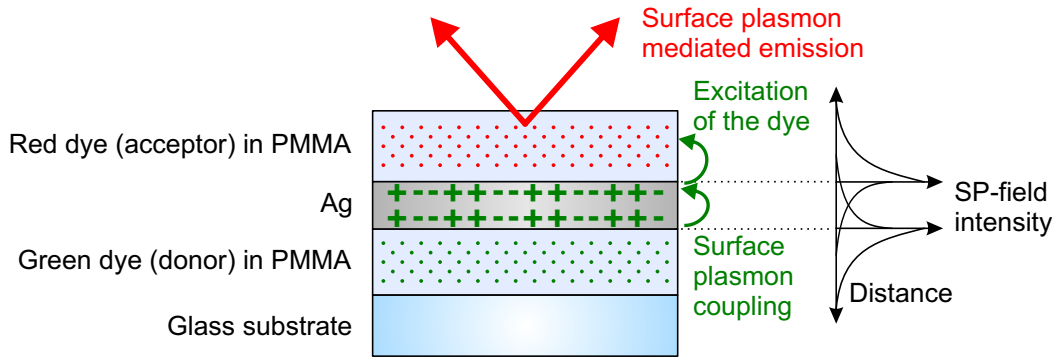


Figure 7.3: Schematic drawing illustrating the near-field coupling method. Surface plasmons are excited by a donor dye and couple to SPs at the opposite silver interface where they excite an acceptor which is positioned within the near-field of the SPs. Thus, some of the power which was coupled by the donor to SPs is recovered.

be discussed in more detail in Sec. 9.3.4. In general, the separation of the two SP modes is stronger when the Ag thickness is reduced, i.e. when the Ag film loses more and more of its bulk nature and the interaction between SPs on both sides increases¹⁸⁹.

It should be noted that the bulk permittivity of Ag was used to calculate the effective SP index from the simulated dispersion in Fig. 7.2(d). Actually, this is not absolutely correct as can be seen by the fact that n_{SP1} and n_{SP2} do not converge to the bulk value of Alq₃ and glass. Nevertheless, this simplified picture of an effective SP index is a descriptive way to visualize the phenomena of SPs propagating at thin films.

7.2. Basic principle

In order to use coupled SPs to transfer energy from one silver interface to the opposite side, it is necessary to have media with comparable optical constants on both sides of the silver layer. As discussed in the previous section for the general case of a stack with two different adjacent media like glass/silver/Alq₃, the thickness of the Alq₃ layer must be chosen carefully in order to obtain an effective SP index on the bottom side which matches the refractive index of glass.

By choosing a more specific stack layout with similar materials on both sides of the metal, the coupling condition can be fulfilled for a wide range of thicknesses. Andrew and Barnes proposed to use two PMMA layers¹⁶⁹. The basic principle is illustrated in Fig. 7.3. The bottom PMMA layer is doped with a green dye and excited by a laser. While some part of the photoluminescence signal is directly emitted in bottom direction, a considerable amount of power is dissipated to SPs at the bottom Ag interface via optical near-field coupling. Since there is also a PMMA capping layer on the top side of the Ag layer, the dispersion relation for SPs at both Ag interfaces is almost similar. Since the fields of the SPs penetrate through the finite silver layer, SPs traveling at the bottom side may couple with SPs at the top interface, thus enabling an exchange of

energy between both SP modes. The upper PMMA layer is doped with a red dye whose absorption should match the emission of the green dye. Therefore, the red dye molecules can be excited by SPs because the evanescent SP field penetrates into the PMMA layer. Altogether, some part of the energy lost to SPs by the green donor is recovered and used to excite the red acceptor dye inside the PMMA capping layer, which results in emission of red light into the top hemisphere.

The described technique is often called index coupling according to the requirement of identical refractive indices on both sides of the metal^{184,187}. However, to avoid confusion with the high-index coupling method described in Chapter 10, the method will be referred to as near-field coupling because it makes use of the overlap of the evanescent fields of the SPs with the near-field of the oscillating dipole emitter.

The refractive index on the bottom side nearly corresponds to the bulk value of PMMA because the glass substrate adjacent to PMMA has almost the same refractive index, cf. Sec. A.2 in the appendix. In order to have comparable optical constants on both Ag sides, i.e. SPs traveling at both Ag interfaces have a similar dispersion, the upper PMMA layer must be sufficiently thick to ensure that the SPs mainly sense the PMMA without penetrating too much into the surrounding air. According to the general findings in Figs. 7.1(d) and 7.2(d), the bulk value for the SP dispersion is approached for a thickness of the order of 100 nm. However, care must be taken so that no waveguides are supported by the upper PMMA layer. This should be avoided because coupling of acceptor molecules to waveguide modes would reduce the desired emission into air. Therefore, a thickness of 90 nm was chosen as optimal trade-off so that the effective SP index is as large as possible but still no significant coupling to waveguides takes place.

7.3. Material requirements and experimental setup

In order to determine the fraction of power that can be recovered by near-field coupling, it is necessary to use appropriate materials. Alq₃ doped at 10 wt% into a 90 nm thick PMMA layer (Sigma-Aldrich, $M_w = 996.000$) is used as donor on the bottom side of a Ag layer. The acceptor layer on the top Ag side consists of Lumogen Red (LR, BASF) doped at 2 wt% into a 90 nm thick PMMA layer. The doping concentrations are chosen such that the refractive index of PMMA is not altered too much and the value of neat PMMA can be assumed.

Samples were fabricated on cleaned glass microscope slides. The dye-doped PMMA layers were spin cast from a solution with 1.2 wt% PMMA dissolved in a mixture of chloroform and toluene. Alq₃ can be well dissolved in chloroform, but this solvent alone would result in a rippled PMMA surface. The Ag layers were fabricated by electron beam evaporation in a vacuum between 10^{-6} and 10^{-7} mbar, the thicknesses were determined by profilometry (Veeco Dektak). No encapsulation is required because the bottom PMMA layer is protected by the layers above and the upper PMMA layer

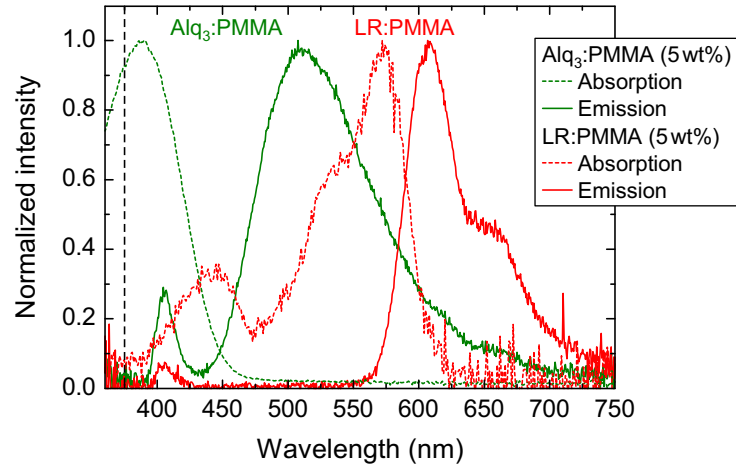


Figure 7.4: Absorption and PL emission spectra of Alq₃ and Lumogen Red doped at 5 wt% into PMMA. Although the concentration differs from the value which was actually used in the experiments, the basic optical properties of Alq₃ and Lumogen Red can be deduced. Absorption was measured with a UV-Vis spectrophotometer (Varian Cary 50). The black dashed line at 375 nm indicates the wavelength of the excitation laser. This laser is also responsible for the small peaks in the fluorescence spectra around 400 nm. In later measurements this secondary emission is cut off by an additional 375 nm band-pass filter.

only absorbs a small fraction of the incident laser beam and therefore suffers less from photodegradation.

Figure 7.4 demonstrates that the emission spectrum of Alq₃ is in a similar wavelength range as the absorption spectrum of LR. This is an inevitable precondition for the near-field coupling method because the SPs which are excited by the green donor dye have the same energy as Alq₃ and thus a similar spectral distribution. In addition, the emission spectra are clearly separated so that it is possible to distinguish emission arising from Alq₃ and LR. Furthermore, the excited state lifetime of Alq₃ is larger than that of LR which will be used to verify the energy transfer from the green donor to the red acceptor.

The experimental setup for investigating the near-field coupling approach is illustrated in Fig. 7.5. A 375 nm continuous wave (cw) laser diode incident from the substrate side under 45° was used to excite the donor Alq₃ molecules. Alq₃ excites SPs at the interface to Ag and the SPs can couple to SPs on the other Ag side. There, SPs can in turn excite the acceptor dye LR. The sample was aligned perpendicular to the collimating lens and no polarizer was used in this case because the emission from LR is expected to be unpolarized.

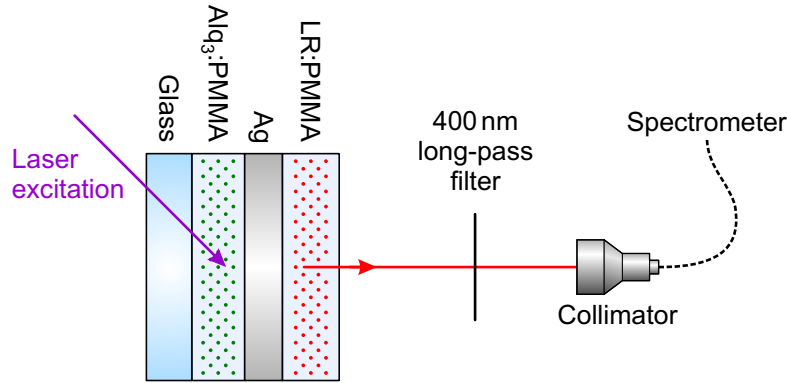


Figure 7.5: Experimental setup (top view) for studying the near-field coupling method. A 375 nm continuous wave laser diode is used to excite the green donor Alq₃. The emission intensity of the sample is measured on the acceptor side of the silver layer in a direction normal to the surface.

7.4. Results

7.4.1. Variation of silver thickness

Besides the excitation of LR through SPs, the 375 nm cw laser beam will be partially transmitted through the Ag layer and directly excite the red dye, although the materials were chosen such that Alq₃ has a high absorption and LR has a minimum absorption at this wavelength, cf. Fig. 7.4. In addition, some emission of Alq₃ will penetrate through the Ag layer and will thus be emitted into top direction or will be reabsorbed by LR molecules. For a conclusive analysis, it is necessary to distinguish between all contributions to the total emission. Therefore, three different samples were prepared for a certain silver thickness, as shown in Fig. 7.6(c).

Samples of type A consist of an Alq₃ doped PMMA layer at the bottom Ag side while the top capping layer is undoped. These samples were used to determine the fraction of Alq₃ emission that penetrates through the Ag film and is measured in top direction, as shown by the green curves in Figs. 7.6(a,b,d,e,f) for a range of different Ag thicknesses. This direct donor emission corresponds to the intensity that is obtained without recovery of SP losses. The integral value from 435 nm to 750 nm is denoted by I_D as displayed in Fig. 7.6(d).

The doping in samples of type B is inverted, i.e. the bottom layer is undoped and the top PMMA layer is doped with LR. The measured intensity of this sample represents the intensity of LR emission that follows from direct excitation by the laser. This direct acceptor emission is plotted as red curves and the integral value is referred to as I_A . Finally, samples of type C contain dye-doped PMMA layers on both sides of Ag and the emission is shown as black curves. The integral intensity obtained from both the donor and acceptor in samples C is denoted by I_{DA} .

Apparently, the acceptor emission is significantly enhanced in the case of samples C

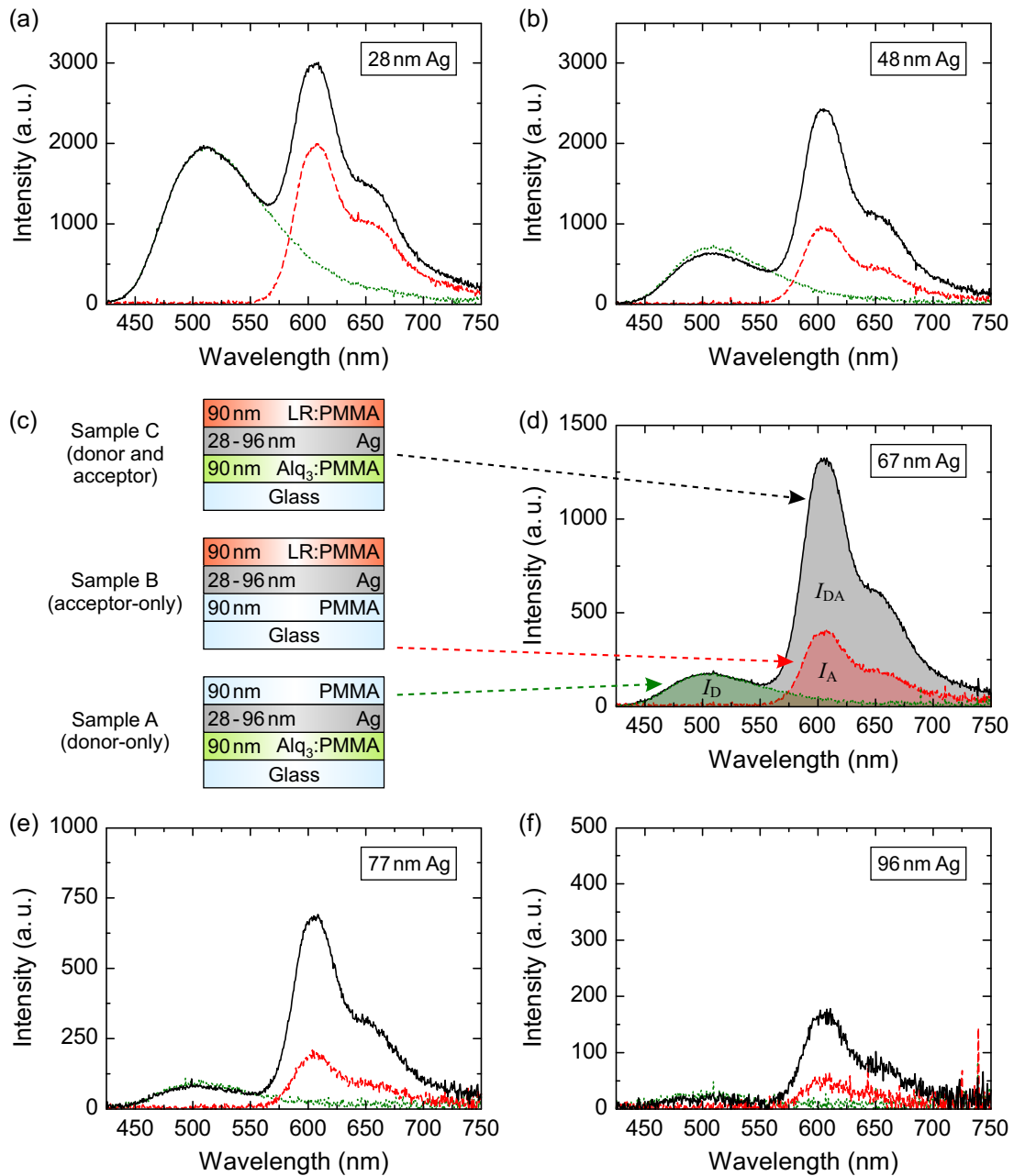


Figure 7.6: (a,b,d,e,f) Spectrally resolved emission intensity for samples with silver thicknesses of 28 nm, 48 nm, 67 nm, 77 nm and 96 nm, respectively. The green dotted lines correspond to samples which contain only the donor Alq₃ and no acceptor molecules, cf. sample A in part (c) of the figure. On the contrary, sample B has only the acceptor Lumogen Red (LR), and the corresponding emission is plotted as dashed red curves. The emission of samples C which include both donor and acceptor dyes is shown as black solid lines. Each measurement was performed at four different positions on the sample with subsequent averaging. Integrating over the emission spectrum of samples A, B, and C yields the integral values I_D , I_A , and I_{DA} , respectively.

Ag thickness (nm)	Donor-only I_D	Acceptor-only I_A	Donor and acceptor I_{DA}	Transferred energy I_T
28	100.0	68.7	183.4	14.6
38	66.8	51.2	142.5	24.5
48	34.2	31.6	103.4	37.7
55	16.3	19.8	69.1	33.0
67	8.7	13.9	50.0	27.4
77	5.2	6.8	25.5	13.5
88	2.8	3.7	13.2	6.7
96	1.8	1.9	6.3	2.6

Table 7.1: Total intensities obtained by integrating over the emission of samples A (donor-only), samples B (acceptor-only) and samples C (donor and acceptor) from 435 nm to 750 nm for eight different Ag thicknesses. The additional energy transferred via near-field coupling is denoted by $I_T = I_{DA} - I_D - I_A$. The intensity I_D at a Ag thickness of 28 nm was set to 100 and all other values were normalized accordingly and rounded to one decimal place.

due to energy transfer from Alq_3 to LR mediated by coupled SP modes, i.e. emission that is obtained by recovering SP losses. The additionally transferred energy is defined as $I_T = I_{DA} - I_D - I_A$, i.e. the intensity obtained from samples C minus the intensity of samples A and B for each Ag thickness. Andrew and Barnes subtracted only a certain fraction of I_D to account for the decrease in donor emission intensity in samples of type C in comparison to donor-only samples¹⁶⁹. Here, this effect can be seen to some extent for the samples with 48 nm thick Ag, cf. Fig. 7.6(b). However, even for the samples with 48 nm thick Ag the decrease is significantly smaller in comparison to the measurements of Andrew and Barnes who used a different acceptor material and other dopant concentrations¹⁶⁹, hence this effect can be neglected here.

The integral intensities for samples with eight different Ag thicknesses between 28 nm and 96 nm are listed in Table 7.1. Although the absolute values of I_D , I_A and I_{DA} decrease with increasing Ag thickness, the transferred energy by means of SP coupling has the highest value for intermediate Ag thicknesses. The dependence on Ag thickness basically agrees with the values obtained by Andrew and Barnes using a slightly different stack design¹⁶⁹.

In general, the energy transfer mediated by SPs is governed by two effects that depend on the Ag thickness in opposite ways. First, coupling of the green donor to SPs is enhanced with increasing thickness. Second, transmission of SPs through the silver is reduced with increasing Ag thickness as is obvious from the thickness dependence of the direct donor emission in Table 7.1. Altogether, there is an optimal value where the excitation of SPs from the donor is strong but still a considerable fraction of SPs is able to couple to SPs on the other Ag side and in turn excite the red acceptor.

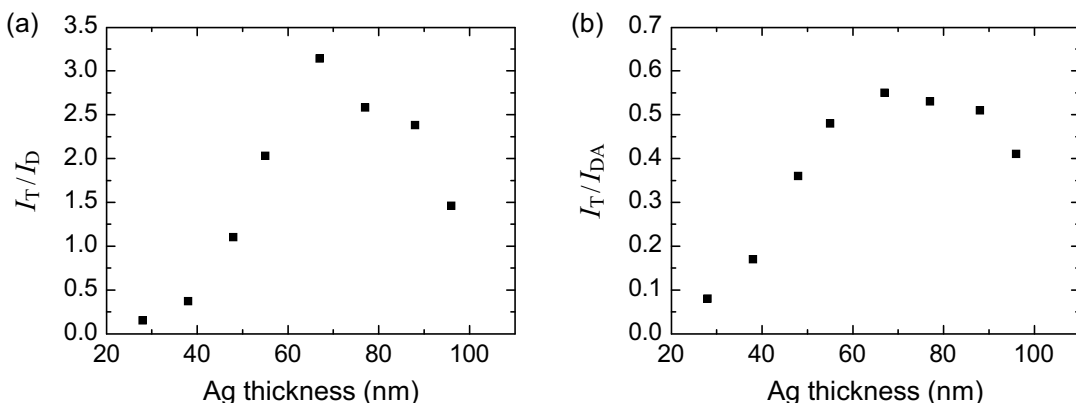


Figure 7.7: (a) Ratio of additionally transferred intensity I_T to donor intensity I_D . (b) Fraction of I_T to the total intensity I_{DA} of samples containing both donors and acceptors.

The dependence on the silver thickness is also obvious in Fig. 7.7(a) which shows the ratio of additionally transferred intensity I_T to donor intensity I_D . In the case of a silver thickness of 67 nm the additional emission I_T is more than three times as intense as the direct donor emission I_D . In other words, the emission in top direction is increased to the fourfold intensity by recovering SP losses if the direct laser excitation of the acceptor is disregarded as would be the case in an electrically driven OLED. Figure 7.7(b) shows the fraction of transferred intensity I_T to the overall intensity I_{DA} of the samples containing both donor and acceptor molecules. For the optimal Ag thickness of 67 nm around 55% of the total intensity in top direction is obtained by recovering SP losses.

It is remarkable that energy transfer between donor and acceptor occurs over a distance of more than 90 nm. This distance is considerably longer than in other transfer mechanisms like Dexter transfer (based on wave-function overlap with a range of approximately 1 nm) or Förster transfer (dipole-dipole interaction with a range of the order of 10 nm)^{105,169}.

It should also be emphasized that the ratio between green donor and red acceptor emission in samples of type C changes depending on the Ag thickness, as can be seen in Fig. 7.6. As a consequence, this provides a certain color tunability of the emission in top direction¹⁸⁹.

7.4.2. Measurement of excited state lifetime

In order to verify energy transfer from Alq_3 to LR, the lifetime of the excited dye molecules was determined by a streak camera system (Hamamatsu Photonics K.K.). For that purpose, samples with a silver thickness of 67 nm were excited by a pulsed nitrogen laser (MNL 200, LTB Lasertechnik Berlin GmbH, 20 Hz repetition rate and 1.2 ns pulse length) coupled with a dye in an automated tuning module so that an

excitation wavelength of 375 nm similar to the experiments above was obtained. The time dependent spectral intensities are plotted in Fig. 7.8.

The measurements in part (a) and (c) of the figure show the lifetime of Alq₃ and LR molecules doped into PMMA next to a 67 nm thick silver layer, respectively, without any energy transfer effects. Obviously, the lifetime of LR is very short in comparison to Alq₃ in these samples. On the contrary, the measurement in Fig. 7.8(e) with SP mediated energy transfer clearly shows a long lifetime component in the spectral region dominated by acceptor emission. Moreover, the spectra which were derived from the measurement with the streak camera system are plotted in Figs. 7.8(b,d,f). It can be seen that the spectra plotted in Fig. 7.6(d) are well reproduced here with a different experimental setup which was used for lifetime measurements.

For a more detailed analysis, the time dependent spectral intensities are integrated over a certain wavelength range and displayed in Fig. 7.9. Integrating the intensities for the donor-only sample between 460 nm and 660 nm and performing a monoexponential fit yields a decay lifetime for Alq₃ in PMMA of 14.8 ns. This value is very close to the result of 14.7 ns obtained by Andrew and Barnes with a lower Alq₃ concentration and a thinner PMMA layer¹⁶⁹. For LR in the sample of type B a very short lifetime of 3.3 ns is found by integrating from 565 nm to 700 nm and using a monoexponential fit. It should be pointed out that the emission within the donor or acceptor layer arises from molecules with varying distances to the Ag interface, hence having different decay rates and lifetimes. Nevertheless, the intensity decay over time can be fitted reasonably well with a monoexponential fit.

As a result, LR decays significantly faster in comparison to Alq₃. On the other hand, if energy is transferred from Alq₃ to LR, it is expected that LR will also exhibit a long lifetime component of the order of the Alq₃ lifetime (if the transfer process mediated by SPs is assumed to occur on a much shorter timescale than the decay of both LR and Alq₃). The decay of sample C is integrated only between 600 nm and 700 nm in order to ensure that the emission intensity originates from LR and not from Alq₃. The result is plotted as black curve in Fig. 7.9. It is evident that LR does not decay with a lifetime of 3.3 ns in this case. Instead, the lifetime can be adequately fitted by assuming a biexponential decay with lifetimes of 3.3 ns and 14.8 ns. This can only be explained if LR is excited by the comparatively slowly decaying Alq₃. From Fig. 7.6 it can be seen that the direct emission of Alq₃ through the Ag layer is much too small in order to cause such a strong red acceptor emission. In addition, by comparing samples A and C it is apparent that there is almost no reduction in the Alq₃ emission intensity if LR is doped into PMMA so that the reabsorption of Alq₃ emission cannot be responsible for the excitation of LR. Consequently, it is very likely that the red acceptor is excited by SPs, which in turn were excited by green donor emission^{169,190}. Therefore, the investigation of excited state lifetimes provides strong evidence for successful near-field coupling, i.e. for the SP mediated energy transfer from Alq₃ to LR through a silver film.

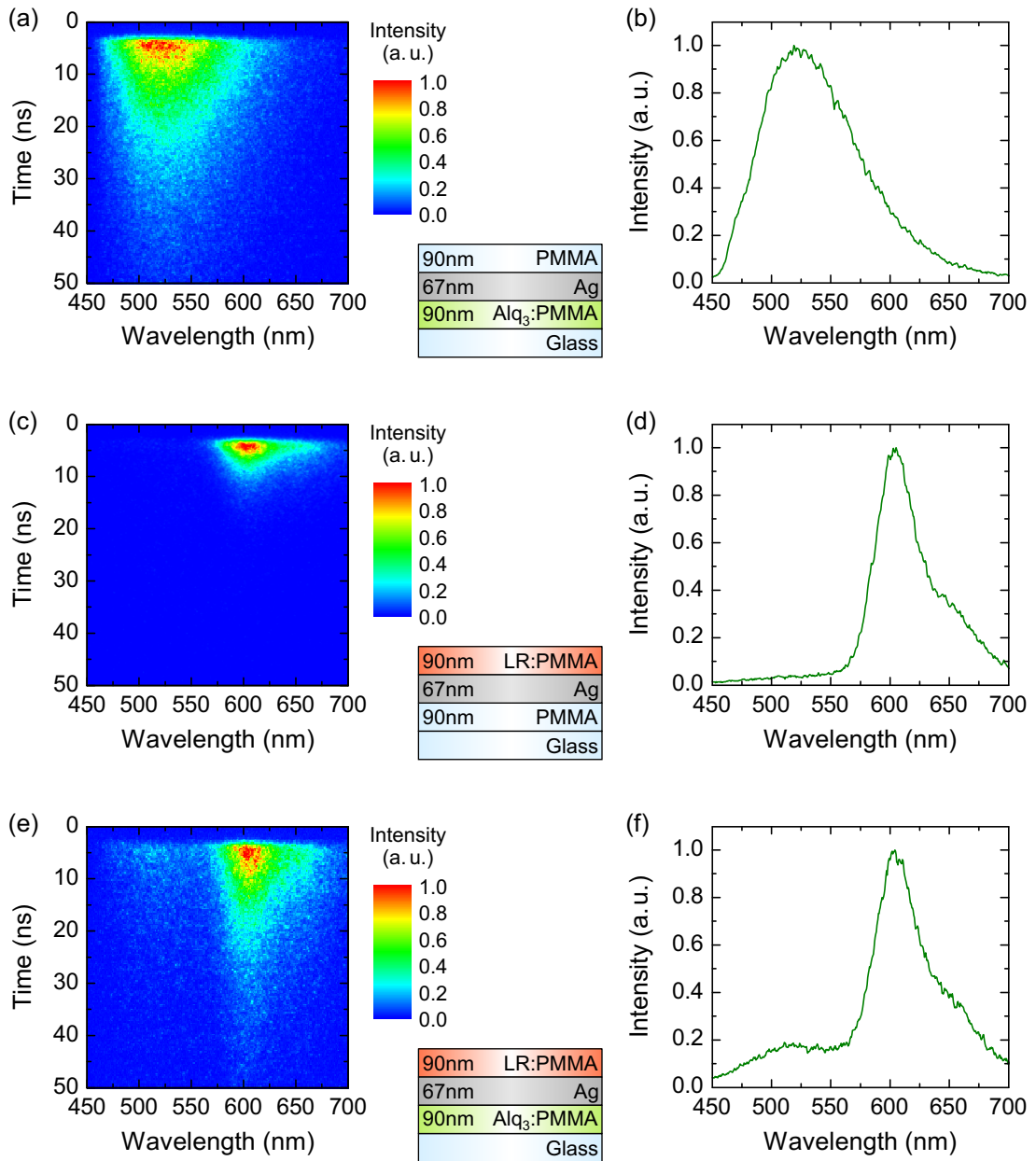


Figure 7.8: (a) Time dependent spectral intensity for a sample of type A (donor-only) with a Ag thickness of 67 nm. The excitation and measurement was done from the side containing the dye-doped PMMA layer in order to increase the detectable intensity. (b) Spectrum obtained by integrating over the measurement in (a) from 0 to 50 ns for each wavelength. (c,d) Similar to part (a,b) of the figure for a sample of type B containing only acceptor molecules. (e,f) Measurement of a sample with both donor and acceptor molecules (type C). In this case, the sample was excited from the donor side and the emission from the acceptor side was detected so that the measurement with SP mediated energy transfer is comparable to the results in Fig. 7.6. All graphs are scaled in order to maximize visualization within each graph.

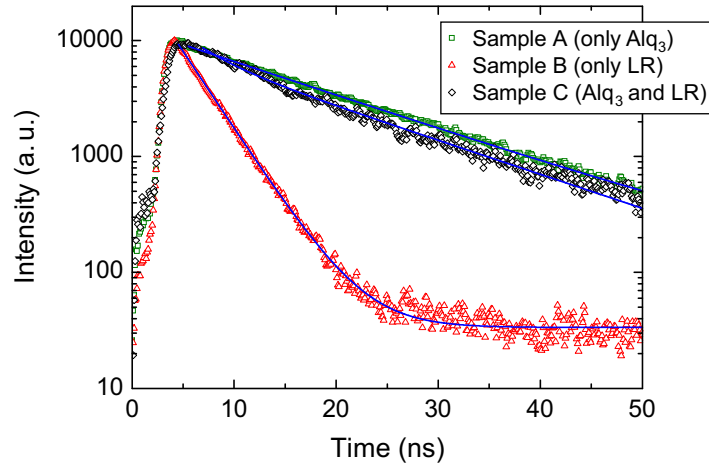


Figure 7.9: Time resolved intensity decay obtained by integrating over a certain wavelength range in Figs. 7.8(a,c,e). The green curve results from integration over the measurement in Fig. 7.8(a) from 460 nm to 660 nm. The red and black curves are obtained from integration over the measurements in Figs. 7.8(c) and (e) from 565 nm to 700 nm and from 600 nm to 700 nm, respectively. The blue lines represent mono- or biexponential fits to the curves as described in the text.

7.4.3. Estimation of extraction efficiency

Concerning the overall transfer efficiency it should be kept in mind that the direct transmission of light through a Ag layer with e.g. 67 nm thickness is very small. Thus, an increase to the fourfold intensity still corresponds to a low intensity. In order to quantify the overall efficiency, the emission in top direction was compared to the bottom emission of the donor Alq₃. For emission in normal direction it was found that, despite a partial recovery of SP losses, the total top emission represents just around 5% of the bottom emission. Hence, the additional SP mediated top emission amounts to only about 3% of the bottom emission. Consequently, the overall efficiency of near-field coupling is very limited.

The main reason for this is the complicated transfer process including several steps, i.e. SP excitation by the donor, coupling of SPs and excitation of acceptor molecules. Each of these steps limits the overall efficiency. Above all, the red acceptor has to be positioned close to the Ag layer so that it can be excited by SPs. As a matter of fact the excited red molecules in turn efficiently dissipate power in the red wavelength range to SPs at the Ag interface. This power is definitely lost and cannot be recovered. The ratio between top and bottom emission could be improved by choosing a smaller silver thickness. However, this also reduces the efficiency of energy transfer mediated by SPs.

The maximum efficiency obtained in this work agrees well with the result from Tien *et al.* who incorporated near-field coupling into complete OLEDs and found a maximum increase of 3%¹⁸⁹. The limited efficiency is further confirmed by Celebi *et al.* who calculated a maximum transfer efficiency of approximately 6%¹⁹¹.

7.5. Conclusions

In summary, the near-field coupling approach is an interesting technique for the recovery of power that was initially lost to SPs^{184,185}. It should be pointed out that the emission of the recycled power in top direction is unpolarized and nondispersive due to the intermediate step of exciting an acceptor dye. This method is particularly interesting for signage applications which often require emission in two directions. Furthermore, the emission color in top direction can be tuned by choosing a certain Ag thickness. For the application of near-field coupling to complete OLEDs it is simply required to add an acceptor layer on top of the OLED. This can also be achieved by co-evaporation of two organic materials. Moreover, the electrical characteristics of an OLED are not modified at all by this method.

Nonetheless, the SP extraction efficiency in this approach is strongly limited and seems to be insufficient for an application in OLEDs. Several measures could be taken in order to enhance the efficiency. For instance, the use of metallic nanoparticles with a limited absorption spectrum might help to reduce losses that arise because the acceptor again couples to SPs. Furthermore, grating structures can be utilized in order to enhance the transmission of energy through a thin metal layer^{186,187,190,192,193}. Especially a grating structure which is not identical on both sides of the silver layer is expected to enhance emission through the metal^{187,193}. It was also reported that metal films with subwavelength hole arrays show an enhanced transmission and also provide a periodic grating that supports coupling between dyes and SPs^{194,195}.

It should be emphasized that a periodic grating structure may directly transform bound SPs into propagating light. Therefore, such a structure can also be used without near-field coupling in order to enhance the bottom emission in case of a thick metallic film, as will be discussed in the following chapter.

8. Grating coupling

In this chapter it will be demonstrated that periodic grating structures may not only be used for coupling light into surface plasmons, as discussed in Sec. 4.3, but also for the reversed process of extracting SPs^{104,184,196}. In general, this is a very promising approach for recovering SP losses, which has already been discussed in literature, e.g. for gratings fabricated by laser interference lithography^{113,188}. After explaining the basic principle of grating coupling, the nanoimprint process will be introduced, which is a very convenient method to fabricate periodic gratings with high quality on a large area. Next, the outcoupling of SPs in simplified stacks under PL excitation will be presented by using line gratings with periods of 555 nm and 833 nm, respectively. In addition, it will be shown that these structures may also be applied to extract waveguide modes which are usually bound within a high-index region. Optical simulations will be used to calculate the dispersion relation of SPs and waveguides, which allows the identification of all scattered modes. Furthermore, it will be demonstrated that SPs can even be coupled out by means of a common digital versatile disc (DVD) structure. Finally, alternative methods for the production of periodic textures will be discussed and compared in terms of their applicability for large-area structuring.

8.1. Basic principle

In the context of planar interfaces, the SP wave vector \vec{k}_{SP} is always larger than the in-plane wave vector of light in the adjacent dielectric medium. Thus, no coupling between SPs and free-space radiation is possible, and power that is coupled to SPs is dissipated as heat and therefore lost. A very promising coupling method for recovering some of this power is to periodically corrugate the interface, e.g. by a grating with period λ_g , as shown in Fig. 8.1(a). Such a microstructure facilitates Bragg scattering of SPs, thus increasing or reducing the wave vector according to the relation^{104,186}

$$\vec{k}'_{\text{SP}} = \vec{k}_{\text{SP}} \pm m \cdot \vec{k}_g, \quad (8.1)$$

where \vec{k}'_{SP} describes the wave vector of the scattered SP mode, \vec{k}_g is the grating wave vector with $|\vec{k}_g| = k_g = 2\pi/\lambda_g$ and m is an integer that defines the order of the scattering process. Depending on the period of the grating and the order of scattering, it is possible to shift the SP dispersion partly into the air or glass light cone, as shown in Fig. 8.1(b). In other words, the grating vector associated with the periodicity in

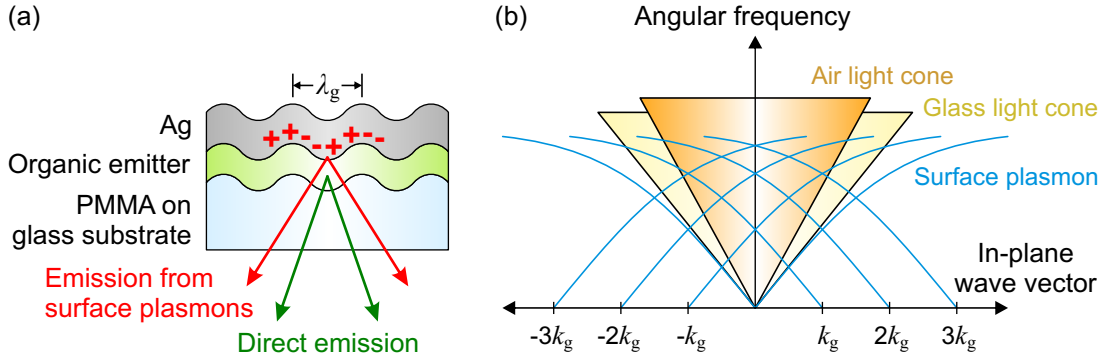


Figure 8.1: (a) Basic stack layout for the grating coupling approach. (b) Schematic dispersion of light and SPs in the case of periodically corrugated interfaces. Bragg scattering of SPs may occur, which shifts the SP wave vector by a multiple of the grating wave vector k_g . In general, band gaps may occur at crossing points of two diffracted modes. However, they are omitted in this simplified diagram for reasons of clarity.

the surface profile provides the missing momentum required to couple nonradiative SP modes and photons²⁵. Consequently, the energy and momentum conservation can be fulfilled for a range of frequencies. Therefore, SPs are allowed to couple to far-field radiation, i.e. $k'_{\text{SP}} = (2\pi/\lambda) \sin \theta$, with λ being the wavelength of light, and θ being the angle under which radiation is emitted into air¹⁸⁸. All in all, SPs on a periodically structured film can be considered as a radiative channel rather than simply as a loss, and some of the power dissipated to SPs can be recovered¹⁹⁷.

8.2. Nanoimprint fabrication of gratings and experimental setup

All gratings investigated in this study were fabricated by nanoimprint lithography¹⁹⁸. This technique facilitates patterning structures from micro to nano scales with high precision and on a large area. It is a low-cost and high-throughput process in comparison to other techniques such as laser interference lithography or electron beam writing¹⁹⁹. Generally, a hard mold that contains a surface relief structure is pressed into a polymeric resist film which is heated above its glass transition temperature T_g , thus transferring the grating structure into the polymer¹⁹⁸, as illustrated in Fig. 8.2. Then the temperature is reduced below T_g and the mold is detached. Afterwards, organic and metallic layers are evaporated on the sample in order to create the OLED-like layer structure. Table 8.1 lists the parameters of all devices which are studied in this chapter.

In detail, the process for devices 1–3 was carried out on cleaned microscope slides with a size of approximately $15 \times 15 \text{ mm}^2$. The samples were covered with PMMA (Sigma-Aldrich, $M_w = 350.000$) spin cast from a toluene solution to form a layer of about 450 nm thickness. Just before the imprint, the samples were heated on a hotplate to 150 °C,

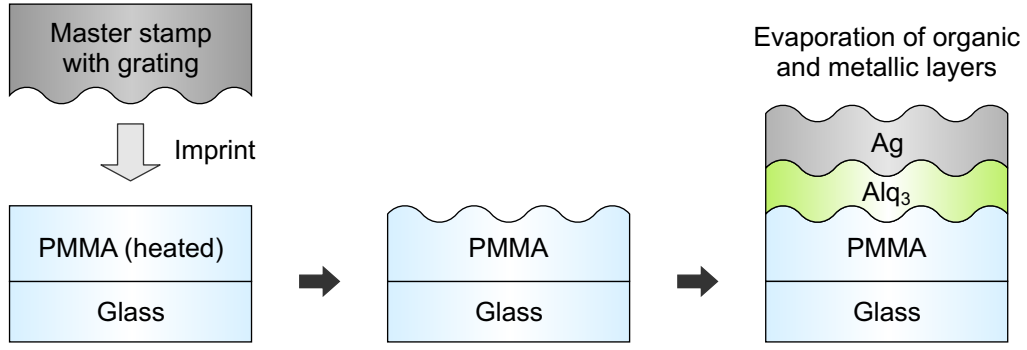


Figure 8.2: Illustration of imprint lithography and sample fabrication. The corrugation of the master stamp is transferred to a heated sample consisting of a PMMA layer on glass, producing a replica of the grating. In the last step, organic and metallic layers are deposited onto the PMMA grating.

which is above the glass transition temperature of PMMA ($T_g = 105^\circ\text{C}$). A pressure on the order of 50 MPa was applied for several minutes to transfer the microstructure into the PMMA layer. The molds used for the imprint process were commercially available diffraction gratings (Thorlabs, GH13-18V and GR13-1205) with a size of $12.7 \times 12.7 \text{ mm}^2$. The gratings comprise 1800 lines/mm (GH13-18V) or 1200 lines/mm (GR13-1205), corresponding to grating periods of 555 nm and 833 nm, respectively. No antisticking layer was used during the imprint. The Alq_3 and Ag layers were thermally evaporated under a vacuum of about 3×10^{-7} mbar at a rate of 1.2 and 1.5 $\text{\AA}/\text{s}$, respectively.

Device 4 demonstrates that it is possible to directly imprint the grating structure into the active layer. In this case, the yellow dye Lumogen Yellow (LY, BASF) was mixed at

Sample	Master stamp	Grating period	Imprint layer	Emitter material	Metallic capping
Device 1	Diffraction grating (GH13-18V)	555 nm	PMMA	30 nm Alq_3	150 nm Ag
Device 2	Diffraction grating (GR13-1205)	833 nm	PMMA	30 nm Alq_3	150 nm Ag
Device 3	Diffraction grating (GR13-1205)	833 nm	PMMA	200 nm Alq_3	180 nm Ag
Device 4	DVD mold	740 nm	180 nm LY:PMMA 5 wt%		150 nm Ag

Table 8.1: Overview of investigated devices. Devices 1–3 were fabricated by using commercial diffraction gratings (Thorlabs, part number given in brackets) as a stamp for the imprint process. Device 4 is based on the periodic structure of a DVD stamp, which was directly imprinted into the active layer (Lumogen Yellow doped into PMMA).

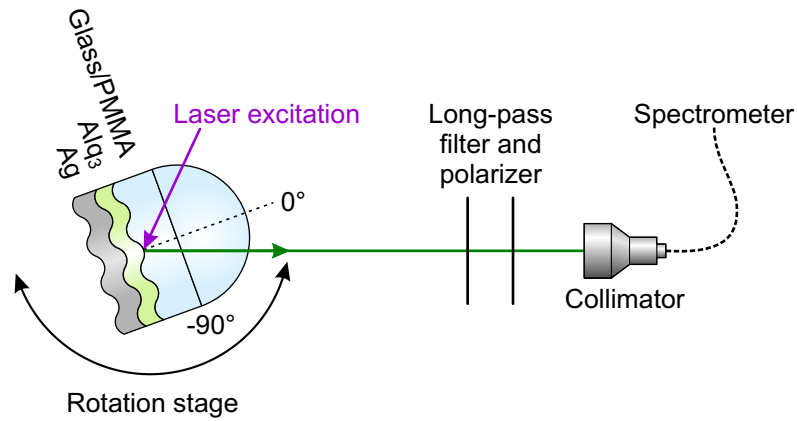


Figure 8.3: Experimental setup (top view) used for the grating coupling method. A 375 nm or 473 nm cw laser diode was used to excite the Alq₃ and LY molecules, respectively. Both the sample and the laser were mounted on a computer-controlled rotation stage. A half cylinder fused silica prism was attached to the substrate side of the samples for some measurements in order to additionally measure some of the light which is emitted into the glass light cone.

5 wt% with PMMA (micro resist technology, ready to use solution, $M_w = 75.000$) and spin cast onto a glass substrate to form a 180 nm thick layer. The mold used for the imprint process consisted of a nickel plate with a standard DVD pattern with 150 nm amplitude and a track pitch of 740 nm. The stamp was covered by a 3 nm titanium layer, which acts as an antisticking layer. During the imprint process, the sample was heated to 160 °C, then a pressure of 5 MPa was applied for 180 s. Afterwards, the sample was cooled down to 80 °C and the mold was released. Finally, 150 nm Ag were evaporated on the sample in the same way as for devices 1–3.

In order to determine the dispersion relation of extracted SPs and waveguides, it was necessary to measure the angular dependent emission intensity. For that purpose, the samples were mounted on a computer-controlled rotation stage, as depicted in Fig. 8.3. The grating grooves were oriented perpendicular to the plane of incidence so that SPs traveling approximately at right angle to the lines of the grating can scatter at the periodic corrugation and thus transform into free-space radiation.

The excitation laser was incident under 45° from the substrate side and rotated together with the sample so that the excitation condition was kept constant during the measurement. The Alq₃ layer in devices 1–3 was excited by a 375 nm cw laser diode. In the case of device 4, a 473 nm cw laser diode was used, which fits well to the absorption of LY. No special encapsulation was required because the Ag layer sufficiently protects the emitting molecules from oxygen and water.

The emission was measured from -90° to +30° in steps of 0.5° through a polarizer, because emission from SPs is expected to be p-polarized. However, it is noteworthy that emission from SPs can also appear as s-polarized light if the grating is not oriented perpendicular to the plane of incidence^{100,113}. Appropriate long-pass filters (400 nm or

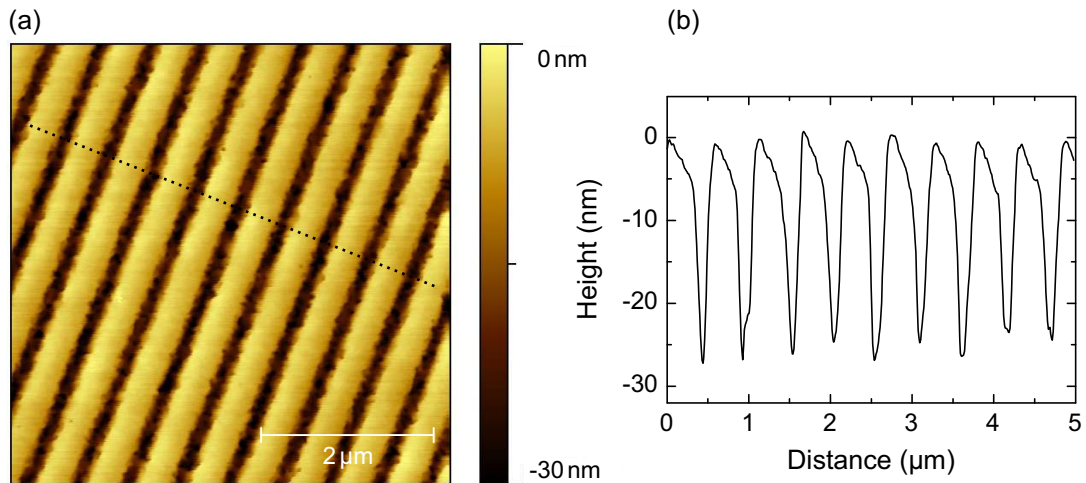


Figure 8.4: (a) AFM image of the structure obtained by imprint of a grating with 555 nm period into PMMA. (b) Profile at the position indicated by the dotted line in (a).

450 nm) were used to protect the spectrometer from the reflected laser beam.

From Fig. 8.1(b), it is obvious that scattered SPs with a specific frequency have fixed wave vectors. In other words, the scattered SPs will be coupled out at a certain angle that depends on the wavelength of the SP. Thus, it is expected that extracted SPs will show a strong angular dispersion in the measurement.

8.3. One-dimensional line gratings with 555 nm period

The first grating texture under investigation has a period of 555 nm. In this case, the grating wave vector is large enough to shift the SP dispersion into the air or glass light cone by first- or second-order scattering.

Figure 8.4(a) shows an atomic force microscopy (AFM) image of the periodic grating structure obtained after imprint into PMMA. The cross section presented in Fig. 8.4(b) illustrates the profile of the grating with an amplitude of up to 30 nm. The grating period deduced from the cross section is approximately 535 nm, which is close to the expected value of 555 nm based on the manufacturer information.

The sample investigated in this section is based on such a grating covered with 30 nm Alq_3 and 150 nm Ag. The chosen Alq_3 thickness is small enough to circumvent the excitation of waveguide modes. Hence, it is possible to exclusively study the extraction of SPs with this device layout.

In order to identify the extracted modes and the scattering order, the dispersion of SPs was calculated by means of optical simulations for the case of planar interfaces, cf. Fig. 8.5(b). The total power dissipation is plotted in Fig. 8.5(a). Obviously, a large fraction of the power is coupled to SPs because the emitter is located close to the Ag

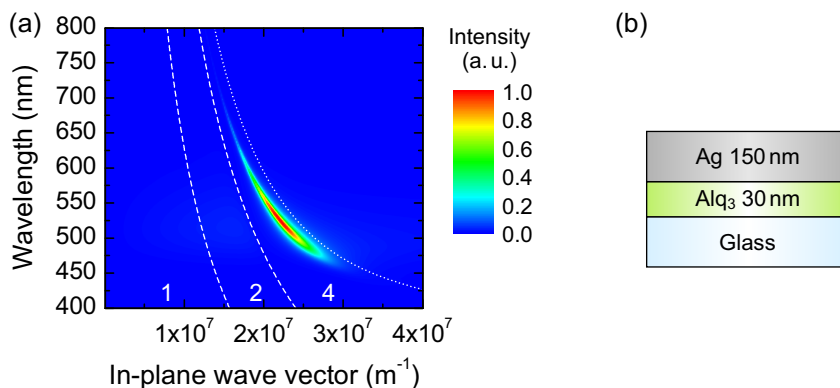


Figure 8.5: (a) Simulation of the total dissipated power in a stack as illustrated in part (b) of the figure. The PMMA layer is omitted because glass has almost the same refractive index as PMMA. An isotropic dipole orientation is assumed for the simulations, and the emitter position is centered in the Alq₃ layer. The dashed white lines divide the graph into different regions similar to Fig. 5.1(c). However, no waveguide modes exist in this case due to the thin Alq₃ layer. The dotted line was calculated using Eq. (4.15) assuming semi-infinite Ag and Alq₃ layers.

layer. It can also be seen that the SP dispersion is located at smaller wave vector values compared to the SP dispersion calculated by Eq. (4.15) for bulk Alq₃ and Ag layers. Here, the evanescent SP field partially penetrates into the adjacent PMMA/glass layer. Thus, the wave vector is based on an effective SP index of Alq₃ and PMMA/glass, as discussed in Sec. 7.1.

It is important to note that the simulations were performed for planar layers to obtain the SP dispersion relation for a non-corrugated sample. If the grating is relatively shallow, k_{SP} on the grating surface will be rather similar to k_{SP} on a planar surface^{100,113,200}. In order to compare simulations to experiments, the wave vector position of the SP dispersion for each wavelength was extracted from Fig. 8.5(a). The influence of the grating was then taken into account by adding or subtracting integer multiples of the grating wave vector according to Eq. (8.1).

Figure 8.6(a) shows the measured p-polarized emission of the corrugated device displayed in Fig. 8.6(b). Besides a small background of directly emitted light, there are several strongly dispersive features that result from scattered SPs which are transformed into visible light. It should be noted that no SP extraction was observable after rotating the grating by 90° so that it was parallel to the plane of incidence. This implies that at least a two-dimensional grating is required for the extraction of SPs traveling in different directions.

The lines in Fig. 8.6(a) correspond to the SP dispersion, which was obtained from the optical simulation in Fig. 8.5(a) and shifted according to Eq. (8.1) by a multiple m of the grating wave vector $k_g = (2\pi/555 \text{ nm})$. The measured and simulated angular positions of the scattered SPs agree very well. The emission intensity at 0° is determined by second-order scattered SPs. It is maximal around a wavelength of 520 nm, where the

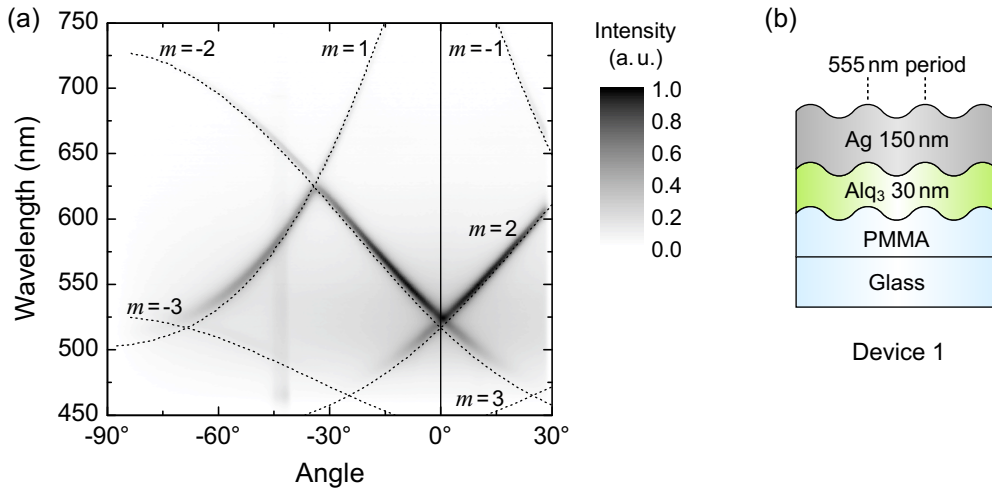


Figure 8.6: (a) Measurement of the p-polarized emission of device 1 (cf. part (b) of the figure). An angle of 0° corresponds to the surface normal in the bottom direction. The lines represent the SP dispersion obtained from optical simulations and shifted by a multiple m of the wave vector of a 555 nm grating. Negative values of m denote scattering of surface plasmons traveling in the positive in-plane wave vector direction and vice versa. The additionally detected emission around -45° results from reflections of the incident laser beam.

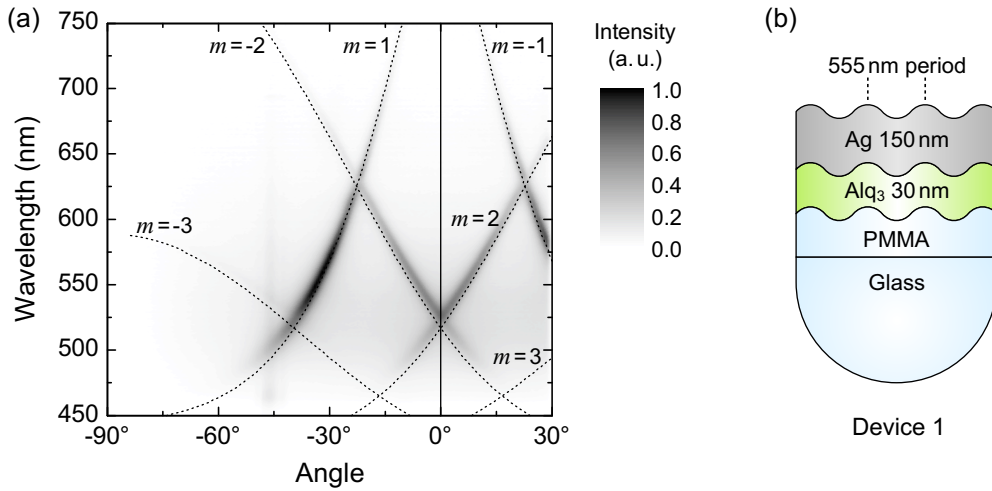


Figure 8.7: (a) Measurement similar to Fig. 8.6(a) except that a fused silica half cylinder prism was attached to device 1, as illustrated in the stack layout shown in (b). Thus, it is possible to additionally extract some of the SPs which are scattered into the glass light cone.

branches of two scattered SPs, traveling in opposite directions, cross each other. First-order scattered SPs lie within the air light cone at larger angles. In order to extract SPs in the green wavelength range into the normal direction by first-order scattering, a grating period of roughly 300 nm would be required.

Figure 8.7(a) shows a measurement of the same sample with outcoupling enhancement, as depicted in Fig. 8.7(b). For this purpose, a fused silica half cylinder prism

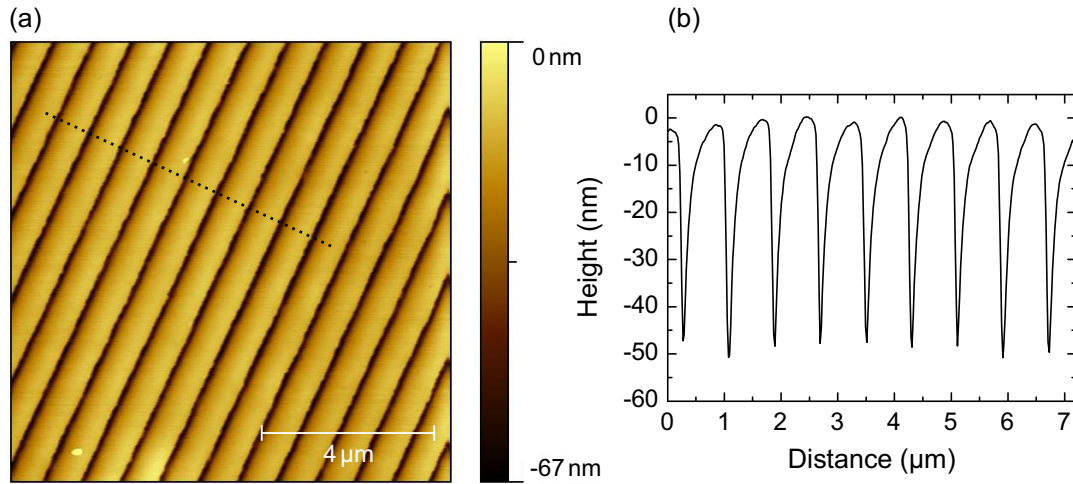


Figure 8.8: (a) AFM image of the structure obtained by imprint of a grating with 833 nm period into a PMMA layer. (b) Profile at the position indicated by the dotted line in (a).

was attached to the glass substrate with index-matching liquid. Thus, the total internal reflection at the interface between glass and air is avoided, and it is possible to extract scattered modes within the glass light cone. Consequently, a mode with a certain scattering order from Fig. 8.6(a) is located at smaller angles in Fig. 8.7(a). In addition, it can be seen that the first-order scattered mode has a higher intensity and can be also extracted for shorter wavelengths. However, the integral intensity of all extracted modes is not significantly changed by applying an outcoupling prism to this sample. Thus, a large fraction of the scattered SPs can be extracted without using an outcoupling enhancement. This makes the grating coupling method especially well suited for applications in flat, large area OLEDs, although additional scattering layers or scattering foils are necessary to transform the angular dispersive SP emission into isotropically emitted radiation.

8.4. One-dimensional line gratings with 833 nm period

Typically, the grating period used in the context of SPs is in the range between about 300 nm and 600 nm^{157, 158, 160, 161, 186–188, 201, 202}. By using such a structure, the SP dispersion is shifted into the air or glass light cone by a low-order scattering process, as presented in the previous section. Here, it is demonstrated that even periods above 800 nm, i.e. almost μm scale, effectively transform surface plasmons into visible light in a scattering process with higher order¹⁹⁶.

Figure 8.8(a) shows a $10 \times 10 \mu\text{m}^2$ AFM image of the topography obtained by imprinting the grating with 833 nm period into PMMA. The structure has almost no contamination and good long range order. The profile presented in Fig. 8.8(b) illus-

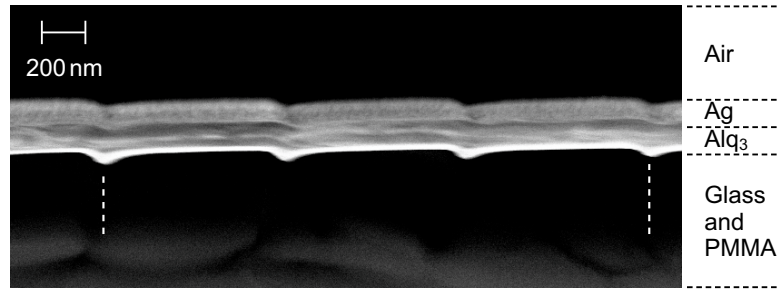


Figure 8.9: SEM cross section image of the grating from Fig. 8.8(a) covered with 200 nm Alq_3 and 180 nm Ag. An average period of about 840 nm is deduced from the distance between the two dashed lines.

trates that the grating has an amplitude of around 50 nm. The grating period deduced from the profile is approximately 810 nm, which is close to the expected value of 833 nm based on the grating manufacturer information.

The AFM image was obtained before evaporation of organic and metallic layers. The structure and amplitude was virtually the same after deposition of Alq_3 and Ag except for a superposition of small Ag islands, which were created during the fabrication of the thick Ag layer.

In general, the distribution of the field intensity within the stack is important, i.e. it must be high in regions where the grating is located^{135,157,203}. However, this is more important in polymer OLEDs, because spin coating of a polymer may planarize the textured surface. In contrast, the periodic modulation in small molecule OLEDs usually is preserved upon evaporation of each layer^{10,160,203}.

In order to demonstrate that the grating is transferred from the structured PMMA layer to Alq_3 and Ag, a scanning electron microscope (SEM) image of a cleaved edge is presented in Fig. 8.9. The sample in the image represents a complete device with approximately 200 nm Alq_3 and 180 nm Ag. The extraction of SPs in this sample will be analyzed in Sec. 8.4.2. The SEM image clearly demonstrates that all deposited layers above the textured PMMA film adopt the periodic structure. In addition, the periodicity of the grating can also be deduced from the SEM image. An average grating period of approximately 840 nm is obtained, which again agrees well with the expected value.

It is also noteworthy that the propagation length of SPs must be large enough to interact with the grating. A value for the propagation length of around $2.3\ \mu\text{m}$ is obtained for a planar interface between silver and a typical organic material. However, for other metals than silver, e.g. aluminum, the propagation length usually is smaller¹⁶⁰, hence a worse extraction efficiency might be expected. In the context of waveguide modes, it is important that the absorption in the waveguide region is as low as possible in order to enhance the propagation length of the guided modes, thus increasing the number of grating periods which the waveguided light may interact with¹⁵⁷.

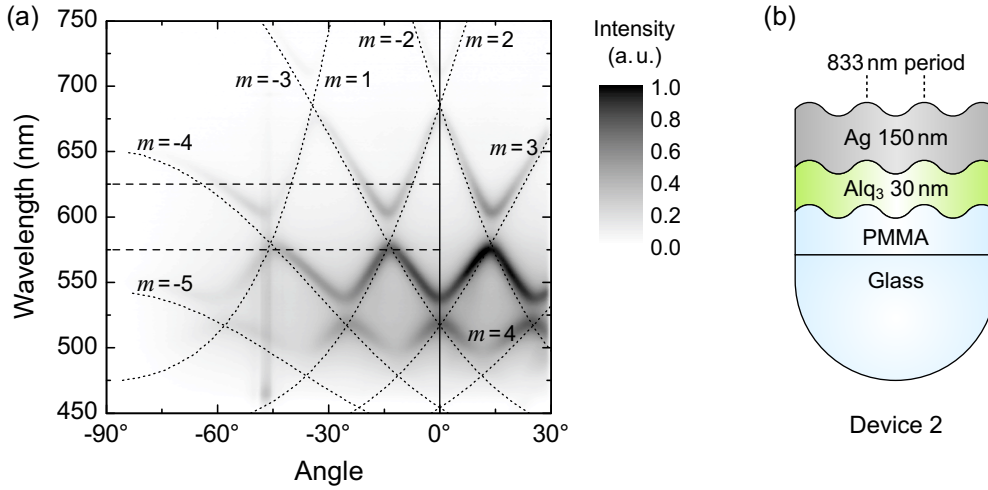


Figure 8.10: (a) Measurement of the p-polarized emission of device 2 (illustrated in part (b) of the figure). A half cylinder prism was attached to the sample, so that not only the scattered modes within the air light cone, but also those within the glass light cone, can be extracted. The dotted lines represent the dispersion of surface plasmons obtained from Fig. 8.5(a) and shifted by a multiple m of the wave vector of a grating with 833 nm period. The additional emission around -47° results from reflections of the incident laser beam. The two horizontal dashed lines indicate the position of the cross sections shown in Fig. 8.11.

8.4.1. Extraction of surface plasmons

Prior to the discussion of the sample featuring a thick Alq_3 layer, this section contains the investigation of a sample with 30 nm Alq_3 and 150 nm Ag deposited onto a PMMA layer with an imprinted grating having a period of 833 nm. Hence, the sample differs from the one in Sec. 8.3 only by the grating period.

The measured p-polarized emission and the stack layout of the sample are presented in Fig. 8.10. Again, the SP dispersion obtained from the simulation in Fig. 8.5(a) is shifted by integer multiples of the grating wave vector according to Eq. (8.1) and is presented as dotted lines. The general agreement between the simulated and measured angular position of the scattered SPs is very good. Small deviations are probably caused by the fact that the SP dispersion is slightly influenced by the grating. In fact, with increasing grating amplitude the actual SP dispersion appears at smaller frequencies, i.e. larger wavelengths, compared to the dispersion on a planar interface²⁰⁰. This agrees with the relation of the measured and simulated SP dispersions in Fig. 8.10(a). In addition, deviations may arise from small errors concerning the period of the grating or the optical constants and thicknesses used in the simulation. Moreover, small deviations may occur if the grating is not aligned exactly perpendicular to the plane of incidence. It should be noted that Eq. (8.1) only gives information about the location of the scattered SPs whereas the intensity of the different orders may also depend on the actual geometry of the grating.

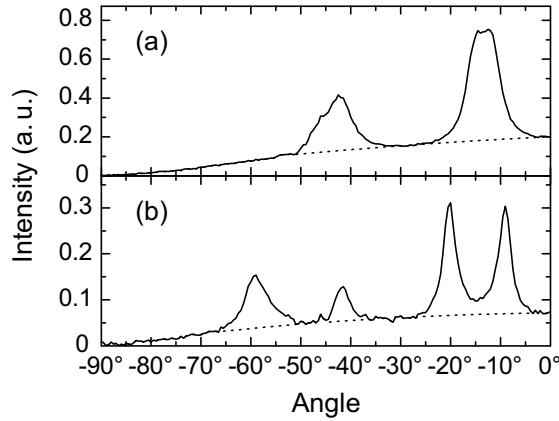


Figure 8.11: Cross sections of Fig. 8.10(a) at a wavelength of (a) 575 nm and (b) 625 nm. The dotted lines approximately indicate the contribution of directly emitted light. The slightly increased intensity around -47° due to the reflected laser, which was observed in Fig. 8.10(a), has been manually subtracted.

Comparing the result to the corresponding measurement of the sample with smaller period, shown in Fig. 8.7(a), it is apparent that more scattered SP modes are observable in the case of the grating with 833 nm period. Furthermore, a higher scattering order is required to extract SPs in normal direction. This can be explained by the fact that the grating wave vector $k_g = (2\pi/833 \text{ nm})$ is smaller by a factor of 1.5 compared to the samples comprising a grating with 555 nm period.

It is noteworthy that a strong SP emission is obtained although the period of the grating is almost on a μm scale. Usually, smaller periods are used so that first-order scattered SPs lie within the air light cone. Here, the larger period is compensated by higher order scattering. Actually, 5th-order scattering can still be detected and identified in Fig. 8.10(a). Therefore, it is anticipated that even gratings with such a large period, thus being easier and cheaper to fabricate, should be considered to be used as outcoupling enhancement in OLEDs. In addition, the occurrence of many diffracted modes may even offer an improvement concerning the color shift of the angular dispersive emission.

A rough estimation of the extraction efficiency can be achieved from an analysis at fixed wavelength and the comparison of directly emitted light versus extracted SPs. For that purpose, Fig. 8.11 shows cross sections of Fig. 8.10(a) at 575 nm and 625 nm. The wavelengths are chosen in such a way that there is almost no SP emission at 0° . Hence, the intensity at this point can be attributed to directly emitted light. The results differ inasmuch as Fig. 8.11(a) shows a cross section close to a point where two diffracted waves having almost the same emission angle overlap, while four distinct peaks are observable in Fig. 8.11(b).

By integrating over the cross sections it is found that the emission arising from extracted SPs amounts to around 70 % of the fraction of directly emitted p-polarized light.

It should be stressed that this value does not correspond to the extraction efficiency of SPs because it is not known to what extent the emitting molecules couple to SPs and to direct emission, even though the coupling to SPs is expected to be the dominant loss channel. For an accurate determination of the extraction efficiency, it would be favorable to use an optical simulation that takes into account structured interfaces with different periods and amplitudes. It should be pointed out that a detailed investigation of the efficiency must also consider the fact that the incident laser can be scattered by the grating, which may considerably change the excitation conditions.

From the position of the peaks in Fig. 8.11(b), it is also possible to derive the grating period. By comparing the cross section to Fig. 8.10(a), it is found that the peaks at -9° and -41.5° originate from SPs propagating in the same direction but differing in the order of scattering by one. The same applies to the peaks at -20° and -59° . The corresponding in-plane wave vector values can be calculated using $k_x = (2\pi \cdot n/625 \text{ nm}) \cdot \sin \theta$ with the refractive index of fused silica of $n \approx 1.457$ at this wavelength. The difference in the values for the in-plane wave vector between two of these peaks is approximately $7.48 \times 10^6 \text{ m}^{-1}$, which corresponds to a grating period of around 840 nm, i.e. close to the value expected from the manufacturer information.

Taking a closer look at the p-polarized measurements of devices 1–3, it is apparent that several optical band gaps are observed at crossing points of two SP branches. In general, a band gap is created if SPs are back-scattered into the opposite propagation direction^{104,204,205}. In this case, the two counter-propagating SP modes set up a standing wave. In fact, two standing wave solutions with different surface charges and field distributions exist. Since they have different energies, a band gap is opened up^{25,204}. In order to scatter SPs in the opposite direction of propagation by means of a grating, the condition $2k_{\text{SP}} = \pm m \cdot k_g$ must be fulfilled¹⁰⁴, i.e. it is required that an integer multiple m of the grating wave vector k_g is equal to twice the SP wave vector k_{SP} . More details concerning the physical origin of photonic band gaps in the propagation of SPs on gratings can be found in Ref. [204]. Usually, the width and the frequency of the band gap depend on the grating shape and period^{200,206}.

8.4.2. Extraction of waveguide modes

The Alq₃ thickness of device 2 is too thin to support bound wave guide modes. In contrast, the thickness of device 3 was chosen such that the emitting molecules can couple to a sharp s-polarized waveguide mode besides excitation of SPs. This effect can also be observed in optical simulations. The total power dissipation of a stack almost similar to device 3, but with planar interfaces, is presented in Fig. 8.12(a). In contrast to the result shown for 30 nm thick Alq₃ in Fig. 8.5(a), the SP dispersion can be well reproduced by Eq. (4.15) assuming semi-infinite Ag and Alq₃ layers, because the exponentially decaying SP field mainly penetrates into the thick Alq₃ layer.

From the p-polarized emission shown in Fig. 8.13(a), it is obvious that the measure-

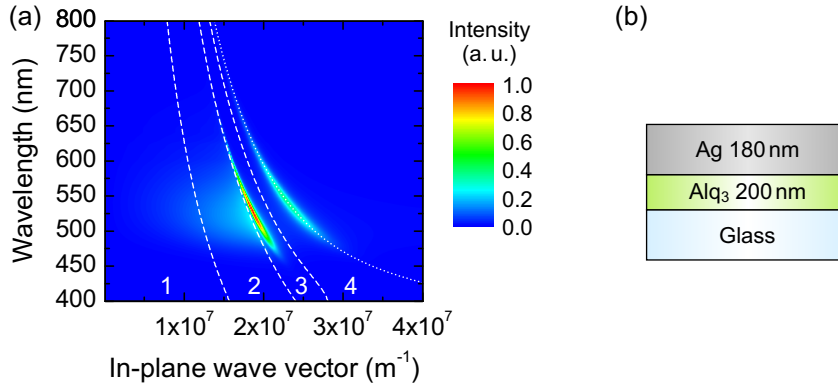


Figure 8.12: (a) Simulation of the total dissipated power similar to Fig. 8.5(a), but for a stack with 200 nm Alq_3 , as illustrated in part (b) of the figure. The dashed white lines divide the graph into different regions similar to Fig. 5.1(c). Besides strong coupling to SPs, a significant amount of power is dissipated into an s-polarized waveguide mode. The dotted line was calculated using Eq. (4.15) assuming semi-infinite Ag and Alq_3 layers.

ment basically looks similar to the emission of device 2. However, the SP dispersion is slightly different because it is determined by a 200 nm thick Alq_3 layer. Using the SP dispersion obtained from the simulation in Fig. 8.12(a), good agreement between the measured and simulated angular positions is obtained.

Here, no outcoupling prism was attached during the measurement of device 3. Therefore, only the modes scattered into the air light cone were accessible by the measurement. Thus, less scattered SP features are observable in Fig. 8.13(a) compared to Fig. 8.10(a). Nevertheless, this demonstrates that it is not necessarily required to attach outcoupling structures in order to extract SPs which are scattered at periodic gratings.

The measured s-polarized emission, displayed in Fig. 8.14(a), demonstrates that a sharp s-polarized waveguide mode exists in the 200 nm thick Alq_3 layer, as it has been expected from the optical simulation in Fig. 8.12(a). Similar to the case of SPs, it is possible that waveguide modes scatter at the periodic surface grating so that the dispersion is shifted into the air or glass light cone. Thus, also waveguide modes are partly transformed into freely propagating light and can be measured in the experiment.

For a comparison between simulation and experiment, the dispersion of the s-polarized waveguide mode is extracted from Fig. 8.12(a). Using Eq. (8.1) also for scattering of waveguides, very good agreement between the measured and simulated angular position is obtained. Scattering up to 4th-order is observed in the measurement. It should be emphasized that the full width at half maximum of the 2nd- and 3rd-order scattered modes typically is below 6 nm (at constant angle) and 2 degrees (at constant wavelength), respectively.

It is noteworthy that the absolute peak intensity is more than ten times larger for the s-polarized measurement in comparison to the measured p-polarized emission. Several reasons are responsible for this behavior. First, as noted above, the extracted s-polarized

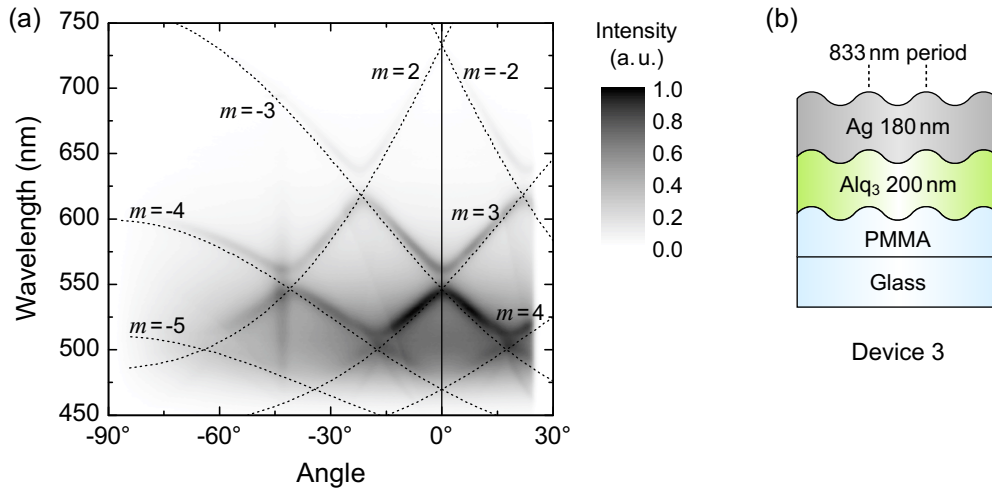


Figure 8.13: (a) Measured p-polarized emission of device 3 (shown in part (b) of the figure). The lines are obtained from the simulated dispersion of surface plasmons in Fig. 8.12(a) and shifted by a multiple of the grating wave vector $k_g = (2\pi/833 \text{ nm})$.

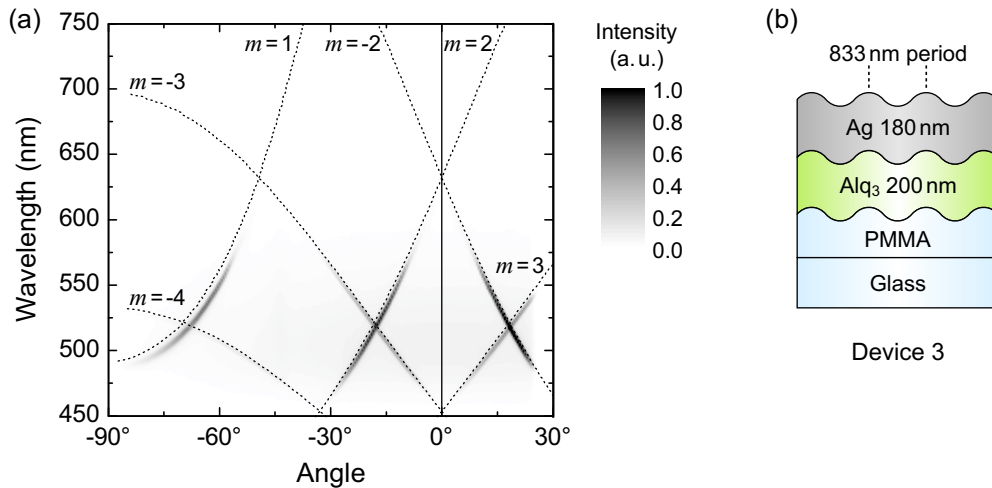


Figure 8.14: (a) Measured s-polarized emission of device 3 (shown in part (b) of the figure). The lines are obtained from the dispersion of the waveguide mode shown in Fig. 8.12(a) and shifted by a multiple of the wave vector of a grating with 833 nm period.

waveguide mode is considerably sharper in comparison to the SP mode. Furthermore, coupling to the s-polarized waveguide mode occurs through the whole 200 nm thick Alq₃ layer, while SPs are mainly excited from molecules close to the silver interface. Finally, since the laser is incident from the glass side, a large fraction of the laser intensity is already absorbed before molecules close to the silver are excited.

In addition to the s-polarized mode, there is also a very weak p-polarized waveguide mode, which emerges at short wavelengths in the measurement and simulation of device 3. However, this feature is hardly visible, and the simulated dispersion lines have thus been omitted in Fig. 8.13(a) for reasons of clarity.

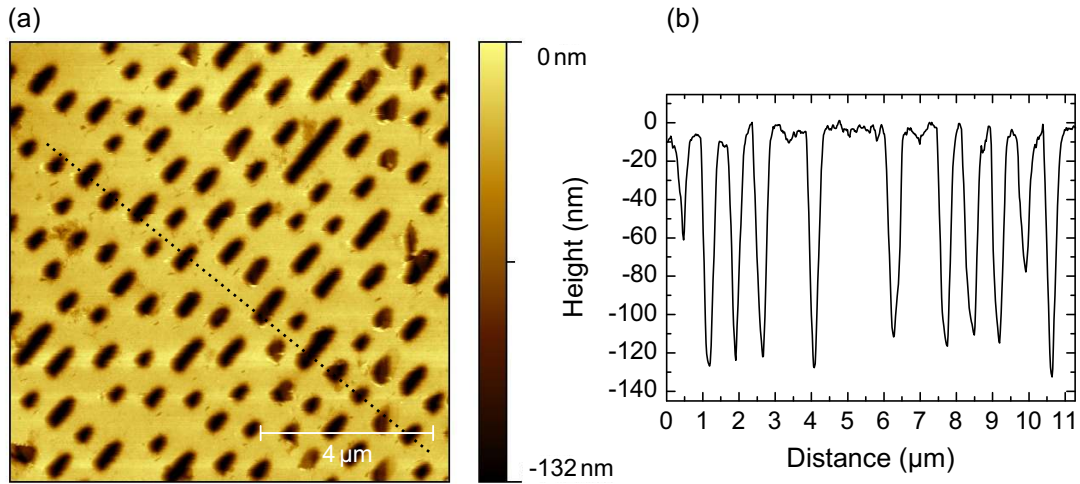


Figure 8.15: (a) AFM image after imprinting a DVD stamp into the LY:PMMA layer used in device 4. The DVD track runs diagonally from the top right to the bottom left corner. (b) Profile at the position indicated by the dotted line in (a).

8.5. DVD gratings

In order to demonstrate the general practicability of the imprint process, this section investigates a microstructured grating which is based on a common DVD stamp¹⁹⁶. Figure 8.15(a) presents an AFM image of device 4 after the imprint process, which shows the individual DVD tracks next to each other. Although each track is discontinuous, there is a periodic spacing between the tracks. This distance is known as track pitch and has a value of 740 nm in a DVD²⁰⁷. From the profile shown in Fig. 8.15(b), an average period of around 730 nm is obtained, which fits quite well to the track pitch.

The amplitude is found to have a value of up to 130 nm. The most efficient coupling between SPs and light occurs for a grating amplitude of some tens of nanometers²⁰⁸. Therefore, PEDOT/PSS was spin cast onto the sample. Since this polymer material is water based, PMMA is not dissolved again. Although the wetting of PEDOT/PSS is very bad on PMMA, the surface was smoothed and the holes were partially filled so that the amplitude was slightly reduced.

The measured p-polarized emission of device 4 is displayed in Fig. 8.16(a). Although the amplitude of the grating still is not optimal, several dispersive SP features can be distinguished. This is remarkable, considering that the individual grating lines are discontinuous and irregular. However, the periodic line pitch of the DVD structure appears to be sufficient to scatter SPs and extract them to some extent as visible light.

The theoretical SP dispersion is again calculated in a similar way as presented for devices 1–3. Here, SPs travel along the interface between Ag and PMMA at smaller wave vectors compared to all other devices, because PMMA has a smaller refractive index than Alq₃. It is noteworthy that no waveguide modes exist in this stack because

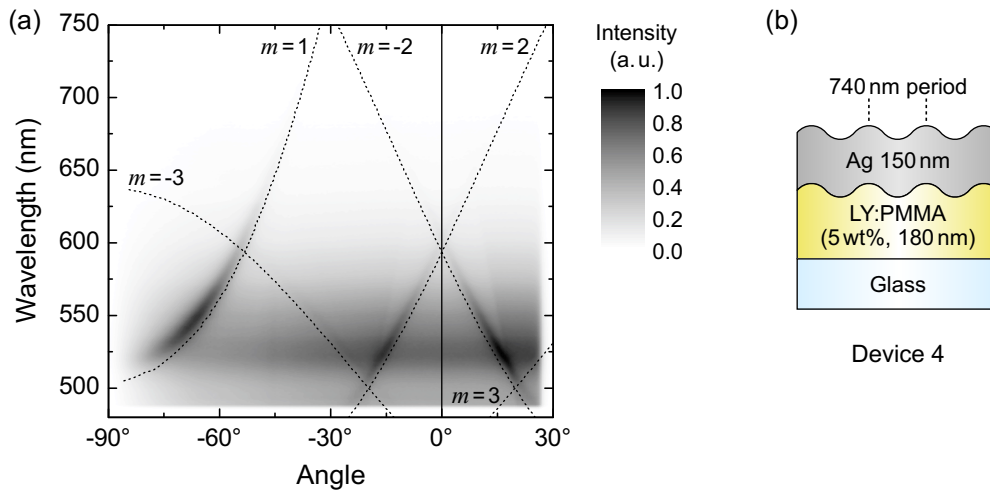


Figure 8.16: (a) Measurement of the p-polarized emission of device 4. The lines represent the SP dispersion obtained from a simulation of a planar version of device 4, which is shifted by a multiple of the wave vector of a 740 nm grating, i.e. corresponding to the track pitch of a DVD.

there is no total internal reflection between PMMA and glass since both materials have a quite similar refractive index, cf. optical constants in the appendix in Sec. A.2. By shifting the calculated SP dispersion by a multiple of the grating wave vector of a 740 nm grating, good agreement with the measured result is obtained, as shown by the lines in Fig. 8.16(a).

Certainly, a continuous grating with optimized amplitude would show a much more efficient SP extraction. However, the fact that the basic principle works even with a DVD structure indicates that SPs can be extracted even if some defects or irregularities occur during the fabrication process.

Further improvement concerning the color shift of the angular dispersive emission could be obtained by using a quasi-periodic structure with broad distribution and directional randomness, as reported for instance by Koo *et al.*, who made use of buckles which were spontaneously formed during cooling of a thin aluminum layer¹⁰. It should be noted that the fabrication of quasi-periodic layers is also compatible with the presented nanoimprint technique if an appropriate mold is used.

All in all, using a DVD stamp for the extraction of SPs demonstrates that it is indeed possible to fabricate gratings for optoelectronic devices with excellent quality on a large area at remarkably low cost, keeping in mind the quality, size and costs of commercially available DVD molds.

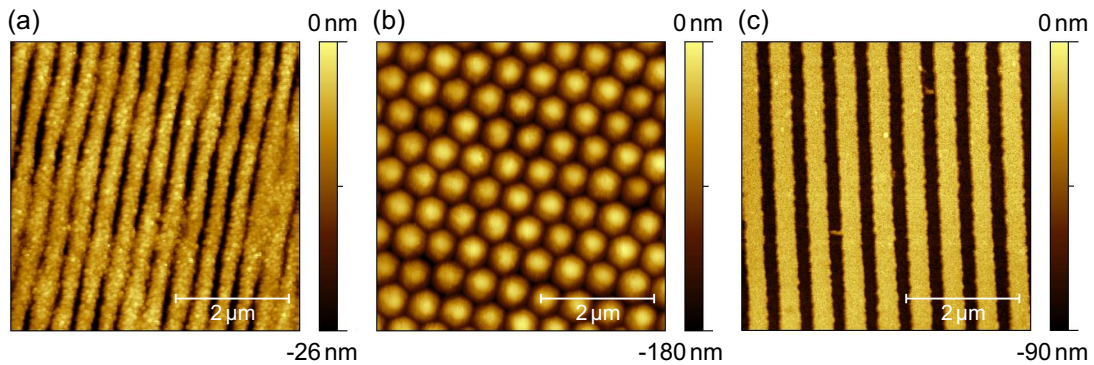


Figure 8.17: AFM images of periodic structures obtained from alternative fabrication methods. (a) Periodic line gratings produced by laser interference lithography (Klaus Huska, LTI Karlsruhe). The period and amplitude are about 400 nm and 20 nm, respectively. The image shows a sample that is already covered with Alq_3 and Ag, therefore small Ag islands can be observed. (b) Monolayer of polystyrene microspheres. The spheres have a diameter of about 600 nm. (c) Line gratings produced by electron beam lithography using PMMA resist and subsequent developing (Jörg Kinzel, University of Augsburg). The period of the grating is approximately 600 nm.

8.6. Alternative fabrication methods for periodically structured films

Besides nanoimprint, several other techniques were tested in order to create a periodic corrugation. This section briefly reviews the basic methods of three alternative approaches.

First, samples may be structured by laser interference lithography. In this method, a photoresist is exposed to a periodic light pattern created by the superposition of two expanded laser beams^{160,203}. Afterwards, the resist is developed to obtain the textured topography. This structure can also be used as a template for a subsequent etching process to structure the substrate^{110,113,188}. Figure 8.17(a) shows a periodic resist structure which can be directly used as a grating in experiments. Although the SP extraction basically works with such a sample, the result (not shown here) is worse in comparison to the line gratings discussed above. This is probably due to an imperfect grating with many defects in the samples under investigation. Nevertheless, this method represents a low-cost and large area scalable process. By rotating the sample during the fabrication process by 90° , it is even possible to fabricate two-dimensional gratings²⁰¹.

A second interesting approach is colloid monolayer lithography^{209–212}. Microspheres (e.g. made from polystyrene) are dispersed at a certain concentration in a fluid and are spread on a substrate. Depending on the inclination of the substrate and the environment, e.g. humidity and temperature, a monolayer of microspheres may be obtained. Such a structure with spheres having a diameter of about 600 nm is presented in Fig. 8.17(b). Here, the amplitude of the corrugation is probably too large to scatter SPs efficiently. However, it is possible to shrink the spheres in a plasma process²¹² and

to use the resulting template in a subsequent etching process in order to transfer the periodic structure into the substrate. Thus, the amplitude can be adjusted by the etching process. Altogether, the application of colloid monolayers basically offers a variety of sphere diameters and inherently results in a multi-dimensional periodic structure. However, in terms of cost and production time, probably other structuring methods should be preferred.

Finally, Fig. 8.17(c) shows a grating which was fabricated by electron beam lithography. In this case, the grating amplitude is very large so that a thin deposited Alq_3 film becomes discontinuous. Consequently, no SP extraction could be detected. Of course, by changing the fabrication conditions, it is possible to modify the amplitude, the period and the duty cycle, i.e. the ratio of the groove width with respect to the period. In general, this technique creates well defined grooves with sharp edges. Additionally, two-dimensional structures can be made. On the other hand, electron beam lithography is limited to rather small areas and has a low throughput. However, the high quality of this method can be applied to produce one master stamp, which is then repeatedly used in an imprint process.

It is noteworthy that nanoimprint is also compatible with a roll-to-roll process¹⁵⁹. Thus, it is possible to structure large areas in a very cost-efficient way. In addition, nanoimprint can produce two-dimensional structures if an appropriate master stamp is used.

8.7. Conclusions

In summary, this chapter studied the light outcoupling enhancement by extraction of surface plasmons and waveguide modes in OLED-like devices using imprinted grating structures with periods between 555 nm and 833 nm. Despite the comparatively large period of almost μm scale, extraction of SPs and waveguides by scattering up to 5th-order could be detected. The determined angular position of the extracted modes agrees very well with the dispersion relation of SPs and waveguides obtained from optical simulations, taking into account shifts by a multiple of the grating wave vector. This demonstrates that it is not always necessary to use gratings with a period below 500 nm, which are usually more expensive and complex in fabrication, although the application of such gratings could result in an increased extraction efficiency due to first-order scattering. On the other hand, an explicit advantage of gratings with larger period is the occurrence of more diffracted modes, hence the emission has less color shift.

In order to demonstrate the low-cost, high-quality and large-area applicability of grating structures in optoelectronic devices, SP extraction by means of a grating structure produced with a common DVD stamp was presented. The extraction efficiency could be further enhanced by optimizing the shape and amplitude of the grating.

It should be pointed out that grating coupling causes a strongly dispersive emission, which is undesired for most applications. Possible measures to solve this issue include the application of an additional layer that contains scattering particles or converter dyes to make the emission isotropic again. Furthermore, gratings with a broad distribution of periods and directional randomness can enhance light extraction without causing a dispersive emission.

Moreover, it is important to note that a corrugation can also have an influence on the charge carrier transport¹⁰. However, the optimal grating amplitude is only a few tens of nanometers versus a period of several hundred nanometers²⁰⁸, hence such a corrugation can still be regarded as shallow and the effect on the current-voltage characteristics should be limited.

Certainly, it would be interesting to determine the efficiency of transforming SPs into free-space radiation by using gratings fabricated by imprint. According to reports in literature, up to 80% of SPs propagating normal to a grating can be converted to light, as published in 1982 by Moreland *et al.*, who used holographic gratings with optimized amplitude²⁰⁸. This result was confirmed and extended in a more recent study by Worthing and Barnes, who obtained an efficiency up to 70% for converting SPs into radiation, even if the SPs travel at a certain angle with respect to the direction normal to the grating¹¹³. By using a grating which is structured in two dimensions, i.e. a bi-grating, they found that the total efficiency of coupling SPs to free-space radiation takes a mean value of 60%, independent of the SP propagation direction¹⁹⁷.

Therefore, grating coupling is definitely a very promising approach for recovering SP losses in OLEDs. Moreover, waveguide modes and to some extent even substrate modes can be coupled out. It is also noteworthy that this method extracts radiation in the bottom direction (i.e. in the same direction as the directly emitted light). Evidently, this is required for many applications in solid state lighting when the OLED is mounted to a wall or to the ceiling.

9. Prism coupling

Besides extracting surface plasmons and waveguide modes by a period grating structure, it is possible to directly transform bound SPs and waveguides into free-space radiation by the prism coupling method^{170,184}. In this technique, the Kretschmann configuration in a stack structure consisting for instance of glass/metal/organic/air is reversed. Guided modes and SPs are excited in the organic film or at the metallic cathode and then extracted through the finite metal film into the adjacent glass prism. Energy and momentum conservation are fulfilled as long as the refractive index on the glass side of the metal is larger than the effective index of organic and air, i.e. as long as the organic film is thin enough. Hence, SPs become radiative^{170,192}, and waveguides can be extracted as leaky modes.

This chapter first explains the basic principle of the prism coupling method. Afterwards, different metals will be studied in terms of their applicability for extracting SPs. Subsequently, the extraction of SPs and guided modes will be investigated by angular dependent PL measurements. The influence of the thickness of both the metal layer as well as the organic film will be analyzed in detail. In addition, the experimental findings will be compared to optical simulations in order to gain deeper insight into the physical processes that affect prism coupling.

9.1. Basic principle

The prism coupling technique is based on a reversed Kretschmann configuration^{104,170}, which was introduced in Sec. 4.3. The basic stack layout is illustrated in Fig. 9.1(a). Here, organic dye molecules on the bottom Ag side are excited by a laser and in turn couple via their near-field to SPs, which propagate at the interface between the organic film and Ag¹⁷⁰. If the organic layer is thin enough (i.e. only a few tens of nanometers), the evanescent SP field penetrates through this layer into the surrounding air. Therefore, the SP dispersion is not determined by the bulk refractive index of the organic material, but by an effective refractive index of organic and air. This value will be called “effective SP index” (cf. Sec. 7.1) in order to reflect that the weighting of the different indices depends on the field of the SPs. Since the dispersion now depends on the thickness of the organic layer, it is possible that the SP dispersion lies within the glass light cone, as depicted in Fig. 9.1(b). If the Ag layer is thin enough, the SPs on the bottom side can transform into free-space radiation in the upper glass medium, because energy and

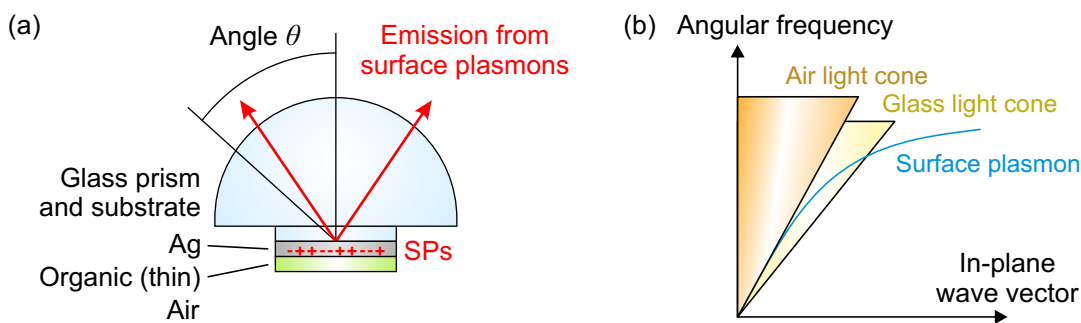


Figure 9.1: (a) Basic stack layout for the prism coupling approach. (b) Illustration of the air and glass light cones and schematic dispersion of SPs traveling at the interface between Ag and a thin organic layer. In the case of prism coupling, the organic layer must be sufficiently thin so that the effective SP index of organic and air on the bottom Ag side is smaller than the refractive index of the prism on the top Ag side.

momentum conservation between SPs and light traveling inside the glass can be fulfilled. Thus, energy lost to SPs can be recovered. The same applies to leaky modes, which propagate within the organic film and partially penetrate through the Ag layer into the glass substrate. By using an outcoupling prism, light that emerges from extracted SPs and leaky modes can be coupled out and measured.

It should be stressed that the prism coupling method does not require any surface structures, but even works for perfectly flat interfaces. However, it is also noteworthy that a grating structure could be implemented to facilitate coupling of an incident laser beam into SPs, which in turn are extracted into the prism¹⁹². In such a case, no dye molecules are required to excite SPs.

An instructive description of the principle can be given by studying the simulated absorption A under reversed optical path, i.e. light of a certain wavelength λ is incident through the prism and reflected at the silver/glass interface. The absorption is determined by $A = 1 - R - T$, where R and T represent the reflectance and transmittance, respectively. A transfer-matrix method, as described in Sec. 3.4, was used to compute R and T . The transmittance through the Ag layer is lower than 10% even if the angle θ inside the glass prism is close to normal incidence. For angles larger than the critical angle for total internal reflection between fused silica and air ($\theta_c = \arcsin(1/1.46) \approx 43.2^\circ$), no light is transmitted through the complete stack in bottom direction, resulting in $T = 0$. The basic idea behind this approach is to find a combination of incidence angle and organic layer thickness which permits coupling of light to a certain optical mode (i.e. SP or leaky mode) on the bottom Ag side.

The p- and s-polarized absorption in case of a 40 nm thick Ag layer are shown in Figs. 9.2(a) and (b), respectively. Obviously, absorption into SPs and leaky modes only occurs for angles $\theta > \theta_c$. This is due to the fact that no SPs and leaky modes exist within the air light cone, i.e. within the angular range of $0^\circ < \theta < \theta_c$. Therefore, all

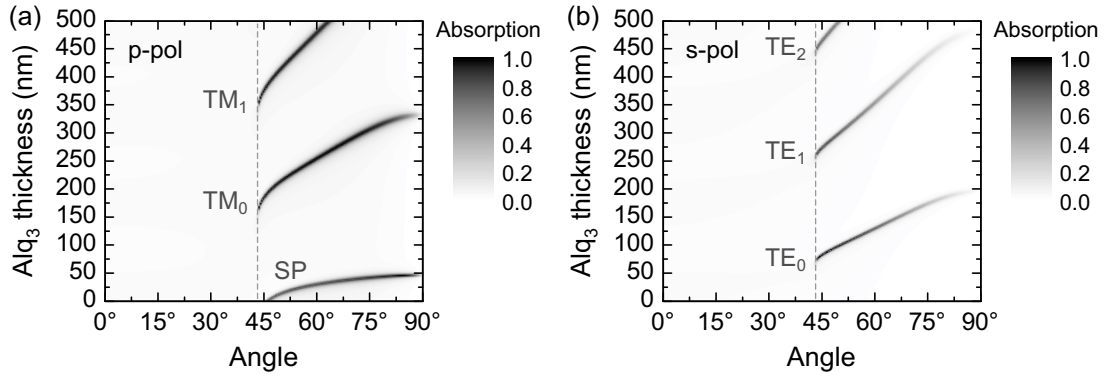


Figure 9.2: (a),(b) Calculated absorption of p- and s-polarized light, respectively, at a wavelength of 530 nm in a stack similar to Fig. 9.1(a) with a fused silica prism, a silver thickness of 40 nm, and Alq₃ as organic layer. Here, light is incident through the prism side. The absorption is plotted as a function of the angle inside the prism for varying thickness of the Alq₃ layer. Dark areas indicate coupling to SPs or leaky modes. TM_x and TE_x refer to p- and s-polarized modes, respectively, with x being the mode number. Surface plasmons are denoted by SP. The optical constants used for the calculation are $n = 1.46$ for the fused silica prism, $n = 0.06$ and $\kappa = 3.4$ for Ag, and $n = 1.73$ and $\kappa = 0.005$ for Alq₃. The vertical dashed line was calculated by $\arcsin(1/1.46)$, i.e. it represents the maximum propagation angle of light in air, converted to an angle inside the prism.

guided modes emerge at angles to the right of the dashed vertical line in Fig. 9.2. The SP mode starts at even slightly larger angles as a consequence of the SP dispersion relation.

In the p-polarized case, coupling of light into SPs is possible up to an Alq₃ thickness of roughly 50 nm (cf. also Fig. 7.2(d)). The excited SPs travel at the Ag/Alq₃ interface, thus their dispersion depends on the actual Alq₃ thickness. With increasing thickness, the resonance angle shifts to higher values. As soon as the effective SP index on the bottom Ag side gets larger than the refractive index of fused silica, the SP dispersion is shifted outside the glass light cone. Hence, the Kretschmann configuration is no more fulfilled and no coupling between light and SPs is possible.

For even thicker organic layers above approximately 160 nm, the incident light may couple to a guided mode (TM₀), which propagates inside the Alq₃ film between the interface to air and the partially reflecting Ag layer. The resonance angle for coupling into this mode is also shifted to larger angles with increasing thickness of the Alq₃ layer. This is in agreement with the transverse resonance condition, cf. Eq. (3.69). Above a certain Alq₃ thickness, the in-plane wave vector of the guided mode becomes larger than the glass light line. Consequently, coupling between incident radiation and the guided mode is no more possible. In case of the TM₀ mode, this happens if the thickness of Alq₃ gets larger than approximately 330 nm.

As a matter of course, no coupling to SPs occurs for s-polarized light. Therefore, no significant absorption is visible in Fig. 9.2(b) for Alq₃ thicknesses below 70 nm. For

a thicker layer, coupling to the first s-polarized guided mode (TE_0) becomes possible. The minimum required Alq_3 thickness for an s-polarized waveguide mode is lower than for p-polarized light, because the cut-off thickness for the s-polarized mode is smaller in comparison to the p-polarized case. It should be mentioned that the maximum absorption as well as the width of the resonance in Fig. 9.2 strongly depend on the Ag thickness.

The findings from the absorption study of p- and s-polarized light has important consequences for the reversed situation that occurs in a PL experiment, as presented in the following sections. In such a case, the organic molecules directly couple to SPs and guided modes. Hence, the optical path is inverted in comparison to the absorption of light incident from the prism side. Assuming that the same pathway which is taken by the radiation from an external light source to couple into SPs and guided modes is used by photons generated inside the organic layer to leave the device¹⁸⁰, the emission is expected to be strong at those angles, where the absorption is high in Fig. 9.2. Thus, depending on the thickness of the organic layer, the modes excited by the dye molecules are allowed to partially escape into the prism. Consequently, SPs become radiative under these circumstances, and waveguide modes can be extracted as leaky modes.

9.2. Sample preparation and experimental setup

In order to analyze the extracted SPs and leaky modes, it is necessary to measure the angular dependent emission intensity. The experimental setup used for the measurements is shown in Fig. 9.3. The samples were mounted on a computer-controlled rotation stage. The excitation laser was rotated together with the samples so that the excitation condition was kept constant during the measurement. In most experiments, the emission was measured in steps of 0.2° through a long-pass filter (400 nm cut-off wavelength) that protects the spectrometer from the laser beam.

The samples investigated in this chapter were fabricated on cleaned glass microscope slides. Silver was deposited either by thermal evaporation in a vacuum of around 2×10^{-7} mbar at a rate of 1.5 \AA/s , or by electron beam evaporation at a pressure of approximately 5×10^{-6} mbar at a rate of 1.0 \AA/s . It was exemplarily checked that the silver layer on glass is smooth enough in order to rule out grating effects. For both deposition methods, a root mean square roughness of less than 2 nm was determined by atomic force microscopy. To study the influence of the metal, gold and aluminum layers were also fabricated by electron beam evaporation similar to silver. The Alq_3 layers were prepared by thermal evaporation in a vacuum of typically 2×10^{-7} mbar at a rate of 1.2 \AA/s .

The glass substrate was attached to a half cylinder fused silica prism with index-matching liquid in order to extract light traveling inside the glass light cone. Because extracted SPs and leaky modes are polarized, the emission was measured with an ap-

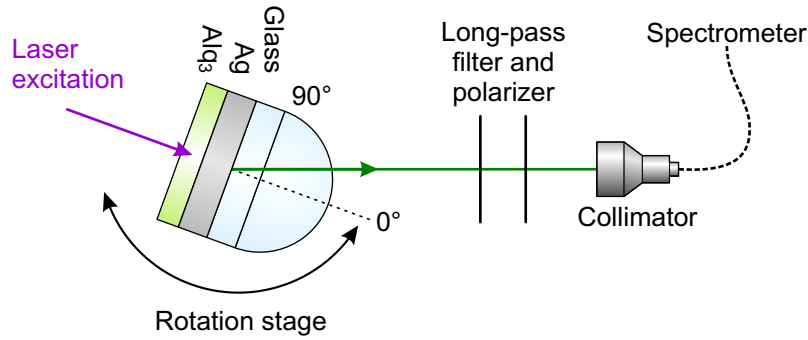


Figure 9.3: Experimental setup (top view) for the prism coupling method. A 375 nm cw laser diode was used to excite the Alq₃ layer. Both the sample and the laser were mounted on a computer-controlled rotation stage. A half cylinder fused silica prism was attached to the substrate side of the samples to extract light which is emitted into the glass light cone.

appropriate polarizer in order to distinguish between p- and s-polarized radiation. It is noteworthy that the specified angular values always refer to angles inside the fused silica prism. Since the dispersion of SPs and leaky modes lies at larger in-plane wave vector values than the air light line, the emission from SPs and leaky modes is coupled into the fused silica prism at angles larger than the critical angle between fused silica and air, i.e. angles larger than 43.2°. Accordingly, the measurements are plotted from 40° to 90°.

9.3. Extraction of surface plasmons

As discussed above, the thickness of the organic layers basically determines the type of mode, i.e. SP or leaky mode, which is accessible by the prism coupling method. This section discusses the extraction of SPs, while the outcoupling of leaky modes will be studied in Sec. 9.4.

Here, samples with varying Alq₃ and metal thicknesses were investigated in order to determine the influence of these parameters on the prism coupling method and to find the optimal conditions. However, first of all it is necessary to find the ideal metal, since the dispersion and absorption of SPs strongly depends on the optical constants of the metal layer.

9.3.1. Influence of different metals

In order to investigate the extraction of SPs and guided modes in PL experiments, it is essential to choose the right materials. In the context of the metal layer, promising materials are silver, aluminum and gold. The real and imaginary parts of the permittivities and their influence on the SP resonance were discussed in Sec. 4.2. From a theoretical point of view, Ag is the material of choice for studying SPs in the visible wavelength

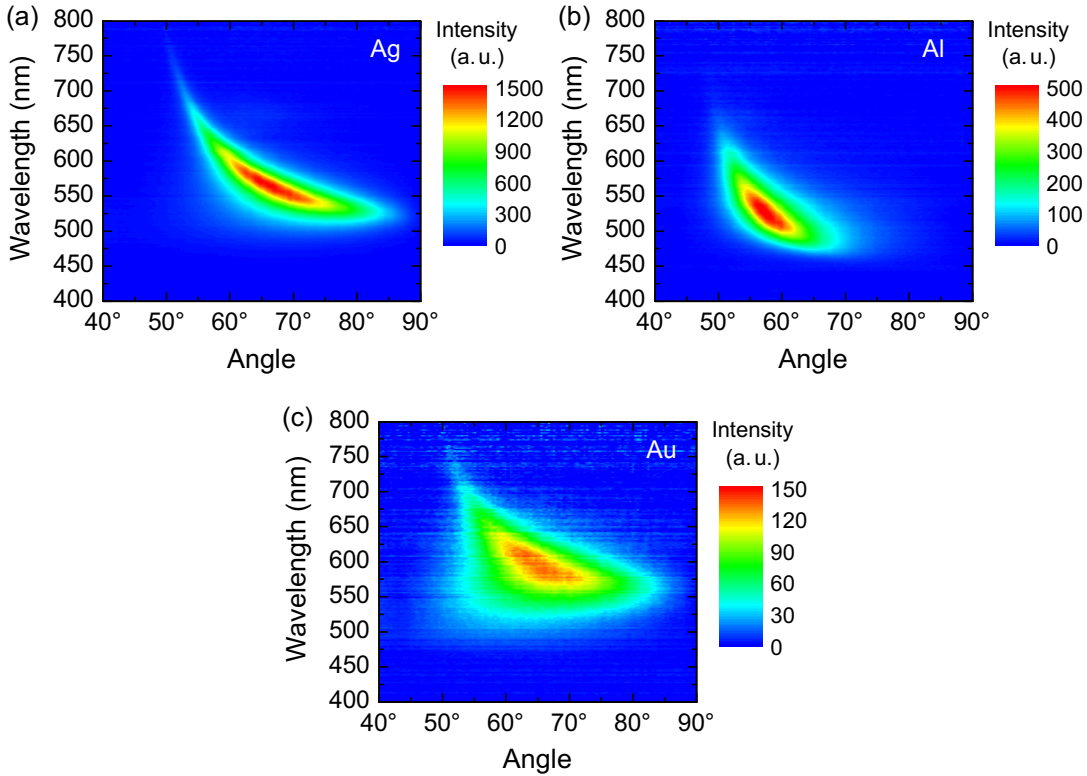


Figure 9.4: Measurement of the p-polarized emission in top direction in a stack according to Fig. 9.1(a) with approximately 30 nm Alq₃ and different metal layers: (a) 40 nm silver, (b) 20 nm aluminum, and (c) 40 nm gold.

regime, because Ag has the lowest damping.

Figure 9.4 displays measurements of extracted SPs for three different metal layers. The thickness of the Ag and Au films was 40 nm. On the contrary, only a 20 nm thin Al film was used, because optical simulations predict that the SP extraction is strongly reduced for thicker Al films due to the high absorption of this material.

For all three metals, an angular dispersive SP emission can clearly be observed. However, the position and intensity are different. In general, the emission angle increases with decreasing wavelength, because the SP dispersion is located further away from the air light line for higher frequencies²¹³. The SP emission angle is highest for the measurement with a Au layer and lowest for an Al film. In case of Au, no SP emission is observed in the blue wavelength range. In contrast, by using Al instead of Au, SPs can also be extracted for wavelengths below 500 nm. This behavior can be explained by the SP dispersion, cf. also Fig. 4.2. At a certain wavelength, SPs traveling at an Al/organic interface have the lowest wave vector, hence SPs emitted through the Al layer are located at smaller angles compared to Ag and Au.

Concerning the intensity of extracted SPs, it should be pointed out that the measured intensity depends on the precise adjustment and positioning of each sample, thus small variations in intensity of the order of 10 % between different measurements must be taken

into account. Nevertheless, it is obvious from Fig. 9.4 that the SP extraction is highest in case of Ag in this wavelength range, hence confirming the theoretical predictions.

Interestingly, the emission intensity seems to be related to the SP propagation length, which differs for Ag, Al and Au. In detail, SPs propagating at the interface between Ag and bulk organic typically have a propagation length of about $2.3\ \mu\text{m}$ at a wavelength of $550\ \text{nm}$ (cf. Sec. 4.2). The value for Al is slightly lower, about $1.5\ \mu\text{m}$, and in case of Au a propagation length below $0.1\ \mu\text{m}$ is obtained by using Eqs. (4.26) and (4.24) in combination with optical constants from the appendix. Certainly, for organic films with a finite thickness, the propagation length should be slightly higher, because the SP field penetrates into air and thus experiences less damping. Nevertheless, the calculated values have the same trend as the measured emission intensities in Fig. 9.4. Hence, it seems that a high propagation length, i.e. small SP damping, is a basic requirement for a good SP extraction efficiency in the prism coupling approach. In other words, if the propagation length is too short, SPs are partially damped and converted into heat before they can be extracted.

Altogether, the best result was obtained by using Ag as metal layer. In addition, Ag has the highest reflectivity of all metals in the visible wavelength range combined with an excellent conductivity, hence it is perfectly suited as electrode material in OLEDs. Therefore, all measurements presented in the following sections are based on samples featuring Ag as metal layer.

9.3.2. Variation of organic layer thickness

In order to study the influence of the organic layer thickness on the SP emission, Figs. 9.5(a)–(c) show the measured SP dispersion for three samples comprising $50\ \text{nm}$ Ag but different Alq_3 thicknesses of $20\ \text{nm}$, $30\ \text{nm}$, and $40\ \text{nm}$. It is obvious that the Alq_3 thickness determines the angular position of the extracted SPs. This agrees with the absorption in the case of a reversed optical path, as discussed above. A larger Alq_3 thickness corresponds to a higher SP wave vector, thus SPs are extracted at larger angles.

This is also apparent from the SP dispersions shown in Fig. 9.5(d), which were extracted from the measurements in Figs. 9.5(a)–(c). By comparing the experimentally determined emission angle at $530\ \text{nm}$ wavelength with the theoretical prediction in Fig. 9.2(a), it is found that the experimental position is always located at higher angles. The most probable explanation is that the true Alq_3 thickness in all samples is slightly larger than the supposed value. This is possible if the profilometer which was usually used for the thickness determination partially carves into the rather soft organic material.

Figure 9.6 presents a photograph of the sample with $50\ \text{nm}$ Ag and $20\ \text{nm}$ Alq_3 . By comparing the picture to the measurement shown in Fig. 9.5(a), the angular dependent SP dispersion is clearly visible. The red part of the SP dispersion is emitted at angles

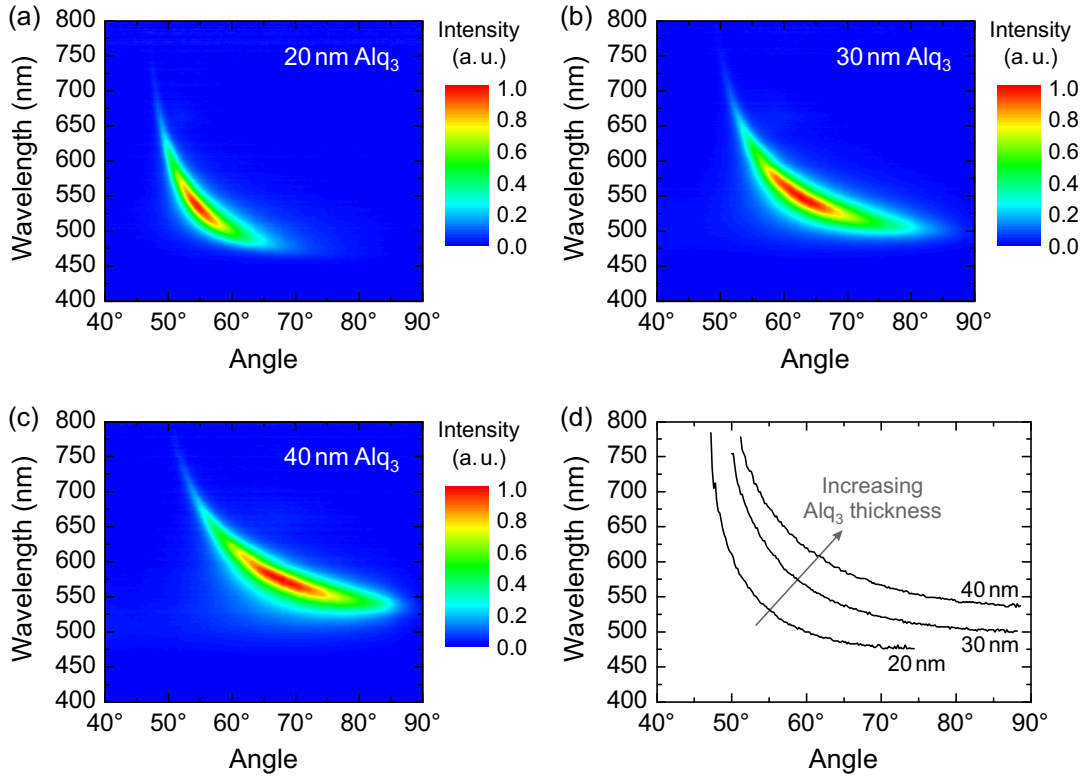


Figure 9.5: (a) Measured p-polarized emission in a structure similar to the basic stack layout of glass/Ag/Alq₃/air for different Alq₃ thicknesses. All samples comprise 50 nm Ag, but the Alq₃ thickness is (a) 20 nm, (b) 30 nm, and (c) 40 nm. (d) Dispersion of SPs obtained from parts (a)–(c) of this figure by determining the angle of maximum emission at each wavelength.

close to 50°, then the green wavelength range follows, and, finally, a long blue tail can be identified in the image at larger angles. Furthermore, the photograph demonstrates that the intensity of the SP emission into the prism has a similar order of magnitude as the direct emission of Alq₃ into air on the bottom Ag side.

It should be noted that the absolute intensity of the measured SP dispersions in Fig. 9.5 is hardly influenced by the Alq₃ thickness. On the contrary, it is expected that a variation of the Ag thickness strongly influences the extracted emission intensity in analogy to the discussion about near-field coupling, cf. Chapter 7. Therefore, the following section investigates samples with a fixed Alq₃ layer but different Ag thicknesses.

9.3.3. Variation of silver thickness

To investigate the influence of the Ag thickness in the prism coupling approach, a series of samples comprising a fixed Alq₃ thickness of approximately 30 nm and different Ag thicknesses between about 20 nm and 90 nm were prepared. Figure 9.7 shows the measured p-polarized emission for four exemplary Ag thicknesses. The dispersion of SPs, coupled out via prism coupling, can be clearly seen. To investigate the influence

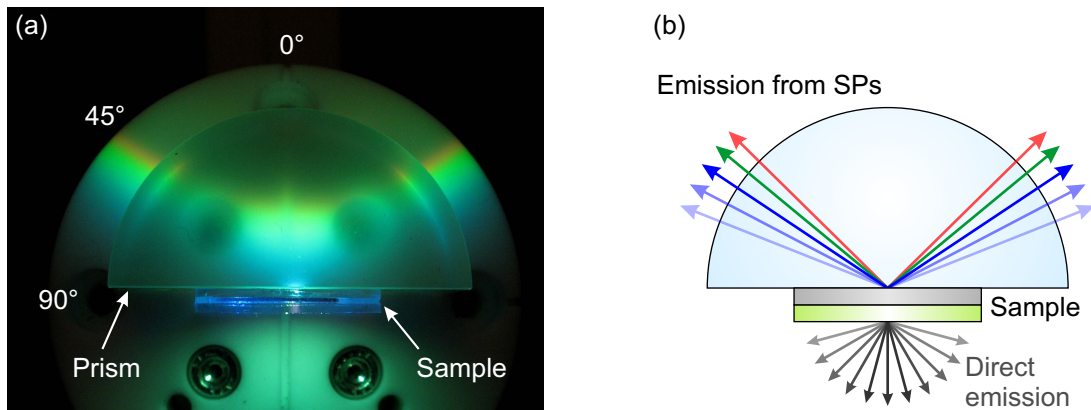


Figure 9.6: (a) Top view photograph of the sample with 50 nm Ag and 20 nm Alq₃. A half cylinder prism was attached to the sample, which was then placed on a white Teflon platform attached to the rotation stage. The corresponding angular dependent measurement is shown in Fig. 9.5(a). (b) Schematic illustration indicating the rather isotropic direct emission and the angular dispersive emission from SPs.

of the Ag thickness on the intensity of the extracted SPs in more detail, cross sections of the measurements at wavelengths of 530 nm and 625 nm are plotted in Fig. 9.8.

Several effects are observable in the measurements in Fig. 9.7 and in the cross sections in Fig. 9.8. First, the emission from SPs narrows with increasing Ag thickness²¹⁴. This is in particular apparent by comparing the width of the cross sections for samples with 40 nm, 50 nm, and 60 nm Ag. It can also be seen that the angular position in all measurements is almost similar. The deviation in angular position for the samples with 30 nm and 90 nm probably arises from an Alq₃ layer which is slightly thicker compared to the other samples. Finally, the peak intensity strongly depends on the Ag thickness. Although the denoted intensity values are subject to small variations depending on the positioning of each sample and due to possible differences in the exact thickness of the Alq₃ films, a clear trend is observable. Starting at a rather low value for the sample comprising a 20 nm thick Ag layer, the peak intensity rises with increasing Ag thickness and reaches a maximum at 50 nm Ag. For even larger thicknesses, the peak intensity decreases again.

Comparing the cross sections at 530 nm and 625 nm, it is apparent that the SP dispersion shifts to smaller angles with increasing wavelength. This can be explained by the fact that the SP dispersion is located closer to the air light line for lower frequencies. In addition, the dispersion becomes narrower with increasing wavelength, similar to the measurement of the SP dispersion using surface plasmon resonance. This effect is due to reduced damping at higher wavelengths.

The peak intensities of the cross sections at wavelengths of 530 nm and 625 nm are displayed as a function of the Ag thickness in Figs. 9.9(a) and (b), respectively. In the case of 530 nm emission wavelength, the highest peak emission is found at a Ag thickness of 50 nm. At 625 nm, the peak emission is slightly shifted to smaller thicknesses and

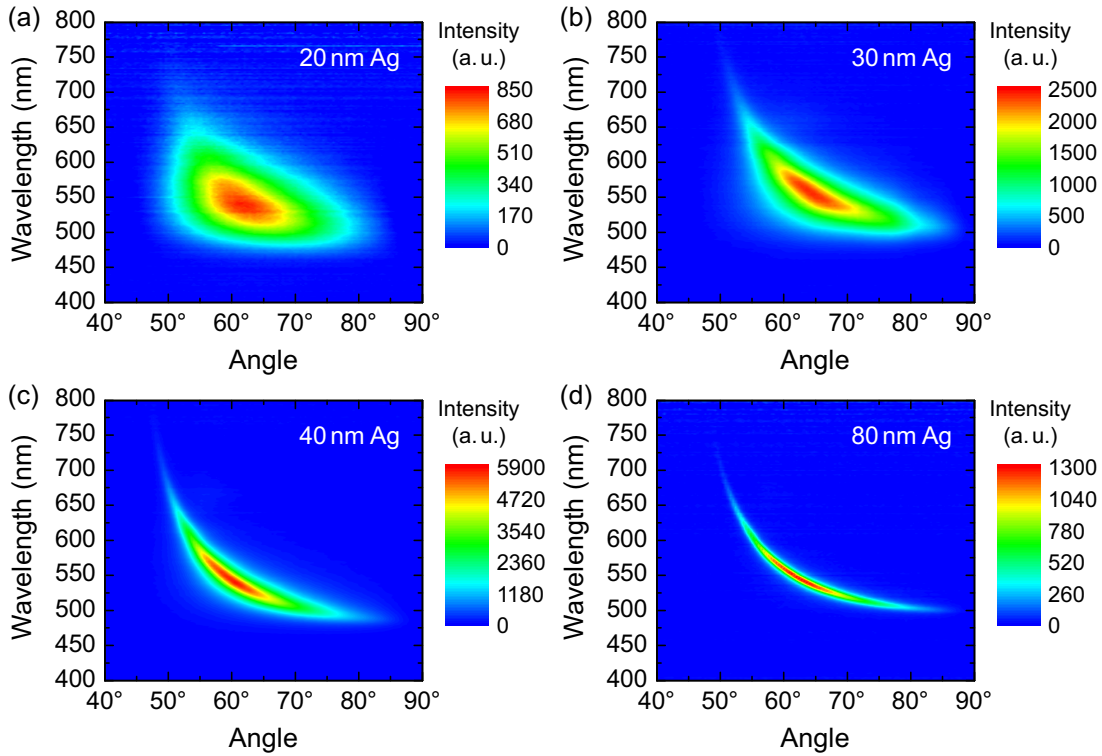


Figure 9.7: Measurement of the p-polarized emission for four exemplary Ag thicknesses in a structure similar to Fig. 9.1(a). All samples comprise around 30 nm Alq₃ but different Ag thicknesses as depicted in each graph. The stated thicknesses are rounded values, which will be used in the following for reasons of clarity. The actual thicknesses determined by profilometry are approximately 21 nm, 30 nm, 40 nm, and 78 nm.

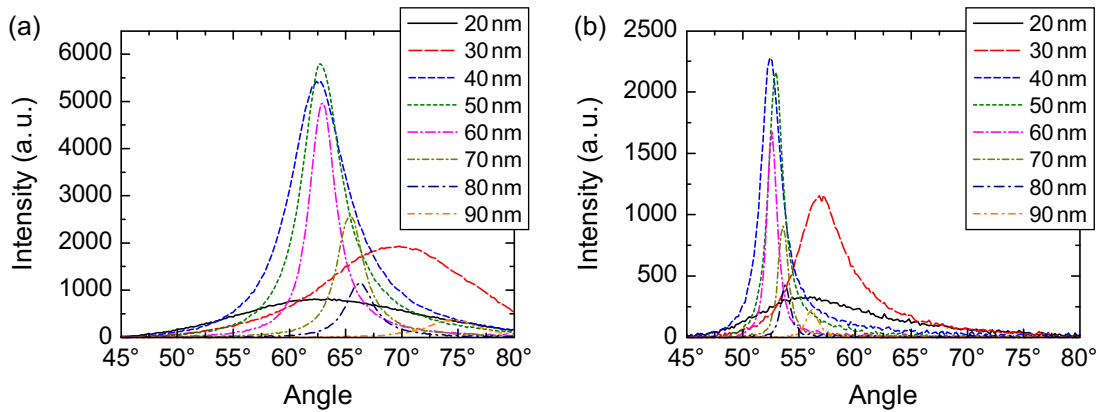


Figure 9.8: (a) Cross sections of the measurements in Figs. 9.7(a)–(d) at a wavelength of 530 nm, which is close to the emission maximum of Alq₃. (b) Cross sections similar to (a), but at a wavelength of 625 nm. In addition to the measurements of Fig. 9.7, the cross sections of four additional measurements are shown. The actual thicknesses determined by profilometry of these samples are approximately 49 nm, 59 nm, 67 nm, and 88 nm.

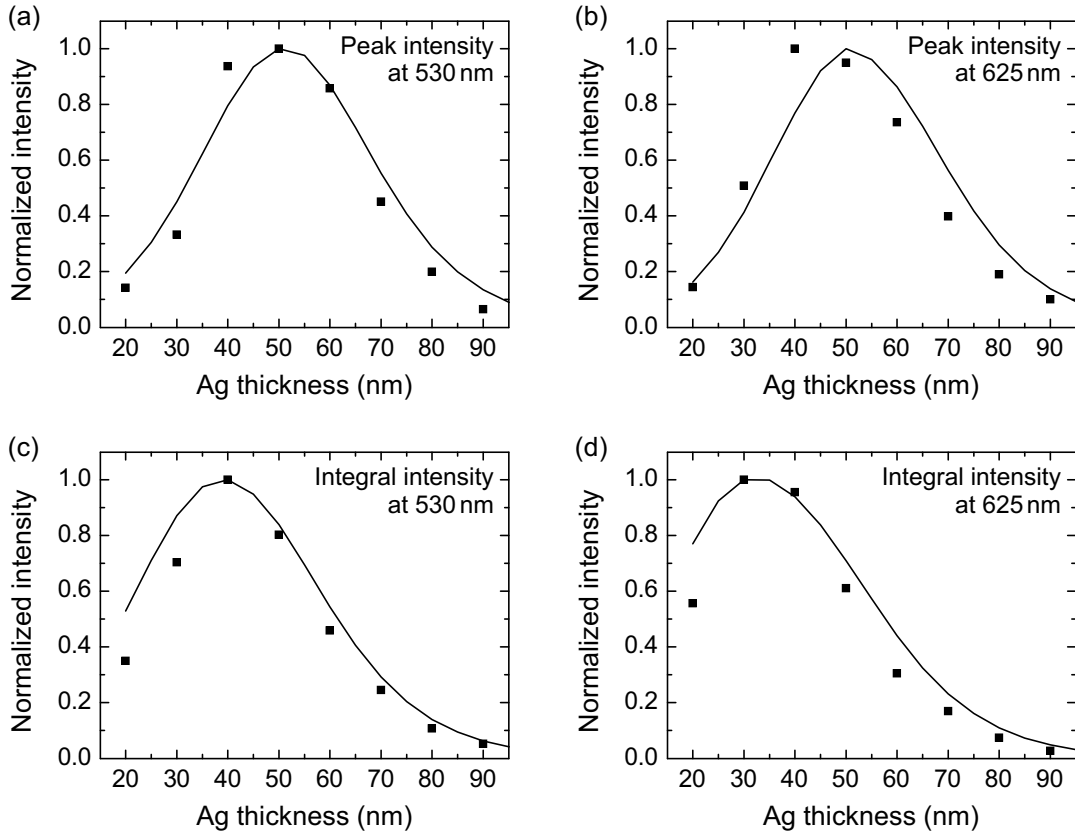


Figure 9.9: (a),(b) Measured peak intensities (square symbols) extracted from Figs. 9.8(a) and (b) at a wavelength of 530 nm and 625 nm, respectively. (c),(d) Integral intensities (square symbols) obtained by integrating the curves in Figs. 9.8(a) and (b) from 44° to 90° , respectively. The integration range corresponds to the area between the light lines of air and fused silica. Although the contribution of light that is directly transmitted through the Ag layer is very small anyway, the chosen range ensures that the contribution to the integral value mainly originates from SP emission. The lines were obtained from optical simulations for different Ag thicknesses in steps of 5 nm. Details regarding the simulations will be explained in Sec. 9.3.4.

already occurs at 40 nm. This basically agrees with the result obtained by Winter and Barnes, who found an almost similar thickness of around 50 nm for the highest peak emission at a wavelength of 625 nm ¹⁷⁰.

Winter and Barnes mainly analyzed the prism coupling method in the context of a potential application in biosensing¹⁷⁰. In order to use this method for an optimization of the light extraction from OLEDs, the integral intensity obtained at a certain Ag thickness should be considered instead of the peak intensity. Therefore, Figs. 9.9(c) and (d) display the intensities obtained by integrating the cross sections from 44° to 90° at wavelengths of 530 nm and 625 nm, respectively. It is important to point out that this result does not correspond to the total integral value over the complete hemisphere, which would require a multiplication with $\sin \theta$ prior to integration. Here, the angular peak positions basically should be located at the same angle, so that a weighting with

$\sin \theta$ would not alter the result significantly. Hence, a simple integration over the angular cross section is performed in order to analyze the influence of the Ag thickness.

The optimal value for highest integral intensity clearly shifts to a smaller Ag thickness of about 40 nm and 30 nm, respectively. This can be explained by the narrowing of the extracted SP dispersion with increasing Ag thickness. By comparing for instance the peak and integral intensities in Fig. 9.9 for samples containing 30 nm and 70 nm Ag, it is obvious that both samples have rather comparable peak intensities. However, the sample with a Ag thickness of 30 nm has a significantly larger integral intensity because the SP dispersion is much broader. Again, the optimal Ag thickness is smaller in the case of 625 nm wavelength compared to 530 nm. This trend is probably caused by the wavelength dependence of the optical constants of Ag, especially a larger extinction coefficient κ at higher wavelengths, cf. optical constants in Sec. A.2.

The appearance of a maximum at a certain Ag thickness can be explained by two competing effects¹⁷⁰. On the one hand, the amount of power coupled to SPs and the enhancement of the electric field at the metal surface increase with a larger Ag thickness. On the other hand, the SP field that transmits through the Ag layer is more attenuated with increasing Ag thickness. These effects will be explained more precisely in the context of optical simulations in the following section.

9.3.4. Comparison to optical simulations

The optical simulation routine which was introduced in Chapter 5 can be used to study the influence of the Ag thickness on the SP emission from a theoretical point of view. Figure 9.10 shows the simulated result for four exemplary Ag thicknesses. The overall agreement with the measured SP emission in Fig. 9.7 is very good. It should be noted that the thickness of Alq_3 was set to 32 nm in the simulations in order to reproduce the angular position of the SP dispersion from Fig. 9.7. Although this thickness is close to the experimentally determined value of 30 nm, it indicates that the thickness measured by profilometry might be slightly underestimated.

Figures 9.11(a) and (b) display the cross sections of the simulations at wavelengths of 530 nm and 625 nm, respectively. The result basically agrees with the experimentally determined cross sections in Fig. 9.8. Again, the narrowing with increasing Ag thicknesses is obvious, as well as the occurrence of an optimal Ag thickness for maximum peak and integral emission.

For a more detailed analysis, the Ag thickness was varied between 20 nm and 95 nm in steps of 5 nm. The peak and integral intensities, obtained by summation between 44° and 90° , were extracted at wavelengths of 530 nm and 625 nm. The result is shown together with the experimental values in Fig. 9.9. Apparently, the simulated result agrees very well with the measured peak and integral intensities. Despite small differences in the exact position, the simulation reproduces the findings that the optimal thickness is smaller at a higher wavelength as well as that the maximum peak emission requires a

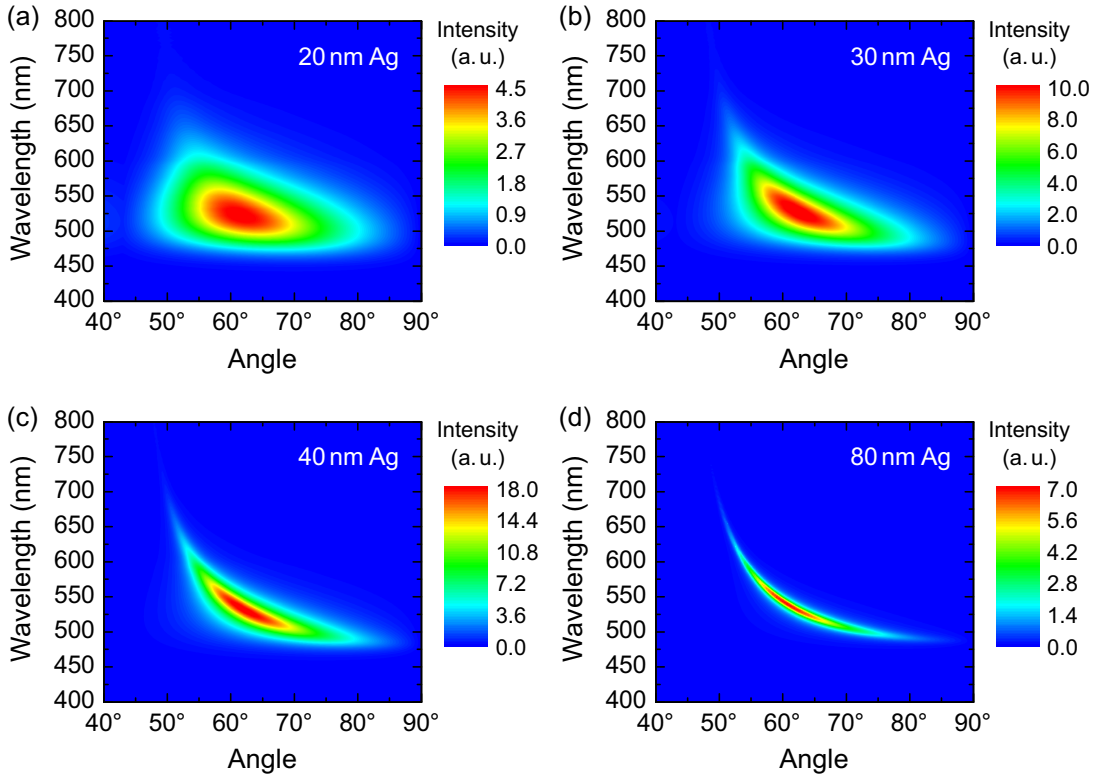


Figure 9.10: Simulation of the p-polarized emission in analogy to Fig. 9.7 for different Ag thicknesses: (a) 20 nm, (b) 30 nm, (c) 40 nm, and (d) 80 nm. The Alq_3 thickness was set to 32 nm in order to obtain the same angular position as in Fig. 9.7, and the emitter was positioned at a distance of 20 nm to the Ag interface. A quantum efficiency of $q = 20\%$ was assumed for Alq_3 in order to account for cavity effects, i.e. the Purcell factor depends on the actual Ag thickness. The simulation was weighted with a spectrum obtained from a PL measurement of a 50 nm thick Alq_3 film on glass. The optical constants used in the simulation are shown in Sec. A.2.

larger Ag thickness compared to the integral emission.

To understand the occurrence of an optimal Ag thickness, it is instructive to analyze the optical power dissipation, as exemplarily shown in Fig. 9.12(a) for a sample comprising 40 nm Ag and 32 nm Alq_3 . Apparently, the dominating loss mechanism is coupling to two SP branches propagating at the Ag/ Alq_3 and the Ag/glass interface¹⁷⁰. For simplicity, the SP at lower in-plane wave vector value will be referred to as SP1, while the other SP branch will be denoted by SP2. It can be seen that the SP1 branch almost completely lies between the air and glass light lines, hence it is in principle possible to partially extract these SPs by the prism coupling method. Only a small fraction of the SP1 dispersion below about 470 nm crosses the glass light line and therefore cannot be coupled out because the reversed Kretschmann configuration is no more fulfilled. On the contrary, the dispersion of SP2 lies outside the glass light cone for all wavelengths, thus it cannot be extracted at all, and all power dissipated into SP2 is eventually lost as heat¹⁷⁰.

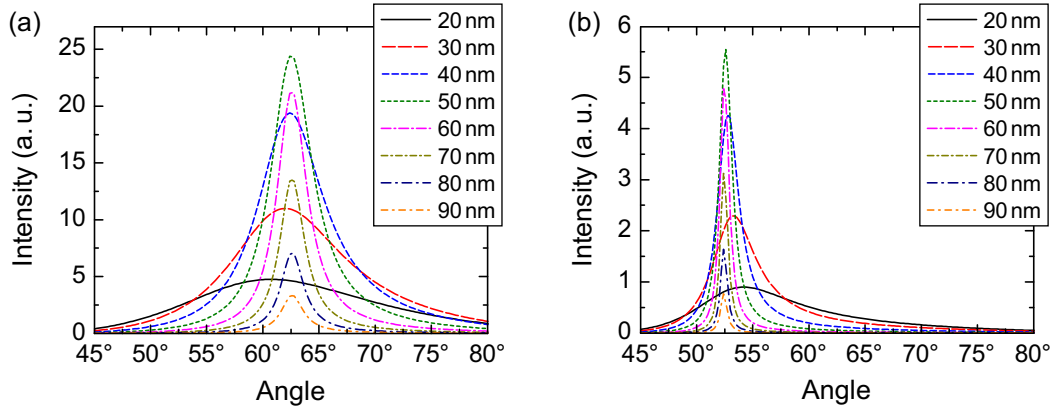


Figure 9.11: Cross sections of the simulated p-polarized emission from Fig. 9.10 and of simulations comprising four additional Ag thicknesses, at wavelengths of (a) 530 nm and (b) 625 nm.

In order to analyze the influence of the Ag thickness, Fig. 9.12(b) shows the cross sections of the total p-polarized power dissipation (black lines) for eight exemplary Ag thicknesses ranging from 20 nm to 90 nm at a wavelength of 530 nm. Apparently, the SP2 branch shifts to smaller wave vector values with increasing Ag thickness. This effect is connected to SP coupling, which was discussed in Sec. 7.1. Although the effective SP index on the organic side is smaller than the refractive index of glass, some coupling between SPs propagating at the Ag/Alq₃ and the Ag/glass interface might occur, especially for small Ag thicknesses when the SP dispersions are very broad. Even though power dissipation to SP2 is rather strong for small Ag thicknesses, it is strongly reduced with increasing Ag thickness. On the contrary, the power coupled into SP1 continuously increases as the thickness of Ag rises and saturates for Ag thicknesses larger than approximately 80 nm.

The red lines in Fig. 9.12(b) represent the fraction of p-polarized power that is extracted through the Ag layer into the glass substrate. With increasing thickness, the ratio of extracted to dissipated power in the region of SP1 is more and more reduced.

By integrating over the dissipated and transmitted power within an in-plane wave vector range of $1.19 \times 10^7 \text{ m}^{-1} \leq k_x \leq 1.8 \times 10^7 \text{ m}^{-1}$, i.e. corresponding to the region between the air and glass light lines, as indicated by the gray area in Fig. 9.12(b), the result shown in Fig. 9.12(c) is obtained. Obviously, there are two competing effects. On the one hand, the amount of power dissipated into SP1, i.e. the SP excitation efficiency, increases with higher Ag thickness. On the other hand, the fraction of power transmitted through the Ag, i.e. the SP extraction efficiency, decreases with increasing Ag thickness. The combination of both contributions is calculated by multiplying the excitation and extraction efficiencies. The result agrees very well with the dependence of the integral emission at a wavelength of 530 nm shown in Fig. 9.9(c). Thus, it can be concluded that the optimal Ag thickness for maximum integral emission is obtained

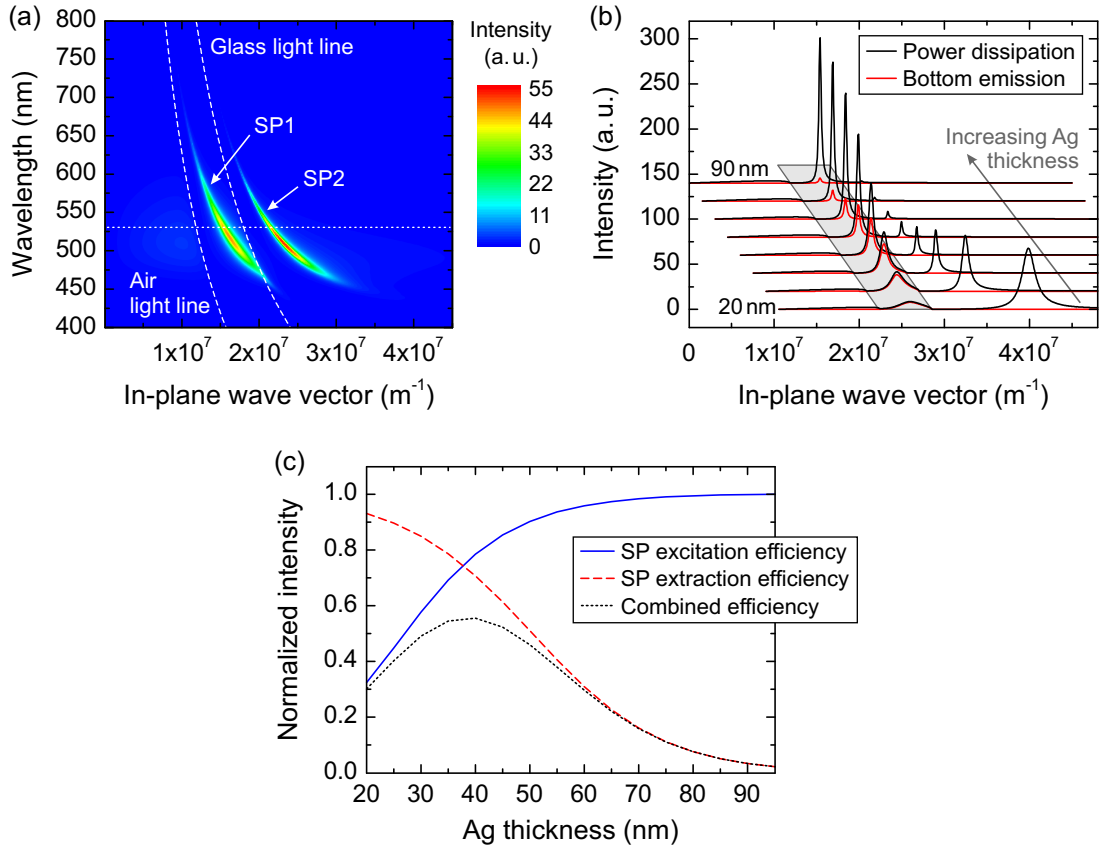


Figure 9.12: (a) Total optical power dissipation for a sample comprising 40 nm Ag and 32 nm Alq₃. The horizontal line shows the wavelength of the cross section in (b). The other lines represent the light lines for air and for the BK7 glass substrate. The abbreviations SP1 and SP2 are used to distinguish both SP branches. (b) Cross sections at 530 nm wavelength, showing a comparison of the p-polarized power dissipation and the power that is transmitted through the Ag film into the glass substrate (bottom emission) for eight exemplary Ag thicknesses. For reasons of clarity, the cross sections are displaced with respect to each other. The shaded area indicates the range between the air and glass light lines. (c) Normalized efficiency of SP excitation and extraction as well as the product of both values, i.e. the combined efficiency. The excitation efficiency was obtained by integrating the p-polarized power dissipation at 530 nm wavelength for Ag thicknesses ranging from 20 nm to 95 nm over the wave vector range indicated by the gray area in part (b), i.e. between the air and glass light lines. The values are normalized with respect to the simulation for 95 nm Ag thickness. The extraction efficiency was computed by taking the ratio between the emitted power and dissipated power, both integrated over the wave vector region marked in part (b) of the figure.

for a Ag thickness, where both the excitation of SPs by dye molecules is strong as well as the outcoupling of SPs through the Ag layer is high.

It should be emphasized that several factors have a strong impact on the simulated power dissipation in the case of an emitter positioned close to a thin silver layer. Certainly, the optical constants of Ag influence the SP dispersion and the amount of extracted power. In addition, also the optical constants of Alq₃ are important. Since the

evanescent SP field penetrates into Alq₃, the width of the SP dispersion is increased for a higher extinction coefficient of Alq₃. Furthermore, the cavity effect, i.e. the Purcell factor, depends on the reflectivity and, thus, on the thickness of the Ag film. Therefore, it is important to perform polychromatic simulations to account for the broad emission spectrum, and to choose the right radiative quantum efficiency of the emitting system, which was set to $q = 20\%$ in this case^{63–66}. It is also important to point out that the upper limit of the in-plane wave vector in the simulations must be large enough to take into account the power dissipation to both SP branches. This is especially important for small Ag thicknesses, where the SP2 branch is located at high wave vector values.

Moreover, the position of the emitter has an impact on the simulation result because it directly influences the interference condition of the emitting dipole and the Ag mirror²¹³. Certainly, it would be desirable to include a distribution of the emission zone to account for the excitation of the whole Alq₃ film by the laser. For such a simulation, it might be required to differentiate between SPs and lossy surface waves. The latter decay channel represents direct energy transfer of the dye to the metal¹³⁵. It dominates the power dissipation at small distances to a metal below about 10 to 20 nm^{25, 109, 213}. Therefore, the emitter was positioned at a distance of 20 nm from the Ag interface to avoid coupling to lossy surface waves in the simulations. For an easier comparison between measurement and simulation, it might be favorable to use only a thin emission layer and a dielectric spacer²¹³. Nevertheless, the good agreement between experimental results and optical simulations is remarkable, although only a single emitter position was assumed.

All in all, it was demonstrated by PL experiments as well as by optical simulations, that the Ag thickness strongly influences the intensity of the extracted SPs, while the angular position of the SP emission is hardly influenced at all. On the contrary, the thickness of the Alq₃ layer strongly alters the position of the SP dispersion, as was shown by varying the Alq₃ thickness between 20 nm and 40 nm.

9.4. Extraction of leaky modes

According to the absorption study shown in Fig. 9.2(a), the SP dispersion shifts out of the glass light cone if the Alq₃ thickness gets too large. Hence, SPs can no longer be extracted by the prism coupling method, and energy coupled to SPs is lost. However, as soon as the Alq₃ thickness exceeds the cut-off thickness, a guided mode is supported by the stack²¹⁴. It is noteworthy that waveguide modes in a typical OLED stack propagate inside the organic layers and ITO. Their in-plane wave vector is larger than the glass light line, and the modes are guided between the metallic cathode and the dielectric glass substrate.

However, it is possible to design a special simplified stack layout that permits the investigation of guided leaky modes. Such a stack basically is comparable to what has

been discussed in the previous sections, i.e. a structure comprising glass/Ag/Alq₃/air. Here, the Alq₃ thickness must be larger in order to support a guided mode. In this case, the mode is bounded by air and a finite Ag film, respectively. This has two important consequences. First, total internal reflection at the boundary to air already occurs for smaller in-plane wave vectors compared to a glass boundary. Second, the semitransparent Ag film on the one hand offers enough reflectivity to create a guided mode, on the other hand the transmittance is large enough in order to partially extract the leaky mode into the glass substrate, thus allowing for an investigation of otherwise inaccessible modes.

9.4.1. Variation of organic layer thickness

This section analyzes the dependence of extracted leaky modes on the thickness of the Alq₃ layer. The analysis is particularly interesting because the thickness determines the number of s- and p-polarized modes that are supported by the stack. Therefore, Figs. 9.13(a)–(f) present measurements of the polarized emission for three stacks having a rather similar Ag thickness of 52–58 nm, but Alq₃ thicknesses of approximately 110 nm, 210 nm, and 460 nm.

The s-polarized measurement of the sample comprising an Alq₃ thickness of 110 nm, shown in Fig. 9.13(a), demonstrates that a sharp guided leaky mode (TE₀) can be extracted by using the prism coupling approach. On the contrary, there is almost no intensity in the p-polarized emission, because SPs can no more be extracted and the stack is too thin to support p-polarized leaky modes. The strong leaky mode emission is also apparent from the photograph shown in Fig. 9.14(a). The angular dispersive emission ranging from red to blue color with increasing angle can be clearly identified.

The polarization of the extracted mode changes if the thickness of the Alq₃ layer is increased to 210 nm, as presented in Figs. 9.13(c) and (d). In this case, the dominating optical channel is coupling to a p-polarized leaky mode (TM₀). Here, the s-polarized TE₀ mode is shifted to larger angles. Therefore, only a small part of the mode can be extracted in the wavelength regime above 600 nm. It is important to point out that the emitter still couples to this mode over the whole spectrum of Alq₃. However, for wavelengths below 600 nm, the propagation angle of the mode inside the Alq₃ film is too large in order to be extracted by the prism coupling method. In other words, the mode propagates at an in-plane wave vector which is larger than the glass light line. It is noteworthy that the next s-polarized mode, i.e. the TE₁ mode, already emerges in the blue wavelength range. A photograph of the sample is displayed in Fig. 9.14(b). Since the image shows the unpolarized emission, all modes are observable at once. Certainly, the TM₀ mode accounts for most of the emission intensity. Nevertheless, also the weak TE₀ emission at large angles in the red wavelength range can be seen, as well as a very weak blue emission arising from the TE₁ mode at rather small angles.

By further increasing the thickness of Alq₃, the number of modes supported by the

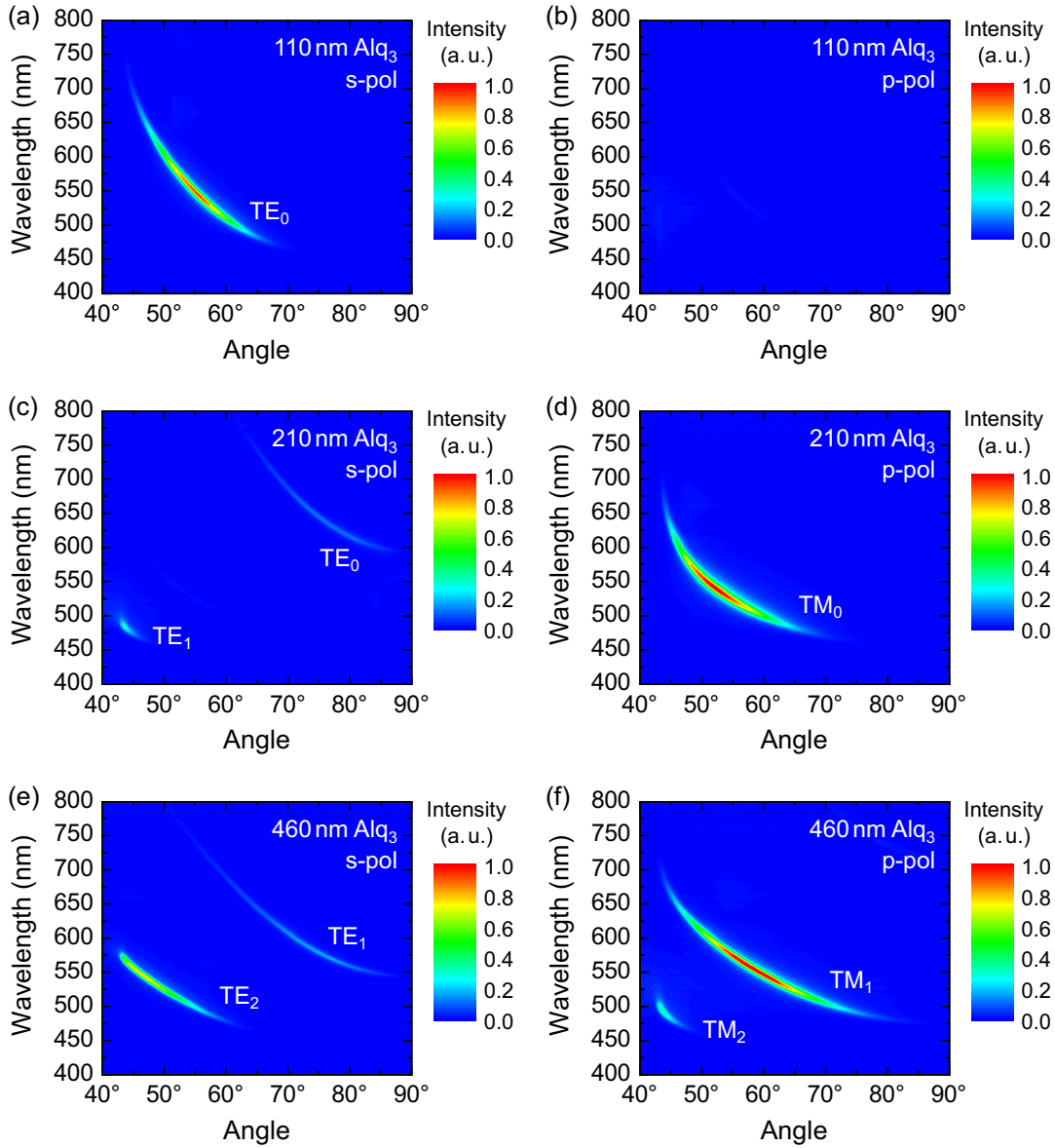


Figure 9.13: Measured s-polarized (left column) and p-polarized (right column) emission of samples comprising glass/Ag/Alq₃/air. The actual thicknesses determined by profilometry are (a),(b) 58 nm Ag and 111 nm Alq₃, (c),(d) 58 nm Ag and 212 nm Alq₃, and (e),(f) 52 nm Ag and 464 nm Alq₃. The measurements for each sample are normalized by the same factor. TE_x and TM_x indicate s- and p-polarized modes, respectively, with x being the mode number.

structure increases. An example for an approximately 460 nm thick Alq₃ film is shown in Figs. 9.13(e) and (f) for s- and p-polarized emission, respectively. In this case, two s-polarized modes (TE₁ and TE₂) and two p-polarized modes (TM₁ and TM₂) are observable. In this case, the TE₀ and TM₀ modes are located at too large wave vectors in order to be extracted into the glass prism.

In summary, the thickness of the Alq₃ film influences the outcoupling of leaky modes

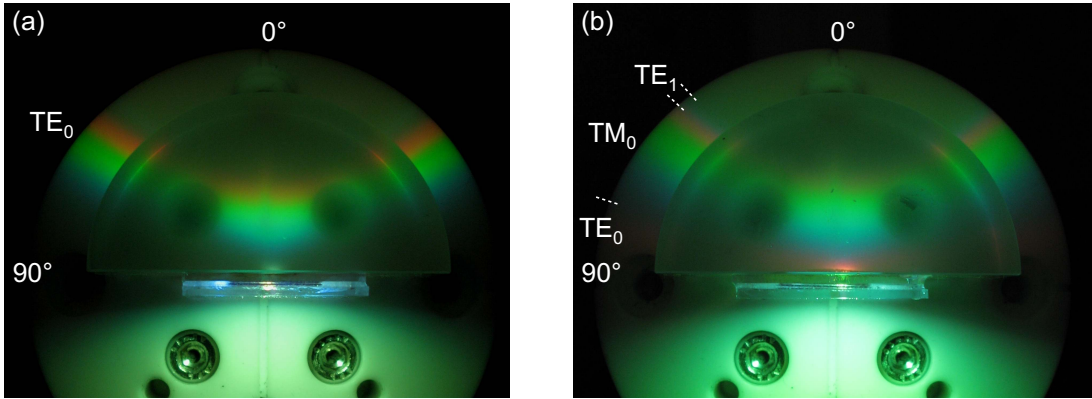


Figure 9.14: (a),(b) Top view photograph of the samples with an Alq_3 thickness of 110 nm and 210 nm, respectively. The corresponding angular dependent measurements are shown in Figs. 9.13(a)–(d). The angular region of each mode is roughly indicated in each picture.

for two reasons. First, the thickness determines the angular position of the extracted modes, similar to SPs. Moreover, the number of supported guided modes increases with the thickness of the organic layer. In general, the TE mode of a specific mode number emerges at a smaller thickness compared to the corresponding TM mode.

9.4.2. Variation of silver thickness

In analogy to the extraction of SPs, it can be expected that the thickness of the Ag film has a strong impact on the intensity of the leaky mode emission. Therefore, a series of samples comprising eight different Ag thicknesses between about 24 nm and 84 nm and an Alq_3 thickness of approximately 114 nm were prepared. The Alq_3 layer was chosen in such a way that exactly one mode, i.e. the TE_0 mode, is supported by the stack.

The samples with varying Ag thickness in this section were prepared by using shadow masks that cover half of the sample. By rotating the masks with respect to the sample, it was possible to fabricate four different Ag layers on one sample. Afterwards, Alq_3 was deposited on top of the Ag structure. This method has the advantage that the Alq_3 layer has a very uniform thickness for all Ag thicknesses. However, changing the masks for the Ag deposition required a vacuum break. Thus, it cannot be excluded that the Ag layer was contaminated. The samples were excited by a 325 nm HeCd laser. The laser light was guided to the sample by a glass fiber, which was attached to the rotary table so that the excitation condition was kept constant during rotation.

The measured s-polarized emission and corresponding optical simulations for four exemplary Ag thicknesses are shown in Fig. 9.15. An Alq_3 thickness of 119 nm, i.e. close to the measured value, was used in the simulations in order to reproduce the measured angular position. The radiative quantum efficiency was set to $q = 20\%$, and the emitter was positioned in the middle of the Alq_3 layer.

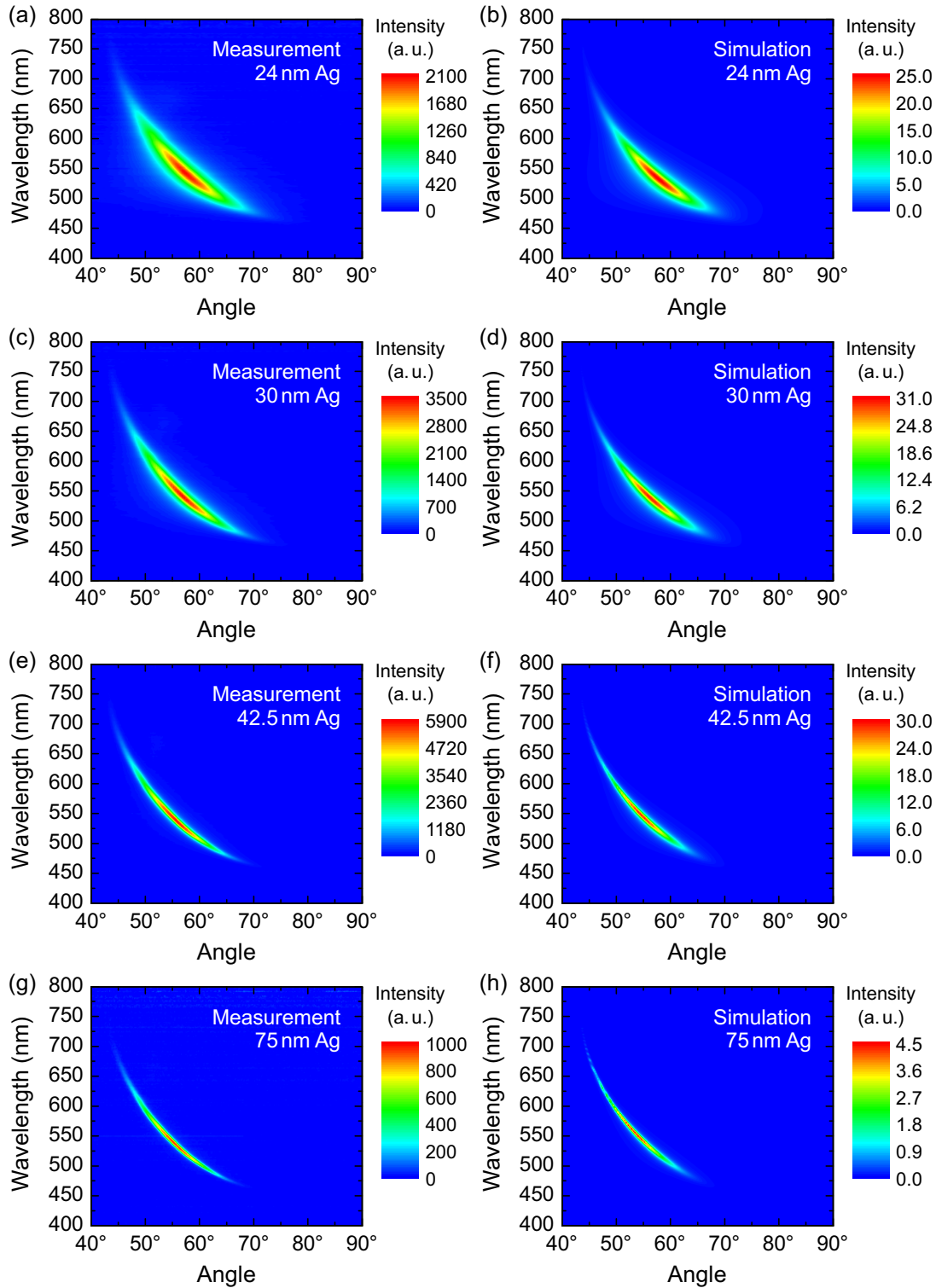


Figure 9.15: Measurement (left column) and simulation (right column) of the s-polarized emission for four exemplary Ag thicknesses in a structure similar to the basic stack layout glass/Ag/Al_{Q3}/air. The samples comprise around 114 nm Al_{Q3} and different Ag thicknesses as depicted in each graph. An Al_{Q3} thickness of 119 nm was used in the simulations in order to reproduce the measured angular position.

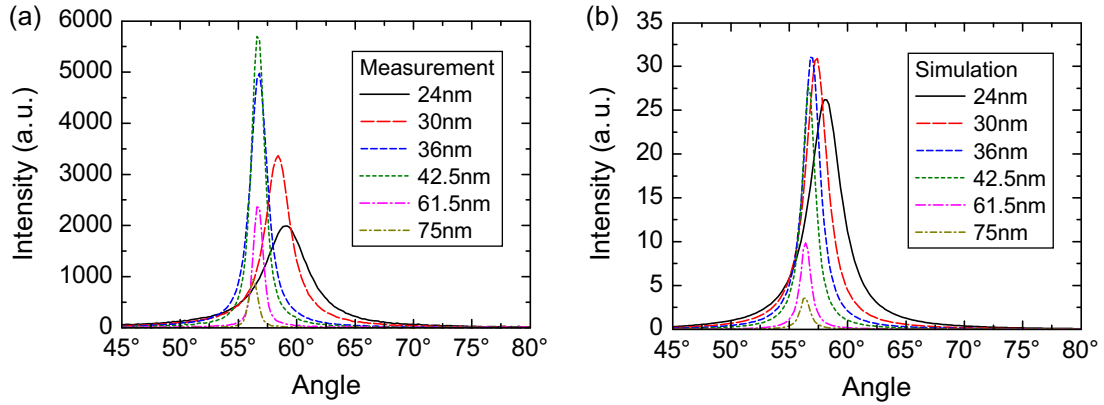


Figure 9.16: (a) Cross sections of the measurements in the left column of Fig. 9.15 at a wavelength of 530 nm. (b) Cross sections of the optical simulations in the right column of Fig. 9.15. In addition, the cross sections of measurements and simulations for two additional Ag thicknesses are presented.

In the experimental result it can be seen that the width of the leaky mode emission decreases with increasing Ag thickness. In addition, the maximum intensity has the highest value for a Ag thickness of 42.5 nm. Thus, it seems that there is also a certain Ag thickness where the emission from leaky modes is highest. However, the maximum intensity rises only slightly in case of the optical simulations. Despite this discrepancy in measured and simulated intensity, the overall shape of the measured leaky mode dispersion agrees well between measured and simulated results.

A more detailed comparison between experiment and simulation can be seen in the cross sections at a wavelength of 530 nm, as shown in Fig. 9.16. Especially for small Ag thicknesses, the measured and simulated results differ considerably. It appears that the Ag thickness, which was determined by profilometry, is overestimated. This probably arises from the vacuum break during the deposition of the Ag layers. By using a smaller value for the simulations, the measured curves could be reproduced reasonably well.

On the other hand, some features can be seen that are observed both in the measurement as well as in the simulation. For instance, the peak in the cross section shifts to larger angles for smaller Ag thicknesses, i.e. when the reflectivity of the semitransparent Ag film is rather low. The consistency in angular position is an evidence for the uniform Alq_3 thickness obtained by this preparation method.

In addition, the width of the curves should be pointed out. Both in the measurement and the simulation, the full width at half maximum typically is below 2° for larger Ag thicknesses. Hence, emission from guided modes is considerably narrower compared to SPs. This can be explained by the fact that the SP is damped more strongly than the other guided modes which do not have their field maxima in the metal surface¹⁰⁴.

The peak and integral intensities in a range from 44° to 90° at a wavelength of 530 nm are shown in Figs. 9.17(a) and (b), respectively. Regarding the measured result (square symbols), the behavior of leaky mode emission is rather similar to the extraction of SPs,

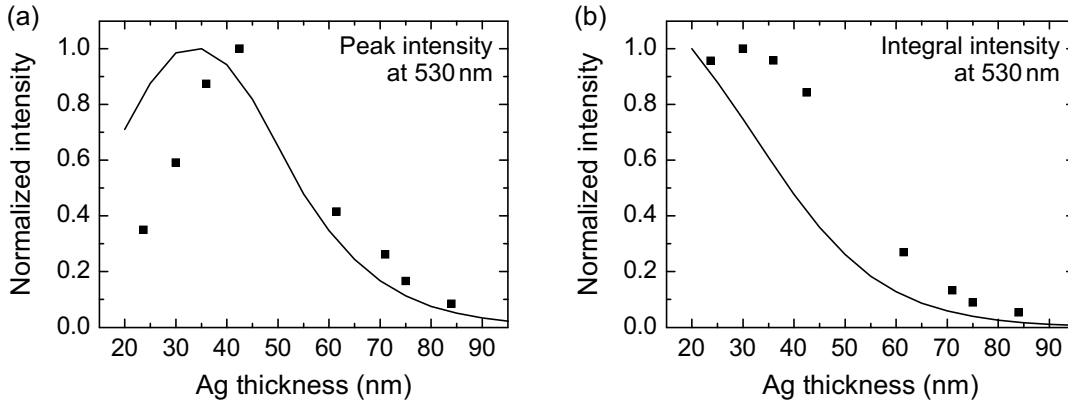


Figure 9.17: (a) Measured (square symbols) and simulated (line) peak intensities extracted from the cross sections in Figs. 9.16(a) and (b), respectively. In addition, the result of two more measurements with samples having Ag thicknesses of 71 nm and 84 nm are shown. (b) Measured (square symbols) and simulated (line) integral intensities obtained by integrating the curves in Figs. 9.16(a) and (b), respectively, from 44° to 90° . The integration range corresponds to the area between the light lines of air and fused silica. For both graphs, additional simulations were evaluated to obtain a smaller step size in Ag thickness of 5 nm.

i.e. an optimal Ag thickness for highest peak and integral emission exists, although the optimal value is slightly smaller compared to SP emission. The general trend observed in the peak and integral intensities obtained from optical simulations (black lines in Fig. 9.17) agrees with the measured result. However, the optimum value in the simulated case is clearly shifted to a smaller Ag thickness.

Several measures could be taken to improve the agreement between experiment and simulation. First, it might be helpful to include a distributed emission zone in the simulations instead of a single emitter position in order to account for the absorption profile of the Alq_3 layer in the measurement. It might also be necessary to consider that the laser is partially reflected at the Ag layer depending on the actual Ag thickness. Hence, the excitation intensity could be stronger in case of thick Ag films. This would result in a higher intensity at larger Ag thicknesses in the measurement, which is in agreement with the observed discrepancy. Finally, the experiment should be repeated by preparing samples without vacuum break to ensure that the Ag layers are not contaminated. In general, it would be beneficial to use an outcoupling prism made of BK7 glass (i.e. the same material as the substrate) instead of fused silica, in order to extract all the light inside the glass substrate.

Altogether, both the measurements and simulations confirm that the Ag thickness strongly influences the intensity of the leaky mode emission which is extracted by the prism coupling approach. A larger Ag thickness corresponds to a higher reflectivity of the semitransparent mirror, thus reducing the fraction of light that is transmitted through the Ag layer. According to the measurements, there is an optimal Ag thickness for highest integral leaky mode emission.

9.5. Conclusions

In summary, this chapter demonstrated the extraction of both SPs and guided leaky modes by the prism coupling approach. It was shown that silver is the metal of choice for extracting SPs, because this material has the lowest SP damping and absorption in the visible region. Only in the case of emission in the blue range of the spectrum, aluminum could also be considered as metal layer.

From the systematic variation of the Alq₃ and Ag thicknesses, it can be concluded that the Alq₃ thickness mainly determines the angular position of the extracted SP mode and has almost no influence on the intensity, which in turn is strongly influenced by the thickness of the Ag layer. Two competing effects, i.e. stronger coupling to SPs versus a reduced extraction efficiency with increasing Ag thickness, were discussed to explain the occurrence of an optimal Ag thickness for highest peak or integral emission, the latter being of particular interest for optimizing light extraction. It should be emphasized that the Ag thickness for maximum integral emission is smaller than the value required for highest peak emission. In order to maximize the overall extracted intensity with this particular sample structure, a silver thickness of about 40 nm offers the best result.

In addition, the extraction of guided leaky modes was presented by using the prism coupling technique, demonstrating that the width of the leaky mode emission is very narrow. The dependence on the Alq₃ and Ag thickness generally agreed with the extraction of SPs, though the optimal Ag thickness for maximum integral emission appeared to be lower.

According to the simulations, a significant fraction of SPs can be extracted. Moreover, photographs indicate that the emission from SPs as well as leaky modes is at least of the same order as the direct emission on the opposite Ag side. Therefore, prism coupling is a highly promising approach for increasing the light extraction in OLEDs.

However, as long as a prism made of fused silica or BK7 glass is used, the big drawback of this method is that just the power located between the air and glass light lines can be extracted. As a consequence, SP extraction only works for thin organic films. For a complete OLED stack with several organic layers, the in-plane wave vector of the SPs is too large. Hence, the SP dispersion is located outside the glass light cone and no outcoupling into the prism is possible. Moreover, waveguide modes cannot be extracted, because they are reflected at the glass substrate and, thus, propagate at larger in-plane wave vectors than the glass light line.

Therefore, the following chapter introduces an advancement so that the basic prism coupling idea can be transferred to OLEDs in order to recover SP and waveguide losses. In order to achieve this, it is required to increase the refractive index of the substrate and prism by using special glasses or transparent crystals. The fundamental results of the present chapter, e.g. the influence of the Ag and organic thicknesses, are still valid in case of “high-index coupling”.

10. High-index coupling

This chapter introduces an advancement of the prism coupling approach in order to apply this technique to OLEDs, which typically feature several organic layers so that the SP dispersion is rather determined by the refractive index of bulk organic materials. To fulfill the Kretschmann configuration, it is required to use materials for the substrate and prism which have a refractive index that is larger than the refractive index of the organic films, i.e. typically above $n = 1.8$. Since this method basically works in an analogous way to the prism coupling approach, it will be denoted high-index prism coupling, or simply high-index coupling²¹⁵.

First, the basic principle will be explained. Next, the influence of the prism material will be analyzed by using several materials with different refractive indices. Afterwards, the high-index coupling approach will be applied to a simplified stack featuring a 200 nm thick Alq_3 layer. Furthermore, the extraction of waveguide modes and SPs will be demonstrated for a real OLED device in PL measurements. Optical simulations will be used to estimate an upper limit of the outcoupling efficiency. Finally, it will be discussed how a technical implementation of this idea can be realized.

10.1. Basic principle

Figure 10.1 illustrates the basic principle of high-index coupling. Part (a) of the figure illustrates the basic stack layout. This approach is based on the same idea as the prism coupling method in the previous chapter, i.e. a reversed Kretschmann configuration is used to extract SPs which are excited by organic dye molecules adjacent to a silver film. In contrast to the previous chapter, the organic layer has no thickness restriction in this case.

The schematic dispersion of SPs propagating at the Ag/organic interface for a thick organic film is shown in Fig. 10.1(b). Apparently, the SP dispersion lies to the right of the light line of normal glass. Hence, SPs cannot be coupled out by means of a normal glass prism.

However, by using an appropriate transparent high-index material with a refractive index $n > 1.8$, it is possible to extract SPs up to a certain angular frequency, which is determined by the crossing point of the SP dispersion and the high-index light line. Similarly, waveguide modes propagating inside the organic layer can be extracted as leaky modes in the case of a high-index material with refractive index greater or equal

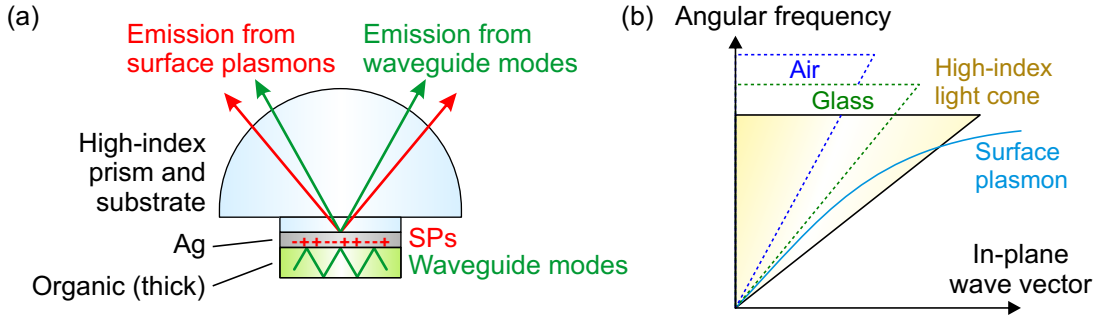


Figure 10.1: (a) Basic stack layout for the high-index coupling approach. Here, both the substrate and the prism are made of transparent materials with a refractive index $n > 1.8$. This allows for extracting SPs and waveguide modes even in the case of thick organic films. (b) Illustration of the high-index light cone and schematic dispersion of SPs traveling at the interface between Ag and a thick organic layer. The dashed lines represent the range of the light cones for air and normal glass.

to that of the organic layer. Altogether, power that is dissipated by the dye molecules to SPs or waveguide modes can be partially recovered and extracted into air²¹⁵.

The method can be explained in a very instructive way by studying the opposite light path, i.e. light is incident from the prism side and partially absorbed upon reflection at the interface between the high-index material and Ag. The absorption A is calculated by $A = 1 - R - T$, with R and T being the reflectance and transmittance, which are computed by the transfer-matrix method. The absorption for p- and s-polarized light in the case of three different prism materials is presented in Fig. 10.2 for a wavelength of $\lambda = 530$ nm.

In general, waveguide modes in a structure like glass/Ag/Alq₃/Air must have an in-plane wave vector k_x in the range $k_0 \leq k_x \leq (n_{\text{Alq}_3} \cdot k_0)$, i.e. between the air light line and the Alq₃ light line¹⁰⁴. Here, $k_0 = 2\pi/\lambda$ is the vacuum wave vector and n_{Alq_3} is the refractive index of Alq₃. These limits can be converted into a corresponding angle θ inside the prism by $\theta = \arcsin[k_x/(n_P \cdot k_0)]$, with n_P being the refractive index of the prism material. The resulting boundaries are plotted in Fig. 10.2 as dashed vertical lines. With increasing n_P , the air and Alq₃ light lines shift to smaller angles inside the prism. It is noteworthy that the lowest SP wave vector is always slightly larger than the air light line even for vanishing Alq₃ thickness¹⁰⁴. This is a consequence of the SP dispersion relation. Similarly, the maximum SP wave vector for thick Alq₃ films lies above the Alq₃ light line.

The absorption of light incident through a BK7 prism is rather similar to that of fused silica, which was studied in detail in the previous chapter. For increasing Alq₃ thickness, both the SP and waveguide modes can no longer be excited by the incident radiation, because the in-plane wave vector of these modes becomes larger than the light line of BK7.

On the contrary, by using a prism and a substrate made of SF6, the waveguide modes

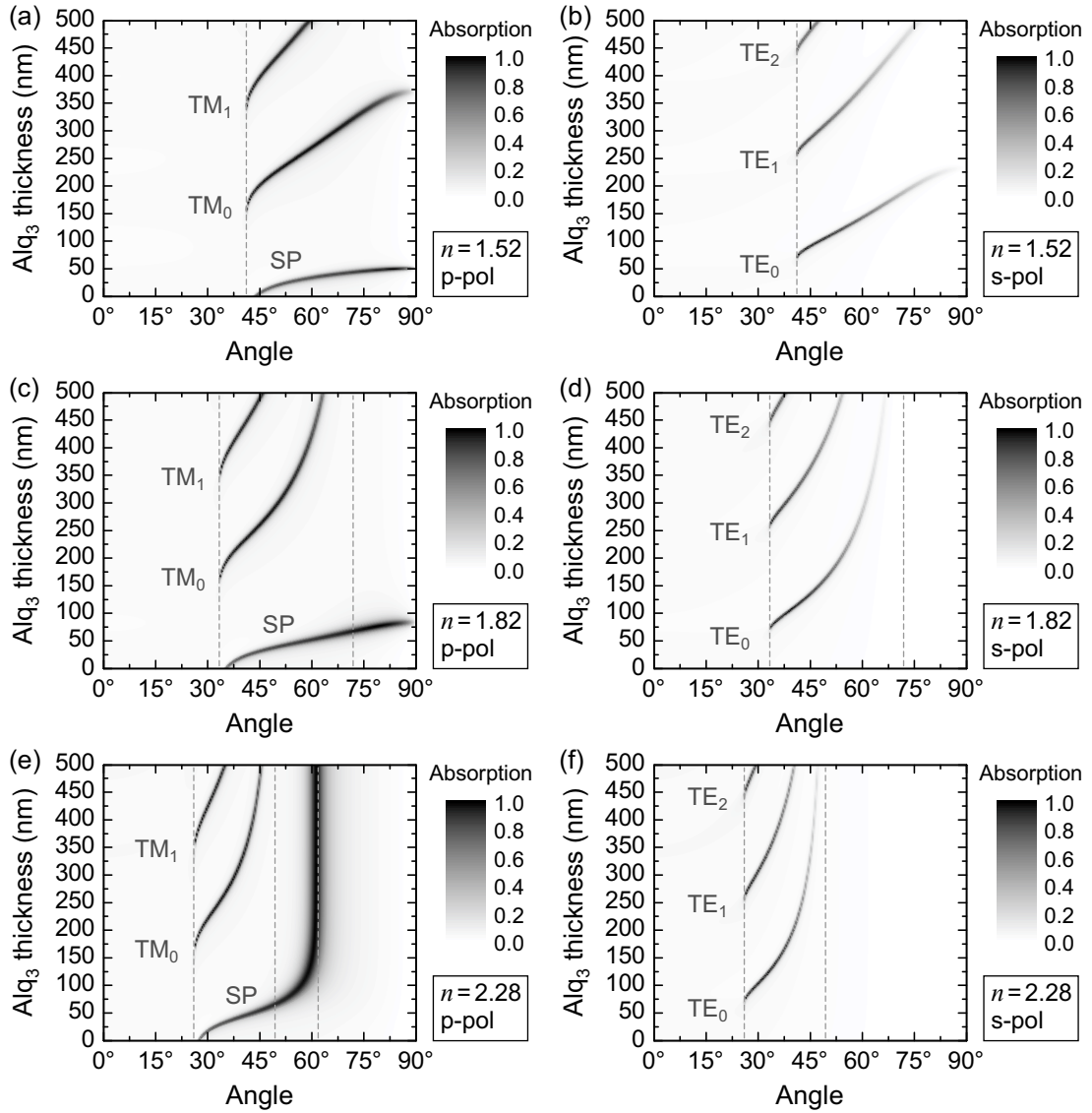


Figure 10.2: Calculated absorption of p-polarized (left column) and s-polarized (right column) light at a wavelength of 530 nm in a stack similar to Fig. 10.1(a) for different prism (and substrate) materials: normal glass (top row, $n_P = 1.52$), SF6 glass (middle row, $n_P = 1.82$), and LiNbO₃ (bottom row, $n_P = 2.28$). The thickness of Ag is set to 40 nm. Here, light is incident through the prism side. The absorption is plotted as a function of the angle inside the prism for varying thickness of the Alq₃ layer. TM_{*x*} and TE_{*x*} refer to p- and s-polarized modes, respectively, with *x* being the mode number. Surface plasmons are denoted by SP. The remaining optical constants used for the calculation are $n = 0.06$ and $\kappa = 3.4$ for Ag, and $n = 1.73$ and $\kappa = 0.005$ for Alq₃. The left dashed vertical line was calculated by $\arcsin(1/n_P)$, i.e. it represents the maximum propagation angle of light in air converted to an angle inside the prism. In the case of SF6 and LiNbO₃, a second vertical line is plotted at larger angles. It illustrates the maximum propagation angle of light in bulk Alq₃ converted to an angle inside the prism, and it was computed by $\arcsin(1.73/n_P)$. By nature, waveguide modes are located between the air and Alq₃ light lines. The third vertical line at 61.8° in part (e) was calculated by using the SP dispersion relation for an interface between bulk Ag and Alq₃, cf. Eq. (4.15), and by converting the k_x value into an angle inside the LiNbO₃ prism.

in the organic layer can be excited for all Alq_3 thicknesses, because the in-plane wave vector of waveguide modes propagating in an Alq_3 layer is always smaller than the light line of SF6 for the whole visible spectral range. In other words, the upper boundary for waveguides (i.e. the Alq_3 light line) lies within the prism light cone. However, coupling of incident light to SPs is limited to Alq_3 thicknesses below approximately 85 nm. For thicker Alq_3 films, the SP wave vector is larger than the maximum possible in-plane wave vector of light in SF6.

When using lithium niobate (LiNbO_3), coupling to waveguide modes is rather similar to SF6, i.e. incident light can excite guided modes for all Alq_3 thicknesses. Due to the larger refractive index of LiNbO_3 in comparison to SF6, the resonance angles shift to smaller values. The most important difference between LiNbO_3 and both other materials is related to SPs. Here, the resonance angle does not shift out of the prism light cone with increasing Alq_3 thickness. Instead, above an Alq_3 thickness of about 150 nm, the resonance angle approaches a rather constant value of approximately 61° , which corresponds to a wave vector that is almost identical to the SP dispersion at an interface between bulk Ag and Alq_3 . Therefore, by using a LiNbO_3 prism, it is possible to couple incident light to SPs for all thicknesses of Alq_3 .

Altogether, the increase of the in-plane wave vector of SPs and guided modes at a larger thickness of the organic layers can be compensated by using a prism with higher refractive index, i.e. by stretching the prism light cone to larger wave vectors.

Certainly, this has important consequences for the opposite optical path, i.e. the reversed Kretschmann configuration. This geometry will be used to enhance light extraction from normally bound modes by the high-index coupling technique. According to the findings from the absorption study, the extraction of SPs and waveguide modes should be possible for all organic layer thicknesses, provided that the refractive index of the prism material is large enough.

10.2. Sample preparation and experimental setup

The samples investigated in the following sections were prepared using three different substrates. First, cleaned glass microscope slides with a size of $20 \times 20 \text{ mm}^2$ and a thickness of 1 mm were used as normal BK7 glass substrates. Second, samples were prepared on cleaned SF6 substrates having a size of $15 \times 15 \text{ mm}^2$ and a thickness of 1.5 mm. These two types of samples were attached to appropriate half-spheres made of BK7 or SF6 with a diameter of 25 mm and 30 mm, respectively, by index-matching gels (Cargille Optical Gel with $n_D = 1.52$ or Cargille Refractive Index Liquid Series M $n_D = 1.795$). Third, in the case of LiNbO_3 , it was also attempted to use thin LiNbO_3 substrates and to attach them to the half-sphere by an index-matching melt (Cargille Refractive Index Melt Series GH with $n_D = 2.24$). However, the index-matching melt is a very brittle solid at room temperature. Even upon heating, it had a low viscosity.

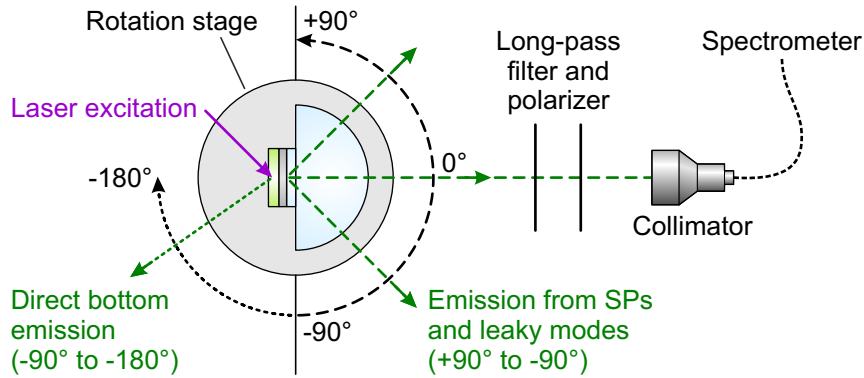


Figure 10.3: Experimental setup (top view) for the high-index coupling method. A 375 nm cw laser diode was used to excite the Alq_3 layer through a 375 nm band-pass filter. Light was extracted in this reversed Kretschmann configuration by means of half-spheres made of BK7, SF6 and LiNbO_3 , respectively. The sample and attached half-sphere as well as the laser were mounted on a computer-controlled rotation stage.

As a consequence, it was not possible to obtain thin index-matching layers. Since the transmission through the layer is proportional to the thickness, the layer remained rather intransparent. It should be mentioned that in general the transmittance for this material almost completely vanishes below a wavelength of about 600 nm even for thin films. Above all, the index-matching melt is chemically very aggressive. It is arsenic based and, thus, highly toxic. Therefore, the samples were directly prepared on a LiNbO_3 half-sphere having a diameter of 30 mm, instead of attaching a substrate to the sphere by index-matching melt.

The Ag films were deposited by thermal evaporation in a vacuum of approximately 2×10^{-7} mbar at a rate of 1.5 \AA/s . The Alq_3 layers were fabricated by thermal evaporation in a vacuum of typically 2×10^{-7} mbar at a rate of 1.2 \AA/s . The samples using BK7 and SF6 substrates were encapsulated by using a cover glass and either a two-component glue or a UV-curing epoxy with small spacers to form a small inert gas cavity. In the case of the LiNbO_3 half-sphere, the organic layer was encapsulated by attaching a cover glass with the aid of double-sided adhesive tape, which had an opening in the center. Although this encapsulation was not perfect, it offered at least some protection and allowed for reusing the expensive half-sphere.

Figure 10.3 illustrates the experimental setup. In order to measure the angular dependent emission intensity, the samples were mounted on a computer-controlled rotation stage. The angles specified in the measurements either refer to angles in air (for direct emission) or to angles inside the particular prism (for emission measured through the prism). The excitation laser was rotated together with the samples so that the excitation condition was kept constant during the measurement. In some cases, the measurement was performed over a range of 270° in order to compare direct bottom emission (-90° to -180°) with top emission arising from extracted SPs and leaky modes (-90° to 0° and similarly 0° to 90°). A long-pass filter (400 nm cut-off wavelength) was utilized to

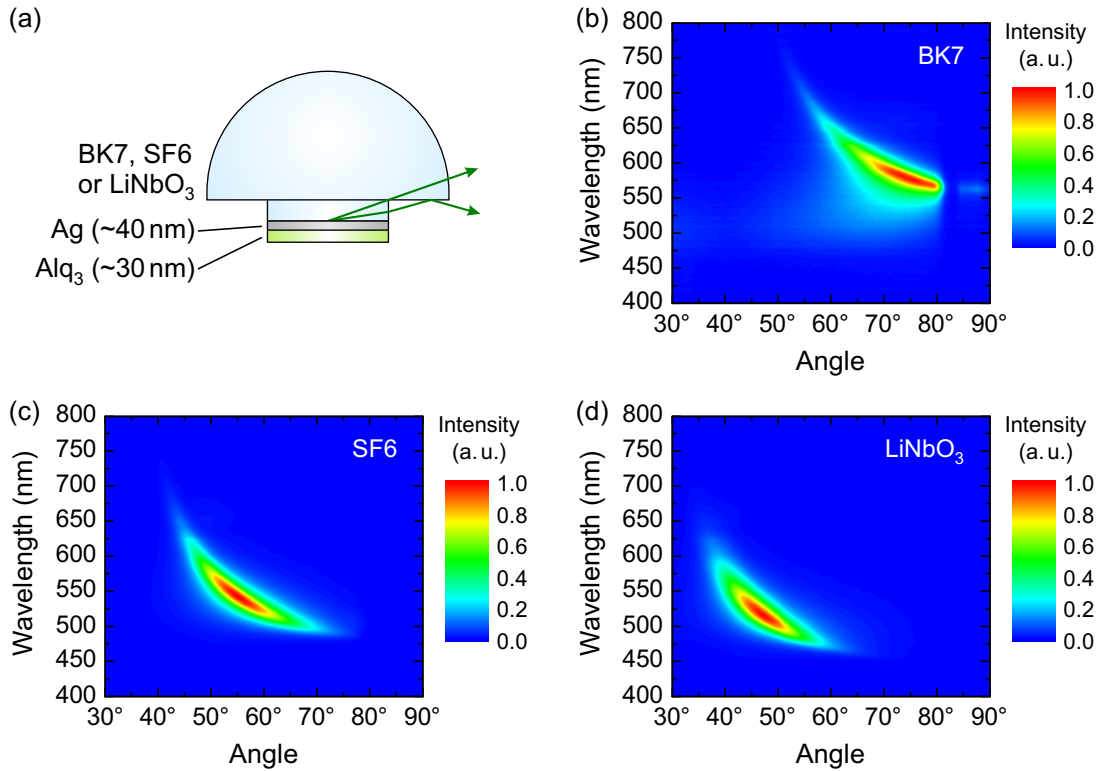


Figure 10.4: (a) Schematic illustration of the stack layout used to study the influence of the prism material. The Ag thickness is about 40 nm, the Alq₃ layer is approximately 30 nm thick. Due to the thickness of the substrate, the emission at large angles cannot be completely extracted in top direction, i.e. into the half-sphere. (b),(c),(d) Measured p-polarized top emission for BK7, SF6 and LiNbO₃ half-spheres, respectively. According to the definition of angles in Fig. 10.3, the presented angular range actually runs from -30° to -90°. However, the negative sign is omitted for reasons of clarity.

protect the spectrometer from the laser beam. In some measurements, the emission was detected through a polarizer in order to distinguish between p- and s-polarized radiation.

10.3. Influence of prism material

Although the implementation of a high-index prism allows for extracting both SPs as well as waveguides, the basic principle is better illustrated by solely comparing the SP emission angle in case of thin organic films for different prism materials. The basic stack layout is shown in Fig. 10.4(a). The samples comprise about 40 nm Ag and 30 nm Alq₃ and were prepared on BK7 and SF6 substrates, which were attached to a corresponding half-sphere. In addition, the same structure was directly deposited onto a half-sphere made of LiNbO₃. The thickness of Alq₃ is too small in order to support waveguides so that only emission from SPs is expected.

The p-polarized measurement is presented in Figs. 10.4(b)–(d). It can be seen that the SP emission clearly shifts to smaller angles with increasing refractive index of the prism material. In case of LiNbO₃ in Fig. 10.4(d), the SP emission is located between around 35° and 60°, and also emission in the blue wavelength range down to almost 450 nm can be detected. It should be mentioned that emission from SPs was sometimes also detected in an s-polarized measurement if a half-sphere made of LiNbO₃ was utilized. This effect can be explained by the birefringence of LiNbO₃. Here, the optical axis of the half-sphere is not known. Hence, depending on the orientation, the polarization of light can be changed during propagation through the half-sphere, similar to the principle of a half-wave plate.

In comparison to the measurements which were presented in Fig. 9.5(b) for a fused silica half cylinder prism, the SP dispersion in Fig. 10.4(b) lies at larger angles although both samples should comprise 30 nm Alq₃. Furthermore, by using a BK7 sphere instead of a fused silica half cylinder, the emission angle should be shifted to smaller values. The most probable explanation is that the Alq₃ thickness of all samples analyzed in Fig. 10.4 is larger than intended. Nevertheless, this does not matter as long as the Alq₃ thicknesses of the samples with BK7, SF6 and LiNbO₃ spheres are comparable, because only the relative shift of the SP emission is important in this section.

Moreover, the behavior of the SP emission in Fig. 10.4(b) for angles above 80° deserves a comment. According to the light paths illustrated in Fig. 10.4(a), the emission above a certain angle leaves through the edge of the BK7 substrate and is then partially reflected at the bottom side of the sphere. Therefore, almost no emission is detected above 80°. This effect also happens in Fig. 10.4(c). However, in this case, the emission at large angles is almost zero anyway. On the contrary, emission over the whole angular range can be detected if Ag and Alq₃ are directly deposited onto the sphere, as in the measurement in Fig. 10.4(d). Just as well, this effect is not observable if a fused silica prism is applied to a BK7 substrate, as in the previous sections. Due to the difference in refractive index of fused silica and BK7, only light propagating in BK7 at angles smaller than $\arcsin(1.46/1.52) \approx 74^\circ$ can enter the fused silica prism. Thus, the critical angles above 80° are not detectable at all in this case.

For a more detailed analysis of the influence of different prism materials, Fig. 10.5 presents cross sections of the measurements in Figs. 10.4(b)–(d) at a wavelength of 600 nm. It is clearly apparent that a larger refractive index of the prism shifts the peak of the extracted SPs to smaller angles. In addition, information about the refractive indices can be obtained by comparing the relative peak positions. For the measurement with the BK7 sphere, the peak angle occurs at $\theta = 68.4^\circ$. Assuming a refractive index of $n = 1.516$ for BK7 at a wavelength of 600 nm, the corresponding SP wave vector can be calculated to $k_{\text{SP}} = 1.516 \cdot k_0 \cdot \sin 68.4^\circ = 1.476 \times 10^7 \text{ m}^{-1}$. Using this result as a fixed value, the refractive indices for SF6 and LiNbO₃ can be computed from the peak positions of $\theta = 47.8^\circ$ and $\theta = 38.5^\circ$, respectively, by the relation $n = k_{\text{SP}} / (k_0 \cdot \sin \theta)$.

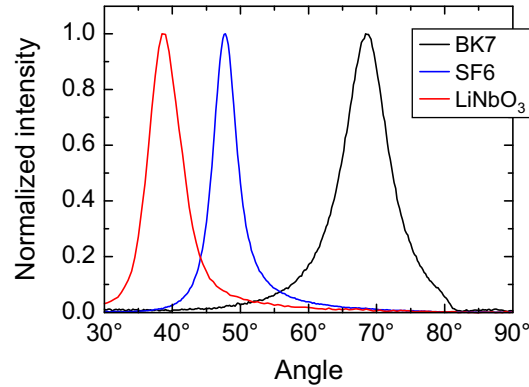


Figure 10.5: Cross sections of the measurements in Figs. 10.4(b)–(d) at a wavelength of 600 nm.

Refractive indices of approximately 1.9 and 2.26 are obtained for SF6 and LiNbO₃, respectively. Although the value of LiNbO₃ matches the expected value quite accurately, the result for SF6 is larger than the expected value of about $n = 1.8$. The difference probably arises from the positioning of the samples. Due to the difficult mounting and alignment of the half spheres, an angular error of around 4° must be considered. In addition, small deviations in the thickness of the Alq₃ layer between different samples as well as an influence of the finite thickness of the substrate on the emission angle cannot be ruled out.

Nevertheless, the measurements for different prism materials clearly confirm the basic principle, which was expected from the absorption study in Fig. 10.2. The implementation of a high-index prism considerably shifts the SP emission to smaller angles. Consequently, it should be possible to extract SPs even for thicker organic films, as will be demonstrated in the following section.

10.4. Extraction of surface plasmons and waveguide modes

In order to investigate the extraction of SPs and waveguides even for thick organic films, this section analyzes a sample comprising 40 nm Ag and 200 nm Alq₃. The layers were directly deposited on a LiNbO₃ half-sphere, as shown in Fig. 10.6(a). The Ag thickness of 40 nm was chosen in order to obtain both a high peak and integral SP emission in the green wavelength regime according to the results in the previous chapter.

The measurement was performed without polarizer to detect the p-polarized SP emission as well as the s- and p-polarized waveguide mode emission at once. The result is displayed in Fig. 10.6(b). The angular range from -180° to -90° shows the direct bottom emission, i.e. the emission that would also be obtained without high-index coupling. This emission feature is very broad and only has a weak angular dispersion. On the other hand, the top emission exhibits several sharp and dispersive modes. In detail, emission from three waveguide modes, which are normally trapped inside the thick or-

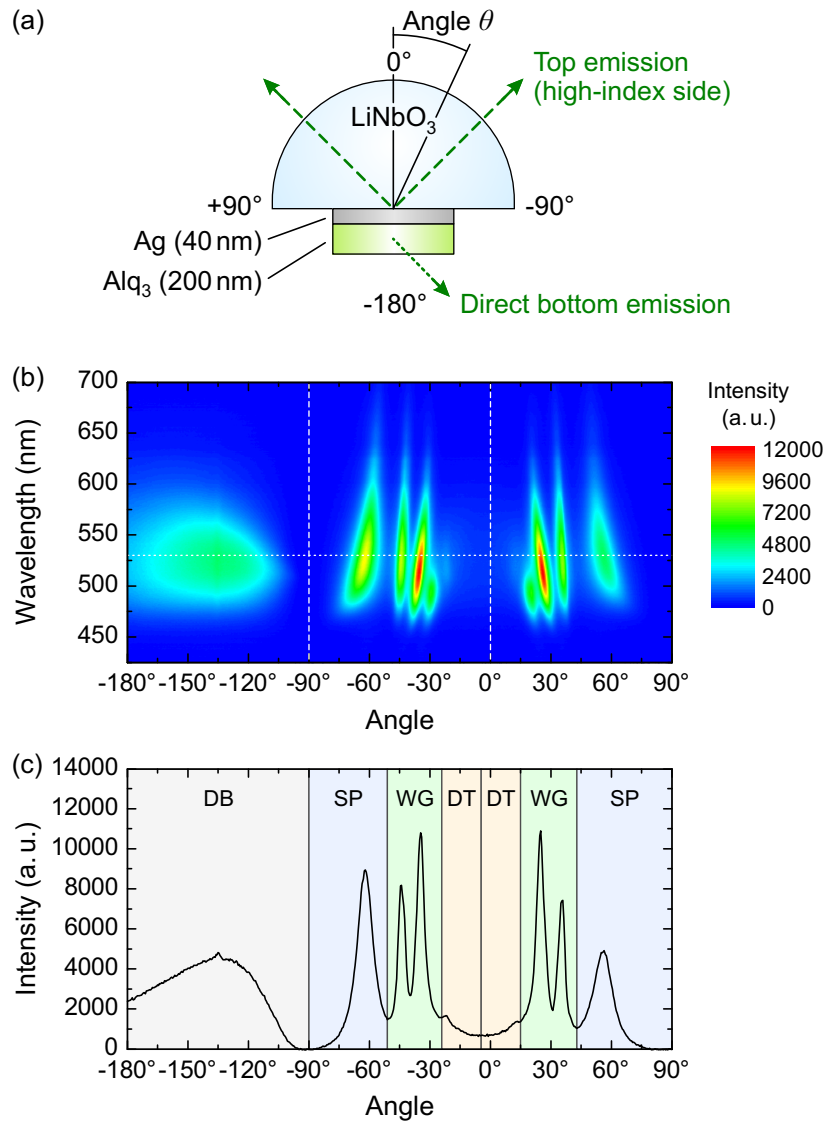


Figure 10.6: (a) Stack layout of the sample investigated in this section. The bottom emission is measured from -180° to -90° , while the top emission on the high-index side is detected from -90° to 0° and as additional control also from 0° to 90° . (b) Measurement of the unpolarized emission. The horizontal line marks the wavelength of the cross section in part (c), while the vertical dashed lines indicate the boundaries at -90° and 0° . (c) Cross section of the measurement at a wavelength of 530 nm. The colored areas represent the integration borders for direct bottom emission (DB), direct top emission (DT), waveguide mode emission (WG), and surface plasmon emission (SP). It should be noted that no substrate modes exist in this stack, because the thick Alq₃ layer is bounded by air. The actual normal direction on the high-index side is displaced by about -4.5° .

ganic layer, can be detected as leaky modes in the high-index half-sphere. Due to a reduced cut-off thickness at smaller wavelengths, one of the modes is mainly located at wavelengths below about 520 nm. In addition, strong emission from SPs is apparent at angles of more than 50° with respect to normal direction on the high-index side.

Figure 10.6(c) shows a cross section of the measurement at a wavelength of 530 nm, i.e. close to the emission maximum of Alq₃. It is apparent that the emission intensity arising from SP and waveguide extraction is on the same order of magnitude as the intensity of the bottom emission. The different intensities of the SP emission at positive and negative angles probably arises from the optical anisotropy of the LiNbO₃ half-sphere or from the experimental setup and positioning. In addition, the positioning of the half-sphere can cause differences in emission intensity during rotation of the sample. Moreover, the half-sphere also complicates the exact alignment of the sample. As a consequence, the top emission in normal direction is detected at about -4.5° instead of 0°.

For a profound comparison of the experiment to optical simulations, it is necessary to take into account the different excitation conditions over the whole Alq₃ layer, which occur in the measurement due to the laser absorption profile of Alq₃. Therefore, the simulation was performed at ten different emitter positions having a distance to the Ag interface between 20 nm and 200 nm in steps of 20 nm. The absorption profile of Alq₃ was calculated from the absorption coefficient of approximately $4.35 \times 10^4 \text{ cm}^{-1}$, cf. Fig. 2.3 and Ref. [64]. This corresponds to a reduction of the laser intensity to 1/e of its initial value over a distance of 230 nm, hence causing a nonuniform absorption profile. In addition, it must be kept in mind that the laser is incident under 45°. Due to refraction, this corresponds to a propagation direction of approximately 24° in Alq₃ with respect to the surface normal. Moreover, about 80 % of the remaining laser intensity is reflected at the Ag interface and propagates back through the Alq₃ layer. To consider all these effects, the simulations are weighted according to the actual excitation intensity at each emitter position. It should be noted that also the different Purcell factors must be taken into account, because the decay rate of an emitter depends on the distance to the Ag layer. An isotropic emitter orientation was used and $q = 20 \%$ was assumed for the radiative quantum efficiency^{63–66}.

By using this simulation procedure, the cross section in Fig. 10.7 is obtained for the unpolarized emission at a wavelength of 530 nm. By comparing the result to the experimentally determined cross section in Fig. 10.6(c), it is apparent that the angular positions of the extracted SPs and waveguides fits quite well if the displacement of the normal direction by -4.5° in the measurement is considered. However, the direct bottom emission shows a different angular dependence in the simulation compared to the measurement. Moreover, the width of the extracted modes is narrower in the simulations. This might result from either a too low absorption in the optical constants of Alq₃ used in the simulations, or a broadening of the measured emission peaks due to the finite angular resolution and the size of the laser spot of approximately $1.5 \times 2.5 \text{ mm}^2$, or due to the optical anisotropy of the LiNbO₃ half-sphere. Nevertheless, the overall trend is reproduced quite well by the simulation.

The colored regions in Fig. 10.6(c) and Fig. 10.7 divide the cross sections into four

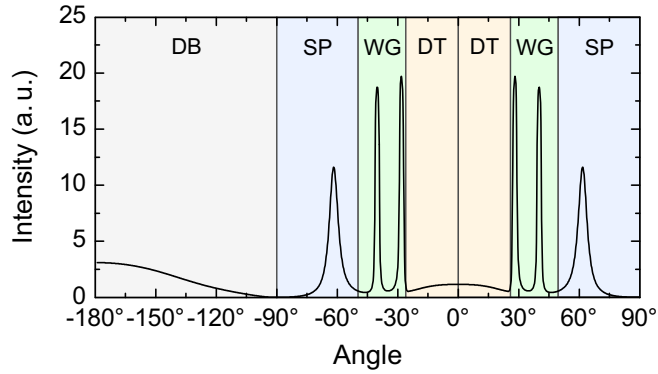


Figure 10.7: Cross section at a wavelength of 530 nm obtained from optical simulations for a stack as shown in Fig. 10.6(a). A series of emitter positions was assumed, each weighted according to the absorption profile of the 200 nm thick Alq_3 layer. Details of the procedure are explained in the text. Since the simulated waveguide modes were extremely narrow, i.e. full width at half maximum below 1° , adjacent averaging over $\pm 1^\circ$ was performed to obtain the displayed cross section. The marked regions correspond to the same emission types as in Fig. 10.6(c).

emission types: direct bottom emission (DB), direct top emission (DT), waveguide mode emission (WG), and surface plasmon emission (SP). In the case of the simulation, the boundaries between regions (DT), (WG), and (SP) were obtained according to the refractive indices of air and Alq_3 in relation to LiNbO_3 . However, in the context of the measurement, the boundaries can differ from the expected value. If the positioning of the LiNbO_3 half-sphere is not exactly on the same height as the incidence and detection plane, and if the excitation spot is not exactly centered, the half-sphere can cause focusing or expanding of the emission. Moreover, the measured emission peaks might be broadened, as discussed above. Therefore, the boundaries in the measurement were set to reasonable positions, i.e. to the bottom of the slope of the waveguide peak for the boundary between (DT) and (WG), and at the minimum between the surface plasmon and waveguide peaks for the border between (WG) and (SP).

By integrating over each region, it is possible to analyze the total emission intensity on the top side in relation to the direct bottom emission. Here, the emission is in principle spherically symmetric, if the optical anisotropy of LiNbO_3 is neglected. Therefore, the cross sections were multiplied with $(\sin \theta)$ prior to integration (cf. Eq. (A.2) in the appendix). In addition, the measured angular positions on the high index side were shifted by $+4.5^\circ$ to account for the displacement of the normal direction.

The integral results are listed in Table 10.1. It is found that the measured direct top emission on the high-index side, i.e. through the 40 nm thick Ag layer, amounts to about 2.4% of the direct bottom emission. More interestingly, the emission arising from the outcoupling of waveguide modes makes up around 40% and 94% according to the measurement and simulation, respectively. The emission intensity obtained from the extraction of SPs amounts to approximately 46% and 117% in the measured and

Type of emission	Measurement Fig. 10.6(c)	Simulation Fig. 10.7
Direct bottom emission (DB)	100 %	100 %
Direct top emission (DT)	2.4 %	7.7 %
Waveguide mode emission (WG)	40.0 %	94.1 %
Surface plasmon emission (SP)	45.8 %	117.3 %

Table 10.1: Total emission intensities obtained by multiplying the cross sections in Fig. 10.6(c) and Fig. 10.7 with $(\sin \theta)$ and integrating over the different regions. The values are specified relative to the direct bottom emission, which was set to 100 %. The experimental values represent the average over the corresponding regions at positive and negative angles.

simulated cross section, respectively. Apparently, the measured values on the high-index side are smaller by a factor of about 2.5–3. This discrepancy probably arises from a too large direct bottom emission in the measurement, which could be caused by a larger Ag thickness than expected or from an inaccurate alignment of the sample. Moreover, the LiNbO₃ half-sphere has previously been covered with different Ag and organic layers, which were removed by a cleaning process. In fact, the appearance of the LiNbO₃ surface slightly changed during this process. Thus, it is likely that the surface of the LiNbO₃ half-sphere has a certain roughness. Consequently, more light was probably extracted in bottom direction through scattering at the rough surface. This effect could also explain the different angular dependence of the measured and simulated direct bottom emission.

Nevertheless, the experiment demonstrates that the total emission can be increased by around 85 % by recovering losses from SPs and waveguides. In other words, the overall emission is almost doubled in comparison to the case without high-index coupling. According to the simulations, the outcoupling could even be enhanced by more than 200 %.

To provide an insight into the physical processes that govern the extraction of SPs and leaky modes, the total power dissipation as well as the transmitted power into both hemispheres at a wavelength of 530 nm is presented as a cross section in Fig. 10.8. The borders at approximately $1.19 \times 10^7 \text{ m}^{-1}$, $2.06 \times 10^7 \text{ m}^{-1}$, and $2.70 \times 10^7 \text{ m}^{-1}$ mark the light lines of air, Alq₃, and LiNbO₃, respectively. These borders divide the power dissipation into different regions similar to the angular cross sections above. It should be mentioned that the simulated integral values listed in Table 10.1 can be directly calculated by integrating over the different regions in Fig. 10.8.

Moreover, these borders determine the in-plane wave vector limit, up to which light can be emitted into both hemispheres. For the direct bottom emission, only radiation up to the air light line can be extracted. On the contrary, the implementation of the LiNbO₃ half-sphere in principle allows for extracting light up to the LiNbO₃ light line. As a consequence, power that is dissipated at in-plane wave vector values larger than

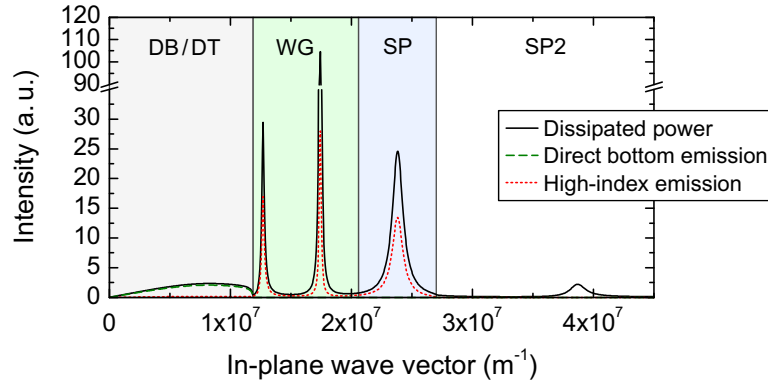


Figure 10.8: Total power dissipation of a stack according to Fig. 10.6(a) at a wavelength of 530 nm. In addition, the graph shows the transmitted power into both hemispheres, i.e. the direct bottom emission on the organic side of the Ag interface, and the top emission on the high-index side. The simulations are performed for a series of emitter positions to consider the absorption profile of the Alq₃ layer in the experiment. The marked regions refer to the same type of emission as in Fig. 10.6(c). Region (SP2) refers to power that is dissipated at in-plane wave vectors that lie outside the LiNbO₃ light cone and, hence, cannot be extracted at all by high-index coupling.

the LiNbO₃ light line, i.e. region (SP2) in Fig. 10.8, cannot be coupled out and, thus, is definitely lost. It is apparent that the main contribution in this region is coupling to a mode centered at an in-plane wave vector of $3.87 \times 10^7 \text{ m}^{-1}$. This refers to the surface plasmon mode that propagates at the interface between Ag and LiNbO₃. Fortunately, the power dissipated to the SP2 mode is about seven times smaller in comparison to the SP mode at the Ag/Alq₃ interface.

In the context of the power dissipated to direct emission in the in-plane wave vector range up to the air light line, i.e. regions (DB) and (DT), around 88.0% of the total power is transmitted into bottom direction and approximately 6.8% is transmitted through the Ag layer into top direction. The remaining power is lost due to absorption in Alq₃ or due to reflection losses at the Ag layer. As a matter of course, the power coupled to modes above the air light line can only be extracted into the LiNbO₃ half-sphere. In detail, about 35.8% of the power dissipated to waveguide modes in region (WG) can be extracted into the half-sphere. Concerning SPs, i.e. region (SP) and (SP2), 45.3% of the dissipated power can be coupled out into the prism. Considering that the power above the LiNbO₃ light line is completely lost, this number implies that roughly half of the power coupled to SPs at the Ag/Alq₃ interface is extracted by the high-index coupling approach for this particular stack layout. Certainly, especially the thickness of the Ag layer will significantly influence the extraction efficiency of SPs and waveguide modes. This will be discussed in Sec. 10.6.

It is noteworthy that the total power dissipated to waveguides is almost identical to the power which is coupled to SPs in this particular stack layout. This is due to the fact that a large fraction of the laser intensity is already absorbed in the Alq₃ layer

far away from the Ag interface, i.e. at distances where coupling to SPs is weak. In a common OLED stack with an emitter located in the first cavity maximum, i.e. at a typical distance of 50–70 nm to the cathode, considerably more power is coupled to SPs than to waveguides. Consequently, also the emission from extracted SPs should be much higher than emission arising from waveguide modes.

To summarize this section, it was demonstrated that the high-index coupling method allows for extracting a significant fraction of SPs and waveguide modes even for an Alq₃ layer with a thickness of 200 nm. For further experiments, it might be favorable to use a thin emitting layer sandwiched between two spacer layers in order to have a specified emitter position and a fixed distance from the Ag layer²⁶. It should be emphasized that the SP dispersion for an Alq₃ layer with a thickness of 200 nm is virtually similar to that of a bulk layer or, similarly, to the case of a real OLED with several organic layers. Thus, the high-index coupling approach should in principle be applicable to actual OLED devices.

10.5. Application to OLEDs

The objective of this thesis is to find ways to enhance the light extraction in OLEDs. After having demonstrated that high-index coupling serves the purpose of extracting both SPs as well as waveguide modes, the next step is to apply this technique to real OLED devices. Therefore, a state-of-the-art OLED was provided in the framework of the BMBF funded project “TOPAS 2012”. Figures 10.9(a) and (b) display the stack layout and the EL spectrum of the OLED, respectively. It is apparent that this white-emitting OLED exhibits a broad emission spectrum, spanning over more than 200 nm across the visible range.

In a normal bottom-emitting OLED, which usually features an Al or Ag cathode with a thickness of 100 nm or more, the waveguide modes are bound inside the organic layers and ITO, i.e. they propagate between the thick cathode and the interface to the glass substrate, where they are totally reflected. The dispersion of SPs at the metallic cathode is determined by the adjacent organic layers. Therefore, both the waveguide modes as well as the SPs have an in-plane wave vector of more than $(n_{\text{organic}} \cdot k_0)$, with a refractive index of the organic layers of typically $n_{\text{organic}} = 1.8$. Of course, it is not possible to extract these modes into the glass substrate ($n_{\text{glass}} \approx 1.5$) in the case of planar devices. Hence, the power dissipated to SPs and waveguide modes is lost in such an OLED structure.

In contrast to a normal bottom-emitting OLED, the device in Fig. 10.9(a) comprises an only 30 nm thick Ag cathode. By applying an appropriate high-index outcoupling structure having a refractive index larger than the organic layers, it should be possible to extract some of the bound modes into the high-index region. The chosen Ag thickness of 30 nm is on the one hand thick enough to offer a good conductivity, on the other hand

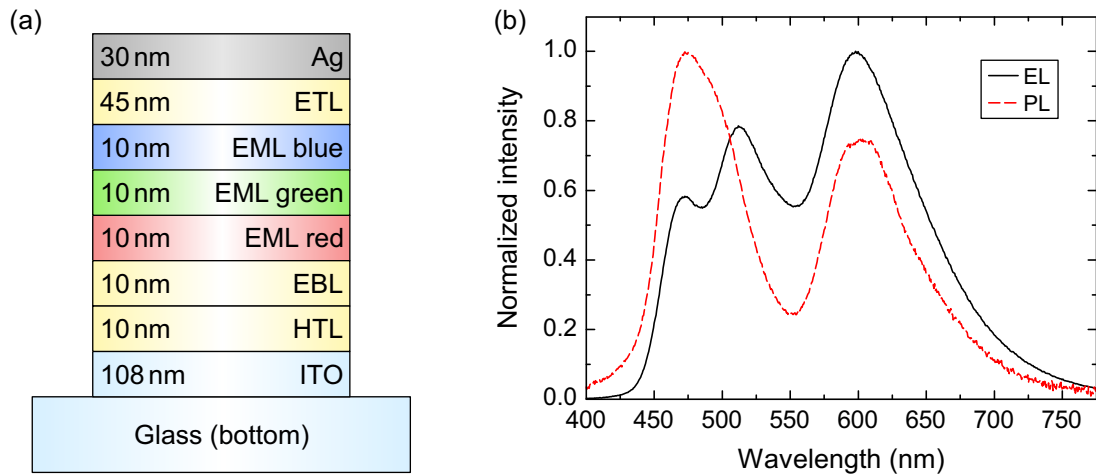


Figure 10.9: (a) Stack layout of the white OLED investigated in this section. The abbreviations refer to electron transport layer (ETL) which includes a thin hole blocking layer, three separate emission layers (EML blue, green, and red), electron blocking layer (EBL), and hole transport layer (HTL). The anode is made of indium-tin oxide (ITO), and the cathode consists of a 30 nm thick Ag layer. The active area of the OLED is about 1.67 cm^2 . Emission on the glass side is denoted as bottom emission, while top emission describes the radiation that is coupled out through the Ag cathode. (b) Electroluminescence (EL) and photoluminescence (PL) spectrum of the OLED. The EL spectrum was measured in bottom direction at a luminance of 1000 cd/m^2 under electrical operation (spectrum provided within the “TOPAS 2012” project). A 375 nm cw laser diode was used to excite the emission layers in order to obtain the PL spectrum, which represents the average of two measurements over a range from 0° to 30° with respect to the normal in bottom direction. The spectrum was corrected to account for the calibration of the experimental setup.

this thickness allows for extracting a considerable fraction of waveguide modes and SPs.

The influence of the Ag thickness on the direct emission into air was tested within the “TOPAS 2012” project using a series of OLEDs having Ag thicknesses of 30 nm, 40 nm, and 150 nm. Since the reflectivity of the Ag layer decreases with smaller thickness, the bottom emission is slightly reduced in the case of 30 nm and 40 nm thick Ag films compared to the OLED comprising 150 nm Ag. However, simultaneously the direct emission in top direction through the thin Ag layer increases. Without outcoupling structures, the total external quantum efficiency at a luminance of 1000 cd/m^2 is reduced for the OLEDs with 40 nm and 30 nm Ag by about 3% and 6%, respectively, relative to the OLED having a Ag thickness of 150 nm. As a consequence, the overall efficiency of the OLED with 30 nm thick Ag can be increased, if the additionally extracted light from waveguide modes and SPs amounts to more than 6% of the total direct emission.

As discussed above, it was not possible to use the index-matching melt with $n = 2.24$ due to its opacity and reactivity. Hence, a half-sphere made of SF6 was applied to the top side by an index-matching liquid with $n = 1.795$. Although this liquid also damaged the OLED layers, it was possible to perform measurements for roughly one hour. Regarding the bottom side, a BK7 half-sphere can be attached to the glass substrate in order to

extract substrate modes into bottom direction. Because of the size of the spheres, it was not possible to contact the OLED and measure the light emission under electrical operation. Thus, a 375 nm cw laser diode was used to excite the emission layers. Since the hole transport layer absorbs UV light, the excitation by a laser from the bottom side requires a thin HTL, as in the case of the OLED in Fig. 10.9(a). PL excitation from the top side is impossible because the SF6 half-sphere and the index-matching liquid absorb UV light. The spectrum obtained under PL excitation is plotted in Fig. 10.9(b). In comparison to the EL spectrum, it can be seen that the blue emission peak dominates the spectrum, while almost no emission from the green EML is detected.

Figure 10.10 presents top view photographs of the OLED with several combinations of applied outcoupling structures. In the case of the completely bare OLED in Fig. 10.10(a), it is apparent that the direct bottom emission has no angular dispersion and a uniform white color. The directly emitted light in top direction, i.e. through the 30 nm thick Ag layer, has a considerably lower intensity. This is also true for Fig. 10.10(b), where a BK7 half-sphere was attached to the glass substrate on the bottom side. Here, substrate modes are extracted into the bottom direction, hence the top emission appears even weaker in relation to the strong bottom emission.

The images in Figs. 10.10(c) and (d) show the same situation as part (a) and (b), respectively, but with an SF6 half-sphere attached to the top side. It is clearly apparent that the application of the SF6 half-sphere completely changes the emission on the top side. Now, several intensive and angular dispersive features are observable. According to optical simulations and polarized emission measurements, these modes arise from the outcoupling of two waveguide modes (WG1 and WG2) and even from extracted SPs. In detail, the waveguide mode denoted by WG1 is located at the smallest angular positions. Only blue emission can be seen from this mode. In contrast, the waveguide mode WG2 spans across the whole spectrum with increasing angle, i.e. from red over green to blue. Finally, SP emission at large angles close to 90° is only obtained in the red wavelength region.

At first, it seems surprising that emission from SPs can be detected at all, because SPs propagating at the interface to thick organic films (assuming $n_{\text{organic}} = 1.8$) exhibit a dispersion relation that requires a high-index material and a corresponding outcoupling structure with a refractive index of more than 1.8 in order to extract SPs. However, due to the finite thickness of the Ag film and an almost similar refractive index on both sides of the Ag layer, SP coupling takes place, as described in Sec. 7.1. As a consequence of this effect, the SP dispersion is shifted to smaller wave vectors and, thus, can be partially extracted into top direction. It is important to point out that the extracted SP emission occurs at very large angles. Therefore, only a small fraction can be actually extracted. In addition, with the current high-index structure, the recovery of SP losses is not possible in the green and blue wavelength regime. Here, the SP dispersion is still located at too large wave vectors and cannot be coupled out into the SF6 half-sphere.

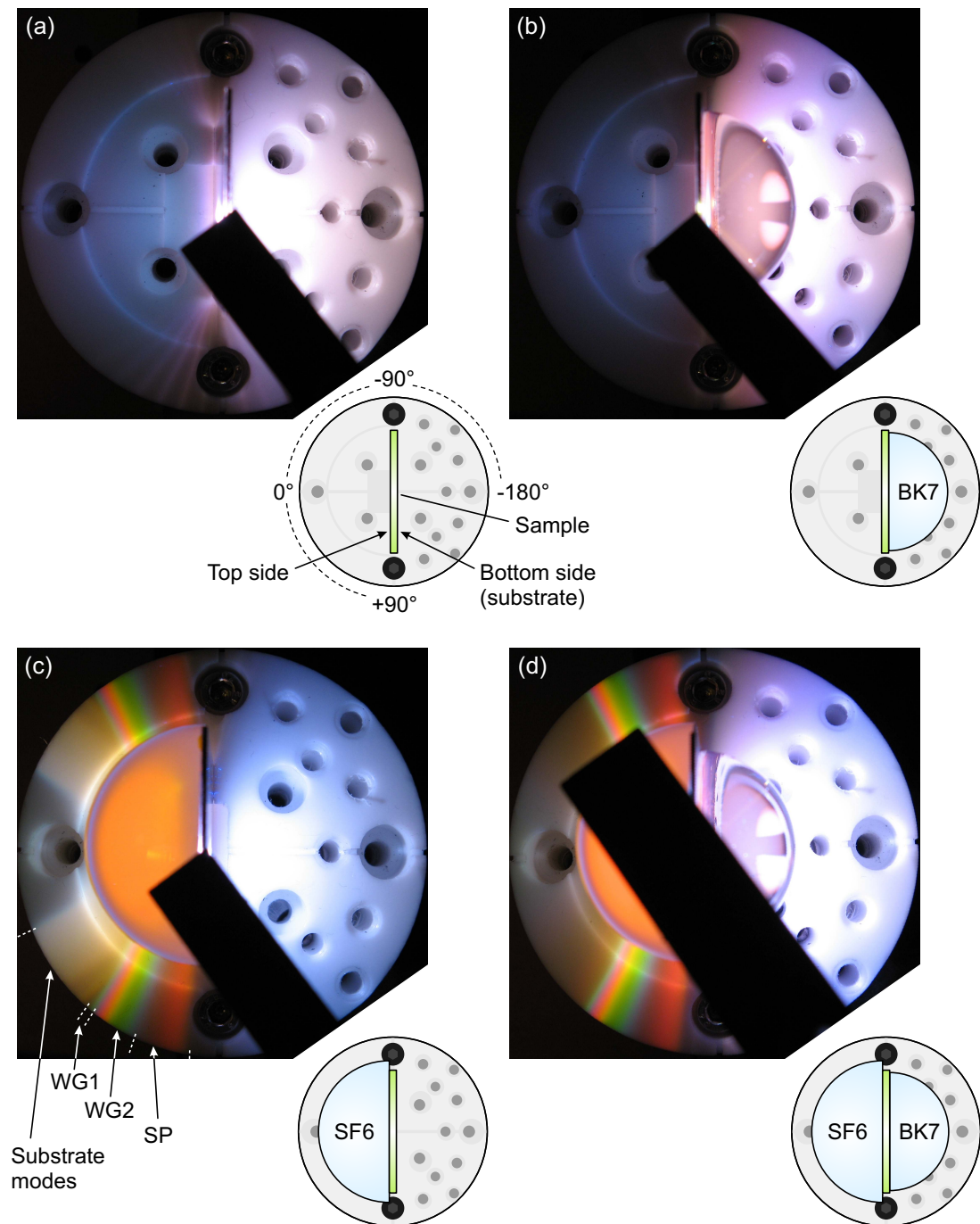


Figure 10.10: (a)–(d) Top view photographs of the white OLED with different combinations of attached outcoupling structures, i.e. BK7 and SF6 half-spheres attached to the bottom and top side, respectively. The configuration for each photograph is illustrated in the small figure next to each picture. The black area in the middle of each picture is caused by the clamp that is used to position the half-spheres and to fix them on the Teflon platform, which in turn is mounted on a rotation stage. The bottom emission in (a) and (b) appears to have a reddish color, because the pictures were taken in a dark room and, thus, the white balance slightly varies for each photograph. The abbreviations WG1, WG2, and SP refer to the two extracted waveguide modes and emission from SPs, respectively.

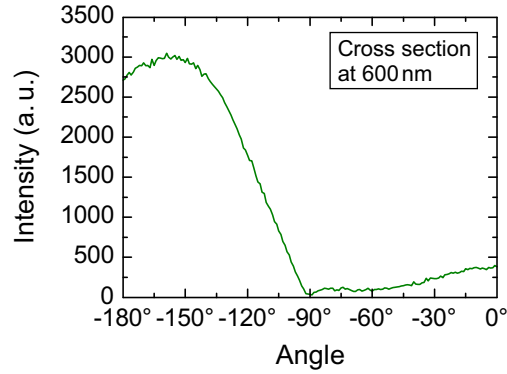


Figure 10.11: Cross section of the angular dependent direct emission at a wavelength of 600 nm in the case of the bare OLED (without attached outcoupling structures) and without polarizer. The angles from -180° to -90° correspond to bottom emission, while emission between -90° and 0° is measured on the top side of the OLED. The emission intensity around -135° and -45° was increased due to reflections of the incident laser beam. These peaks have been manually subtracted.

Nevertheless, the photographs demonstrate that the high-index coupling technique can be successfully applied to real OLED devices.

A very interesting situation occurs in Fig. 10.10(c). Here, the SF6 sphere is applied on the top side, but no BK7 half-sphere is attached to the bottom side of the OLED so that the substrate modes are totally reflected at the substrate/air interface. Consequently, some additional substrate mode emission transmits through the Ag layer and is coupled out into top direction.

Besides the photographs, the angular dependent emission was detected by means of a computer-controlled rotation stage. Figure 10.11 presents a cross section at a wavelength of 600 nm in the case of the completely bare OLED, i.e. corresponding to the photograph in Fig. 10.10(a). In this case, no sharp emission peaks are observable. Apparently, the direct emission through the 30 nm thick Ag layer is very weak compared to the bottom emission.

In order to determine the integral emission in top and bottom direction, the cross section first has to be multiplied with $(\sin \theta)$, cf. Eq. (A.2) in the appendix. By integrating over the whole angular range, it is found that approximately 92.5% of the total intensity is emitted in bottom direction and only 7.5% is emitted through the Ag film into top direction.

The angular dependent spectrally resolved emission for the OLED with attached SF6 half-sphere on the top side is presented in Fig. 10.12. All optical modes which were already observed in the photograph in Fig. 10.10(c) can also be identified in the measurement. While the bottom emission between -180° and -90° is rather broad and shows almost no dispersion, the extracted emission from waveguide modes and SPs shows a strong angular dispersive behavior. In addition, emission arising from substrate modes, which partially pass through the Ag layer, is detected in top direction at angles

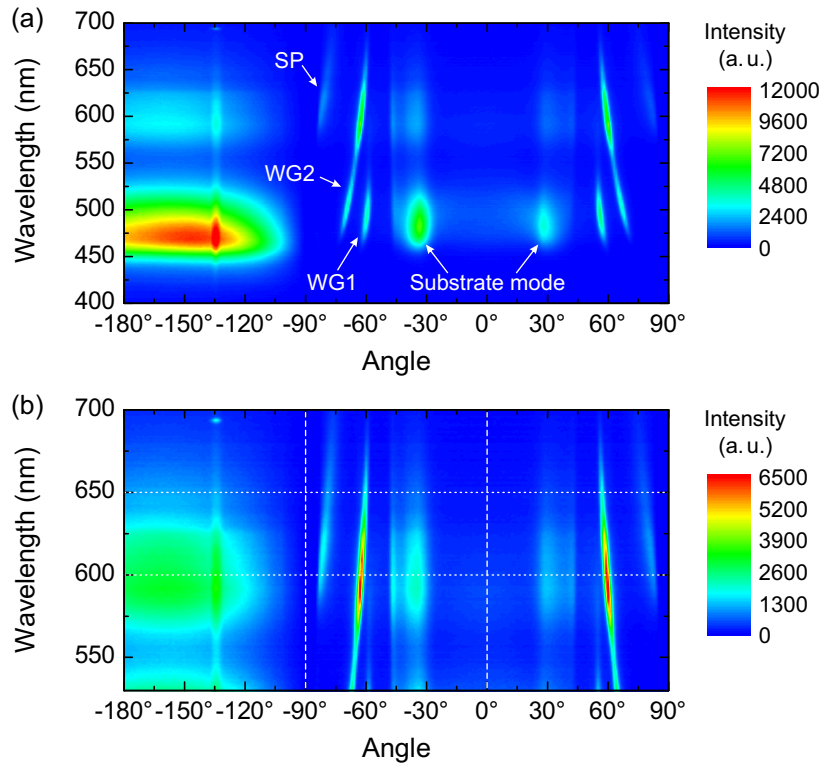


Figure 10.12: (a) Angular dependent spectrally resolved measurement of the OLED emission with attached SF6 half-sphere on the top side. The measurement was performed without polarizer. The abbreviations WG1, WG2 and SP refer to the same modes as in Fig. 10.10(c). The higher emission around -135° , -45° and $+45^\circ$ results from transmission and reflections of the incident laser beam. (b) Similar to (a), but for a wavelength range from 530 nm to 700 nm and adjusted intensity scale. The horizontal lines mark the wavelength of the cross sections in Fig. 10.13, while the vertical dashed lines indicate the boundaries at -90° and 0° .

around $\pm 30^\circ$. The polarization of the extracted modes was investigated by additional polarized emission measurements. It was found that WG2 is s-polarized, while WG1 and of course the extracted SP emission are p-polarized.

As mentioned above, the index-matching liquid with $n = 1.795$ absorbs some of the light in the blue and green wavelength range. This effect is apparent by comparing the angular dependent emission intensity in Fig. 10.12(a) for e.g. 500 nm and 600 nm. Although the direct bottom emission is much higher at 500 nm wavelength, the emission from the extracted WG2 mode is larger at 600 nm wavelength. Certainly, it can be assumed that the power that is initially coupled to guided modes and plasmons is also larger at 500 nm. However, a large fraction of the light is absorbed by the index-matching layer before it passes into the SF6 half-sphere. Consequently, the further discussion concentrates on the red spectral range. In this wavelength regime, it can be assumed that most of the recovered waveguide and SP emission can be ultimately coupled out and detected. The corresponding rescaled emission measurement is displayed

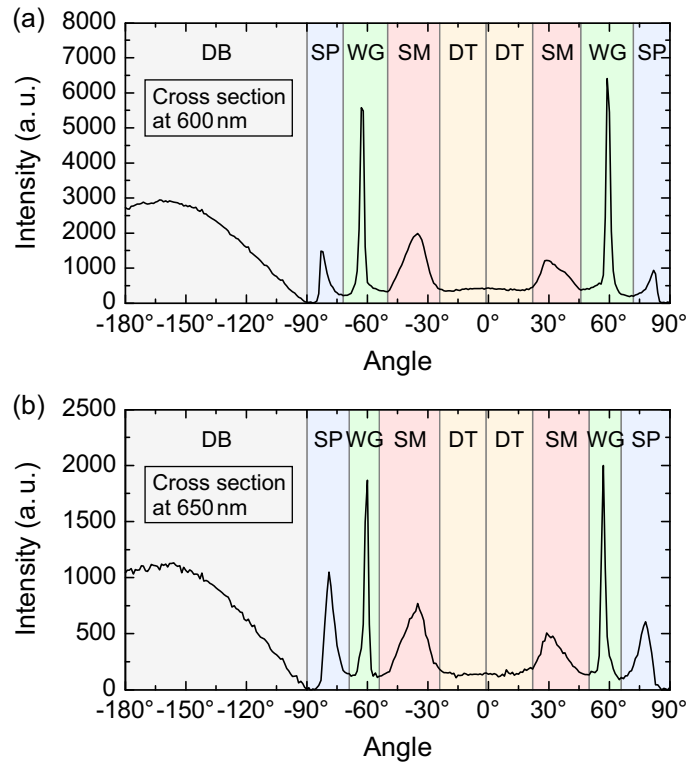


Figure 10.13: Cross sections of the measurement in Fig. 10.12(b) at wavelengths of (a) 600 nm and (b) 650 nm. The increased intensity around -135° , -45° and $+45^\circ$ due to the transmitted and reflected laser has been manually subtracted. The regions corresponding to different emission types are denoted by direct bottom emission (DB), direct top emission (DT), substrate mode emission (SM), waveguide modes (WG), and surface plasmons (SP).

in Fig. 10.12(b).

A detailed analysis of the intensity of each mode can be obtained from cross sections, as shown in Figs. 10.13(a) and (b) at wavelengths of 600 nm and 650 nm, respectively. As discussed above, emission from SPs is more efficient for larger wavelengths. In this case, the SP emission is located at smaller angles. This can also be seen by comparing both cross sections. At a wavelength of 650 nm, the peak emission from extracted SPs is shifted by about 4° compared to the peak at 600 nm wavelength, and the relative intensity is significantly increased. However, it is likely that considerably more emission from SPs could be extracted with a higher refractive index on the top side.

A comment should be made regarding the substrate mode emission. According to the refractive index ratio of air ($n = 1$) and the high-index material (SF6, $n \approx 1.8$), the substrate mode emission should occur at angles above around 33.7° . However, here the substrate mode emission in top direction can already be detected at angles below 25° . This is a result of the optical path of the substrate modes. First, the radiation propagates at an oblique angle through the substrate to the glass/air interface, where it is totally reflected. When the light travels back and passes through the Ag layer into

Type of emission	Cross section at 600 nm	Cross section at 650 nm
Direct bottom emission (DB)	100 %	100 %
Direct top emission (DT)	1.9 %	1.9 %
Substrate mode emission (SM)	15.7 %	16.8 %
Waveguide mode emission (WG)	22.8 %	16.0 %
Surface plasmon emission (SP)	7.8 %	16.4 %

Table 10.2: Total emission intensities obtained by integrating over the different regions in the cross sections in Figs. 10.13(a) and (b). All values are specified relative to the direct bottom emission, which was set to 100 %. The values represent the average over the corresponding regions measured at positive and negative angles. The cross sections were multiplied with $(\sin \theta)$ prior to integration to compute the integral emission over all azimuthal angles. In addition, the measured angular positions on the top side were shifted by $+1^\circ$ so that symmetric peaks with respect to the surface normal were obtained.

the high-index material, it is no more in the center of the SF6 half-sphere. As a consequence, the emission does not impinge under normal incidence on the SF6/air interface. This causes refraction and, thus, a modification of the emission angle. Altogether, the emission is focused to smaller angles. Therefore, it partially overlaps with the direct top emission. Moreover, the finite size of the laser spot even enhances this effect.

By integrating over the different regions marked in Figs. 10.13(a) and (b), the total intensity in each region can be compared to the direct emission that would also be obtained without high-index coupling. The result is listed in Table 10.2. As a consequence of the integration boundaries and the focused substrate mode emission, a few percent of the direct top emission is mistakenly counted as substrate mode emission. Nevertheless, the overall intensity of the OLED is significantly enhanced compared to the total direct emission. In fact, the recovery of waveguide mode and SP losses increases the total intensity by approximately 30 %. If also the additional emission from substrate modes is taken into account, the overall increase in intensity amounts to more than 45 %.

This enhancement is remarkable for two reasons. First, the actual OLED device represents a device structure that is already designed to obtain a very high direct emission. Certainly, it is not straightforward to further increase the overall light extraction. Second, the refractive index of the high-index material is just large enough to extract the waveguide modes and a small fraction of the power dissipated to SPs. It is expected that considerably more SP emission could be extracted by using a material with higher refractive index.

In the context of the OLED discussed in this section, it would be promising to perform optical simulations in order to further analyze the measured results. However, the actual thickness of the index-matching layer is unknown. Thus, the absorption of this layer cannot be taken into account in polychromatic simulations. Instead of comparing this particular OLED to optical simulations, the general dependence of the high-index

coupling on several parameters will be investigated by means of optical simulations in the following section.

10.6. Efficiency prediction by optical simulations

In the context of high-index coupling, the most important parameters are the refractive index n_{HI} of the high-index region and the thickness of the Ag film. Taking the OLED from the previous chapter as a starting point, optical simulations are performed to investigate the physical processes in detail. Using an OLED stack in the simulations has the advantage that the location of the emitter is rather well defined due to the narrow emission region. Since the simulations are performed monochromatically at a wavelength of 600 nm, the emitter is positioned in the middle of the red emission layer.

Figure 10.14(a) presents the stack layout for investigating the influence of the refractive index of the high-index region. In order to thoroughly analyze the results, the total emission is divided into bottom and top emission, i.e. emission into the direction of the substrate and the high-index region, respectively. The bottom emission can be divided into direct bottom emission (DB) and substrate bottom emission (SB). In detail, DB corresponds to power dissipated in an in-plane wave vector range of $0 \leq k_x \leq k_0$, with $k_0 \approx 1.047 \times 10^7 \text{ m}^{-1}$ being the vacuum wave vector. The substrate bottom emission describes light that has an in-plane wave vector between the air light line ($k_x = k_0$) and the glass light line ($k_x \approx 1.51 \cdot k_0$). Similarly, the direct and substrate top emission (DT and ST) cover the same in-plane wave vector ranges, but the emission occurs into the high-index region. In addition, the top emission comprises two more contributions, which are denoted waveguide modes (WG) and surface plasmons (SP).

It is noteworthy that it is not straightforward to define the border between waveguide modes and SPs, because the in-plane wave vector of waveguide modes depends on the combination of all organic layers and ITO. To complicate the picture, the dispersion of waveguides and especially SPs is broadened and both modes may overlap. Therefore, the border between WG and SP is manually determined by the minimum position between both adjacent modes. Even if some emission is accidentally assigned to SPs instead of waveguides or vice versa, this does not change the overall emission that is additionally extracted by high-index coupling, because it is desirable to extract both waveguides as well as SPs.

The total power dissipation for n_{HI} varying between 1.5 and 2.5 in steps of 0.1 is plotted in Fig. 10.14(b). Regarding the waveguide mode at about $k_x = 1.67 \times 10^7 \text{ m}^{-1}$, it can be seen that the position of the waveguide mode is constant for all values of n_{HI} . The power coupled to the waveguide mode is only slightly changed with varying n_{HI} . On the contrary, the SP dispersion is strongly influenced. In fact, two SP branches can be identified in the graph, owing to the existence of two Ag interfaces. Besides the surface plasmon branch next to the waveguide mode (denoted by SP in the graph), a

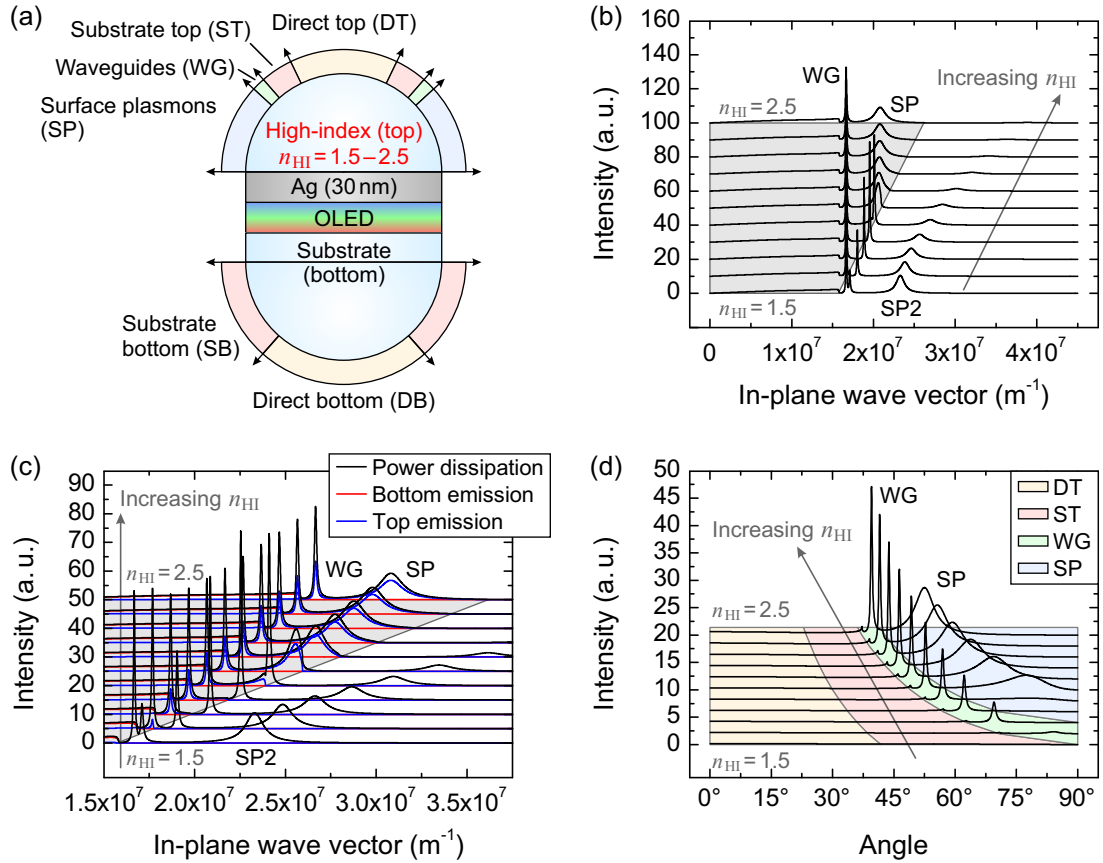


Figure 10.14: Influence of the refractive index n_{HI} of the high-index region on the high-index coupling method studied by optical simulations. The refractive index is varied between 1.5 and 2.5. The simulations are performed monochromatically at a wavelength of 600 nm. (a) OLED device structure and definition of optical modes emitted in top and bottom direction. The detailed OLED layout is similar to Fig. 10.9(a). In particular, the Ag layer has a fixed thickness of 30 nm. A quantum efficiency of $q = 100\%$ and an isotropic emitter orientation are assumed. (b) Total power dissipation. The gray area indicates the high-index light cone. SP2 denotes the second surface plasmon branch located at larger wave vectors. (c) Detail of (b) showing the total power dissipation as well as the emission in bottom and top direction. Here, the simulations are also displaced in horizontal direction for reasons of clarity. (d) Angular dependent unpolarized top emission.

second branch (SP2) can be seen at larger in-plane wave vectors. For $n_{\text{HI}} = 1.5$, most of the power is coupled to SP2, which in this case can be regarded as SPs propagating at the Ag/organic interface. With increasing n_{HI} , both SP branches shift to larger wave vectors. As soon as the refractive indices on both sides of Ag are almost equal, i.e. $n_{\text{HI}} \approx 1.7 - 1.8$, coupling of both SP branches occurs (cf. Sec. 7.1). For even higher n_{HI} , the first SP branch takes a rather fixed position around $k_x = 2.08 \times 10^7 \text{ m}^{-1}$, while SP2 continuously shifts to higher k_x values. In this case, the SP branch at lower k_x can be assigned to the Ag/organic interface, while SP2 propagates at the interface between Ag and the high-index region. Of course, the SP2 branch can never be extracted

and all power dissipated to SP2 is definitely lost. Fortunately, coupling to SP2 strongly decreases with increasing n_{HI} . Consequently, this unfavorable optical channel represents no limitation to the efficiency of this coupling method.

The gray area in Fig. 10.14(b) illustrates the high-index light cone, which is determined by $0 \leq k_x \leq (n_{\text{HI}} \cdot k_0)$. This defines the maximum in-plane wave vector that can be extracted into the high-index region. Apparently, a certain value of n_{HI} is required in order to extract waveguide modes or even SPs. This is more obvious by calculating the light that is transmitted through the Ag film into the high-index region, i.e. the top emission, which is depicted in Fig. 10.14(c) as blue curves. In the context of SPs, an even larger refractive index of $n_{\text{HI}} > 2.0$ is necessary to efficiently extract power coupled to SPs. The graph also shows the bottom emission (red curves). Of course, only direct and substrate emission contribute to light extracted into bottom direction because waveguide modes and SPs are not allowed to propagate in the substrate.

In terms of an application, it is important to know the angular dependent emission in top direction, which can be computed by converting the in-plane wave vector values into an angle inside the high-index region. The result is presented in Fig. 10.14(d). Obviously, emission from waveguides and SPs is strongly non-Lambertian. Hence, certain measures must be taken in order to obtain a uniform emission profile, as will be discussed in the next section. With increasing n_{HI} , the emission of each mode is shifted to smaller angles, i.e. the light is extracted at an angle closer to normal direction. Regarding the direct bottom emission (not shown), the angular dependence of the emission is close to Lambertian and virtually unchanged. In detail, the maximum and minimum intensity of the bottom emission for all values of n_{HI} differ by less than 1%. This is an important finding that implies that the direct bottom emission of the OLED is almost completely independent of the high-index region for a constant Ag thickness of 30 nm. Thus, any additionally extracted emission in top direction enhances the overall light extraction.

The efficiency of the high-index coupling technique can be estimated by integrating over the k_x range that corresponds to each optical mode. The result is shown in Fig. 10.15(a). The values are given relative to the direct bottom emission. This is a good reference value because it represents the amount of extracted light which would also be obtained without a high-index region on top of the Ag film. As a result of this normalization, the assumed radiative quantum efficiency (here $q = 100\%$) has no influence on the comparison of different simulations. Due to the 30 nm thick Ag layer, the direct and substrate emission in top direction are significantly smaller compared to the bottom emission. Regarding the dependence on n_{HI} , the direct and substrate emission in top as well as bottom direction show a rather constant behavior.

In contrast, the waveguide mode emission depends on the actual value of n_{HI} . As discussed above, a refractive index of about $n_{\text{HI}} \geq 1.7$ is required to extract most of the WG emission. For even larger values, this emission approaches a value of almost 40%

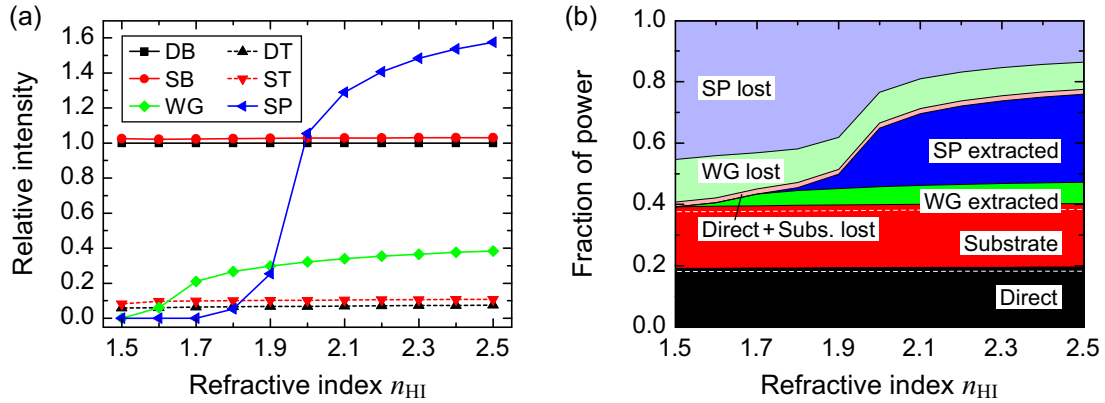


Figure 10.15: (a) Integral intensity of all extracted modes in Fig. 10.14(c) relative to the direct top emission, which changes by less than 1% between all simulations. (b) Fraction of power coupled to all optical channels. The contribution to each mode is split into two parts to differentiate between power that is lost and power that can be extracted. In addition, the direct and substrate emission are further divided into the fraction on the bottom and top side by horizontal dashed lines, where the smaller fraction represents the emission in top direction. The outcoupling efficiency is given by the sum of direct, substrate, WG extracted, and SP extracted.

relative to the direct bottom emission. It should be pointed out that the minimum n_{HI} required for extracting the waveguide mode generally depends on the effective index of the mode and, thus, on the actual device structure.

Regarding the emission from SPs, an even more pronounced dependence on n_{HI} can be seen. Emission from SPs is not observed for a refractive index $n_{\text{HI}} < 1.8$. However, for higher values, the SP emission strongly increases and approaches an emission intensity of more than 150% relative to the direct bottom emission.

In order to estimate the overall efficiency of high-index coupling, the extracted power is compared to the total dissipated power, as shown in Fig. 10.15(b). The power in each mode is split into a fraction that can be extracted as free-space radiation in either bottom or top direction, and a fraction that cannot be coupled out and, thus, is finally lost. It can be seen that roughly 20% of the total power is extracted as direct emission. The same applies to substrate emission. Only a small amount of power from these optical modes is lost due to absorption in the device. Concerning extracted emission from waveguide modes, approximately 7% of the total power can be coupled out into the high-index region, provided that the refractive index is large enough. The extracted radiation arising from SPs even amounts to almost 30% for an optimal value of n_{HI} . By adding all extracted modes, the total outcoupling efficiency η_{out} is obtained. While η_{out} takes a value of about 20% (direct emission only) or 40% (direct emission and substrate emission) for small values of n_{HI} , a total outcoupling efficiency of more than 75% is achieved for the highest simulated value of $n_{\text{HI}} = 2.5$. In other words, the overall intensity is almost doubled with respect to the sum of direct and substrate emission.

If no outcoupling structure is applied to the bottom side of the OLED, the additional

emission from waveguides and SPs is roughly twice as large as the bottom emission. Thus, the total intensity is tripled by means of high-index coupling, if all of the emission in the high-index region could be extracted into air. Moreover, in this case the substrate bottom emission will be reflected at the substrate/air interface. Due to the Ag thickness of 30 nm, a certain fraction of light will be transmitted through the Ag film into the high-index region, hence increasing the emission on the high-index side even further.

It is also interesting to analyze the fraction of waveguides and SPs which can be extracted as free-space radiation. By comparing the extracted power and the lost power in Fig. 10.15(b), it is found that roughly 44 % of all waveguide modes and 68 % of SPs can be coupled out, given that the refractive index of the high-index region is around $n_{\text{HI}} = 2.5$. Even for a more moderate value of $n_{\text{HI}} = 2.2$, around 40 % of all waveguides and 60 % of SPs can be extracted according to the simulations.

Besides the refractive index n_{HI} of the high-index region, the thickness of the Ag film is an important parameter that determines the efficiency of high-index coupling. In order to study the influence of the Ag thickness, optical simulations are performed with a Ag thickness varying between 10 nm and 60 nm in steps of 5 nm, as schematically illustrated in Fig. 10.16(a). A constant $n_{\text{HI}} = 2.3$ is assumed for the simulations, because this value is high enough to allow for extracting both waveguide modes as well as SPs. Moreover, several promising transparent materials are available with a refractive index of 2.3 or larger in the visible spectral range²¹⁶. Besides LiNbO₃, for instance titanium dioxide (TiO₂) or strontium titanate (SrTiO₃) could be implemented. The remaining OLED layers are similar to the OLED stack from the previous section.

The total optical power dissipation is presented in Fig. 10.16(b). For a small Ag thickness, the peaks corresponding to the waveguide mode and the SP mode are very broad and overlap. With increasing Ag thickness, both optical modes become considerably narrower. It should be noted that the SP dispersion is located at smaller k_x values for thin Ag layers. This effect reduces the value of n_{HI} which is required to extract SPs in case of Ag films with a small thickness. Regarding the second SP branch (SP2), it can be seen that coupling to this mode is very weak in comparison to the power dissipated to waveguides and to the first SP branch. The position of SP2 shifts to very high wave vectors with decreasing Ag thickness. For a 10 nm thick Ag film, the maximum of the SP2 peak is located at about $k_x = 6.65 \times 10^7 \text{ m}^{-1}$. Although this peak is not recognizable due to the scaling in Fig. 10.16(b), the upper k_x limit in the simulation should be set to at least $8 \times 10^7 \text{ m}^{-1}$ to include coupling to this optical channel.

Figure 10.16(c) shows the part of the total power dissipation that lies within the light cone of the high-index region with $n_{\text{HI}} = 2.3$. In addition, the transmitted emission in top and bottom direction is presented. Concerning the direct and substrate emission ($k_x < 1.58 \times 10^7 \text{ m}^{-1}$), it can be seen that a certain fraction is emitted into the high-index region as long as the Ag layer is thin. With increasing Ag thickness, the emission transmitted through the Ag film decreases. Regarding the recovery of waveguide and

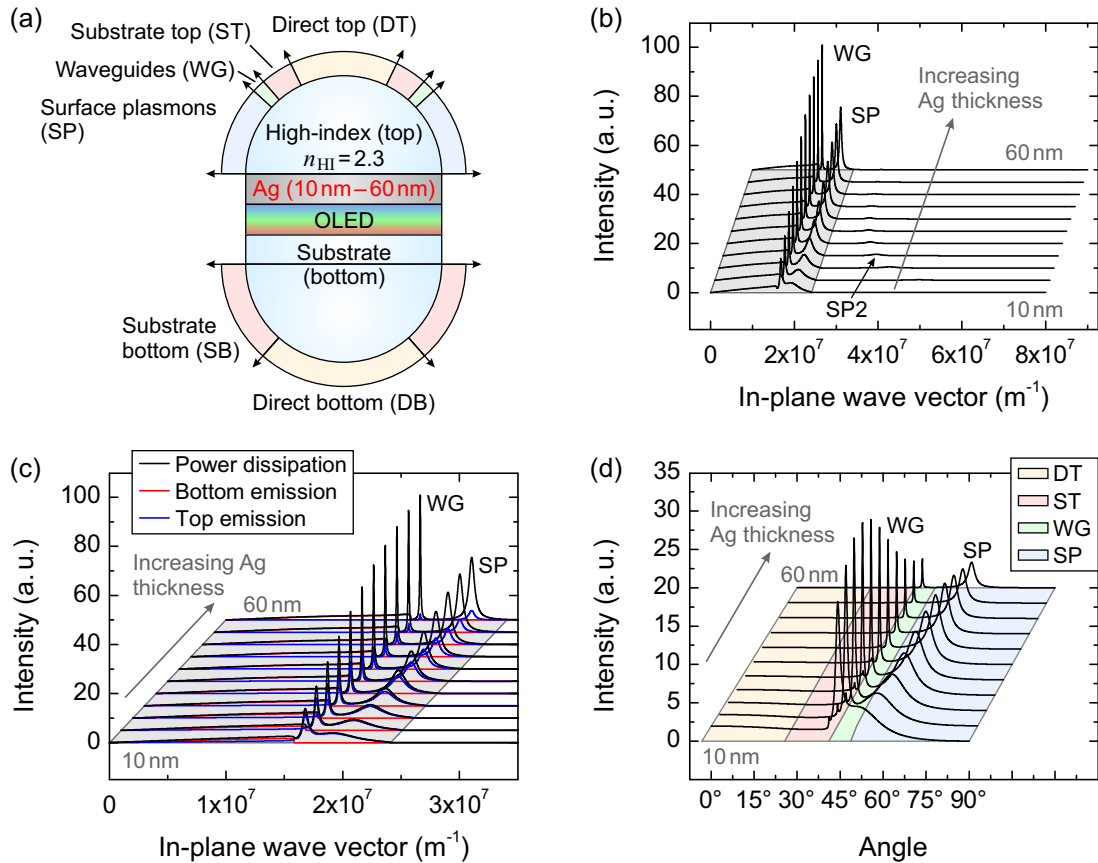


Figure 10.16: Influence of the Ag thickness on the high-index coupling method studied by optical simulations. The thickness of the Ag layer is varied between 10 nm and 60 nm. The simulations are performed monochromatically at a wavelength of 600 nm. (a) OLED device structure and definition of optical modes emitted in top and bottom direction. The refractive index of the high-index region is set to 2.3. A quantum efficiency of $q = 100\%$ and an isotropic emitter orientation are assumed. (b) Total power dissipation. The gray area indicates the high-index light cone. (c) Detail of (b) showing the total power dissipation as well as the emission in bottom and top direction. (d) Angular dependent unpolarized top emission.

SP losses, of course only emission into the high-index region takes place. Apparently, the emission strongly depends on the Ag thickness, i.e. almost the complete dissipated power can be extracted for small Ag thicknesses, while the ratio of extracted power to dissipated power decreases with increasing Ag thickness.

The angular dependent emission into the high-index region is shown in Fig. 10.16(d). Here, the position of the extracted waveguide and SP emission is rather constant. However, the peak intensity and width of the emission are considerably influenced by the actual thickness of the Ag film.

Figure 10.17(a) illustrates the dependence of the high-index coupling efficiency on the Ag thickness, which is estimated by integrating over appropriate k_x ranges in Fig. 10.16(c). All values are given relative to the total direct emission, i.e. the sum

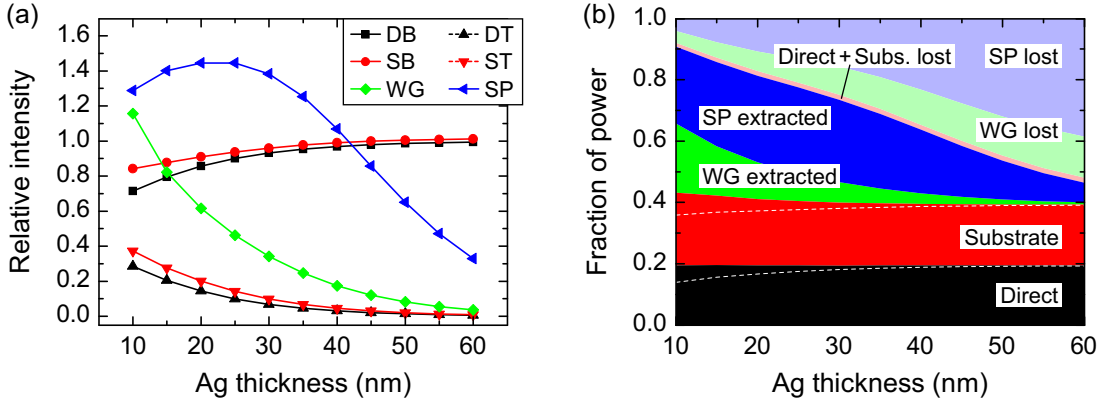


Figure 10.17: (a) Integral intensity of all extracted modes in Fig. 10.16(c) relative to the sum of direct top and bottom emission. (b) Fraction of power coupled to all optical channels. The contribution to each mode is split into two parts to differentiate between power that is lost and power that can be extracted. In addition, the direct and substrate emission are further divided into the fraction on the bottom and top side by horizontal dashed lines. The outcoupling efficiency is given by the sum of direct, substrate, WG extracted, and SP extracted.

of direct bottom and direct top emission, because this value varies by less than 1 % for all simulations. It can be clearly seen that direct emission as well as substrate emission occur in both directions, but the emission in top direction quickly diminishes with increasing thickness of the Ag film, because the reflectance of the Ag layer increases and the transmittance decreases.

The dependence of waveguide modes on the Ag thickness is basically similar to the direct and substrate top emission, i.e. the relative intensity monotonically decreases with increasing Ag thickness. On the contrary, the emission arising from SPs first rises and reaches a peak at 20–25 nm Ag and then decreases. This behavior can be explained by two competing effects. On the one hand, coupling to SPs increases as the Ag layer gets thicker. On the other hand, the fraction of SPs that can be extracted gets smaller with increasing Ag thickness. Altogether, this leads to a certain Ag thickness that corresponds to a maximum SP emission.

However, for an OLED the total light extraction should be maximized, not only the emission arising from single modes like recovered SPs. Therefore, Fig. 10.17(b) shows the extracted power in relation to the dissipated power (i.e. the outcoupling efficiency η_{out}). According to the optical simulations, a maximum η_{out} of more than 90 % could be obtained for the smallest Ag thickness of 10 nm. In this case, one third of the light is emitted in bottom direction and two thirds in top direction. More than half of the total emission arises from recovered waveguides and SPs. This clearly illustrates the enormous potential of the high-index coupling approach.

In terms of an application, a certain minimum Ag thickness might be required for good charge transport and to obtain a strong emission in bottom direction. For in-

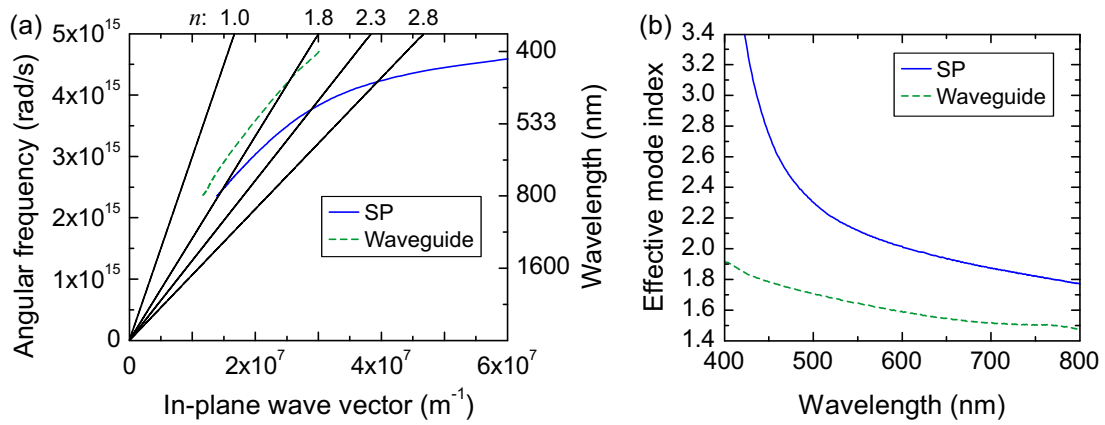


Figure 10.18: (a) Dispersion relation of the s-polarized waveguide mode and of SPs in a stack similar to Fig. 10.9(a) except for a bulk Ag cathode. The emitter is positioned closer to the Ag cathode at a distance of 35 nm to increase coupling to SPs, thus simplifying the determination of the SP dispersion. In addition, the light lines for materials having refractive indices of 1.0, 1.8, 2.3, and 2.8 are shown. (b) Effective mode index of waveguides and SPs. The values are calculated by $n_{\text{eff}} = (k_x/k_0)$, with k_x being the in-plane wave vector of waveguides or SPs from part (a) of the figure, and k_0 describing the vacuum wave vector for a certain angular frequency. For wavelengths above approximately 740 nm, the waveguide mode becomes a leaky mode, i.e. it can partially escape into the glass substrate.

stance, in the case of a 30 nm thick Ag film, the emission in bottom direction is only slightly reduced in comparison to a bulk Ag cathode. Nevertheless, due to the high-index coupling, the total light extraction can be almost doubled in comparison to the bottom emission alone, still yielding a very high η_{out} of more than 70 % according to the simulations. Even if the radiation cannot be completely extracted from the high-index region due to some reflection or absorption losses, the outcoupling efficiency still could be significantly enhanced.

A comment should be made regarding the substrate emission. If no outcoupling structure is applied to the substrate of the OLED, the substrate emission will be totally internally reflected at the substrate/air interface. As a consequence, the radiation is guided between the substrate and the Ag film, and a certain amount of light is transmitted through the Ag layer upon each reflection. Hence, the substrate emission can be partially extracted into the high-index region, thus further increasing the emission into top direction.

Up to now, the simulations discussed in this section were performed monochromatically at a wavelength of 600 nm. In the context of white OLEDs with a broad emission spectrum, it is necessary to discuss the influence of the wavelength on the high-index coupling technique. Therefore, Fig. 10.18(a) shows the dispersion of the main waveguide mode as well as of SPs in a typical OLED structure. In order to extract waveguides and SPs into a high-index material, the light line of the high-index region must lie at a larger in-plane wave vector compared to the dispersion of waveguides and SPs, respectively.

A more detailed picture can be obtained by converting the dispersion relations into an effective mode index. This value corresponds to the minimum refractive index of a high-index region which is required to extract waveguides and SPs, respectively. The result is plotted in Fig. 10.18(b). Regarding the effective mode index of waveguides, it can be seen that a refractive index of about $n_{\text{HI}} = 1.8$ is sufficient to extract the waveguide mode. Only in the deep blue wavelength range a slightly higher refractive index would be required. It should be noted, however, that the dispersion of waveguide modes depends on the actual stack layout, in particular on the refractive indices and thicknesses of the organic layers and ITO.

In the context of SPs, a higher refractive index of the high-index material allows for extracting SPs down to smaller wavelengths, i.e. higher frequencies. In detail, a rather moderate refractive index of $n_{\text{HI}} \approx 2.0$ is required to convert SPs into free-space radiation for wavelengths above 600 nm. For extracting SPs down to wavelengths of around 500 nm, the high-index material must have a refractive index of approximately 2.3. It is apparent from Fig. 10.18(b) that the recovery of SPs by high-index coupling becomes more challenging at smaller wavelengths as a result of the SP dispersion in this range. Furthermore, the effective mode index only describes the maximum of the SP dispersion. Due to the width of the dispersion, an even slightly higher refractive index should be used.

Using common metal oxides like TiO_2 as high-index material allows for converting SPs into light for a broad range of wavelengths spanning the entire visible spectrum except for the blue and blue-green range. Nevertheless, waveguide modes can still be extracted in the blue wavelength range, thus increasing the outcoupling efficiency for the entire spectrum. In fact, optical simulations using a blue emitter spectrum predict that high-index coupling allows for increasing the outcoupling efficiency to about 60 %, if $n_{\text{HI}} = 2.3$ and a Ag thickness of 30 nm are assumed and if substrate modes are extracted. Around 1/3 of this value can be attributed to high-index coupling. By performing separate simulations for blue, green, and red emitters, an overall outcoupling efficiency for white OLEDs of well above 65 % can be estimated.

Moreover, several measures can be taken to improve SP extraction. First, the implementation of an Al cathode could be advantageous to extract SPs in the deep blue wavelength range because the SP dispersion at an interface to Al is located at smaller k_x values in comparison to an interface to Ag. However, this would probably strongly reduce the extraction efficiency in the green and red wavelength range. Second, by using a Ag film with a finite thickness of a few tens of nanometers, the SP dispersion shifts to smaller k_x values compared to a thick Ag film. Hence, a smaller value of n_{HI} is sufficient to extract SPs for a certain device layout. Finally, the SP dispersion can be influenced by the organic materials close to the cathode. By using materials with a low refractive index, the dispersion can be further shifted towards smaller k_x values.

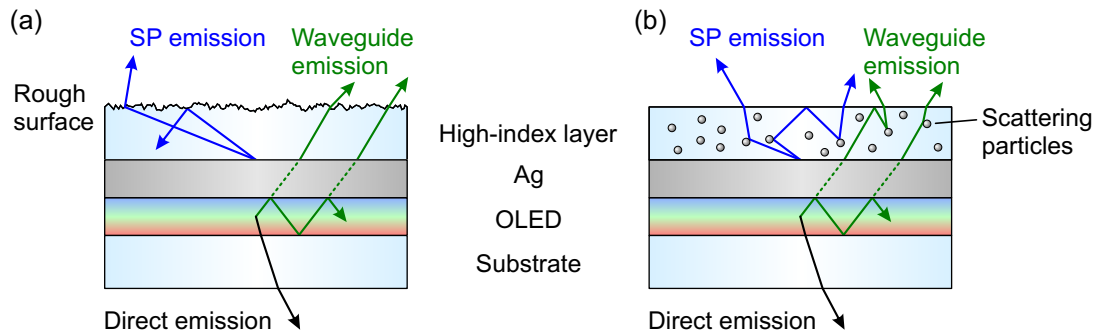


Figure 10.19: Schematic illustration of two concepts to extract light from a high-index layer. (a) Rough surface at the interface between the high-index layer and air. (b) Scattering particles implemented into the high-index layer.

10.7. Technical implementation of high-index coupling

In order to enhance light outcoupling in commercial OLEDs, it is required to find a way to combine high-index coupling with large-area OLEDs. As a matter of course, it is not practicable to apply large outcoupling structures like half-spheres. Fortunately, a very recent and promising way of encapsulating OLEDs is perfectly suited to be combined with high-index coupling. Meyer *et al.* proposed to use thin film barriers of metal oxides fabricated by atomic layer deposition, which allows for uniform high-quality coatings^{217,218}. Moreover, it is possible to use many different metal oxides and to tailor the properties of such an encapsulation^{219,220}. It is noteworthy that a capping layer has no influence on the electrical properties of the device¹⁷².

This leaves only two challenges to be solved. First, the thickness of the cathode must be reduced. Usually, bottom-emitting OLEDs have a Ag or Al cathode with a thickness of 100 nm or more. Since Ag has an excellent conductivity, it should be possible to reduce the film thickness to 30 nm or even less. However, the second challenge is more complex. Once the light is extracted into the high-index layer, it must be coupled out into air. This is not straightforward, since the radiation recovered from waveguide and SP losses is emitted at angles which lead to total internal reflection at the interface between the high-index layer and air. If the light is reflected and again impinges on the Ag film, it is reabsorbed into waveguides and SPs, respectively. Hence, the total internal reflection at the interface to air must be overcome.

Figure 10.19 illustrates two possible methods that could solve this issue²¹⁵. First, the interface can be corrugated so that light is incident under a range of angles and partially coupled out into air, as depicted in Fig. 10.19(a). Even if light is still reflected, it is likely that the direction of propagation is changed. Thus, light can no more be reabsorbed into waveguide modes or SPs because energy and momentum conservation cannot be fulfilled. In principle, such a surface structure can consist of a periodic corrugation, as discussed in the context of grating coupling in Chapter 8. However, for

many applications it would be advantageous to implement a random grating in order to turn the strongly dispersive emission from waveguides and plasmons into an isotropic emission. Such a structure could be obtained for instance in an etching process, by laser structuring, by mechanical roughening, or by intentionally producing rough films by adjusting the deposition conditions.

A second approach is presented in Fig. 10.19(b). Here, scattering particles are implemented into the high-index layer in order to scatter light so that it arrives at the interface to air at an angle smaller than the critical angle of total internal reflection. For scattering to occur, there must be a refractive index contrast between the scattering particles and the surrounding medium. Generally, metallic nanoparticles offer a high contrast, but it is also possible to embed nanoparticles made of a metal oxide. For instance, it was reported that titanium dioxide nanoparticles can be dispersed into a polymer matrix²²¹. Moreover, nanoparticles can even be combined with an epoxy²²², thus also offering an encapsulation effect. Another interesting approach is the implementation of phosphor particles in the high-index layer to obtain both a scattering effect as well as partial color conversion^{35,37}. Finally, it is worth mentioning that the implementation of scattering particles may improve the angular dispersive emission arising from waveguides and SPs, similar to the effect of a rough surface.

It should be pointed out that all outcoupling structures discussed above cannot completely extract the emission from the high-index layer because some radiation still suffers total internal reflection and may be absorbed in the high-index layer or at the Ag interface. Thus, the results from the optical simulations represent an upper limit to the outcoupling efficiency. Furthermore, reflection losses occur upon propagation from a high-index medium to air even at angles below the critical angle of total internal reflection. According to Eq. (3.41), a notable reflectance of around 15.5% is obtained under normal incidence on the interface, assuming $n_{\text{HI}} = 2.3$ for the high-index layer and $n = 1.0$ for air. These losses can be reduced by implementing additional layers with gradually decreasing refractive index²²². For instance, by simply adding a PMMA layer with $n_{\text{PMMA}} \approx 1.5$ on top of the high-index layer, the reflection losses are 4.4% and 4.0% for the high-index/PMMA and the PMMA/air interface, respectively. Thus, the overall reflection losses are reduced to almost half the initial value. By adding more layers with optimized refractive index, the losses can be further decreased²²².

It should be mentioned that several reports exist in literature that describe the application of a high-index capping layer in order to modify the transmittance of a thin cathode depending on the thickness and the refractive index of the dielectric capping layer, as demonstrated for instance by Riel *et al.*^{76,172}. However, the extraction of waveguide modes or SPs was neither intended nor observed, and the capping layer was just used to optimize the emission through the cathode²²³.

10.8. Conclusions

In summary, the outcoupling of SPs by the high-index coupling approach was studied in this chapter. It is important to point out that the extraction works for organic layers with arbitrary thicknesses as long as the refractive index n_{HI} of the transparent high-index material is larger than the refractive index of the organic layers. Moreover, this technique allows for extracting waveguide modes into the high-index layer.

The basic principle was illustrated by varying the refractive index of the substrate material and by extracting SPs and waveguide modes from a 200 nm thick Alq₃ film, thus demonstrating almost a doubling of the total light extraction.

Furthermore, the high-index coupling method was successfully applied to real OLED devices studied under PL excitation. The outcoupling efficiency η_{out} in the red wavelength range could be enhanced due to the recovery of SP and waveguide losses by approximately 30 % compared to the direct bottom emission of the OLED. In addition, the substrate modes were partially extracted into the high-index region, which increased the total efficiency enhancement to almost 50 %. The successful outcoupling of waveguide modes and SPs was also visualized by photographs.

It is important to emphasize that both the index-matching liquid as well as the refractive index n_{HI} still significantly limited the extraction of SPs. Nevertheless, this result demonstrates the considerable potential of the high-index coupling approach.

Optical simulations were performed to investigate the influence of both the refractive index n_{HI} and the Ag thickness. In general, a larger value of n_{HI} shifts the emission from SPs and waveguides to smaller angles. Moreover, coupling to the second SP branch at the interface between Ag and the high-index region is strongly reduced for larger n_{HI} , thus reducing losses to this unfavorable mode.

A theoretical outcoupling efficiency of $\eta_{\text{out}} > 80\%$ can be achieved by using thin Ag films, a high-index material having $n_{\text{HI}} = 2.3$, and by outcoupling of substrate modes. Even a rather moderate Ag thickness of 30 nm allows for recovering SP and waveguide losses with an intensity that is equal to twice the regular direct bottom emission, yielding $\eta_{\text{out}} \approx 55\%$ or even above 70 % if also substrate modes are extracted. It should be mentioned that the regular bottom emission remains almost unchanged. The efficiency boost primarily results from extraction of SPs and waveguides. By choosing a certain Ag thickness, it is even possible to achieve a similar emission intensity on both sides of the OLED, which might be interesting for many applications.

Besides the tremendous enhancement of η_{out} , the high-index coupling offers additional benefits concerning stack design. If SPs can be recovered to a large extent, the emitter could be positioned closer to the cathode. Hence, the cavity effect can be optimally used and the total thickness of the organic layers can be decreased, which in turn reduces coupling to waveguide modes. Of course, the high-index coupling method can also be applied to top-emitting OLEDs if the substrate consists of a high-index material or

if a high-index layer is deposited onto a corrugated glass substrate²¹⁵. Moreover, one could design an “SP-OLED”, i.e. a device that has an emitter positioned between two thin metallic cathodes adjacent to high-index materials. In such a structure, the emitter would mainly couple to SPs, which in turn could be extracted into the high-index region. Such an OLED would represent a strong cavity and, thus, especially boost emitters with a rather low quantum efficiency.

11. Emitter orientation

The influence of non-isotropic emitter orientation on the efficiency of OLEDs is the topic of this chapter^{224,225}. It is well known that emitters having their transition dipole moment horizontally oriented with respect to the substrate plane typically increase the outcoupling efficiency η_{out} and, thus, the external quantum efficiency η_{EQE} by a factor of about 1.5¹³⁷.

This effect has long been known in the context of polymer OLEDs, which often have the advantage of emitters being oriented parallel with respect to the substrate plane^{14,43,135,137,226–228}. Thus, the transition dipole moment that is usually oriented along the π -conjugated polymer chain is horizontally oriented, i.e. in the substrate plane. In contrast, for more than 20 years it has generally been believed that evaporated amorphous films in small molecule OLEDs are isotropically oriented, i.e. that they have no preferential orientation of the molecules¹³⁵. This is especially likely in the case of phosphorescent molecules that contain a heavy metal ion and usually have a rather bulky form.

Though there have been some reports about horizontally oriented molecules in evaporated neat films^{166–168}, only recently a non-isotropic dipole orientation in dye-doped films has been reported¹⁶⁸. This opens up new possibilities for improvement of light out-coupling efficiency of dye-doped small molecule OLEDs, which already are superior to their polymeric counterparts concerning efficiency and lifetime. For instance, due to the straightforward implementation of doped transport layers as well as additional blocking and injection layers, a better charge balance factor and a well-defined recombination zone can be achieved in small molecule OLEDs.

First, the effect of molecular orientation will be explained by studying optical simulations that distinguish between horizontal and vertical orientation of the transition dipole moment. The potential of horizontally oriented emitters in a typical two-layer OLED as well as in OLEDs comprising a high-index substrate or a microcavity structure will be discussed. Then, an experimental technique will be introduced which enables straightforward determination of the dipole orientation even in guest-host systems²²⁴. The convenience of this method will be demonstrated by analyzing the orientation of two materials that have very similar properties except for their orientation. These materials will then be used to demonstrate the influence of emitter orientation in dye-doped small molecule OLEDs for the first time²²⁵. By measuring the external electroluminescence quantum efficiency of these OLEDs, experimental evidence will be provided

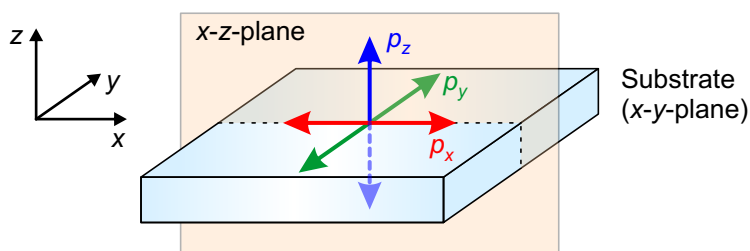


Figure 11.1: Definition of coordinate system and dipole orientations used in the optical simulation.

that a mainly horizontal dipole orientation enhances light outcoupling by a factor of around 1.45 for the given emitter system. Finally, measurements of a red triplet-emitting guest-host system will demonstrate that even phosphorescent materials can have a considerable non-isotropic orientation, thus promising the fabrication of OLEDs having an external quantum efficiency of more than 30 % without additional outcoupling structures.

11.1. Influence of dipole orientation on OLED efficiency

The impact of the dipole orientation on the efficiency of an OLED is most obvious by studying the results of an optical simulation for differently oriented transition dipole moments. The underlying coordinate system is illustrated in Fig. 11.1. Without loss of generality, the substrate plane is assumed to be in the x - y -plane, and the emission into the x - z -plane is considered. The simulation distinguishes three discrete dipole orientations p_x , p_y and p_z . It is important to note that any dipole distribution can be represented as a weighted sum of these three discrete cases²⁵. However, it should be pointed out that the weighting is not a simple averaging. Instead, different cavity effects for each orientation must be taken into account.

Usually, the transition dipole moment, which is responsible for absorbing and emitting light, has a certain orientation with respect to the molecule. For instance, the transition dipole moment may be aligned with the long molecular axis of a molecule²²⁹. Therefore, in the following the terms molecular orientation, dipole orientation and orientation of the transition dipole moment are interchangeable. However, it should be pointed out that the following discussions are not related to a permanent dipole moment of the molecules. For instance, centrosymmetric molecules can show considerable orientation effects without having a permanent dipole moment at all.

According to the chosen coordinate system, the p_x - and p_y -dipoles are horizontally oriented, whereas the p_z -dipoles have a vertical orientation. Regarding the polarization of the emitted light, the p_y -dipoles emit only s-polarized light, whereas the p_x - and p_z -dipoles account for the p-polarized emission. The characteristics of all dipole orientations are summarized in Table 11.1.

Dipole	Orientation relative to substrate plane	Polarization relative to x - z -plane
p_x	horizontal (parallel)	p-polarized (TM)
p_y	horizontal (parallel)	s-polarized (TE)
p_z	vertical (perpendicular)	p-polarized (TM)

Table 11.1: Summary of the discrete dipole orientations assumed in the simulation and the corresponding orientation relative to the substrate (x - y -)plane as well as the polarization relative to the emission (x - z -)plane.

11.1.1. Power dissipation spectra

The simulations are performed for an exemplary two-layer green OLED stack based on an Alq₃ emission layer, as displayed in Fig. 11.2(a). The total optical power dissipation was already shown in Fig. 5.1(c) for an isotropic dipole orientation, i.e. an equal distribution of p_x -, p_y -, and p_z -dipoles. Here, the simulations are separately computed for each of the three dipole orientations. The results are presented in Figs. 11.2(b)–(d).

Apparently, coupling to the individual optical channels shows a strong dependence on the actual dipole orientation²⁵. In detail, the p_x -dipole is responsible for most of the p-polarized fraction of the emission into regions (1) and (2), i.e. direct emission and substrate modes. Additionally, this dipole couples to a p-polarized waveguide mode and to surface plasmons. The p_y -dipole provides the major contribution of the emission into air and substrate and couples to an s-polarized waveguide mode. On the contrary, the p_z -dipole has nearly no emission into air or substrate but almost exclusively couples to SPs¹⁴⁵.

For a better comparison, Fig. 11.3 presents a cross section of all three power dissipations at a wavelength of 510 nm. Obviously, the vertically oriented p_z -dipole shows almost no emission into air or substrate but couples most of its power to SPs²³⁰. This behavior can be explained by taking into account that linear dipoles radiate most strongly perpendicular to their direction of oscillation²³¹. Thus, the vertically oriented p_z -dipole mainly emits at large angles, i.e. high in-plane wave vectors, hence dissipating its power to an unfavorable loss channel.

The fraction of power dissipated by each dipole to different optical channels is displayed in Table 11.2. Again, the values for the p_z -dipole clearly show that this dipole orientation does hardly contribute at all to the desired emission into air or substrate. Consequently, the outcoupling efficiency can be significantly enhanced if no p_z -dipoles are present and if the total energy is redistributed to p_x - and p_y -dipoles. This is apparent from the last two columns in Table 11.2, which show a comparison of simulations for OLEDs consisting of a completely isotropic (1/3 p_x -dipoles, 1/3 p_y -dipoles, and 1/3 p_z -dipoles) and a purely horizontal (1/2 p_x -dipoles and 1/2 p_y -dipoles) dipole orientation, respectively. Both the direct emission and the substrate emission are enhanced by more than a factor of 1.5, demonstrating the enormous potential of using

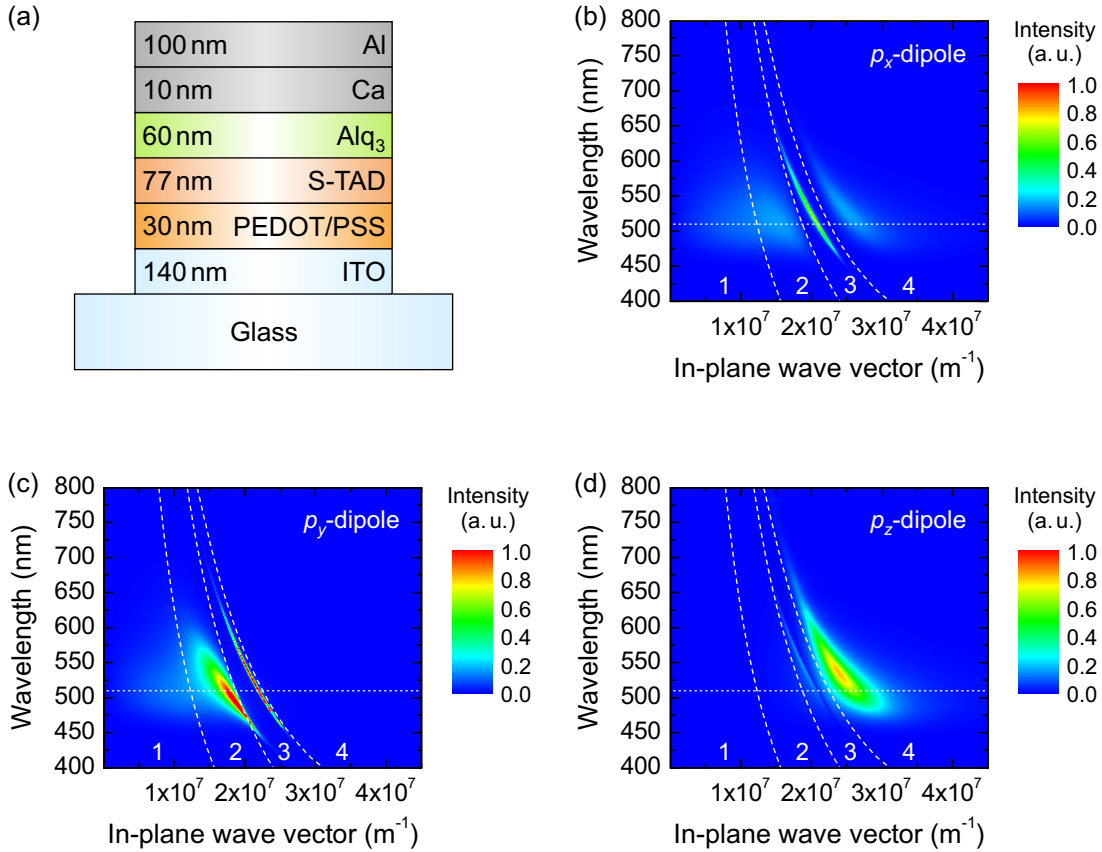


Figure 11.2: (a) Stack layout of the two-layer green OLED. The emission layer is assumed at the interface between Alq₃ and S-TAD. (b)-(d) Simulation of the optical power dissipation for different dipole orientations: (a) p_x -dipole, (b) p_y -dipole, and (c) p_z -dipole. Red areas indicate high amount of dissipated power. All graphs are normalized by the same factor. The dashed lines divide the graph into four regions: (1) emission into air, (2) emission into the glass substrate, (3) waveguide modes, and (4) coupling to surface plasmons. The horizontal line marks the cross section shown in Fig. 11.3.

horizontally oriented emitters in OLEDs. It could be expected that the redistribution of power from p_z -dipoles to horizontal dipoles cannot increase the efficiency by more than a factor of 1.5. However, the enhancement of even slightly more than this factor can be explained by the fact that the p_z -dipole experiences stronger cavity effects in this particular OLED geometry. In other words, the Purcell factor of the p_z -dipole is larger compared to both other dipole orientations. Hence, the p_z -dipole has a higher effective radiative decay rate in this case and, thus, has a higher contribution to the total power dissipation.

11.1.2. Influence of electron transport layer thickness

The main reason for the increased efficiency in case of a purely horizontal dipole orientation is a reduced coupling to SPs. This is even more obvious by investigating the

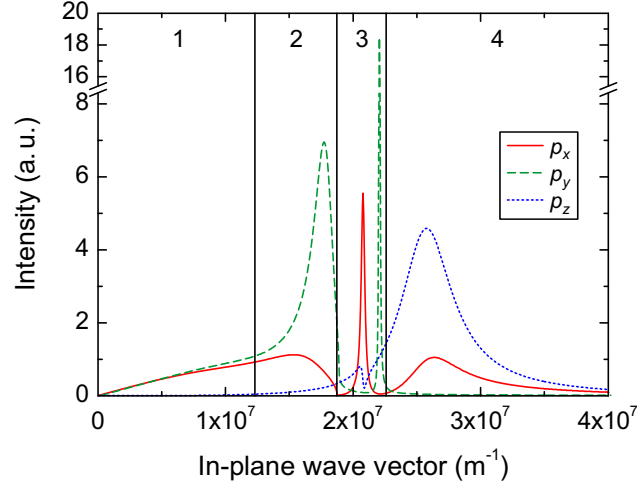


Figure 11.3: Cross section of Figs. 11.2(b)–(d) at a wavelength of 510 nm. The vertical lines divide the graph into four regions similar to Figs. 11.2(b)–(d).

	p_x -dipole	p_y -dipole	p_z -dipole	Isotropic ($p_x / p_y / p_z$)	Horizontal (p_x / p_y)
Direct emission	26.5 %	24.1 %	0.1 %	15.3 %	25.1 %
Substrate emission	23.5 %	51.9 %	0.7 %	24.3 %	39.6 %
Waveguide modes	12.1 %	12.9 %	8.6 %	11.0 %	12.5 %
Surface plasmons	32.5 %	2.0 %	87.7 %	43.7 %	15.3 %
Absorption	5.4 %	9.1 %	2.9 %	5.7 %	7.5 %

Table 11.2: Dissipated power coupled into different optical channels depending on the orientation of the transition dipole moment obtained by integrating over the different regions in the simulations in Figs. 11.2(b)–(d). The values for direct emission also correspond to the outcoupling efficiency of the OLED stack. Absorption describes the fraction of both direct and substrate emission that is lost due to absorption in ITO and the organic layers as well as upon reflections at the cathode. The small contribution of the p_y -dipole to SPs results from an overlap of the waveguide mode into the SP region. For the last two columns it should be noted that these numbers are not simply the average of the corresponding values of each dipole. Instead of that, a weighting according to cavity effects has been considered.

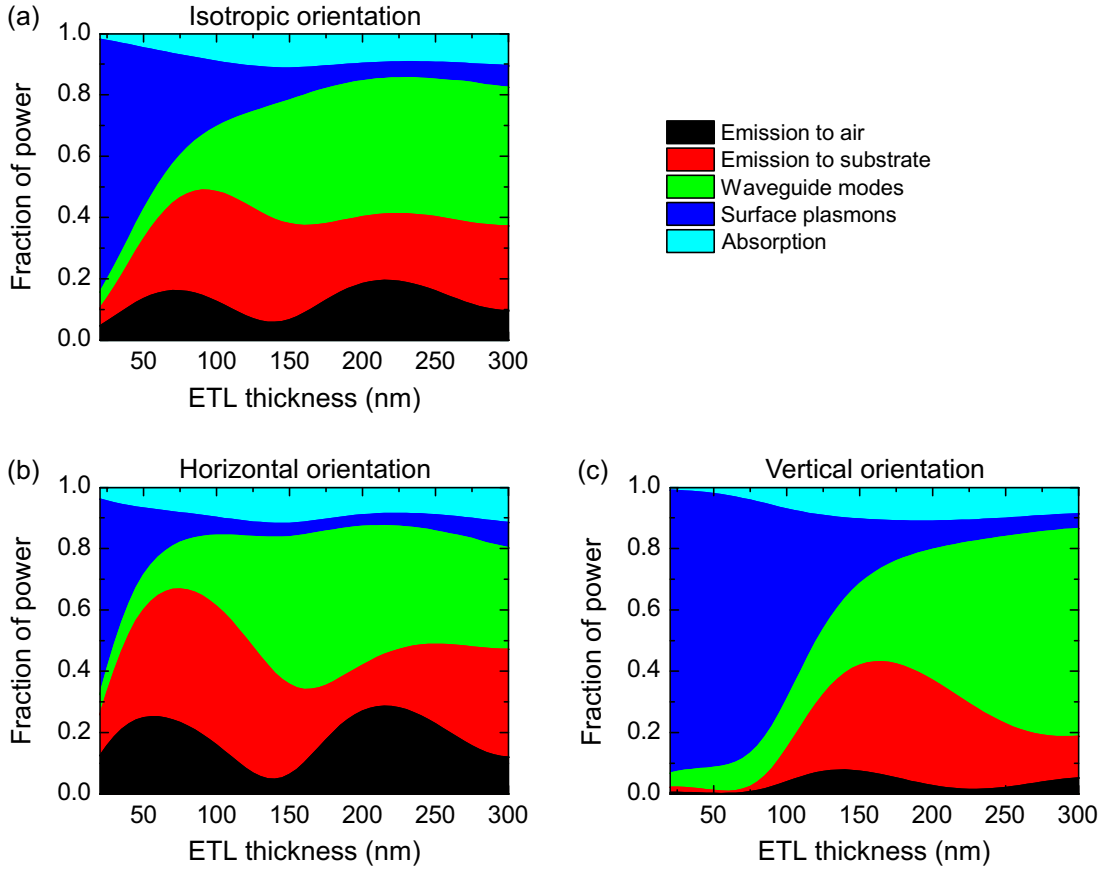


Figure 11.4: (a)-(c) Dissipated power for a stack as shown in Fig. 11.2(a) as a function of the electron transport layer thickness, i.e. the distance between the emitter and the cathode, for (a) isotropic dipole orientation (p_x, p_y, p_z), (b) horizontal dipole orientation (p_x, p_y), and (c) vertical dipole orientation (p_z). The radiative quantum efficiency was assumed to be $q = 100\%$.

distance dependence of the emitter to the metallic mirror. Figures 11.4(a)–(c) show a variation of the electron transport layer (ETL) thickness for an isotropic, horizontal, and vertical dipole orientation, respectively. The oscillatory behavior of the emission into air and into the substrate results from interference effects of the emitter with its image dipole^{26,231,232}. It is worth mentioning that some of the power coupled to waveguide modes might be misleadingly attributed to SPs and vice versa, because both optical modes have a certain width in wave vector space, thus resulting in an overlap between both modes. In addition, it is not possible to exactly determine the border between waveguides and SPs. These effects for instance cause the increase of SP emission in Figs. 11.4(a) and (b) for large ETL thicknesses.

The graphs clearly demonstrate the increased outcoupling efficiency for a horizontal dipole orientation in comparison to an isotropic orientation. In addition, in the case of horizontally oriented dipoles, the emission layer may be positioned much closer to the cathode before coupling to SPs becomes the dominant loss channel.

The highest direct emission of 28.5% in Fig. 11.4(b) is obtained in the second cavity maximum at an ETL thickness of 215 nm. Positioning the emitter in the first maximum still results in a considerable direct emission of 25.2% at an ETL thickness of 55 nm. If also substrate emission is extracted by an appropriate outcoupling structure, an ETL thickness of 75 nm should be chosen. In this case, a combined direct and substrate mode emission of 66.8% is predicted by the simulations. In other words, around two thirds of the total power is dissipated to optical channels that can in principle be extracted from the OLED device.

In the context of a purely vertical dipole orientation, as displayed in Fig. 11.4(c), it is obvious that coupling to SPs is the dominant optical loss channel even for a distance of 100 nm to the cathode. On the contrary, the vertical dipole shows almost no direct emission, independently of the ETL thickness. This can be explained by the fact that direct emission must occur within a rather small angular cone with respect to the surface normal, i.e. in a direction close to the dipole axis of the p_z -dipole.

It is interesting to investigate the difference between completely horizontally and purely vertically oriented dipoles in more detail by comparing Figs. 11.4(b) and (c). Apparently, vertically oriented dipoles have the highest coupling to direct emission and especially substrate emission at an ETL thickness around 170 nm. Concerning horizontally oriented dipoles, this ETL thickness rather corresponds to a minimum in the direct and substrate emission. This effect results from opposite interference conditions for the emission from horizontal and vertical dipoles, as explained by Flämmich *et al.* in Ref. [228]. In detail, constructive interference for horizontal dipoles is expected for ETL thicknesses roughly equal to odd multiples of $\lambda/(4 \cdot n_{\text{organic}})$, while the thickness should be close to even multiples of $\lambda/(4 \cdot n_{\text{organic}})$ in case of vertical dipoles²²⁸. Here, λ represents the emission wavelength, and n_{organic} describes the refractive index of the emitting material. Using $\lambda = 510$ nm and $n_{\text{organic}} = 1.7 - 1.8$ yields $\lambda/(4 \cdot n_{\text{organic}}) \approx 71 - 75$ nm, which basically agrees with the values obtained from the optical simulations in Fig. 11.4.

As a matter of course, optimized OLEDs usually comprise a distance between the emitter and the cathode that favors horizontally oriented dipoles in order to obtain a maximum outcoupling efficiency, i.e. a high coupling to direct emission and optionally to substrate emission. Unfortunately, such a thickness causes the vertical dipoles to couple almost completely to unfavorable optical modes like SPs and waveguide modes. Therefore, an enhancement factor of typically 1.5 can be achieved in the case of a horizontal orientation in comparison to an isotropic orientation.

Altogether, the simulations performed in this section clearly illustrate the enormous benefit that can be obtained from an orientation control of the emitting molecules. This effect is most pronounced at small distances to the cathode due to the stronger coupling to SPs. However, even in the second cavity maximum, the outcoupling efficiency could be significantly increased by using emitters with a mainly horizontal orientation.

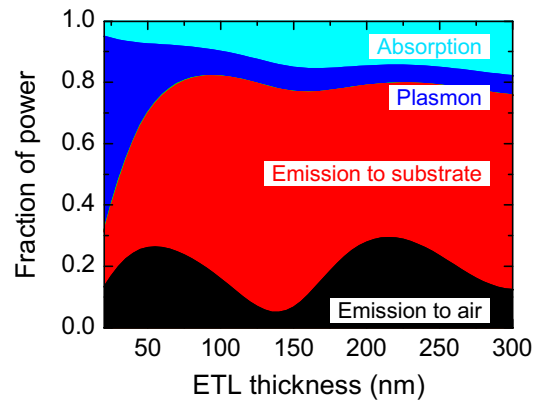


Figure 11.5: Dissipated power as a function of the electron transport layer thickness in the case of a horizontal dipole orientation (p_x, p_y) and a high-index substrate. The OLED stack used for the simulation basically corresponds to the structure shown in Fig. 11.2(a), except for a high-index substrate (SF6, $n \approx 1.8$).

11.1.3. Potential of horizontally oriented emitters

One of the advantages of horizontally oriented emitters is the fact that molecular orientation is an intrinsic property of the emission layer. Hence, it is possible to combine oriented emitters with additional external measures, e.g. high-index substrates or a microcavity device structure, to further enhance the outcoupling efficiency of an OLED. Therefore, this section discusses optical simulations to demonstrate the potential of a horizontal emitter orientation combined with special stack layouts.

Figure 11.5 shows the power dissipation in dependence of the ETL thickness for the exemplary green OLED assuming a horizontal dipole orientation and a high-index substrate. Here, two effects play an important role. First, the horizontal emitter orientation strongly reduces coupling to SPs even for rather small distances to the cathode. Second, the high-index substrate prevents coupling to waveguide modes. This is obvious by comparing the simulated ETL dependence with the result for the same OLED with a BK7 substrate, as shown in Fig. 11.4(b). Due to these two effects, a very high total emission to air and substrate of more than 75 % is achieved over a very broad range of ETL thicknesses. Such a high efficiency is already obtained for an ETL thickness as low as 60 nm. In contrast, in the case of a high-index substrate and an isotropic emitter orientation (cf. Fig. 6.5), an ETL thickness of almost 200 nm is required for such a high outcoupling efficiency because much more power is dissipated to SPs if vertical dipoles are present. It is worth mentioning that the efficiency could be even further increased by implementing an ETL material with lower absorption.

In many cases, it is desired to use an OLED without applied outcoupling structures, for instance if a mirror-like off-state appearance is required. In this case, it is necessary to maximize the direct emission to air. This can be achieved by combining horizontally oriented emitters with a microcavity structure. It should be noted that microcavity

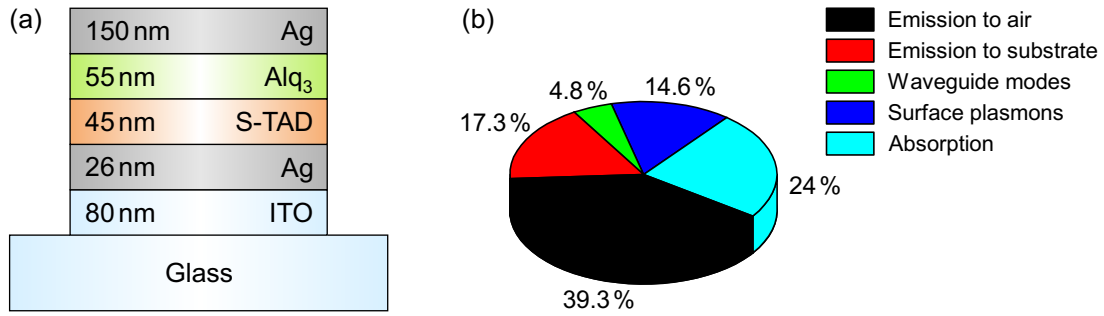


Figure 11.6: (a) Stack layout of an optical microcavity device consisting of a thick silver cathode and an additional 26 nm thick silver layer on ITO. (b) Fraction of power coupled to different optical channels assuming a radiative quantum efficiency of $q = 100\%$ and a horizontal dipole orientation.

devices are not optimal in the case of white OLEDs with a broad emission spectrum. Nevertheless, the use of monochromatic microcavity OLEDs promises exceptionally high efficiencies.

Figure 11.6(a) shows a microcavity OLED comprising a thick Ag cathode and an additional semitransparent Ag layer on top of the ITO anode. The outcoupling efficiency is displayed in Fig. 11.6(b). Although the absorption inside the stack is very high, a remarkable direct emission of 39.3% is obtained. This outcoupling efficiency for directly emitted light is significantly larger than all other simulations studied so far.

According to the optical simulation, vertical dipoles would dissipate 99% of their power to SPs in such a microcavity geometry. In addition, the Purcell factor for vertical dipoles is larger in comparison to horizontal dipoles for this specific OLED stack. Therefore, the outcoupling efficiency is considerably reduced if the emitter is not perfectly horizontally oriented. For instance, in the case of an isotropic orientation, the direct emission is decreased to 22.2%, as shown in Fig. 6.3(b).

The results of this section demonstrate that it is required to have accurate information about the actual emitter orientation in order to find the optimum OLED layout. However, it is not straightforward to determine the molecular orientation in thin organic films, particularly in guest-host systems that comprise only a very small amount of the emitting material within a matrix environment. In order to find a suitable and reliable method that allows for the determination of the dipole orientation, it is instructive to study the emission pattern of emissive dipoles in more detail.

11.2. Dipole emission pattern

The fundamental emission pattern of a radiating dipole is obtained by placing the dipole in an infinite, homogeneous medium without absorption. The simulated angular dependent emission is plotted in Fig. 11.7(a). Due to the chosen coordinate system, the p_x -dipole has the highest emission intensity along the z -direction. In contrast,

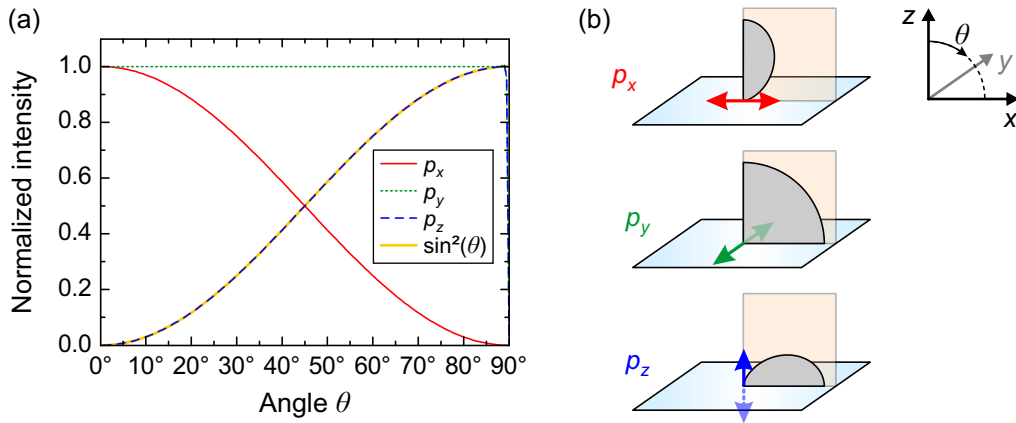


Figure 11.7: (a) Far-field dipole emission pattern in an infinite medium without absorption obtained by optical simulations. Emission into the x - z -plane is considered, θ describes the angle with respect to the z -axis. The reduced intensity at angles close to 90° results from a numerical problem upon converting the simulated in-plane wave vector k_x to angles due to the finite step size in k_x . (b) Schematic polar plot of the emission pattern of each dipole orientation derived from part (a) of the figure.

the p_y -dipole has a constant emission over all angles. Finally, the angular dependent emission of the p_z -dipole shows an opposite behavior to the p_x -dipole, i.e. the emission intensity is zero along the z -direction and rises with increasing angle.

The simulated result perfectly resembles the theoretical radiation pattern of an oscillating dipole, i.e. the angular dependence is proportional to $\sin^2(\theta)$, with θ being the angle with respect to the dipole axis^{96,102}. It can be seen that linear dipoles radiate most strongly perpendicular to their direction of oscillation²³¹, while the emission is zero along the dipole axis⁹⁶. Moreover, the radiation is symmetric around the dipole axis, as can be seen by the emission of the p_y -dipole in Fig. 11.7(a). The angular dependent emission intensity can be transformed into a polar plot to obtain the typical radiation pattern of an oscillating dipole, as presented in Fig. 11.7(b).

It would be rather straightforward to determine the orientation of an oscillating dipole in an infinite medium just by measuring its radiation characteristics. However, the situation is more complicated in an actual OLED device. By nature, an OLED comprises several interfaces and usually a metallic cathode. Hence, the emission pattern of an oscillating dipole is strongly altered inside the OLED cavity, as shown in Fig. 11.8 for the exemplary green Alq₃ based OLED. It can be seen that the emission pattern for each dipole orientation considerably differs from the case of an infinite medium. In particular, the emission from the p_z -dipole is close to zero for all angles, which mainly results from a strong coupling to SPs. In contrast, the p_x -dipole and p_y -dipole have a high emission intensity and account for the major part of the p- and s-polarized emission, respectively. Hence, the emission characteristics of such an OLED makes it complicate to determine the orientation of the transition dipole moment, as will be discussed in the following section.

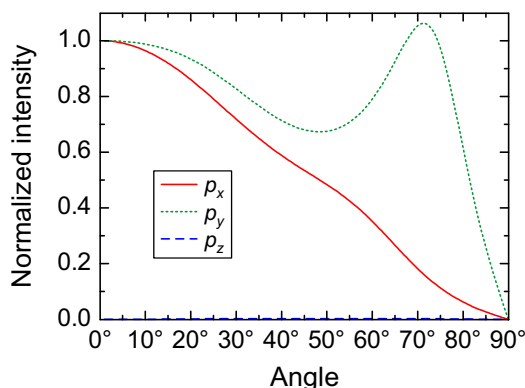


Figure 11.8: Simulated dipole emission pattern into the glass substrate at a wavelength of 510 nm in the case of the exemplary green OLED stack (cf. Fig. 11.2(a)). All curves are normalized by the same factor.

11.3. Determination of molecular dipole orientation by PL measurements

In order to benefit from the enormous efficiency boost of horizontally oriented emitters in OLEDs, it is required to implement suitable materials with a mainly horizontal orientation. Hence, it is essential to develop reliable and straightforward methods in order to unambiguously determine the ratio between horizontal (p_x and p_y) dipoles and vertical (p_z) dipoles for a given material system. Since the p_z -dipoles hardly contribute to the emission intensity at all in a common OLED, it is not easily possible to determine the fraction of p_z -dipoles in such an OLED device by measuring the emission characteristics. Therefore, other methods have to be used in order to estimate the presence of vertical dipoles in organic thin films.

In principle, variable angle spectroscopic ellipsometry yields information about the orientation of the transition dipole moment^{166,168}. However, ellipsometry is usually not sensitive enough to detect small amounts of dopants within a matrix. Several additional techniques have been proposed in literature, for instance edge (or cut-off) emission measurements^{166,168,233} as well as surface plasmon coupled emission²³⁴. Although these methods basically work, the extraction of the relevant information on molecular orientation is not straightforward. It is also possible to determine the orientation by measuring the excited state lifetime in microcavity structures^{17,18,231}. This requires the preparation of a series of samples with systematically varying distance between the emission zone and a metal layer. Though being more elaborate, this method has the benefit of independently yielding the value of the radiative quantum efficiency of the emitter, too.

Recently, Flämmich *et al.* presented an interesting method based on the analysis of OLED emission spectra²²⁸. This approach requires to use OLED structures that are designed to enhance the emission from vertical p_z -dipoles by choosing a certain

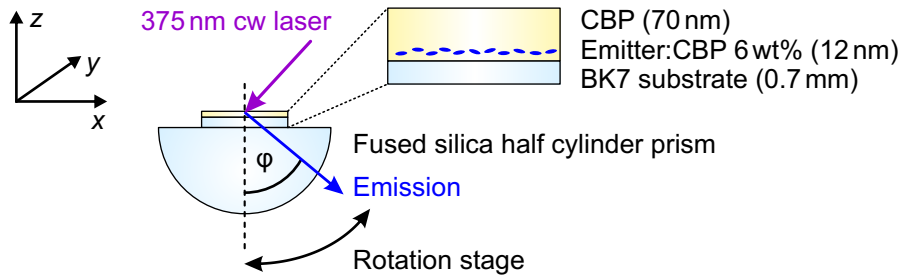


Figure 11.9: Experimental setup (top view) and cross-sectional schematic layout of the layer structure used for the determination of the molecular orientation in a PL measurement. The angular dependent emission into the x - z -plane is detected.

distance to the cathode. For instance, an ETL thickness of about 140 nm must be chosen to obtain a maximum direct emission for the OLED stack discussed in the previous sections, cf. Fig. 11.4(c). This technique has the advantage that the orientation can be detected in an actual OLED device under electrical operation, even though the thickness and cavity effects differ from an optimized OLED structure which would be used for a commercial product. On the other hand, this method demands the fabrication of a complete OLED stack and, thus, is not perfectly suited to screen new material systems in a short amount of time.

Therefore, it is desirable to find a simple approach that permits the straightforward investigation of many guest-host combinations. Here, a novel technique is presented which is based on the angular dependent measurement of the photoluminescence emission spectrum of a specific layer structure and the subsequent comparison to numerical simulations²²⁴.

11.3.1. Basic principle and experimental setup

The experimental setup used for the determination of molecular orientation in a PL measurement is shown in Fig. 11.9. An exemplary stack layout consists of a 12 nm thick guest-host layer on a glass substrate, covered by a 70 nm thick spacer layer. For instance, CBP can be used both as a matrix and spacer material. The doped region should be narrow, because the optical simulation assumes a discrete emitter position.

It should be pointed out that the structure is free of metallic layers, so that the p_z -dipoles cannot couple to SPs. Hence, p_z -dipoles are forced to dissipate their power as direct emission and especially as substrate emission, thus contributing to the overall emission. The substrate modes can be extracted by applying a fused silica half cylinder prism using index-matching liquid.

All three dipole orientations are simulated separately, permitting subsequent weighting for arbitrary dipole distributions. The only required input parameters for the simulation are the optical constants of the CBP matrix, the total thickness, and the PL spectrum of the doped layer, the latter only being required in the case of a polychromatic

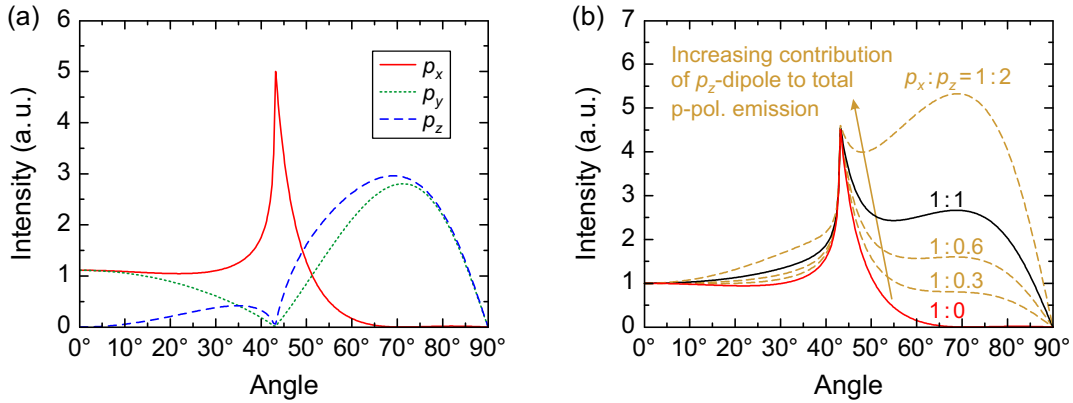


Figure 11.10: (a) Simulated dipole emission pattern into the fused silica prism in the case of the stack shown in Fig. 11.9. All curves are normalized by the same factor. (b) Combined angular dependent emission of the p_x - and p_z -dipoles, i.e. the p-polarized emission, for different ratios between the number of p_x - and p_z -dipoles. For simplicity, the terms p_x , p_y , and p_z in this notation are used to represent the number of dipoles for each orientation. The emitter position is assumed in the center of the doped emission layer. All curves are normalized to the emission at 0°, because the emission intensity in normal direction only depends on the p_x -dipole. If an equal distribution of p_x - and p_y -dipoles is assumed, a ratio of $p_x : p_z = 1 : 0$ represents a purely horizontal orientation, whereas a ratio of $p_x : p_z = 1 : 1$ corresponds to a completely isotropic orientation.

simulation. The small birefringence of the CBP matrix¹⁶⁸ is not taken into account, as this considerably increases the complexity of the simulation without significantly changing the overall result. It is noteworthy that the optical constants of the dopant are not required, emphasizing that this technique is exceptionally useful for the analysis of newly developed materials with unknown optical properties.

Similar to the dipole emission patterns studied above, Fig. 11.10(a) displays the simulated angular dependent emission of each dipole orientation. The p_x - and p_y -dipoles have the same emission intensity at 0°, but the emission for larger angles is different. In contrast to the horizontal dipoles, the emission from the p_z -dipole is equal to zero at normal emission, i.e. along the dipole axis. Nevertheless, a considerable overall emission of the vertical p_z -dipole can be obtained since no metallic layer is present in the chosen stack structure. Keeping in mind that dipoles radiate most strongly perpendicular to their direction of oscillation, the p_z -dipoles mainly emit at large angles.

According to the chosen coordinate system, the p_y -dipoles emit only s-polarized light, whereas the p_x - and p_z -dipoles are responsible for the p-polarized emission. In order to find materials that have the potential to increase the outcoupling efficiency of OLEDs, the ratio between horizontal and vertical dipoles must be determined. It should be kept in mind that only the combined p-polarized emission of the p_x - and p_z -dipoles can be detected in a measurement by using a polarizer. Therefore, it is necessary to thoroughly analyze the p-polarized emission and to distinguish between both orientations according to the angular dependency of the emission.

The simulated p-polarized emission for several ratios of p_x - to p_z -dipoles is shown in Fig. 11.10(b). It can be seen that the emission close to normal direction is independent of the fraction of p_z -dipoles. On the contrary, the emission at larger angles above 45° is strongly influenced by the presence of p_z -dipoles.

In other words, the emission at small angles is mainly governed by the p_x -dipoles, while the emission at large angles particularly depends on the amount of p_z -dipoles. Thus, the dipole orientation can be determined by comparing a measured angular dependent emission pattern with the simulations. This will be exemplarily shown for two guest-host systems in the next section.

11.3.2. Investigation of organic guest-host systems

The determination of the orientation of the transition dipole moment is demonstrated for two blue fluorescent dyes²²⁵: 4,4'-bis[4-(diphenylamino)styryl]biphenyl (BDASBi, sometimes also referred to as BDAVBi)²³⁵ and 4-(2,2-diphenylethenyl)-N,N-bis(4-methylphenyl)benzenamine (PEBA)²³⁶. The molecular structures of both materials are displayed in Fig. 11.11(a).

Organic semiconductor films often show a large optical anisotropy if the molecules have a very long or planar shape^{167,168}. While BDASBi has an elongated structure, PEBA represents a shorter and more compact molecule. Thus, it is expected that PEBA will show much less pronounced orientation effects than BDASBi. From a chemical point of view, BDASBi is quite similar to 4,4'-bis[(N-carbazole)styryl]biphenyl (BSB-Cz), which is known to exhibit mainly horizontally oriented dipoles in neat and doped films^{168,233}. Thus, it is expected that the emitting dipoles in BDASBi are as well oriented predominantly parallel to the substrate plane.

Both materials may be doped into a CBP matrix. The PL spectra of BDASBi and PEBA doped into CBP at 6 wt% are illustrated in Fig. 11.11(b). It is apparent that both materials feature a rather similar emission spectrum with a peak wavelength at about 470 nm.

The stack layout used for the determination of the molecular orientation is similar to the stack shown in Fig. 11.9. In detail, 12 nm thick doped films of 6 wt% BDASBi or PEBA in CBP were deposited on cleaned glass substrates and capped with a 70 nm thick neat CBP layer. The samples were encapsulated in a glovebox by using a cover glass and thin spacers to form a small inert gas cavity. For the measurement, a fused silica half cylinder prism was attached to the substrate side of the samples by index matching gel, and the samples were mounted on a computer controlled rotation stage. A 375 nm cw laser diode incident under 45° from the encapsulation side was used as excitation source. The light from the laser diode is primarily p-polarized in this configuration. Since CBP only has a small absorption at this wavelength, emission from the matrix is suppressed. The angular dependent PL spectrum from 0° to 90° was measured with a fiber optical spectrometer and a polarizer to distinguish between s- and p-polarized

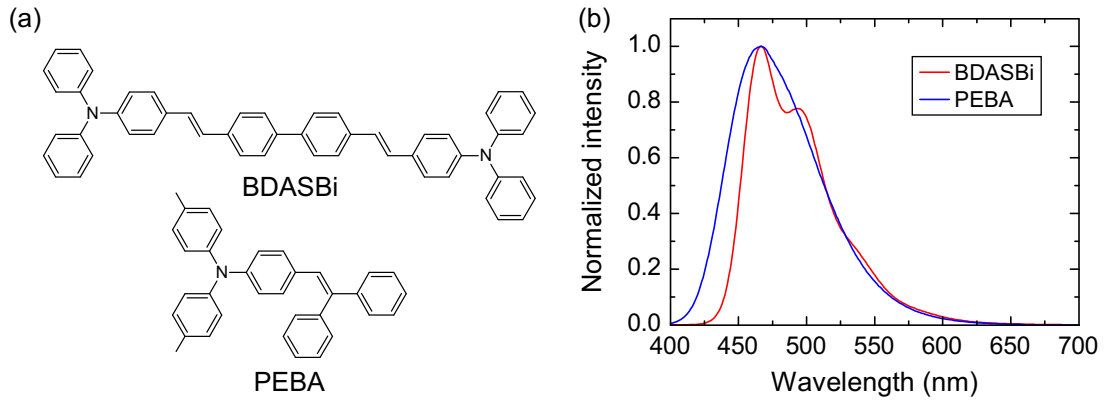


Figure 11.11: (a) Molecular structures of BDASBi and PEBA. (b) Photoluminescence emission spectra of 50 nm thick films of BDASBi and PEBA doped into CBP (6 wt%) measured perpendicular to the silica glass substrate using a fluorescence spectrometer (FP-6500, Jasco Co.). The chosen thickness of the samples ensures that the spectra are not changed too much by waveguiding effects and that they match the emission spectra in free space.

emission. In addition, a 400 nm long-pass filter was used to protect the spectrometer from laser light. For some measurements, the edges of the sample were blackened in order to prevent edge emission at large angles.

Figures 11.12(a) and (b) display the polychromatic p-polarized simulation results of the BDASBi sample for a completely isotropic and a purely horizontal dipole orientation, respectively. By comparing the measurement shown in Fig. 11.12(c) to the simulations, it is apparent that the transition dipoles in a BDASBi:CBP layer are primarily horizontally oriented. The measurement of a similar device with PEBA doped into CBP agrees well with the simulation for perfectly isotropic dipole orientation (cf. Ref. [229] for details).

A precise analysis of the dipole orientation is performed by comparing the cross sections of measurement and simulations at a wavelength of 470 nm, i.e. close to the emission maximum, as displayed in Fig. 11.13. In addition, the measured cross section of a stack containing PEBA instead of BDASBi with otherwise identical structure is shown. It should be pointed out that the simulation of a cross section is generally valid for a certain combination of matrix and spacer. In particular, it is independent of the actual dopant, meaning that no information about the PL spectrum of the emitter itself is required.

Comparing the measured cross section for PEBA with the simulated curves yields excellent agreement assuming an equal amount of p_x - and p_z -dipoles. Thus, PEBA doped into CBP shows no preferred molecular orientation, and the dipole orientation is completely isotropic, i.e. on average 2/3 of the dipoles are horizontally and 1/3 vertically oriented.

On the contrary, the cross section of the sample containing BDASBi shows a clear

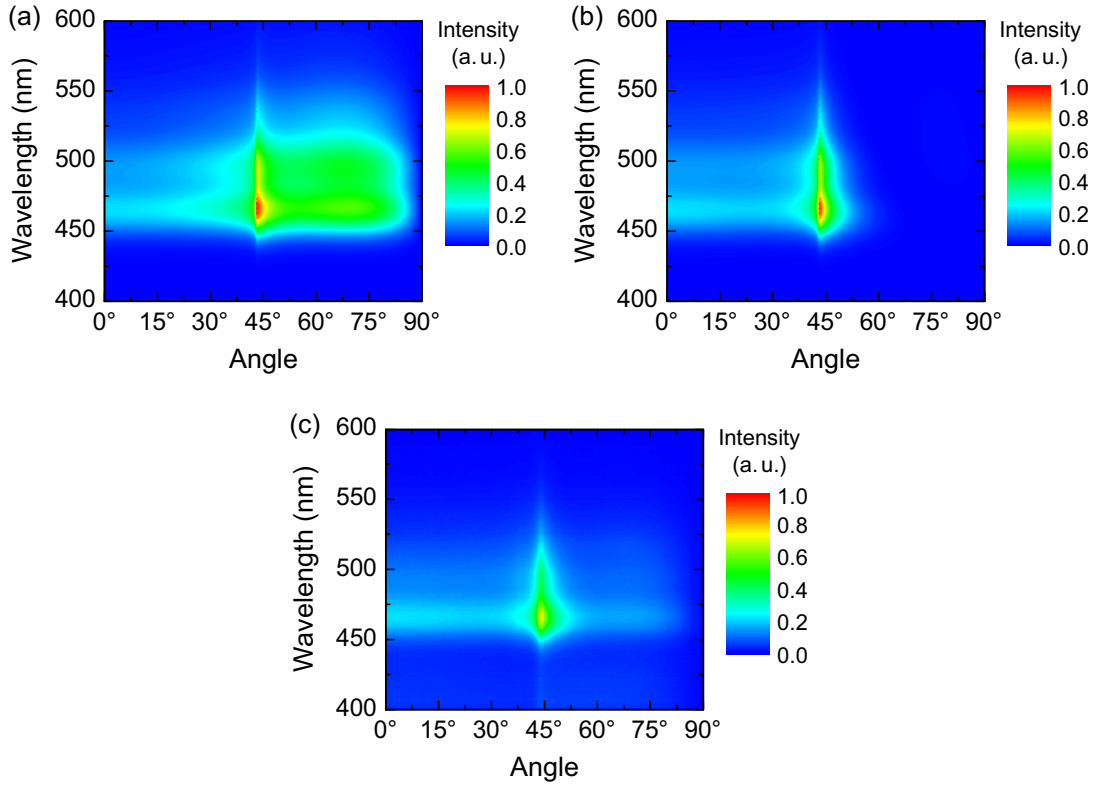


Figure 11.12: Simulation and measurement of the angular dependent p-polarized emission spectrum of a 12 nm thick film of BDASBi:CBP (6 wt%) on a glass substrate capped with 70 nm of neat CBP. Simulation assuming (a) an isotropic dipole orientation and (b) a purely horizontal dipole orientation. The simulated result at 1° was also used for 0° , since the difference is small and no simulation result is obtained for an angle of exactly 0° . (c) Measurement of the angular dependent emission spectrum. The measured emission intensity is scaled in such a way that the emission at small angles corresponds to the simulations.

tendency towards horizontal orientation. By assuming a ratio of $p_z : p_x = 0.27 : 1$ for the simulations, very good agreement between the simulated and measured curve can be obtained.

Generally, the horizontal p_x - and p_y -dipoles are uniformly distributed, unless special substrate treatments are applied²³⁷, for instance rubbing^{238–241} or friction transfer^{242,243}. Since no such treatment was used here, the horizontal p_x - and p_y -dipoles can be assumed to be uniformly distributed in the substrate plane. Thus, the overall fraction of vertical (p_z) dipoles is $0.27/2.27 = 12\%$, the fraction of horizontal (p_x, p_y) dipoles is $2/2.27 = 88\%$. These values are in very good agreement with Ref. [224]. This result promises a strong enhancement in outcoupling efficiency for OLEDs using BDASBi doped into CBP, as will be demonstrated in Sec. 11.4.

It should be noted that the direction of the transition dipole moment is almost perfectly aligned with the long molecular axis of the molecule in the case of BDASBi²²⁹. Therefore, the measured preferential orientation of the transition dipole moment also

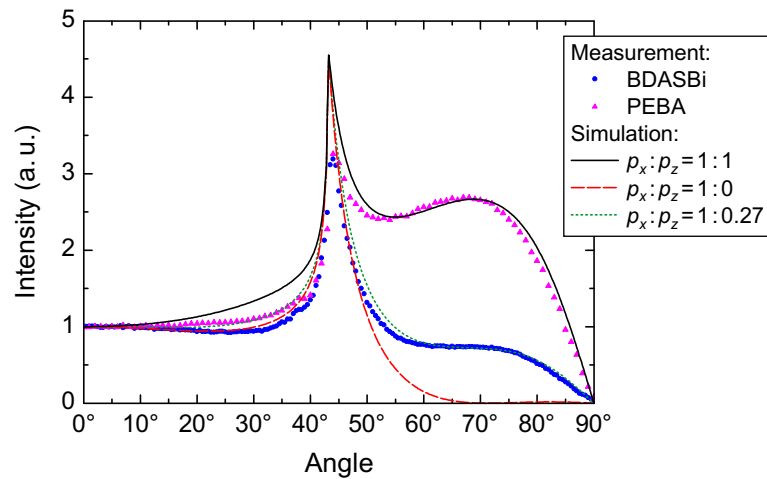


Figure 11.13: Angular dependent cross section at 470 nm of the simulated and measured p-polarized emission spectra shown in Fig. 11.12 and of a measurement with a sample containing PEBA instead of BDASBi. All cross sections are normalized to the emission at small angles because the emission in this range is exclusively caused by the horizontal p_x -dipoles. On the other hand, the emission at angles around 70° is dominated by the p_z -dipoles.

implies an anisotropic molecular orientation when doped into CBP. In the case of PEBA, the transition dipole moment is also associated with the molecular structure²²⁹. Since the direction of the transition dipole moment of PEBA was determined to be isotropic, the molecular orientation for PEBA doped into CBP must also be rather isotropic. The result agrees with variable angle spectroscopic ellipsometry measurements performed on neat films of BDASBi and PEBA, which showed a strong optical anisotropy for BDASBi, while the optical constants obtained for PEBA showed almost no anisotropy, thus indicating no preferential orientation in neat films²²⁹.

11.3.3. Thickness control using s-polarized measurements

Besides the p-polarized analysis, it is also possible to compare an s-polarized measurement with the corresponding optical simulation. The result is depicted in Fig. 11.14, showing good agreement between the measured and simulated curves.

Regarding s-polarized light, the emission exclusively originates from horizontally oriented p_y -dipoles. Thus, the cross section is independent of the ratio between horizontal and vertical dipoles. That is the reason why there is only a small difference between the measurements of the BDASBi and PEBA samples in contrast to the p-polarized measurements. Although no information about orientation can be obtained, the comparison of the s-polarized measurement with an optical simulation represents an excellent control of the optical constants and thicknesses used for the simulations. Hence, errors in the determination of the orientation arising from wrong input parameters can be avoided by also performing an s-polarized analysis.

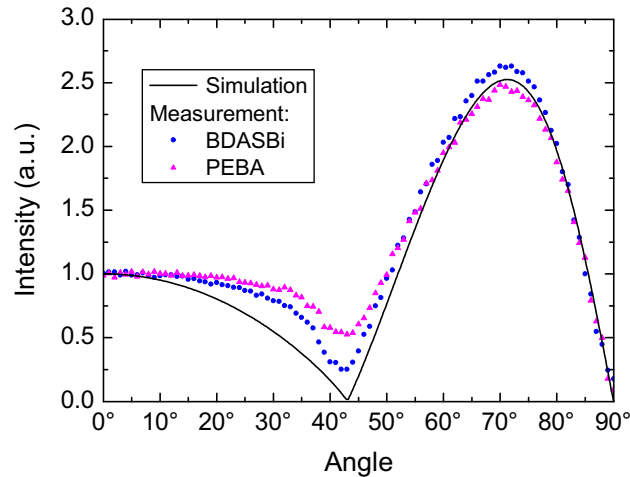


Figure 11.14: Angular dependent cross section at 470 nm of the simulated and measured s-polarized emission spectra of 12 nm thick BDASBi or PEBA films doped into CBP (6 wt%) and capped with 70 nm of neat CBP. All cross sections are normalized to the emission at small angles.

11.3.4. Optimization of device layout and discussion

The thickness of the spacer layer studied in the previous sections was chosen based on optical simulations so that the difference in the emission spectrum is clearly pronounced, depending on whether the orientation of the emitting dipoles is completely isotropic or exclusively in the substrate plane. This section gives further insight into the function of the spacer layer. In addition, several effects are discussed which can cause an error in the determined degree of orientation.

From an optical point of view, the spacer between the emission region and the interface to air is important in terms of interference effects. To study these effects, Fig. 11.15 shows optical simulations with spacer layers ranging from 0 nm to 120 nm in steps of 30 nm. The result for the p-polarized case is illustrated in parts (a)-(e) of the figure, while the s-polarized simulations are shown in part (f).

All p-polarized simulations have in common that the emission at angles above 50° is rather small in case of only horizontally oriented p_x -dipoles. In contrast, if also p_z -dipoles are present, the emission at larger angles shows a pronounced dependence on the spacer layer thickness. The biggest difference between both simulated curves is obtained for a thickness of about 60 nm. For larger thicknesses, the difference between both simulations decreases again and almost vanishes at a spacer layer thickness of 120 nm. This is a strong evidence for interference effects, keeping in mind that a quarter of ($470 \text{ nm}/n$) is equal to about 64 nm, with $n \approx 1.83$ being the refractive index of CBP at a wavelength of 470 nm.

It should be mentioned that the peak around 43° arises both from interference as well as from total internal reflection effects, i.e. the critical angle for totally reflected light at the CBP/air interface corresponds to 43° inside the fused silica prism.

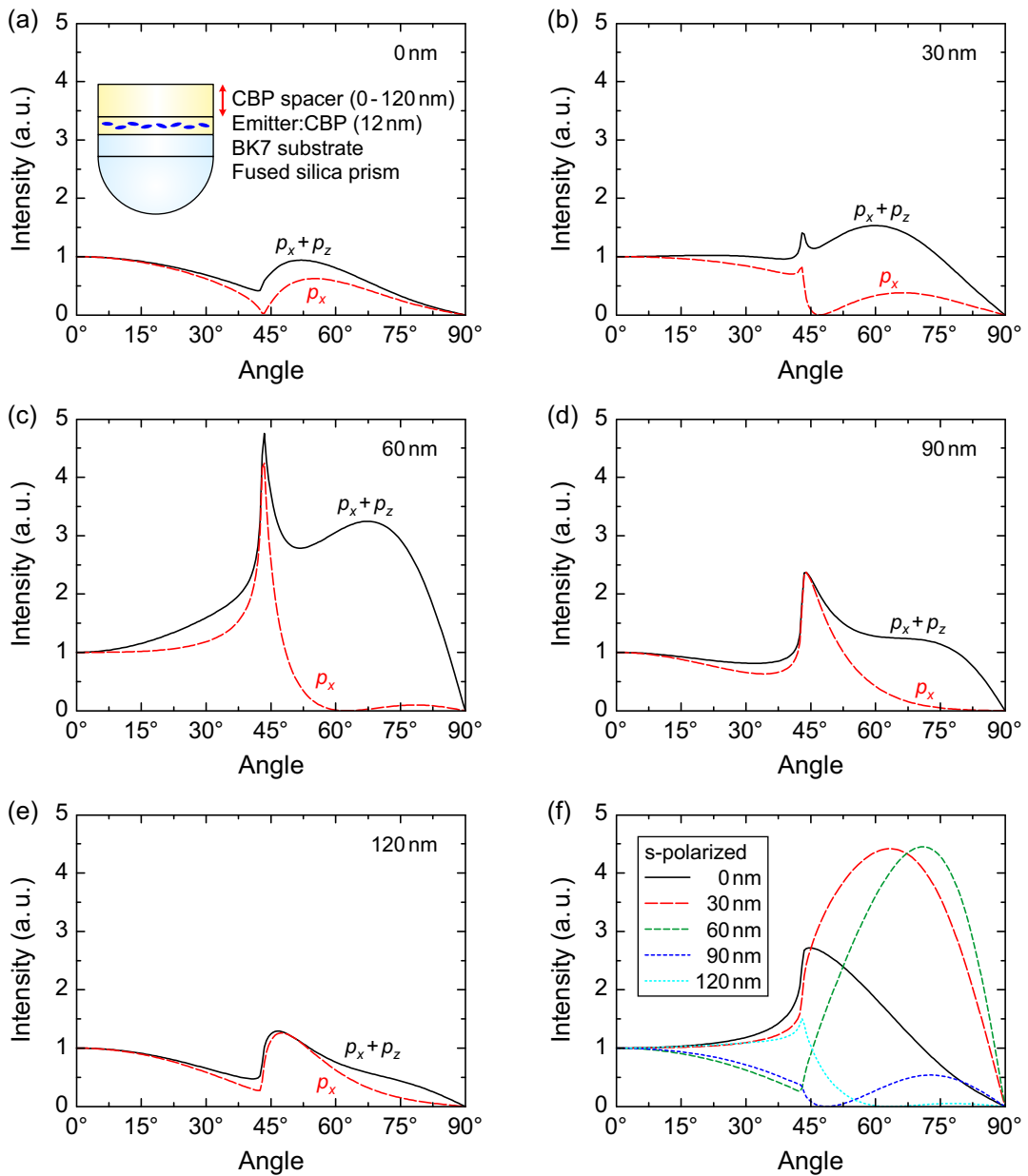


Figure 11.15: (a)-(e) Simulated p-polarized cross sections at 470 nm of a stack as shown in part (a) of the figure for varying spacer layer thicknesses between 0 nm and 120 nm, as indicated in each graph. (f) Simulated s-polarized cross sections for the same stack as in part (a) of the figure.

The s-polarized simulations in part (f) of the figure also show a significant dependence on the actual spacer layer thickness. Thus, performing s-polarized measurements allows for controlling the thickness and optical constants of the spacer layer, as discussed in the previous section.

In addition to a top spacer layer, it is also possible to use one or several bottom spacers between the emission layer and the substrate²²⁴. However, from an optical point of view, the bottom spacer only has a very limited influence because interference

and reflection effects are much weaker in comparison to the interface to air.

Generally, one would assume that it is optimal to implement a spacer layer which maximizes the difference between isotropic and horizontal orientation. However, this additional layer also reduces the accuracy of the result because small deviations in the optical constants or in the thickness of the spacer layer strongly modify the result of the analysis. In particular, if the spacer layer thickness of e.g. 70 nm has an uncertainty of ± 5 nm, the absolute degree of orientation is changed by approximately ± 2 %. Moreover, if the refractive index of CBP is changed by ± 0.05 , the orientation differs by about ± 1 %. Therefore, it is always recommended to perform s-polarized measurements in order to obtain a basic check of the optical constants and thicknesses.

Furthermore, it must be taken into account that the spacer layer may be fluorescent itself, as it is the case for CBP. In general, this can be problematic because the emission from the spacer has a different angular dependent emission behavior. However, since the CBP emission occurs in the deep blue or almost UV wavelength range, the influence at a wavelength of 470 nm is small. For both BDASBi as well as PEBA it can be estimated that the emission from the 70 nm thick CBP spacer amounts to considerably less than 10 % compared to the emission from BDASBi or PEBA, thus being virtually negligible. Of course, the undesired emission from the spacer generally depends on the absorption and quantum efficiency of the spacer and the emitting layer as well as on the thickness of the spacer.

To avoid errors arising from the spacer, this layer can be completely omitted. Hence, only a thin doped emission layer is deposited on glass. Figures 11.16 and 11.17 show the simulations and measurements for p- and s-polarized emission, respectively, for a 12 nm thick BDASBi:CBP (6 wt%) layer on glass.

It is apparent that the difference between the two simulated curves for isotropic and horizontal orientation is much less pronounced if no spacer is implemented. To obtain the degree of orientation, the p-polarized simulations in Fig. 11.16 are weighted in order to reproduce the measured curve. Assuming a ratio of $p_z : p_x = 0.43 : 1$ yields excellent agreement. Hence, the overall fraction of vertical (p_z) dipoles is $0.43/2.43 = 18$ %, the fraction of horizontal (p_x, p_y) dipoles is $2/2.43 = 82$ %. This value is slightly lower than the result obtained from the sample with a 70 nm thick spacer layer, probably due to the different sample layout or due to a partial crystallisation of the sample without spacer layer. Nevertheless, both results clearly indicate a strong orientation of BDASBi when doped into a CBP matrix.

The s-polarized measurement in Fig. 11.17 shows perfect agreement with the simulation, thus confirming the correctness of the optical constants of the CBP matrix.

It is worth mentioning that first evidence was found in this work that crystallization of the matrix considerably changes the degree of orientation. In fact, it was even found that the emitter seems to be mainly vertically oriented after the samples crystallized over a period of several weeks. However, further experiments are required in order to

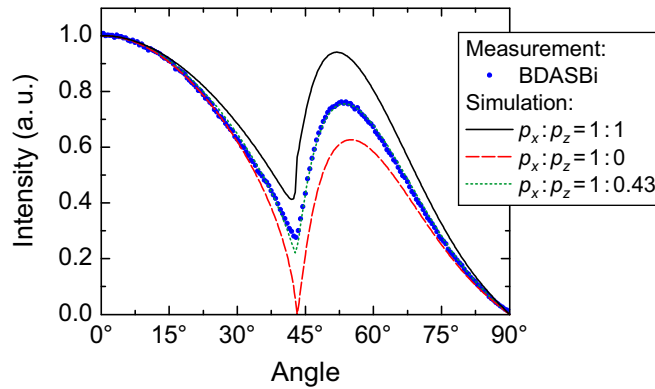


Figure 11.16: Angular dependent cross section at a wavelength of 470 nm of the simulated and measured p-polarized emission spectra of 12 nm thick BDASBi:CBP (6 wt%). No spacer layer was used in this case. All cross sections are normalized to the emission at small angles.

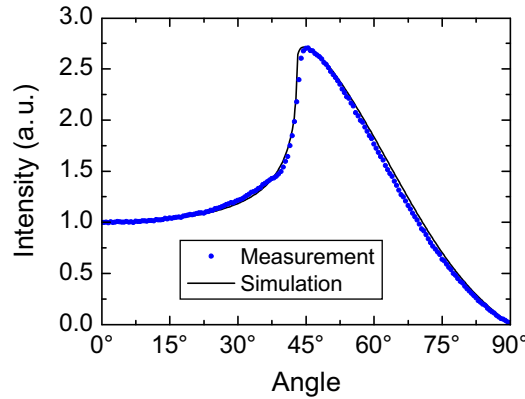


Figure 11.17: Angular dependent cross section at a wavelength of 470 nm similar to Fig. 11.16, but for s-polarized emission.

determine whether this effect really results from a reorientation of the emitter in the matrix material or if the difference is caused by changes in the optical constants of the matrix. Certainly, a reorientation of the emitter in the matrix would represent a totally new degradation mechanism, which would considerably reduce the outcoupling efficiency of an OLED without strongly changing any other properties like the electrical characteristics.

Besides uncertainties in the thicknesses and optical constants used for the simulations, several other aspects have to be taken into account. First, problems might arise from the experimental setup. For instance, small differences are detected if the rotation table is moved in the opposite direction. In addition, the thickness of the glass substrate is not taken into account, i.e. the emitted radiation does not originate from the center of the prism²¹⁴. Therefore, the radiation does not exactly impinge on the interface between the glass prism and air under right angle, thus causing a slight focusing effect¹⁴¹. Moreover, it is not considered that the light first travels through the glass substrate and then gets

refracted into the prism. Although the influence of all these effects is rather small, an improvement could be achieved by using a glass prism made of BK7 instead of fused silica and by positioning the emitting region in the center of the prism. Using a BK7 prism would also allow for extracting light that is otherwise totally internally reflected at the substrate/prism interface.

Furthermore, it is important to note that the excitation condition in principle can have a significant influence on the result of the PL measurement. The 375 nm laser diode is mainly p-polarized, and light was usually incident under 45° . Due to refraction at the interface between air and organic, the laser enters the organic film under an angle smaller than 45° . Hence, it can be expected that mainly p_x -dipoles are excited, because they have the best overlap with the electric field of the incident radiation. Of course, this selective excitation principally could strongly alter the result. However, it was reported for instance in the case of Alq_3 and Eu^{3+} ions that the dipole samples all orientations in space during the emission lifetime^{14,25,84} and, thus, takes an average value independent of the excitation condition. This effect can also be understood by the diffusion process of excitons. Usually, an exciton moves to several other molecules before it decays⁸⁴, hence causing a randomization of the orientation between the absorbing and emitting dipole state. Of course, if no redistribution would occur for a certain emitter, one would expect a different result for the degree of orientation upon changing the excitation conditions. Therefore, measurements on a series of emitters were performed with the laser light incident under both 45° and normal direction²⁴⁴. Moreover, the laser was rotated so that the excitation light was varied between p- and s-polarization. All experiments demonstrated that the obtained degree of orientation is virtually independent of the excitation. Nevertheless, it cannot be fully ruled out that the actual excitation has an influence for other emitter systems²¹⁴, in particular for neat fluorescent emitters with a short excited state lifetime. Moreover, it must also be ensured that the emitter does not degrade during the angular dependent measurement, because this would result in an inaccurate degree of orientation. Therefore, all measurements were repeated to exclude any degradation effects.

Regarding the optical simulations, the CBP matrix was assumed to be isotropic. In reality, CBP is slightly birefringent with a difference between ordinary and extraordinary refractive index of approximately 0.05 in the visible region¹⁶⁸. Here, the small birefringence is not taken into account. Moreover, the emitter position was assumed to be centered in the emission layer for sake of simplicity. Certainly, it is possible to simulate a distributed emission region to account for the fact that the whole region is excited by the laser in the experiment. However, it was found that the difference between both simulation methods is of the order of 1% as long as the emitting region is narrow. Hence, the assumption of a centered emitter position is reasonable and saves computation time.

Furthermore, the simulation does not account for light that is emitted into the direc-

tion of the encapsulation, where it is partially reflected and then also emitted through the glass prism. Basically, it is possible to account for this phenomenon and also for birefringence by improving the simulation program or by using other simulation routines²⁴⁵.

Finally, the calculated orientation can slightly differ if the cross sections are analyzed at different wavelengths. To keep the analysis consistent, all cross sections were investigated close to the emission maximum of the corresponding emitter system. Taking all these effects into account, it can be estimated that the total uncertainty amounts to at least 3 – 5 % depending on the stack layout.

In summary, a method to determine the orientation of the transition dipole moment of light-emitting organic thin films was demonstrated²²⁴. In contrast to other procedures, this is a straightforward and expeditious approach that does not only result in a rough estimate but quantitatively determines the fraction of horizontally oriented dipoles even in doped films. It should be emphasized that it is not necessary to know any information about the dopant for the detailed analysis of the cross sections. Neither the optical constants nor the PL spectrum are required, rendering this method particularly useful for a reliable investigation of newly developed materials.

It is important to note that this approach is in principle also applicable to neat films as well as to phosphorescent emitters. In fact, in the meantime this method has been applied to the analysis of numerous small molecular materials both in doped and neat films as well as light-emitting polymers. Moreover, weakly fluorescing materials which are typically implemented in organic photovoltaic cells were investigated, because orientation effects are also important for the absorption of light and for improved charge transport^{246,247}. The experimental details and results are described in the diploma thesis of Christian Mayr²⁴⁴.

Altogether, it was found that many materials exist which show a pronounced horizontal dipole orientation, thus opening up new possibilities to enhance the outcoupling efficiency of OLEDs. One of the highest degrees of horizontal orientation was found for BDASBi doped into CBP. Consequently, the next step is to implement this emitter system into a complete OLED device to demonstrate the enhanced outcoupling under electrical operation.

11.4. Increased light extraction efficiency in dye-doped small molecule OLEDs with horizontally oriented emitters

11.4.1. Stack layout and sample preparation

As a result of the previous analysis, BDASBi and PEBA are ideal candidates for studying the effect of molecular orientation in actual OLED devices²²⁵. The basic idea is to

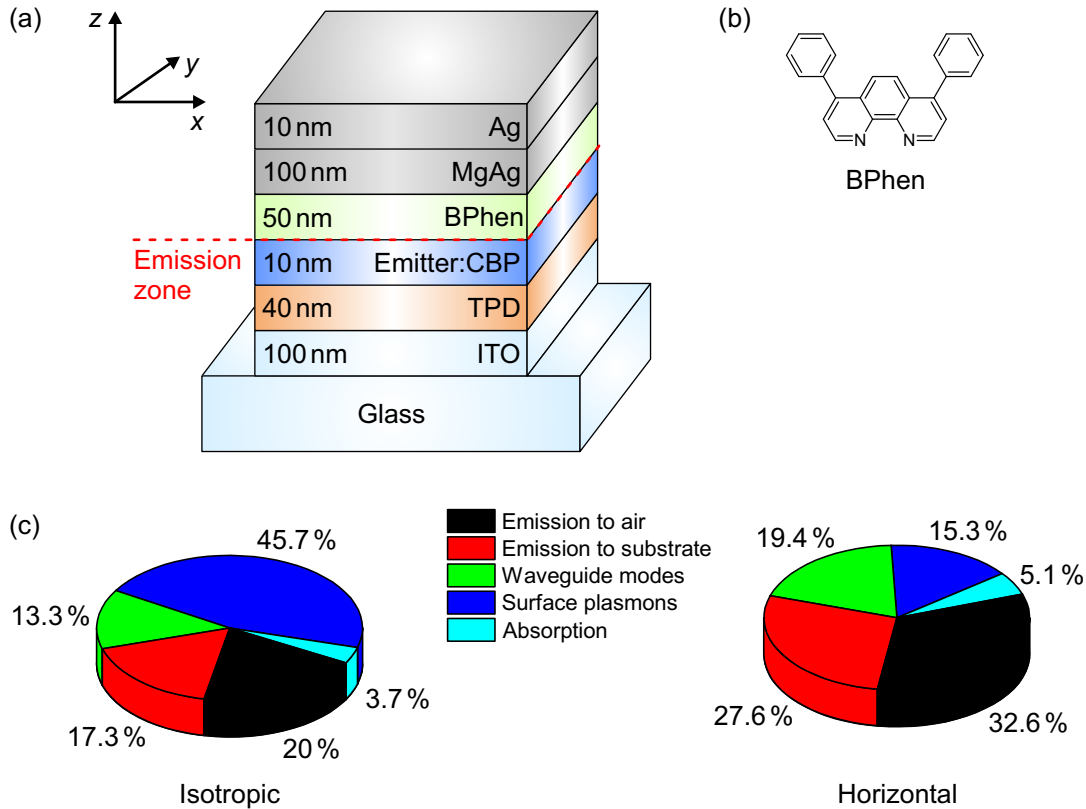


Figure 11.18: (a) Schematic device layout of the blue fluorescent OLEDs and definition of the coordinate system and dipole orientations used in the simulation. As emitting materials, BDASBi or PEBA were doped into a CBP matrix. The emitter position is assumed to be at the CBP/BPhen interface. (b) Molecular structure of BPhen. (c) Fraction of power coupled to different optical channels assuming a radiative quantum efficiency of $q = 100\%$ and an emission spectrum resembling that of BDASBi:CBP (6 wt%) for either isotropic or horizontal emitter orientation. Details concerning the power dissipation spectra and the influence of the distance of the emitter to the metallic cathode can be found in Ref. [225].

demonstrate the enhanced outcoupling by comparing the external quantum efficiency of two almost identical OLED stacks that only differ in the orientation of their emitter materials. Therefore, both BDASBi and PEBA were incorporated in a rather simple device structure in order to rule out differences in device fabrication. The stack layout is illustrated in Fig. 11.18(a). The devices consist of a glass substrate covered with a patterned indium tin oxide layer with 100 nm thickness, followed by 40 nm of the hole transport material TPD, 10 nm of either BDASBi or PEBA doped into CBP (6 wt%), 50 nm of the electron transport material 4,7-diphenyl-1,10-phenanthroline (BPhen, molecular structure shown in Fig. 11.18(b)) and a cathode consisting of 100 nm Mg:Ag (10:1) and a 10 nm thick Ag capping layer. A very thin emission layer was selected to ensure that the emission originates from the same position within the stack for both emitter systems.

All organic layers were deposited in a vacuum of less than 3×10^{-5} mbar at an evaporation rate of approximately 2 \AA/s except for the cathode, which was fabricated

at a rate of about 1 Å/s. All layers of the BDASBi and PEBA OLEDs except for the doped emission layer were deposited simultaneously in order to rule out differences in layer thicknesses. In addition, the substrates were rotated at equivalent positions from the axis during deposition. The active area of the OLEDs was circularly shaped with a diameter of 1 mm.

The current-voltage-luminance characteristics of the OLEDs were measured using a semiconductor parameter analyzer (E5273A, Agilent Co.) with an optical power meter (1930C, Newport Co.). The zero-degree spectra of the OLEDs were measured using a multichannel spectrometer (SD2000, Ocean Optics Co.) through an optical fiber whose end was positioned vertically towards the substrate of the OLEDs. The silicon photodiode of the optical power meter was calibrated at a wavelength of 485 nm, corresponding to the emission peak wavelength of the OLEDs. The emission spectra of the OLEDs are sufficiently narrow to neglect the spectral dependence of the response of the silicon photodiode. The photodiode captures light within a cone of approximately 56°. For the calculation of EQE values from the measurement, a Lambertian emission was assumed, which compares reasonably well with measured and simulated angular dependent spectra²²⁹. Samples for radiative quantum efficiency measurements comprised 50 nm thick doped films of 6 wt% BDASBi or PEBA in CBP deposited on cleaned fused silica substrates. Radiative quantum efficiencies were determined using an absolute PL quantum yield measurement system (C9920-02, Hamamatsu Photonics K.K.).

The stack layout was optimized by optical simulations in order to obtain a high direct emission for both isotropically or horizontally oriented emitting molecules, as can be seen in the integral optical power dissipation shown in Fig. 11.18(c). Even for a completely isotropic emitter orientation, the simulations predict a rather high outcoupling efficiency η_{out} for direct emission of 20%. If all emitting dipoles were perfectly horizontally oriented, the outcoupling efficiency would amount to a remarkable value of 32.6%. This considerable enhancement is due to the fact that the vertical p_z -dipole couples to more than 94% to surface plasmons in this particular OLED stack²²⁵. Consequently, by redistributing power from p_z -dipoles to horizontally oriented dipoles, the emission to air and substrate can be increased. It is important to emphasize that this enhancement is solely based on the effect of emitter orientation. If additional outcoupling structures were implemented to also extract substrate emission, the total outcoupling efficiency could be increased from around 37% for isotropic orientation to approximately 60% in the case of horizontally oriented emitters.

It was already demonstrated in Fig. 11.11(b) that BDASBi and PEBA doped into CBP have an almost similar emission spectrum with a peak at about 470 nm. In addition, a rather comparable radiative quantum efficiency q of 65% and 55% was determined for BDASBi:CBP and PEBA:CBP films (6 wt%), respectively. Neglecting any effects of orientation, it is expected that the BDASBi OLED has a 1.16 times larger external quantum efficiency than the PEBA OLED due to the difference in radiative

quantum efficiencies. This value is slightly smaller than the ratio 0.65 : 0.55 because PEBA benefits slightly more from the cavity enhancement (i.e. Purcell effect) due to the smaller intrinsic value of q .

The simulations can also be used to predict the influence of orientation, which should additionally boost the efficiency of the OLED with BDASBi. Assuming $q = 65\%$ and 88% horizontal orientation from the analysis in the previous sections, it is expected that the OLED based on BDASBi gains an extra enhancement of outcoupling efficiency (and external quantum efficiency) by a factor of 1.37 in comparison to an isotropic orientation. If BDASBi molecules were perfectly horizontally oriented, this enhancement would even amount to a factor of 1.59. It should be noted that a slightly larger enhancement would be expected from Fig. 11.18(c). However, the ratio between isotropic and horizontal orientation changes a little bit if also cavity effects and a quantum efficiency $q < 1$ are considered.

11.4.2. Current-voltage characteristics and emission spectra

For a conclusive determination of η_{out} from a measurement of η_{EQE} it is critical that all other factors in Eq. (2.1) are comparable. First, the spin-allowed exciton fraction η_{ST} is generally accepted to have a value of 25% in small molecule OLEDs based on fluorescent emitters^{39,40}. Second, the radiative quantum efficiency q was determined to be 65% for the BDASBi:CBP and 55% for PEBA:CBP layers, as discussed above. This difference must be included in optical simulations due to different cavity enhancement^{8,49,52}. Finally, the charge balance factor γ is mainly governed by the transport layers TPD and BPhen. Since both OLEDs comprise the same structure, it can be assumed that γ is rather similar in both devices.

In addition, it is necessary to have information concerning the emitter position and the distance to the cathode, because this has an important influence on the simulated outcoupling efficiency. Since both BDASBi and PEBA contain triphenylamine substituents, it is expected that they have a higher hole than electron mobility. CBP also shows a slightly larger hole than electron mobility⁸⁸, therefore it is reasonable to assume that the emission takes place close to the interface between the emitting layer and BPhen.

In the following, the assumptions concerning charge balance and emitter position are further verified by investigating the current-voltage characteristics and the zero-degree emission spectra at different current densities. Figure 11.19 shows the current-voltage characteristics for two OLEDs based on BDASBi and PEBA as emitters, respectively. Since the OLEDs only differ in their dopant, the measured current density is nearly the same for both devices. This strengthens the assumption of comparable charge balance.

Although charge trapping effects in the doped CBP matrix cannot be fully ruled out due to slightly different LUMO energies of BDASBi and PEBA²²⁵, the almost identical current-voltage characteristics give strong evidence that differences in charge carrier

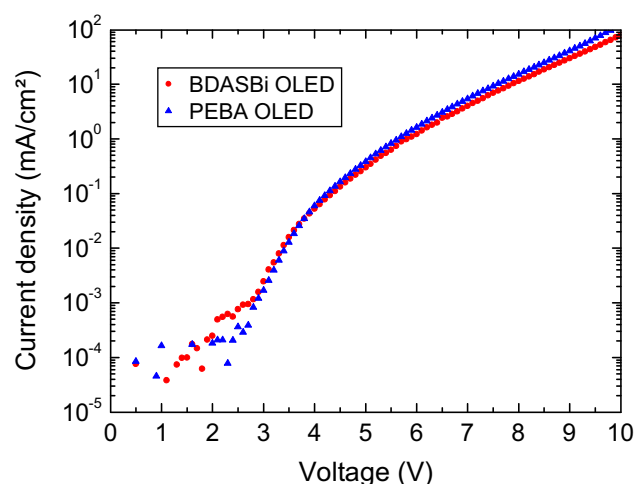


Figure 11.19: Measured current-voltage characteristics for OLEDs comprising either BDASBi:CBP or PEBA:CBP as emitting layer.

transport and recombination in both devices do not play a dominant role. HOMO levels of BDASBi and PEBA were determined by Daisuke Yokoyama (Yamagata University, Japan) using vacuum-deposited films analyzed by atmospheric ultraviolet photoelectron spectroscopy (Riken Keiki, AC-3). Both materials have a HOMO of 5.6 eV. In addition, a HOMO level of about 6.0 eV was reported for CBP²⁴. LUMO levels were calculated from the HOMO levels and the low energy edges of the absorption spectra^{81,89} of neat BDASBi, PEBA and CBP films on fused silica. The values are about 2.9 eV for BDASBi, 2.7 eV for PEBA and 2.6 eV for CBP. Hence, it cannot be completely ruled out that electron trapping plays a slightly more important role in the BDASBi devices. However, strong trapping effects probably would cause significant differences between BDASBi and PEBA OLEDs in the current-voltage characteristics, which has not been observed in the measurement. Regarding energy levels, it should be kept in mind that it is not possible to determine exact values for organic films. Hence, the values differ depending on the reference. For instance, HOMOs between 5.9 eV and 6.3 eV as well as LUMOs between 2.6 eV and 3.0 eV have been reported for CBP^{24,76,77}.

Zero-degree spectra of both OLEDs are plotted in Fig. 11.20 for different current densities. The spectra are almost independent of current density, confirming that the emitter position does not significantly depend on current density, as otherwise the spectra would shift due to changing cavity effects²⁶. In addition, Fig. 11.20 illustrates again that the spectra of OLEDs fabricated with both materials are well comparable.

11.4.3. External quantum efficiency

The external quantum efficiency η_{EQE} is shown in Fig. 11.21. Apparently, η_{EQE} of the OLED based on BDASBi compared to η_{EQE} of the PEBA OLED is significantly larger than only a factor of 1.16, which would be expected from the difference in radiative

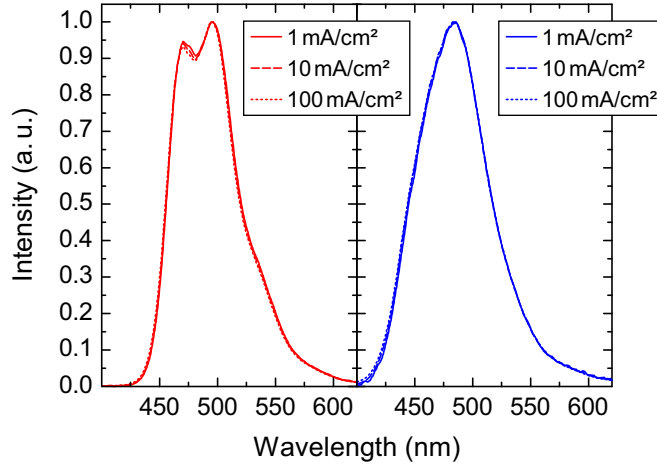


Figure 11.20: Measured zero-degree emission spectra at different current densities for OLEDs based on BDASBi:CBP (left) and PEBA:CBP (right).

quantum efficiencies. An average in the range between 0.1 mA/cm^2 and 10 mA/cm^2 yields an η_{EQE} of 2.7% for the BDASBi stack and 1.6% for the device based on PEBA. It should be noted that the absolute values of η_{EQE} for both devices are smaller than expected from simulations of the outcoupling efficiency, which yields approximately 3.9% for isotropic orientation and 5.9% for perfectly parallel orientation in case of BDASBi and 3.3% for isotropically oriented PEBA molecules, respectively²²⁹. This is probably due to imperfect charge balance owing to the fact that no doped transport layers and selective carrier blocking layers were used in this rather simple OLED stack. However, since both types of OLEDs utilize identical HTL and ETL (fabricated in the same evaporation run) as well as the same matrix for the EML, it is believed that both devices have quite comparable charge balance factor γ . In addition, it should be emphasized that mainly the relative increase of outcoupling efficiency is of interest. Thus, any effects that reduce the efficiency and that occur in both types of OLEDs cancel out.

Taking into account the difference in radiative quantum efficiency, it follows that the OLED based on BDASBi exhibits an increase of outcoupling efficiency compared to an isotropic orientation by a factor of 1.45 due to the strongly horizontally oriented dipoles. This is even slightly higher than the value expected from the analysis of dipole orientation in both materials, but it validates the basic result of mainly horizontally oriented dipoles in BDASBi obtained by ellipsometry²²⁹ and the angular dependent photoluminescence measurement. Even allowing for different emitter positions in the simulation of both devices or small deviations from a Lambertian emission pattern, the outcoupling and external quantum efficiency of the OLED based on BDASBi is significantly larger²²⁹. Considering that the orientation of BDASBi is not yet perfectly horizontal, this manifests the enormous efficiency enhancement that can be obtained by incorporating oriented emitters into OLED devices based on small molecules.

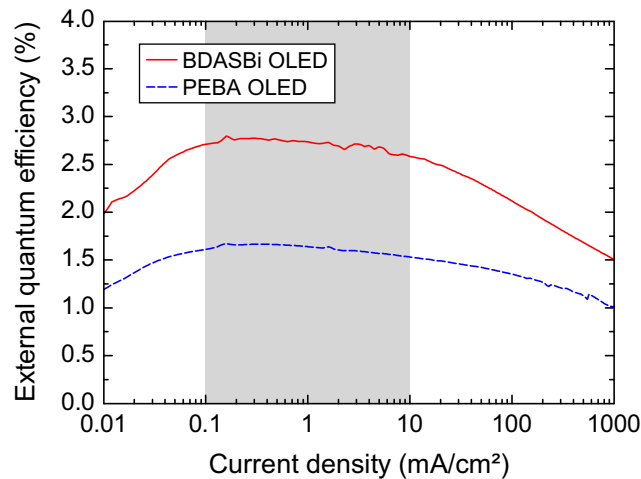


Figure 11.21: Experimentally determined external EL quantum efficiencies as a function of the current density. The blue curve represents an average of two measured pixels in order to account for small deviations between different pixels. The EQE values are averaged in the range between 0.1 mA/cm^2 and 10 mA/cm^2 because the measured curves have almost a plateau in this region, yielding an η_{EQE} of 2.7% for the BDASBi stack and 1.6% for the device based on PEBA. For smaller current densities there is probably no stable charge balance⁷¹, while quenching processes occur for higher current densities⁸⁹.

11.5. Phosphorescent guest-host systems

In the previous section, it was demonstrated for a blue fluorescent emitter that a horizontal orientation can significantly enhance the efficiency of OLEDs. Certainly, for a commercial application it is necessary to use also green and red emitters to obtain white light. Moreover, in terms of efficiency it is desirable to implement phosphorescent emitter systems. However, many phosphorescent emitters are rather bulky, which led to the generally supported opinion that they show an isotropic orientation. Here, it is demonstrated that partially oriented phosphorescent emitters do in fact exist, thus opening up new prospects for extremely high OLED efficiencies.

The device layout used for determining the orientation by a PL measurement is shown in Fig. 11.22(a). In this case, the stack represents an almost complete OLED. Only the cathode was omitted, so that no coupling to surface plasmons takes place. As a consequence, it is also possible to detect emission from vertical p_z -dipoles. The material under investigation is the red phosphorescent emitter bis(2-methyldibenzo-[f,h]quinoxaline)(acetylacetonate)iridium(III) $[\text{Ir}(\text{MDQ})_2(\text{acac})]$ doped into a N,N'-bis-(naphthalen-1-yl)-N,N'-bis(phenyl)benzidine (α -NPD) matrix (8 wt%). The structures of both materials are displayed in Fig. 11.22(b). Similar stacks were also prepared as real OLED devices with an additional Ag cathode to check the thicknesses of all layers by comparing the emission spectra to optical simulations (Daniel Setz, OSRAM OS, Regensburg, Germany).

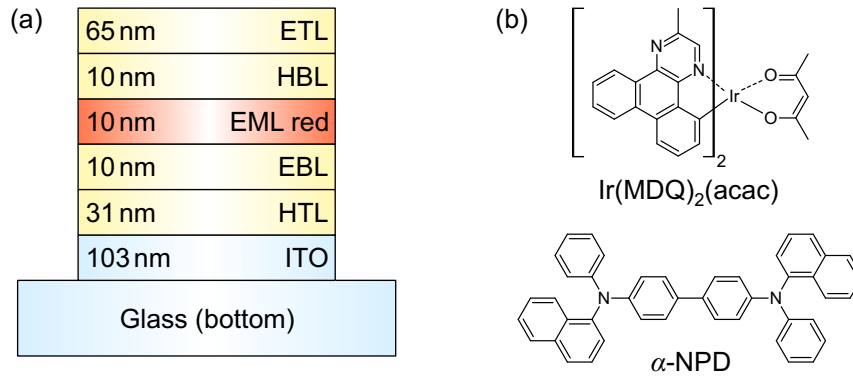


Figure 11.22: (a) Schematic illustration of the stack layout used for the determination of the orientation by a PL measurement. The emitting layer is made of the red phosphorescent material Ir(MDQ)₂(acac) doped into α -NPD (8 wt%). In addition, the stack comprises electron and hole transport layers (ETL and HTL) as well as electron and hole blocking layers (EBL and HBL). The cathode was omitted so that no coupling to surface plasmons occurs. The fabrication of the devices was carried out at OSRAM OS, Regensburg, Germany, and is described in detail in Ref. [248]. (b) Molecular structures of Ir(MDQ)₂(acac) and α -NPD.

In order to determine the dipole orientation, angular dependent PL measurements were performed according to the method introduced in Sec. 11.3. Cross sections at a wavelength of 610 nm of the simulated and measured p-polarized emission spectra are presented in Fig. 11.23(a). It is apparent that the measured curve can be very well reproduced by using a ratio of vertical p_z - to horizontal p_x -dipoles of 0.6 : 1. Assuming that the horizontal p_x - and p_y -dipoles are uniformly distributed, the total ratio of vertical to horizontal dipoles is 0.6 : 2. This corresponds to a fraction of $0.6/2.6 = 23\%$ vertical dipoles and $2/2.6 = 77\%$ horizontal dipoles. The comparison of the s-polarized measurement with the corresponding simulation in Fig. 11.23(b) generally shows good agreement, except for a certain deviation at angles around 55° .

The overall result demonstrates that the method of determining the orientation by PL measurements can also be applied to OLED-like architectures without cathodes, so that the environment of the emitter is similar to the actual OLED device and that influences of adjacent layers are taken into account. To make sure that the result is not influenced by the excitation condition, the sample was excited by both s- and p-polarized light. In addition, the angle of incidence was varied between 45° and normal incidence. It was found that the degree of orientation is independent of the actual excitation condition, thus demonstrating that the absorbed laser energy is redistributed among the dipole ensemble before the absorbed energy is re-emitted.

The result was also confirmed by using a different simulation program that also accounts for reflections at the encapsulation glass^{245,248}. In this case, a rather similar result of vertical to horizontal orientation of 0.67 : 2 was found, which corresponds to a horizontal orientation of 75%. By taking reflections at the glass interface into account,

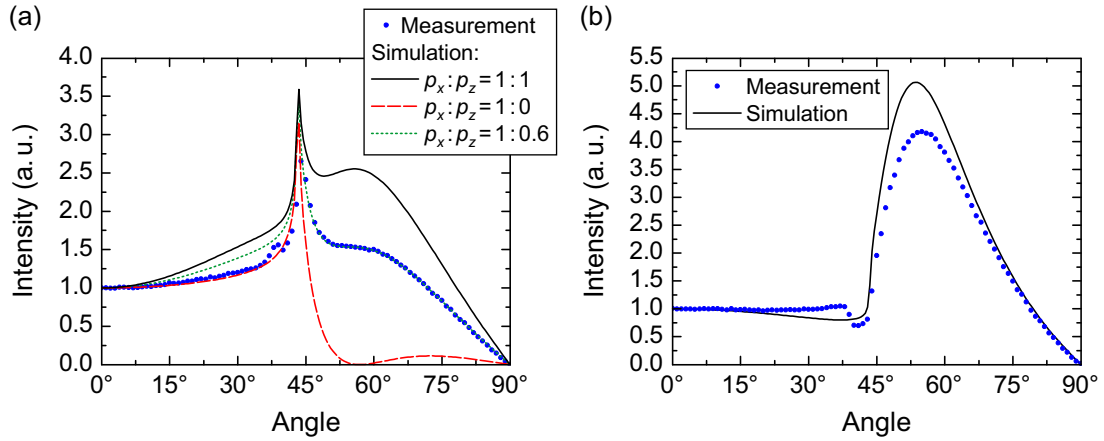


Figure 11.23: (a) Angular dependent cross section at 610 nm of the simulated and measured p-polarized emission spectra of the device shown in Fig. 11.22(a). The measured emission intensity is scaled so that the emission at small angles corresponds to the simulations. (b) Similar to part (a), but for s-polarized emission.

the agreement between measured and simulated curves can especially be improved in the range below 40° , yielding an almost perfect fit over the whole angular range. Moreover, very good agreement for the s-polarized case can be achieved. Details can be found in Ref. [248]. It is worth mentioning that the orientation was also controlled by Flämmich *et al.* using complete OLEDs under electrical operation with a chosen ETL thickness that favors emission from vertical dipoles²⁴⁸, as discussed in Sec. 11.3. A quite similar result for the ratio between vertical and horizontal dipoles of $0.63 : 2$ was obtained. This corresponds to a horizontal orientation of 76 %, hence confirming the value obtained from Fig. 11.23(a).

11.6. Conclusions

In summary, this chapter was dedicated to the influence of molecular orientation on the efficiency of OLEDs. It was demonstrated by means of optical simulations that emitting dipoles oriented horizontally with respect to the substrate plane boost the outcoupling efficiency of OLEDs by a factor of typically 1.5. The main reason for this enhancement is the fact that vertical dipoles dissipate their power almost completely to surface plasmons in common optimized OLED devices.

In order to experimentally study orientation effects, it is required to determine the orientation of the transition dipole moment of a given emitter system. Based on the different emission patterns of vertical and horizontal dipoles, a method was introduced that allows for the determination of the degree of orientation by performing angular dependent emission measurements and comparing the results to optical simulations. In contrast to other procedures, this is a straightforward and expeditious approach that does not only result in a rough estimate but quantitatively determines the fraction

of horizontally oriented dipoles even in doped films. The method has the advantage of requiring only a very simple stack layout, thus making it possible to determine the dipole orientation without the need of fabricating a complete OLED. It should be emphasized that the detailed analysis of the cross sections only requires knowledge about the matrix environment. Hence, neither the optical constants nor the PL spectrum of the dopant are required, rendering this method particularly useful for a reliable investigation of newly developed materials. To further simplify the method, it would even be sufficient to detect the emission intensity only at two fixed angles, e.g. 0° and 60° , thus rendering the rotary table unnecessary.

Concerning the stack layout used for the determination of orientation, it was found that either an optical spacer layer should be used between the emitting layer and air with a thickness of about 50 – 70 nm in case of CBP or that the spacer layer should be completely omitted. The first layout has the advantage that the difference between isotropic and horizontal orientation at large emission angles is maximal, whereas the second structure offers the advantage that no uncertainties regarding the thickness and optical constants of the spacer play a role.

The convenience of the presented measurement technique was demonstrated by the investigation of two blue fluorescent small molecular emitters doped into a CBP matrix, resulting in a considerable horizontal dipole orientation of around 88% in the case of BDASBi, while PEBA seemed to be perfectly isotropically oriented.

To verify the enhanced outcoupling efficiency of horizontally oriented emitters, experimental results for a BDASBi OLED were presented and compared to a reference PEBA OLED having a similar device layout but isotropic emitter orientation. It was found that the OLED incorporating oriented BDASBi molecules shows better light out-coupling and higher external quantum efficiency by a factor of about 1.45 compared to the efficiencies that a BDASBi OLED would have in case of isotropically oriented emitters. This basically agrees with the expected increase according to the determined orientation of the emitter system. For perfectly flat-lying molecules, an increase of even more than a factor of 1.5 would be expected.

The concept of non-isotropic emitter orientation to achieve enhanced light out-coupling, presented here for the first time in dye-doped small molecule OLEDs, is of course not limited to fluorescent materials only, but can also be applied to phosphorescent dyes. Since the latter are usually rather bulky metal-organic complexes, achieving horizontally oriented emitter molecules will be more challenging than with rod-like linear molecules. However, it was demonstrated that the red triplet-emitting material $\text{Ir}(\text{MDQ})_2(\text{acac})$ shows a significant non-isotropic orientation when doped into an α -NPD matrix. For the future, tailoring phosphorescent materials with respect to this feature, e.g. by asymmetric organic ligands, might allow for a substantial increase in external quantum efficiency from about 20% with isotropic emitter orientation to well beyond 30% in the case of flat-lying dipoles - without any additional outcoupling structure.

It should be emphasized that using horizontally oriented emitters fabricated in a common evaporation process does not change production costs at all. On the contrary, comparably efficient outcoupling enhancement techniques like scattering at grating structures significantly complicate the fabrication process and raise the costs accordingly.

It is also important to point out that horizontally oriented emitters simply enhance the existing emission of an OLED without changing the angular dependent emission characteristics. This is also relevant in the context of applications, which usually require that the emission shows no strong angular dispersion (as in the case of gratings) or no emission in different directions (as in the case of prism coupling). In contrast to all methods discussed in the previous chapters, which are based on recovering power lost to surface plasmons in order to increase the outcoupling efficiency, implementing horizontally oriented emitters means to be one step ahead, i.e. the initial coupling to surface plasmons is already reduced by about two thirds, and the power is redistributed to more favorable optical channels like emission to air or substrate modes.

Regarding the material choice, it must be taken into account that the effect of horizontally oriented emitter molecules can to some extent compensate for a lower radiative quantum efficiency as compared to an isotropic material. For example, the search for the longed-for stable deep-blue phosphorescent emitter could take a turn: The general difference of a factor of 4 in the external quantum efficiency between phosphorescent and fluorescent emitters reduces to only about 2.5 if the fluorescent emitter is horizontally oriented. Thus, present stability problems with blue phosphorescent emitters may be avoided without sacrificing too much in terms of efficiency.

Besides the enormous boost in outcoupling and external quantum efficiency, the use of oriented emitters in OLEDs offers a series of additional benefits. First, the emitter position may be shifted closer to the cathode without losing too much energy to surface plasmons. Thus, the emitter can be placed at a position where it receives optimal interference and cavity enhancement. Additionally, with horizontally oriented emitters both the first and second cavity maxima are comparable in outcoupling efficiency, which offers more freedom in stack design. The possibility to place the emitter close to the cathode is especially important in white OLEDs and stacked OLEDs that comprise several emitting layers²⁴⁹⁻²⁵².

Furthermore, it is essential to know the correct dipole orientation in any analysis of measured η_{EQE} values, since the outcoupling efficiency can change by more than a factor of 1.5. If the emitter orientation is not properly taken into account, this implies equivalently large errors in the determination of the internal quantum efficiency and, for instance, the spin-allowed exciton fraction^{52,226}. Moreover, optimizing the stack layout, for instance finding the optimal distance to the cathode, requires accurate knowledge about the actual degree of orientation in order to obtain maximum efficiency. Finally, oriented molecules can also have a positive influence on the electrical behavior. Because alignment enlarges the overlap of molecular orbitals between adjacent molecules,

non-isotropic orientation can contribute to an improvement of the charge transport characteristics not only in OLEDs^{246,247} but also in organic field effect transistors. In addition, organic photovoltaic cells could benefit from both a better charge transport as well as from an increased absorption due to horizontally oriented emitters.

12. Summary and outlook

Organic light-emitting diodes are flat and large-area light sources with a huge potential for applications in general lighting. Laboratory samples have proven that these light sources are very efficient, and first commercial products are already available. Nevertheless, the overall efficiency of OLEDs is still far below the theoretical maximum. This is mainly due to a rather low light extraction with losses resulting from total internal reflection in the OLED multilayer stack and from coupling to surface plasmons at the metallic cathode. Typically, 80 % of the optical power is trapped as substrate or waveguide modes, or is coupled to SPs.

The motivation of this thesis was to fundamentally investigate the physical processes that govern power dissipation and light extraction in OLEDs. By analyzing and understanding the physics inside an OLED multilayer stack, it was possible to develop novel ways of enhancing OLED efficiency by either recovering some of the optical losses or by reducing the coupling to unfavorable optical channels. This section summarizes the main results of this work and gives an outlook on interesting future investigations.

Summary

The basic processes which take place in an OLED as well as some basic rules regarding stack design were introduced and explained by means of four exemplary OLEDs. In order to obtain maximum efficiency, four factors must be optimized. First, it is important to have a balanced hole and electron transport. This can be achieved by using injection layers, blocking layers, as well as doped transport layers. Second, it is favorable to use phosphorescent emitters so that also triplet states contribute to the emission. Third, emitter materials with a high radiative quantum efficiency should be implemented. Finally, it is necessary to extract as much light as possible from the thin film structure, i.e. the light extraction must be optimized.

In order to understand the optical processes that determine the optical power dissipation in an OLED, the basic interactions of electromagnetic waves with matter were discussed, e.g. reflection and refraction at interfaces, as well as the occurrence of guided modes in planar thin film structures.

Since OLEDs usually comprise a metallic cathode, it is required to account for coupling to surface plasmons, i.e. p-polarized electromagnetic surface waves traveling at the organic/metal interface. The dispersion relation of SPs was derived, and it was explained that special techniques (near-field coupling, grating coupling, or prism coupling)

are required to couple SPs and light. This is due to the fact that SPs have a larger wave-vector compared to electromagnetic radiation in the adjacent organic layer for a given frequency. The prism coupling technique was demonstrated by means of a novel surface plasmon resonance sensor which features an integrated OLED light source. The sensor was also used to measure the angular and wavelength dependent SP dispersion at thin layers of silver and gold adjacent to air.

Moreover, it was demonstrated that optical simulations based on a dipole model are excellently suited to gain more insight into the optical processes that take place in an OLED. It was explained that the radiative decay of an excited molecule is strongly affected by interference effects and by the proximity to a metallic surface. Moreover, it was shown that it is possible to distinguish between coupling to different optical channels by studying the power dissipation of an excited dipole in an OLED cavity.

The simulation result was verified by comparing measured and simulated angular dependent emission spectra. It was demonstrated that substrate modes can be extracted by applying an index-matched outcoupling prism to the glass substrate. Furthermore, it was shown that the comparison to optical simulations allows for a precise determination of the actual thicknesses of the organic layers in the OLED stack.

Optical simulations were also used to quantitatively determine the fraction of power coupled to each optical channel by integrating over the power dissipation. The simulation of an exemplary OLED stack confirmed that waveguide modes and in particular SPs typically cause losses of about 50% of the total power, thus representing a fundamental limitation to OLED efficiencies. Although an improvement was to some extent obtained by optimizing the layer thicknesses, it was essential to reduce coupling to waveguide modes and SPs, or to recover some of the losses.

Various ideas to extract substrate modes, waveguide modes or SPs have been reported in literature. After explaining the basic physics behind each approach, optical simulations were used to illustrate the influence of a special microcavity environment. Although the direct emission can be enhanced, microcavities are limited to monochromatic OLEDs and are not appropriate in the case of white OLEDs. Using high-index substrates combined with outcoupling structures allows for the extraction of substrate modes and even waveguided modes. However, substrates based on high-index materials are currently too expensive for an implementation in large-area OLEDs.

In this thesis, several approaches for enhanced light extraction were analyzed both from a theoretical as well as from an experimental point of view. Most of the methods are in particular compatible with common fabrication methods and applicable to a wide range of OLEDs. Specifically, the main discussed methods were

- near-field coupling,
- grating coupling,
- prism coupling,

- high-index coupling and
- emitter orientation.

The near-field coupling technique is based on the fact that SPs on two sides of a thin metal film can couple and exchange energy if the refractive indices on both sides are equal. By using appropriate acceptor molecules, the power lost to SPs can be partially recovered and extracted as free-space radiation. The influence of thin films on the SP dispersion was explained by analyzing the result of optical simulations for simplified stack layouts. Furthermore, the basic concept was verified by photoluminescence experiments using thin silver layers adjacent to doped PMMA films. By systematically varying the thickness of the silver film, an optimal thickness for maximum SP mediated energy transfer was determined. Evidence for the energy transfer was found by measuring the excited state lifetime of the donor and acceptor molecules. In principle, SPs can be partially recovered by using the near-field coupling method. However, the estimated efficiency of this method seems to be insufficient for an application in OLEDs.

A more promising method for enhanced light extraction is the implementation of grating structures to allow for outcoupling of bound modes by Bragg scattering. Periodic one-dimensional grating structures were fabricated by nanoimprint lithography. By measuring the angular dependent emission spectra under PL excitation, the extraction of SPs and waveguide modes was demonstrated. The influence of different periods was investigated by comparing grating periods of 555 nm and 833 nm, i.e. almost μm scale. This illustrates that it is not always necessary to use gratings with a period below 500 nm, which are usually more complex and thus expensive in fabrication. Moreover, the scattering order of all extracted modes was identified by comparison to optical simulations. In order to demonstrate that grating coupling can also be cost-efficient, the extraction of SPs by means of a common DVD structure was presented, i.e. by scattering at the DVD track pitch having a period of 740 nm.

The main disadvantage of grating coupling is an angular dispersive emission, i.e. the emission color changes with viewing angle. This must be corrected for a possible application in general lighting. Nevertheless, grating coupling has the advantage that the additional radiation arising from scattering is extracted into the same direction as the directly emitted light, e.g. through the substrate in case of a bottom-emitting OLED. In principle, it is possible to extract all bound modes by grating coupling, and high efficiencies have been reported in literature. All in all, this technique is very well suited for an application in OLEDs if the processes for grating fabrication can be further improved and reduced in terms of cost.

Another interesting method to transform SPs into free-space radiation is the prism coupling method. This technique is based on a reversed Kretschmann configuration, i.e. SPs traveling on one side of a thin metal film can transform into radiation on the opposite side of the metal if there is a medium with larger refractive index. The ba-

sis physics of this approach was investigated in measurements using simplified stacks having the structure organic/metal/glass combined with an index-matched outcoupling prism. The organic emitter was excited by a laser, and the extraction of SPs was successfully demonstrated. By varying the material of the metal film, it was found that silver is the metal of choice. Furthermore, it was shown that the thickness of the organic layer directly influences the SP dispersion. This was verified by measuring the angular position of the extracted radiation for different organic layer thicknesses. Moreover, the silver thickness has a crucial impact on this coupling method. An optimal silver thickness of about 40 nm for maximum SP extraction was found as a consequence of two competing effects: coupling of the organic emitter to SPs is stronger with increasing silver thickness, but the transmission through the silver film decreases. The experimental findings regarding the influence of the silver thickness were also supported by optical simulations.

The prism coupling geometry is also appropriate for extracting waveguide modes through the thin silver layer as leaky modes. This was demonstrated by increasing the organic layer thickness above 100 nm. Depending on the actual thickness, several s- and p-polarized guided modes propagate in the organic film. This effect was verified by measuring the angular dependent emission in the case of organic films having different thicknesses. Similar to the case of SP extraction, the outcoupling of waveguide modes strongly depends on the Ag thickness, as was verified by a systematic variation of the Ag thickness and by optical simulations.

Based on the fundamental investigations of the prism coupling technique, this concept is in principle well suited for an application in OLEDs. However, the situation in an OLED is more complex because organic layers typically have a refractive index around 1.8. Therefore, prism materials with a very high refractive index are required. By using a prism made of LiNbO_3 , it was demonstrated by PL measurements of simplified stacks that SPs and waveguide modes can be extracted for arbitrarily thick organic layers.

In order to apply this “high-index coupling” technique to real OLED devices, it was necessary to produce OLEDs having a thin silver cathode. Although it was not possible to attach the LiNbO_3 prism due to the lack of an appropriate index-matching liquid, the basic functionality of this concept was shown by applying a prism made of SF6 high-index glass ($n \approx 1.8$). It was demonstrated for the first time that not only substrate modes, but in particular waveguide modes and even SPs can be partially recovered from a state-of-the-art OLED by high-index coupling. Besides angular dependent measurements, the concept was visualized by photographs, which clearly allowed for an identification of each extracted optical mode.

The theoretical efficiency of high-index coupling was estimated by performing optical simulations. A remarkable outcoupling efficiency above 80% was predicted by optimizing the refractive index of the high-index material as well as the thickness of the

silver layer. Of course, such a high efficiency makes this method ideally suited for an application in OLEDs. Several ideas for a technical implementation were discussed. For instance, modern OLEDs sometimes have a high-index thin film encapsulation. By adding scattering particles or a certain surface roughness, very high outcoupling efficiencies could be realized.

A completely different approach to all methods discussed so far is to reduce the initial coupling of the excited molecules to unfavorable optical channels. Since power dissipation to SPs accounts for most of the optical losses, it is especially desirable to reduce coupling to SPs. A very efficient method is based on the orientation of the transition dipole moment of the molecule. Although this effect has already been known for polymer materials, which often show a predominantly horizontal orientation with respect to the substrate plane, small molecular materials usually have been assumed to be isotropically oriented. The influence of horizontally oriented emitters was investigated using optical simulations for different dipole orientations. It was shown that horizontally oriented dipoles typically gain an enhancement in light outcoupling efficiency by a factor of 1.5 compared to an isotropic orientation. This effect mainly results from the fact that vertical dipoles almost completely couple to SPs in the case of an optimized OLED structure.

For a profound investigation of the emitter orientation in OLEDs, it was required to quantitatively determine the orientation in fluorescent organic thin films. A novel straightforward method was presented which allows for a determination of orientation even for doped films, which are usually used in modern OLEDs. This technique is based on angular dependent emission measurements and comparison to optical simulations. The stack layout used for the analysis of orientation was optimized according to the results of simulations. The feasibility of this method was demonstrated by analyzing the orientation of the two fluorescent emitters BDASBi and PEBA doped into a CBP matrix. While PEBA shows an isotropic orientation, i.e. 67% horizontally and 33% vertically oriented emitters, a horizontal orientation of 88% was discovered in the case of BDASBi.

To demonstrate the impact of orientation, two kinds of OLEDs were prepared, having a similar device layout and using either BDASBi or PEBA as emitter materials. It was found that the OLED based on BDASBi gains an enhancement in light extraction by a factor of about 1.45, which agrees well with the expected enhancement taking into account the mainly horizontal orientation of BDASBi in the CBP matrix. Thus, the efficiency boost of horizontally oriented emitters in OLEDs based on small molecules was demonstrated for the first time.

Moreover, it was shown that even phosphorescent emitters which usually have a rather bulky structure can show a considerable non-isotropic orientation. The enhancement of OLED efficiency on the basis of oriented emitters is particularly interesting from a commercial point of view. This is due to the fact that certain guest-host systems

intrinsically show a horizontal orientation. No additional layers or surface structuring are required. Moreover, a horizontal dipole orientation does not cause any negative effects like an angular dispersive emission. Based on these findings, the implementation of horizontally oriented emitters in OLEDs is an excellent way to achieve a significant boost in efficiency.

Altogether, this thesis presented a profound analysis of the physical processes involved in power dissipation and light extraction in OLEDs. Several novel approaches for enhanced light outcoupling were developed and thoroughly investigated in order to understand the working principle of each method. By using one of these approaches or by combining several of them, it should be possible to achieve very high efficiencies, which is a basic requirement for a widespread application of OLEDs in general lighting.

Outlook

The purpose of this thesis was to fundamentally analyze all aspects related to light extraction in OLEDs and to understand the optical processes inside the OLED multi-layer structure. Although several novel approaches were demonstrated which have the potential to significantly enhance the light extraction in OLEDs, there are still many interesting tasks for future investigations.

In the context of grating coupling, the influence of the grating period, amplitude and of the grating shape could be investigated. Using a simulation program that takes periodic structures into account might help to support the experiments. Clearly, the effect of grating structures in real OLED devices under electrical operation will also be an important topic for future work. In addition, the determination of the extraction efficiency in OLEDs should be analyzed by combining angular dependent experiments and integrating sphere measurements in order to distinguish all optical modes. It is recommended to use emitters with a high quantum efficiency so that the intrinsic losses are close to zero. In this case, the uncertainty regarding the effective radiative quantum efficiency in the OLED cavity is small as long as moderate current densities are used.

The application of multidimensional gratings, e.g. produced by colloid monolayer lithography, might be superior to one-dimensional gratings regarding the overall efficiency. It should also be investigated if the implementation of random scattering structures, which principally provide a less dispersive emission, can compete with periodic structures in terms of efficiency.

Future investigations could also be devoted to the high-index coupling method. Certainly, it would be very interesting to investigate waveguide and SP extraction in an OLED under electrical operation. In addition, the extraction efficiency should be determined, e.g. by using an integrating sphere. These measurements, together with angular dependent measurements, could be used to verify the results obtained by optical simulations.

For a technical application of high-index coupling, it is required to investigate different ways to extract radiation once it is inside the high-index layer. Besides the implementation of converter dyes into the high-index layer, the incorporation of metallic particles is definitely an interesting approach²⁵³. By combining high-index coupling with a grating structure, light traveling inside the high-index region could be Bragg scattered and extracted. This approach is especially interesting for top-emitting OLEDs. In this case, it would be sufficient to deposit a rather thin high-index layer onto a structured glass substrate instead of using expensive high-index substrates.

In the context of emitter orientation, there are many open questions since the investigation of orientation effects in the case of small molecules has just begun. The method for determination of the molecular orientation introduced in this thesis is particularly well suited for the screening of novel material systems, because no information regarding

the properties of the dopant material is required.

From a chemical point of view, the question arises if it is possible to modify the chemical structure of some materials in order to enhance the horizontal orientation without changing the emission properties too much. For instance, it was found that materials having a long or planar molecular structure show more pronounced orientation effects¹⁶⁷, although the reason of orientation in amorphous organic thin films is not yet understood.

Besides investigating novel materials, it is of central interest to analyze different possibilities in order to influence the orientation of a given emitter. This can in principle be achieved by changing the deposition conditions, e.g. evaporation rate or temperature, or by modifying the roughness of the substrate²⁴⁷. Another task for future research is the influence of an electric or magnetic field or of polarized light during the deposition process.

In addition, the crystallization process could be further investigated. So far, changes of the angular dependent emission pattern upon crystallization of the matrix were detected, but it is not yet clear whether the effect is really based on a re-orientation of the dopant or on a modification of the optical properties of the crystallized matrix.

It would also be interesting to combine orientation effects and prism coupling. Depending on the degree of orientation, the emitter should couple more or less to surface plasmons. By measuring the SP emission in a Kretschmann configuration and by comparing the intensity to the directly emitted light, it should be possible to experimentally verify that coupling to SPs mainly depends on the vertically oriented dipoles.

Moreover, the preparation of microcavity OLEDs using horizontally oriented emitters is a promising topic for future research. In such an OLED geometry, it is possible to tailor the OLED cavity in order to optimally boost horizontally oriented emitters. According to the simulations presented in this thesis, very high outcoupling efficiencies close to 40 % for direct emission are predicted if the transition dipoles were completely horizontally oriented.

Finally, the influence of emitter orientation in OLEDs could be verified by preparing OLEDs based on the same emitter material but with different degrees of orientation. A potential candidate for such a study is polyfluorene^{254,255}, which can also exist in a liquid crystalline phase. Depending on the preparation conditions, the transition dipole moment of this material is either mainly horizontally or predominantly vertically oriented²⁴⁴. Thus, the material is perfectly suited for directly measuring the influence of orientation on OLED efficiency with only one type of emitter.

A. Appendix

A.1. Abbreviations

Materials

α -NPD	N,N'-bis(naphthalen-1-yl)-N,N'-bis(phenyl)benzidine
Alq ₃	Tris-(8-hydroxyquinoline)aluminum
BCP	2,9-dimethyl-4,7-diphenyl-1,10-phenanthroline
BDASBi	4,4'-bis[4-(diphenylamino)styryl]biphenyl
BPhen	4,7-diphenyl-1,10-phenanthroline
BSB-Cz	4,4'-bis[(N-carbazole)styryl]biphenyl
CBP	4,4'-N,N'-dicarbazole-biphenyl
DCM	4-(dicyanomethylene)-2-methyl-6-(4-dimethylaminostyryl)-4H-pyran
F ₄ -TCNQ	Tetrafluoro-tetracyanoquinodimethane
Ir(MDQ) ₂ (acac)	Bis(2-methyldibenzo[f,h]quinoxaline)(acetylacetonate)-iridium(III)
Ir(ppy) ₃	Tris(2-phenylpyridine) iridium
ITO	Indium-tin oxide
LiNbO ₃	Lithium niobate
LR	Lumogen Red
LY	Lumogen Yellow
NaCl	Sodium chloride
PEBA	4-(2,2-diphenylethenyl)-N,N-bis(4-methylphenyl)benzenamine
PEDOT/PSS	Poly(3,4-ethylenedioxythiophene) poly(styrenesulfonate)
PMMA	Polymethylmethacrylate
PtOEP	2,3,7,8,12,13,17,18-octaethyl-21H,23H-porphine platinum
S-DPVBi	4,4'-bis(2,2'-diphenylvinyl)-1,1'-spirobiphenyl
S-TAD	2,2',7,7'-tetrakis-(N,N-diphenylamino)-9,9'-spirobifluoren
SrTiO ₃	Strontium titanate
TiO ₂	Titanium dioxide
TPD	N,N'-diphenyl-N,N'-bis(3-methylphenyl)-1,1'-biphenyl-4,4'-diamine

General abbreviations

a. u.	Arbitrary units
AFM	Atomic force microscopy
ATR	Attenuated total (internal) reflection
CIE	Commission internationale de l'éclairage
CRI	Color rendering index
cw	Continuous wave
DB	Direct bottom emission
DT	Direct top emission
DVD	Digital versatile disc
EBL	Electron blocking layer
EIL	Electron injection layer
EL	Electroluminescence
EML	Emission layer
EQE	External (electroluminescence) quantum efficiency
ETL	Electron transport layer
HBL	Hole blocking layer
HIL	Hole injection layer
HOMO	Highest occupied molecular orbital
HTL	Hole transport layer
ISC	Intersystem crossing
LED	Light-emitting diode
LUMO	Lowest unoccupied molecular orbital
OFET	Organic field-effect transistor
OLED	Organic light-emitting diode
OPVC	Organic photovoltaic cell
PDCalc	Power Dissipation Calculator
PL	Photoluminescence
SB	Substrate bottom emission
SEM	Scanning electron microscope
SM	Substrate mode / Substrate mode emission
SP	Surface plasmon
SPP	Surface plasmon polariton
SPR	Surface plasmon resonance
ST	Substrate top emission
TE	Transverse electric
TM	Transverse magnetic
WG	Waveguide mode

A.2. Optical constants

This section shows the optical constants which were used for most of the simulations in this thesis in alphabetical order. For a few materials, a second data set was used for some simulations. It should be noted that only the optical constants of the matrix material were used in the case of doped layers. Some optical constants were determined by Daisuke Yokoyama (Yamagata University, Japan) using variable angle spectroscopic ellipsometry.

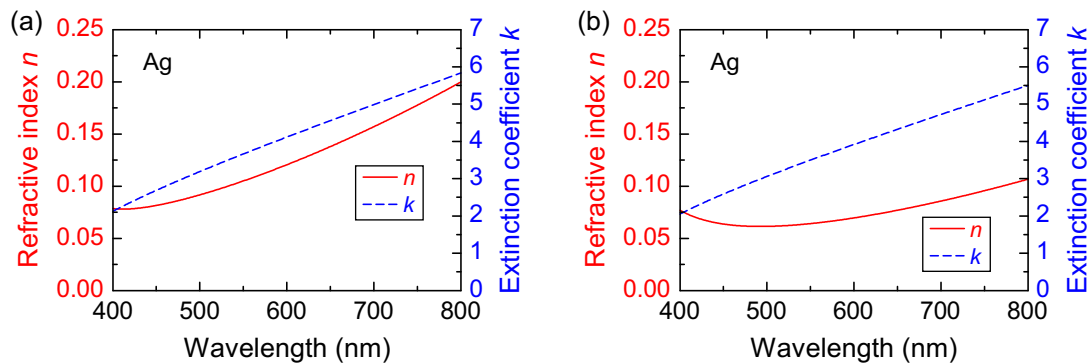


Figure A.1: Optical constants of silver. The data set in (a) was used for most simulations, while the data set in (b) was used in Chapter 9, Secs. 10.1–10.4 and Sec. 11.4.

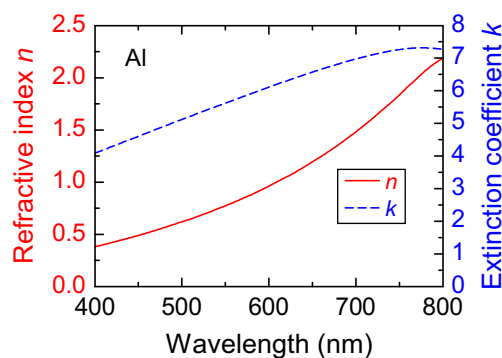


Figure A.2: Optical constants of aluminum.

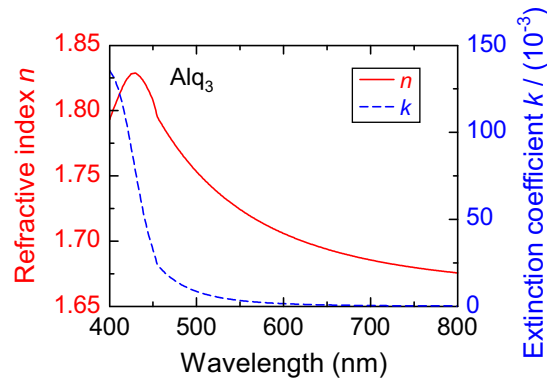


Figure A.3: Optical constants of Alq₃.

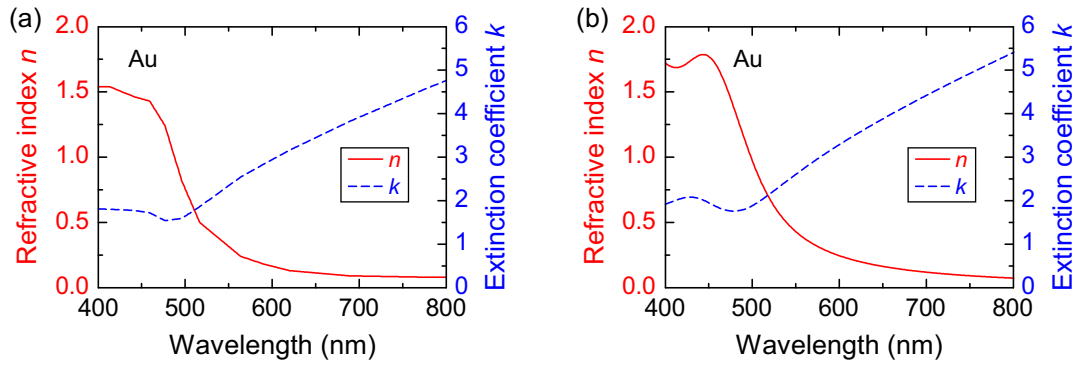


Figure A.4: Optical constants of Au. The data set in (a) was used for most calculations, while the data set in (b) was used for the simulation in Fig. 4.11.

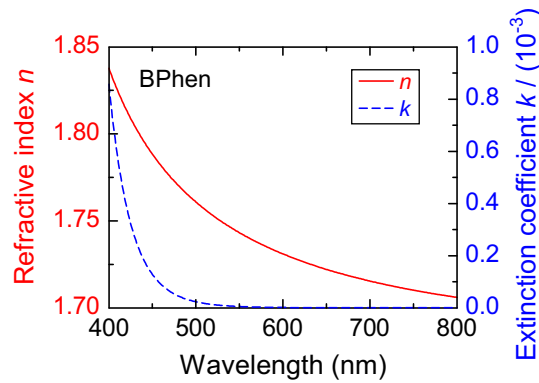


Figure A.5: Optical constants of BPhen.

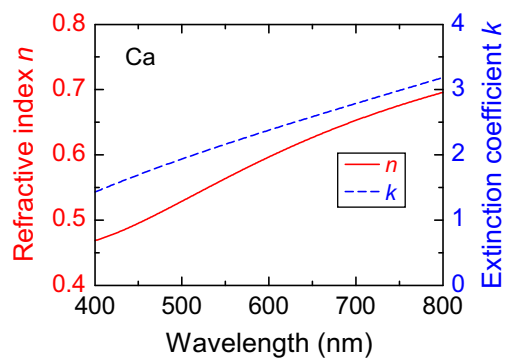


Figure A.6: Optical constants of calcium.

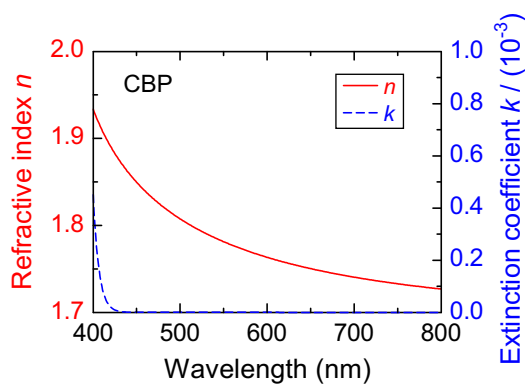


Figure A.7: Optical constants of CBP. The birefringence of CBP was not taken into account. The optical constants shown in the figure were determined by variable angle spectroscopic ellipsometry assuming an isotropic material for the fitting procedure.

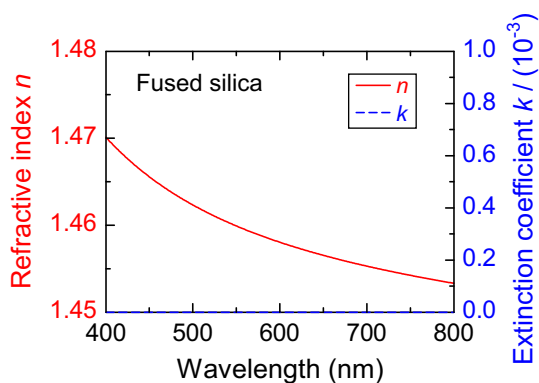


Figure A.8: Optical constants of fused silica.

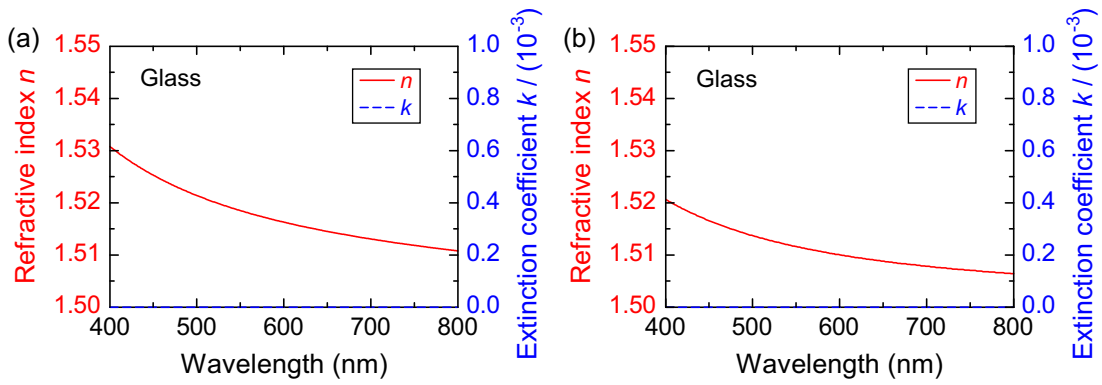


Figure A.9: Optical constants of (BK7) glass. The data set in (a) was used for most simulations, while the data set in (b) was used in Secs. 11.3 and 11.4.

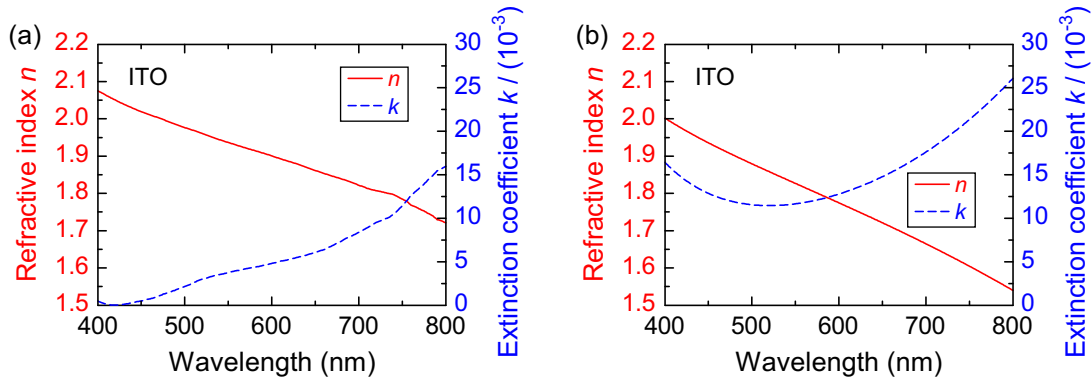


Figure A.10: Optical constants of ITO. The data set in (a) was used for most simulations, while the data set in (b) was used in Sec. 11.4.

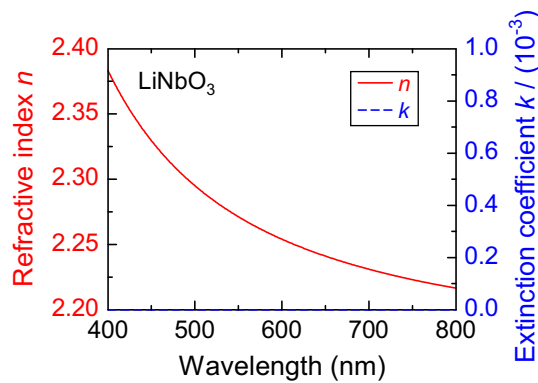


Figure A.11: Optical constants of LiNbO_3 . The birefringence of LiNbO_3 was not taken into account. Instead, the plotted refractive index represents an average of the ordinary and extraordinary refractive indices.

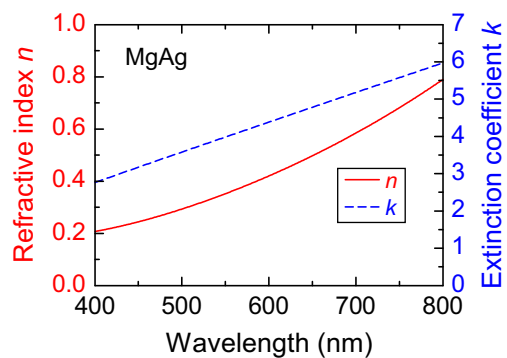


Figure A.12: Optical constants of MgAg (Mg : Ag = 10 : 1).

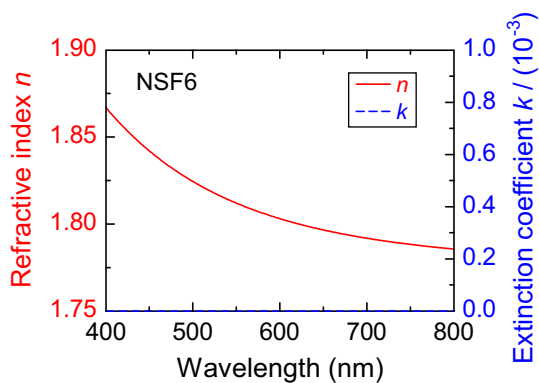


Figure A.13: Optical constants of NSF6 glass (almost identical to SF6 in this wavelength range).

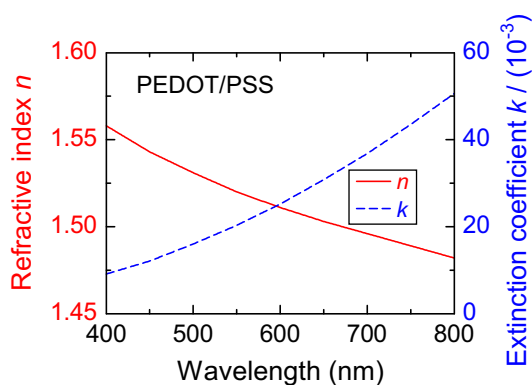


Figure A.14: Optical constants of PEDOT/PSS.

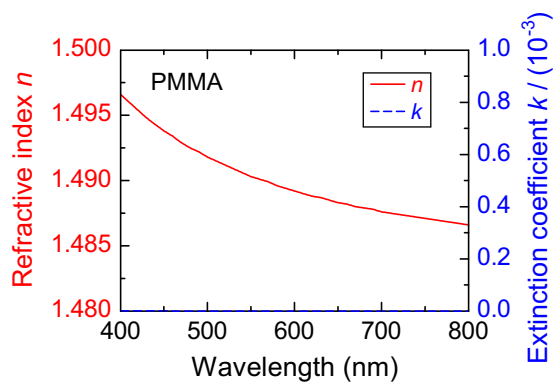


Figure A.15: Optical constants of PMMA.

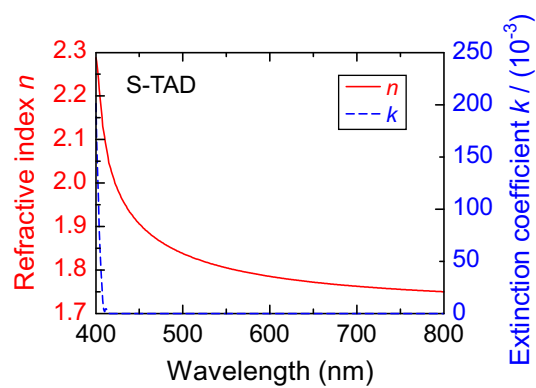


Figure A.16: Optical constants of S-TAD.

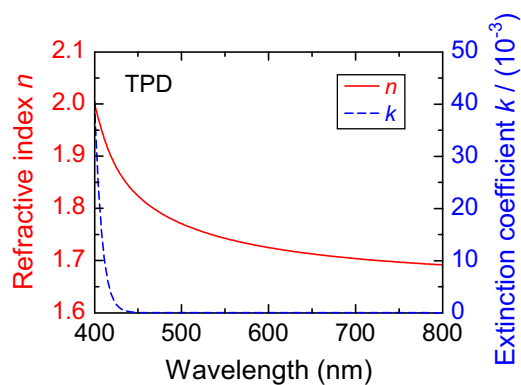


Figure A.17: Optical constants of TPD.

A.3. Optical simulation program

This section gives a brief overview of the optical simulation program “PDCalc” which was used for almost all optical simulations in this work. Considering the required input parameters, the thickness of each layer has to be specified, whereas an infinite expansion within the substrate plane is assumed. It is furthermore necessary to specify the distance of the emitter position to the next interfaces. This is required for the computation of the Fresnel coefficients of the upper and lower hemisphere, which assumes an infinite emitting layer. It should be noted that the emitting region is assumed infinitely sharp. Nevertheless, an extended emitter region could be calculated by running several simulations and by performing a subsequent weighting according to the distribution of the emitter zone. The complex optical constants of each layer in a wavelength range between 400 nm and 800 nm have to be included as separate files. The substrate and superstrate must have vanishing absorption if light should be emitted into these regions.

The spectrum of the emitting species must be provided in a range similar to the optical constants. The specified spectrum is used to weight the simulation which computes each wavelength separately. Typically, the simulation is performed over the whole visible region from 400 nm to 800 nm. If the underlying spectrum only covers a certain spectral region, the wavelength range for the simulation can be limited in order to reduce the computation time. The spectrum is automatically normalized by the simulation program. It is reasonable to use a spectrum which has been determined by photoluminescence of a thin film on glass in order to minimize cavity effects and thus changes of the intrinsic spectrum. For instance, the spectrum of 50 nm Alq₃ on glass was shown in Fig. 2.3. Alternatively, the spectrum used for simulating an OLED can be re-calculated. In this case, the simulation is first performed with an arbitrary or perfectly white spectrum (i.e. a spectrum which has the same value for all wavelengths). Then, the result is adjusted in order to reproduce the measured unpolarized spectrum of the OLED in normal direction. This method was used for the reference OLED in this work. The agreement between the spectrum determined in this way and the measured PL spectrum is excellent. Hence, it is also reasonable to use only the PL spectrum for all simulations.

All layers contributing to waveguide propagation should be specified so that the border between waveguides and surface plasmons can be estimated similar to the capacitance of a plate capacitor with several dielectric media, cf. Ref. [131] for details. However, this computation may lead to small errors in the case of very thick layers or when layers with considerably different refractive indices are present. Then, the border does not perfectly separate waveguides and surface plasmons. As a consequence, some fraction of power coupled to waveguide modes is misleadingly attributed to surface plasmons or vice versa, as can be seen in Fig. 5.9 for large ETL thicknesses. It is also possible that waveguide and surface plasmon modes are broadened due to absorption in the

stacks and that an overlap between waveguides and plasmons occurs. Nevertheless, this usually has no influence on the main result because it does not affect the direct emission and substrate modes.

It is further required to define the photoluminescence quantum efficiency $0 < q \leq 1$ in order to account for radiative and nonradiative decay channels, the latter not being influenced by cavity effects. However, it is also possible to convert the simulated result to other values of q subsequently.

The decay rates are numerically calculated by integrating over all in-plane wave vector magnitudes from k_{\min} to a certain upper integration limit k_{\max} . It should be noted that the integration basically should run from zero to infinity. However, since $k_x = 0$ corresponds to an infinitely small angular cone in the hemisphere, the minimum value is set to e.g. $k_x = 1 \times 10^5 \text{ m}^{-1}$. The upper limit is often set to a value of $k_x = 4 \times 10^7 \text{ m}^{-1}$ because no significant contribution to optical channels takes place for higher in-plane wave vectors¹³¹. However, for certain stacks the upper limit should be increased. For instance, if there is also some surface plasmon contribution in the blue wavelength regime at high k_x values, the upper limit should be at least set to $k_x = 4.5 \times 10^7 \text{ m}^{-1}$. This was done for most of the simulations in this work. Moreover, for particular stacks like microcavity devices with several metallic layers, a significant increase in the maximum k_x value may be required. However, it should be noted that a too large value of k_x causes a major problem if the emitter is positioned directly at the interface between two media with different optical constants¹³¹, because the dipole model requires that the size of the dipole is small compared to the distance from an interface²⁵. Positioning the emitter directly at the interface results in a power contribution that rises proportionally to k_x^2 , thus leading to errors for large k_x ¹³¹. By limiting the upper integration boundary, this problem can be circumvented. The emitter may also be positioned a few nanometers away from the interface to prevent this problem.

An example which requires a larger upper integration limit is the microcavity OLED which was introduced in Sec. 6.4. This stack supports a second surface plasmon at the additional 26 nm thick silver film. Since the thickness significantly differs from a bulk layer, also the surface plasmon dispersion is considerably changed and located at higher k_x values. This can be seen in the power dissipation plot in Fig. A.18. Obviously, the second surface plasmon branch is not taken into account if the upper integration limit is set to only $4 \times 10^7 \text{ m}^{-1}$ or $4.5 \times 10^7 \text{ m}^{-1}$. Therefore, the simulation was performed up to $6 \times 10^7 \text{ m}^{-1}$ with 1200 steps. In addition, the emitter was positioned 2 nm away from the interface to S-TAD in order to prevent the problem discussed above, although the influence of the diverging power for this device at k_x up to $6 \times 10^7 \text{ m}^{-1}$ is still negligible. It is instructive to also discuss the result for a monochromatic simulation at a wavelength of 510 nm for which the cavity was optimized. In this case, the direct emission has a value of 34.7%, i.e. a factor of 1.56 more than in the polychromatic case assuming an Alq₃ spectrum, cf. Fig. 6.3(b). This clearly visualizes the strong

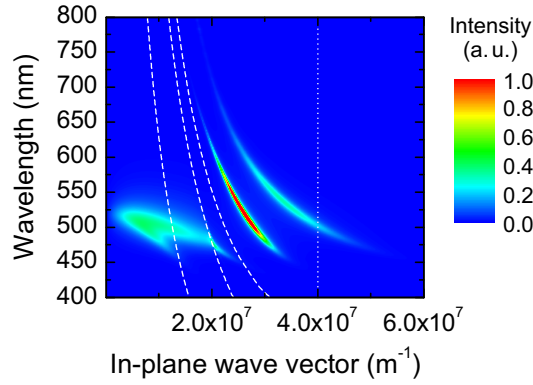


Figure A.18: Simulation of the total dissipated optical power for the microcavity OLED shown in Fig. 6.3(a). The emitter position is assumed to be located in the Alq₃ layer at a distance of 2 nm from the interface to S-TAD. The simulation assumes an isotropic dipole orientation and a PL quantum efficiency of $q = 100\%$. Red areas indicate a high amount of dissipated power. The dashed white lines divide the graph into four regions similar to Fig. 5.1(c). The dotted vertical line marks the value of $k_x = 4 \times 10^7 \text{ m}^{-1}$ which is typically used as upper integration limit.

cavity effects and the accompanying unfavorable interference effects for spectral regions that differ too much from the optimal wavelength. Clearly, the cavity could be further optimized by taking into account the broad emission spectrum and by choosing other materials or completely different layer thicknesses.

The step size for the in-plane wave vector used in the simulation should also be briefly explained. Typically, it is set to $1 \times 10^5 \text{ m}^{-1}$. In general, this is accurate enough in order to correctly compute the contribution to waveguide modes. Using this value, a computation runtime around 2 to 3 hours is obtained. Nevertheless, some simulations were performed with a smaller step size of $0.5 \times 10^5 \text{ m}^{-1}$, and accordingly the number of steps was doubled. However, for example in the microcavity simulation discussed above, the discrepancy between 1200 and 600 k_x steps amounts to less than 0.1%. On the other hand, for monochromatic variations it is recommended to further increase the step size because the runtime is automatically reduced if the simulation at a single wavelength is modeled. For instance, the monochromatic variation of both the HTL and ETL thickness was performed with a step size of only $1 \times 10^4 \text{ m}^{-1}$ and 4500 steps. It should be noted that the width of waveguide modes critically depends on the absorption in the layers. Without absorption, the modes become infinitely narrow and thus can no more be identified due to the finite k_x step size⁵⁰.

It is further noteworthy that the simulation does not distinguish between surface plasmons (i.e. surface plasmon polaritons) and lossy surface waves. The latter decay channel is mainly due to electron-hole excitations, i.e. it is nonradiative and the lost power cannot be recovered^{109,135}. It dominates the overall power dissipation at small distances to a metal up to around 20 nm ^{25,109}. Hence, it is recommended to have at least distances of the order of 20 nm between the emitter and a metal. An exception

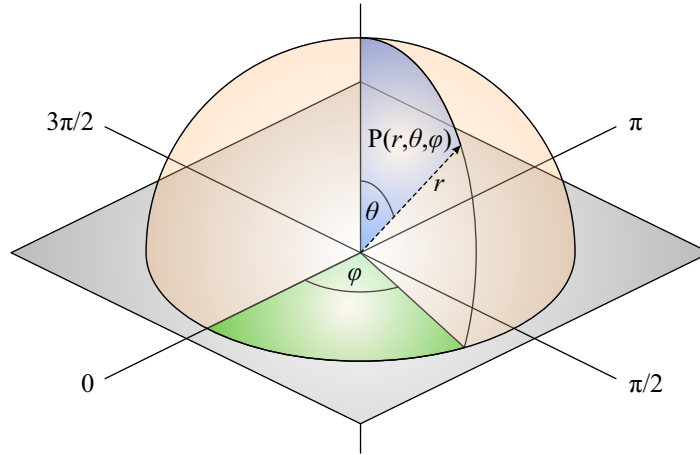


Figure A.19: Spherical coordinate system. A point $P(r, \theta, \varphi)$ is defined by radius r , polar angle θ , and azimuthal angle φ .

was made for the calculations of the surface plasmon dispersions in Sec. 7.1 and Chapter 8. However, in these cases only the wave vector position of the surface plasmon was of interest and not the amount of power coupled to each optical channel, thus no differentiation between surface plasmons and lossy surface waves was required.

Concerning the output of the simulation, several files are generated including the total power dissipation as well as the power dissipation for each of the three dipole orientations and the combinations for the horizontal and isotropic case. Moreover, the results are integrated according to their contribution to direct emission, substrate emission, waveguide modes and surface plasmons. In addition, the enhancement or damping of the radiative rate by the cavity is considered. A separate analysis is performed for each dipole. Finally, the transmission of radiation into the substrate and air is computed.

For comparison to measurements, the in-plane wave vector k_x may be converted to an angle of emission in a certain medium like air or glass. Several corrections are required which can be derived by comparing two expressions for the total emission I_{total} in one of the hemispheres, i.e. top or bottom. In the following, emission into glass in bottom direction will be assumed. Of course, the discussion is also valid for top direction and all other media besides glass. It is convenient to use a spherical coordinate system which is illustrated in Fig. A.19.

First, the total emission can be derived from the basic simulation result by integrating over the in-plane wave vector range from $k_x = 0$ to $k_x = k_1 = 2\pi n_{\text{glass}}/\lambda$:

$$I_{\text{total}} = \int_0^{2\pi} \int_0^{k_1} I_{\text{sim}}(k_x) dk_x d\varphi = \int_0^{2\pi} \int_0^{\pi/2} I_{\text{sim}}(\theta) \cdot \frac{2\pi \cdot n_{\text{glass}} \cdot \cos \theta}{\lambda} d\theta d\varphi, \quad (\text{A.1})$$

where $I_{\text{sim}}(k_x)$ (or $I_{\text{sim}}(\theta)$) describes the simulated emission intensity for a certain k_x -value (or angle). For this equation, the relation $dk_x/d\theta = (2\pi \cdot n_{\text{glass}} \cdot \cos \theta/\lambda)$ was used as well as the fact that the in-plane wave vector k_1 corresponds to an angle of 90° in

glass.

The second expression for I_{total} is computed by integrating over a cross section $I_{\text{cross}}(\theta)$ using a spherical coordinate system and assuming a constant distance r of the observer or detector from the emitter location:

$$I_{\text{total}} = \int_0^{2\pi} \int_0^{\pi/2} I_{\text{cross}}(\theta) \cdot \sin \theta \, d\theta \, d\varphi. \quad (\text{A.2})$$

This formula is also valid for computing the integral emission from a measured cross section.

By comparing both expressions for I_{total} , the correction factor required for transforming the simulated emission $I_{\text{sim}}(\theta)$ into an emission over a cross section $I_{\text{cross}}(\theta)$ is found to be $[2\pi \cdot n_{\text{glass}} \cdot \cos \theta / (\lambda \cdot \sin \theta)]$. In addition, the transmission through the stack has to be taken into account, which reduces the intensity due to absorption and reflection losses. It should be emphasized that the discrete k_x values correspond to different angles θ at each wavelength. To account for all these specifications, a Maple program was developed which performs the conversion and makes an interpolation so that a matrix in terms of wavelength versus angle is obtained.

If desired, the angular dependent spectra can be normalized with respect to the sum of radiative and nonradiative decay channels, which might be required if a comparison of the emitted intensities between different simulations is requested. As mentioned above, the value $k_x = 0$ is not computed in the simulation, hence no value at an angle of 0° can be determined. However, a typical value of the minimum k_x of $1 \times 10^5 \text{ m}^{-1}$ corresponds to an angle smaller than 1° . Therefore, it is reasonable to use this value for normal emission, keeping in mind that the emission of an OLED typically is close to Lambertian so that there is hardly any difference between 0° and 1° .

Bibliography

- [1] M. Schwoerer and H. C. Wolf. *Organic Molecular Solids*. Wiley-VCH (2007).
- [2] C. W. Tang and S. A. VanSlyke. *Organic electroluminescent diodes*. *Appl. Phys. Lett.* **51**, 913–915 (1987).
- [3] J. H. Burroughes, D. D. C. Bradley, A. R. Brown, R. N. Marks, K. Mackay, R. H. Friend, P. L. Burns, and A. B. Holmes. *Light-emitting diodes based on conjugated polymers*. *Nature* **347**, 539–541 (1990).
- [4] Y.-S. Tyan. *Organic light-emitting-diode lighting overview*. *J. Photon. Energy* **1**, 011009 (2011).
- [5] [http://www.osram.de/osram_de/Presse/Fachpresse/Optohalbleiter_\(LED,_Laser\)/2010/100729_Orbeos_OLED.html](http://www.osram.de/osram_de/Presse/Fachpresse/Optohalbleiter_(LED,_Laser)/2010/100729_Orbeos_OLED.html).
- [6] [http://www.osram.de/osram_de/Presse/Fachpresse/Optohalbleiter_\(LED,_Laser\)/2010/101105_PirOLED.html](http://www.osram.de/osram_de/Presse/Fachpresse/Optohalbleiter_(LED,_Laser)/2010/101105_PirOLED.html).
- [7] U.S. Department of Energy. *Solid-State Lighting Research and Development: Manufacturing Roadmap*. (2010).
- [8] S. Nowy, B. C. Krummacher, J. Frischeisen, N. A. Reinke, and W. Brütting. *Light extraction and optical loss mechanisms in organic light-emitting diodes: Influence of the emitter quantum efficiency*. *J. Appl. Phys.* **104**, 123109 (2008).
- [9] S. Reineke, F. Lindner, G. Schwartz, N. Seidler, K. Walzer, B. Lüssem, and K. Leo. *White organic light-emitting diodes with fluorescent tube efficiency*. *Nature* **459**, 234–238 (2009).
- [10] W. H. Koo, S. M. Jeong, F. Araoka, K. Ishikawa, S. Nishimura, T. Toyooka, and H. Takezoe. *Light extraction from organic light-emitting diodes enhanced by spontaneously formed buckles*. *Nature Photon.* **4**, 222–226 (2010).
- [11] Y. Sun and S. R. Forrest. *Enhanced light out-coupling of organic light-emitting devices using embedded low-index grids*. *Nature Photon.* **2**, 483–487 (2008).
- [12] H.-Y. Lin, J.-H. Lee, M.-K. Wei, C.-L. Dai, C.-F. Wu, Y.-H. Ho, H.-Y. Lin, and T.-C. Wu. *Improvement of the outcoupling efficiency of an organic light-emitting device by attaching microstructured films*. *Opt. Commun.* **275**, 464–469 (2007).

-
- [13] S. Nowy, J. Frischeisen, and W. Brütting. *Simulation based optimization of light-outcoupling in organic light-emitting diodes*. Proc. of SPIE **7415**, 74151C (2009).
- [14] L. H. Smith, J. A. E. Wasey, I. D. W. Samuel, and W. L. Barnes. *Light out-coupling efficiencies of organic light-emitting diode structures and the effect of photoluminescence quantum yield*. Adv. Funct. Mater. **15**, 1839–1844 (2005).
- [15] C. Féry, B. Racine, D. Vaufrey, H. Doyeux, and S. Cinà. *Physical mechanism responsible for the stretched exponential decay behavior of aging organic light-emitting diodes*. Appl. Phys. Lett. **87**, 213502 (2005).
- [16] K. H. Drexhage. *Influence of a dielectric interface on fluorescence decay time*. J. Lumin. **1-2**, 693–701 (1970).
- [17] R. R. Chance, A. Prock, and R. Silbey. *Lifetime of an emitting molecule near a partially reflecting surface*. J. Chem. Phys. **60**, 2744–2748 (1974).
- [18] R. R. Chance, A. Prock, and R. Silbey. *Molecular fluorescence and energy transfer near interfaces*. Adv. Chem. Phys. **37**, 1–65 (1978).
- [19] W. Brütting, editor. *Physics of Organic Semiconductors*. Wiley-VCH (2005).
- [20] D. Y. Kondakov, T. D. Pawlik, T. K. Hatwar, and J. P. Spindler. *Triplet annihilation exceeding spin statistical limit in highly efficient fluorescent organic light-emitting diodes*. J. Appl. Phys. **106**, 124510 (2009).
- [21] Y. Luo and H. Aziz. *Correlation between triplet-triplet annihilation and electroluminescence efficiency in doped fluorescent organic light-emitting devices*. Adv. Funct. Mater. **20**, 1285–1293 (2010).
- [22] N. C. Greenham, I. D. W. Samuel, G. R. Hayes, R. T. Phillips, Y. A. R. R. Kessener, S. C. Moratti, A. B. Holmes, and R. H. Friend. *Measurement of absolute photoluminescence quantum efficiencies in conjugated polymers*. Chem. Phys. Lett. **241**, 89–96 (1995).
- [23] C. Adachi, T. Tsutsui, and S. Saito. *Confinement of charge carriers and molecular excitons within 5-nm-thick emitter layer in organic electroluminescent devices with a double heterostructure*. Appl. Phys. Lett. **57**, 531–533 (1990).
- [24] N. Matsumoto, M. Nishiyama, and C. Adachi. *Exciplex formations between tris(8-hydroxyquinolate)aluminum and hole transport materials and their photoluminescence and electroluminescence characteristics*. J. Phys. Chem. C **112**, 7735–7741 (2008).
- [25] W. L. Barnes. *Fluorescence near interfaces: The role of photonic mode density*. J. Mod. Opt. **45**, 661–699 (1998).

- [26] H. Becker, S. E. Burns, and R. H. Friend. *Effect of metal films on the photoluminescence and electroluminescence of conjugated polymers*. Phys. Rev. B **56**, 1893–1905 (1997).
- [27] Q. Q. Shu, P. K. Hansma, P. Das, and H. Metiu. *A study of fluorescent intensity emitted by Eu^{3+} ions near dielectric interfaces*. J. Lumin. **40-41**, 745–746 (1988).
- [28] J. A. E. Wasey and W. L. Barnes. *Efficiency of spontaneous emission from planar microcavities*. J. Mod. Opt. **47**, 725–741 (2000).
- [29] M. Pope, H. P. Kallmann, and P. Magnante. *Electroluminescence in organic crystals*. J. Chem. Phys. **38**, 2042–2043 (1963).
- [30] W. Helfrich and W. G. Schneider. *Recombination radiation in anthracene crystals*. Phys. Rev. Lett. **14**, 229–231 (1965).
- [31] D. F. Williams and M. Schadt. *A simple organic electroluminescent diode*. Proc. IEEE **58**, 476–476 (1970).
- [32] A. Dodabalapur. *Organic light emitting diodes*. Solid State Commun. **102**, 259–267 (1997).
- [33] C. Adachi, T. Tsutsui, and S. Saito. *Organic electroluminescent device having a hole conductor as an emitting layer*. Appl. Phys. Lett. **55**, 1489–1491 (1989).
- [34] L. S. Hung, C. W. Tang, and M. G. Mason. *Enhanced electron injection in organic electroluminescence devices using an Al/LiF electrode*. Appl. Phys. Lett. **70**, 152–154 (1997).
- [35] B. C. Krummacher, V.-E. Choong, M. K. Mathai, S. A. Choulis, F. So, F. Jermann, T. Fiedler, and M. Zachau. *Highly efficient white organic light-emitting diode*. Appl. Phys. Lett. **88**, 113506 (2006).
- [36] B. W. D’Andrade and S. R. Forrest. *White organic light-emitting devices for solid-state lighting*. Adv. Mater. **16**, 1585–1595 (2004).
- [37] F. So, B. Krummacher, M. K. Mathai, D. Poplavskyy, S. A. Choulis, and V.-E. Choong. *Recent progress in solution processable organic light emitting devices*. J. Appl. Phys. **102**, 091101 (2007).
- [38] T. Tsutsui, E. Aminaka, C. P. Lin, and D. U. Kim. *Extended molecular design concept of molecular materials for electroluminescence: sublimed-dye films, molecularly doped polymers and polymers with chromophores*. Phil. Trans. R. Soc. Lond. A **355**, 801–814 (1997).

- [39] M. A. Baldo, D. F. O'Brien, M. E. Thompson, and S. R. Forrest. *Excitonic singlet-triplet ratio in a semiconducting organic thin film*. Phys. Rev. B **60**, 14422–14428 (1999).
- [40] M. Segal, M. A. Baldo, R. J. Holmes, S. R. Forrest, and Z. G. Soos. *Excitonic singlet-triplet ratios in molecular and polymeric organic materials*. Phys. Rev. B **68**, 075211 (2003).
- [41] M. Wohlgenannt, K. Tandon, S. Mazumdar, S. Ramasesha, and Z. V. Vardeny. *Formation cross-sections of singlet and triplet excitons in π -conjugated polymers*. Nature **409**, 494–497 (2001).
- [42] Z. Shuai, D. Beljonne, R. J. Silbey, and J. L. Brédas. *Singlet and triplet exciton formation rates in conjugated polymer light-emitting diodes*. Phys. Rev. Lett. **84**, 131–134 (2000).
- [43] P. K. H. Ho, J.-S. Kim, J. H. Burroughes, H. Becker, S. F. Y. Li, T. M. Brown, F. Cacialli, and R. H. Friend. *Molecular-scale interface engineering for polymer light-emitting diodes*. Nature **404**, 481–484 (2000).
- [44] A. Köhler, J. S. Wilson, and R. H. Friend. *Fluorescence and phosphorescence in organic materials*. Adv. Mater. **14**, 701–707 (2002).
- [45] C. Rothe, S. M. King, and A. P. Monkman. *Direct measurement of the singlet generation yield in polymer light-emitting diodes*. Phys. Rev. Lett. **97**, 076602 (2006).
- [46] M. A. Baldo, D. F. O'Brien, Y. You, A. Shoustikov, S. Sibley, M. E. Thompson, and S. R. Forrest. *Highly efficient phosphorescent emission from organic electroluminescent devices*. Nature **395**, 151–154 (1998).
- [47] J. S. Wilson, A. S. Dhoot, A. J. A. B. Seeley, M. S. Khan, A. Köhler, and R. H. Friend. *Spin-dependent exciton formation in π -conjugated compounds*. Nature **413**, 828–831 (2001).
- [48] Y. Sun, N. C. Giebink, H. Kanno, B. Ma, M. E. Thompson, and S. R. Forrest. *Management of singlet and triplet excitons for efficient white organic light-emitting devices*. Nature **440**, 908–912 (2006).
- [49] B. C. Krummacher, S. Nowy, J. Frischeisen, M. Klein, and W. Brütting. *Efficiency analysis of organic light-emitting diodes based on optical simulation*. Org. Electron. **10**, 478–485 (2009).
- [50] K. A. Neyts. *Simulation of light emission from thin-film microcavities*. J. Opt. Soc. Am. A **15**, 962–971 (1998).

- [51] X.-W. Chen, W. C. H. Choy, C. J. Liang, P. K. A. Wai, and S. He. *Modifications of the exciton lifetime and internal quantum efficiency for organic light-emitting devices with a weak/strong microcavity*. Appl. Phys. Lett. **91**, 221112 (2007).
- [52] J. A. E. Wasey, A. Safonov, I. D. W. Samuel, and W. L. Barnes. *Efficiency of radiative emission from thin films of a light-emitting conjugated polymer*. Phys. Rev. B **64**, 205201 (2001).
- [53] C. Adachi, M. A. Baldo, M. E. Thompson, and S. R. Forrest. *Nearly 100% internal phosphorescence efficiency in an organic light-emitting device*. J. Appl. Phys. **90**, 5048–5051 (2001).
- [54] E. L. Williams, K. Haavisto, J. Li, and G. E. Jabbour. *Excimer-based white phosphorescent organic light-emitting diodes with nearly 100% internal quantum efficiency*. Adv. Mater. **19**, 197–202 (2007).
- [55] J. H. Seo, S. J. Lee, B. M. Seo, S. J. Moon, K. H. Lee, J. K. Park, S. S. Yoon, and Y. K. Kim. *White organic light-emitting diodes showing nearly 100% internal quantum efficiency*. Org. Electron. **11**, 1759–1766 (2010).
- [56] D. Kühnke. *Optik: Grundlagen und Anwendungen*. Verlag Harri Deutsch (2007).
- [57] S. R. Forrest, D. D. C. Bradley, and M. E. Thompson. *Measuring the efficiency of organic light-emitting devices*. Adv. Mater. **15**, 1043–1048 (2003).
- [58] K. Diekmann. *OLLA White paper on the necessity of luminous efficacy measurement standardisation of OLED light sources* (2008). http://www.hitech-projects.com/euprojects/olla/news/press_release_4_september_2007/ollaupdatewhitepaper_publicversion2.pdf.
- [59] N. C. Greenham, R. H. Friend, and D. D. C. Bradley. *Angular dependence of the emission from a conjugated polymer light-emitting diode: Implications for efficiency calculations*. Adv. Mater. **6**, 491–494 (1994).
- [60] S. Nowy, N. A. Reinke, J. Frischeisen, and W. Brütting. *Light extraction and optical loss mechanisms in organic light-emitting diodes*. Proc. of SPIE **6999**, 69992V (2008).
- [61] Z. Y. Zhong and Y. D. Jiang. *Surface treatments of indium-tin oxide substrates for polymer electroluminescent devices*. phys. stat. sol. (a) **203**, 3882–3892 (2006).
- [62] X. Yang, D. C. Müller, D. Neher, and K. Meerholz. *Highly efficient polymeric electrophosphorescent diodes*. Adv. Mater. **18**, 948–954 (2006).
- [63] H. Mattoussi, H. Murata, C. D. Merritt, Y. Iizumi, J. Kido, and Z. H. Kafafi. *Photoluminescence quantum yield of pure and molecularly doped organic solid films*. J. Appl. Phys. **86**, 2642–2650 (1999).

- [64] M. Tzolov, W. Brütting, V. Petrova-Koch, A. Mückl, S. Berleb, J. Gmeiner, and M. Schwörer. *Subgap absorption in tris (8-hydroxyquinoline) aluminium*. Synth. Met. **119**, 559–560 (2001).
- [65] C.-C. Wu, W.-Y. Hung, T.-L. Liu, L.-Z. Zhang, and T.-Y. Luh. *Hole-transport properties of a furan-containing oligoaryl*. J. Appl. Phys. **93**, 5465–5471 (2003).
- [66] Y. Kawamura, H. Sasabe, and C. Adachi. *Simple accurate system for measuring absolute photoluminescence quantum efficiency in organic solid-state thin films*. Jpn. J. Appl. Phys. **43**, 7729–7730 (2004).
- [67] T. Spehr, R. Pudzich, T. Fuhrmann, and J. Salbeck. *Highly efficient light emitters based on the spiro concept*. Org. Electron. **4**, 61–69 (2003).
- [68] L. Niu and F. Zhang. *Enhanced performance by inserting ultrathin SiO₂ layer in organic light-emitting devices*. phys. stat. sol. (a) **204**, 900–906 (2007).
- [69] H. W. Choi, S. Y. Kim, W.-K. Kim, K. Hong, and J.-L. Lee. *Effect of magnesium oxide buffer layer on performance of inverted top-emitting organic light-emitting diodes*. J. Appl. Phys. **100**, 064106 (2006).
- [70] K. R. Choudhury, J.-h. Yoon, and F. So. *LiF as an n-dopant in tris(8-hydroxyquinoline) aluminum thin films*. Adv. Mater. **20**, 1456–1461 (2008).
- [71] X. Zhou, M. Pfeiffer, J. Blochwitz, A. Werner, A. Nollau, T. Fritz, and K. Leo. *Very-low-operating-voltage organic light-emitting diodes using a p-doped amorphous hole injection layer*. Appl. Phys. Lett. **78**, 410–412 (2001).
- [72] J. Kido and T. Matsumoto. *Bright organic electroluminescent devices having a metal-doped electron-injecting layer*. Appl. Phys. Lett. **73**, 2866–2868 (1998).
- [73] S. Mladenovski, K. Neyts, D. Pavicic, A. Werner, and C. Rothe. *Exceptionally efficient organic light emitting devices using high refractive index substrates*. Opt. Express **17**, 7562–7570 (2009).
- [74] D. S. Setz, T. D. Schmidt, M. Flämmich, S. Nowy, J. Frischeisen, B. C. Krummacher, T. Dobbertin, K. Heuser, D. Michaelis, N. Danz, W. Brütting, and A. Winnacker. *Comprehensive efficiency analysis of organic light-emitting devices*. J. Photon. Energy **1**, 011006 (2011).
- [75] M. Kröger, S. Hamwi, J. Meyer, T. Dobbertin, T. Riedl, W. Kowalsky, and H.-H. Johannes. *Temperature-independent field-induced charge separation at doped organic/organic interfaces: Experimental modeling of electrical properties*. Phys. Rev. B **75**, 235321 (2007).

- [76] H. Riel. *Optimization of multilayer organic light-emitting diodes*. Ph.D. thesis, University of Bayreuth, Germany (2002).
- [77] C. Adachi, R. Kwong, and S. R. Forrest. *Efficient electrophosphorescence using a doped ambipolar conductive molecular organic thin film*. *Org. Electron.* **2**, 37–43 (2001).
- [78] H. Mu, W. Li, R. Jones, A. Steckl, and D. Klotzkin. *A comparative study of electrode effects on the electrical and luminescent characteristics of Alq₃/TPD OLED: Improvements due to conductive polymer (PEDOT) anode*. *J. Lumin.* **126**, 225–229 (2007).
- [79] Y. Yang, T. Peng, K. Ye, Y. Wu, Y. Liu, and Y. Wang. *High-efficiency and high-quality white organic light-emitting diode employing fluorescent emitters*. *Org. Electron.* **12**, 29–33 (2011).
- [80] M. Ben Khalifa, D. Vaufrey, and J. Tardy. *Opposing influence of hole blocking layer and a doped transport layer on the performance of heterostructure OLEDs*. *Org. Electron.* **5**, 187–198 (2004).
- [81] M. A. Baldo and S. R. Forrest. *Transient analysis of organic electrophosphorescence: I. transient analysis of triplet energy transfer*. *Phys. Rev. B* **62**, 10958–10966 (2000).
- [82] P. van Gemmern, V. van Elsbergen, S. P. Grabowski, H. Boerner, H.-P. Löbl, H. Becker, H. Kalisch, M. Heuken, and R. H. Jansen. *Influence of carrier conductivity and injection on efficiency and chromaticity in small-molecule white organic light-emitting diodes based on 4,4'-bis(2,2'-diphenylvinyl)-1,1'-spirobiphenyl and rubrene*. *J. Appl. Phys.* **100**, 123707 (2006).
- [83] H. A. Al Attar and A. P. Monkman. *Dopant effect on the charge injection, transport, and device efficiency of an electrophosphorescent polymeric light-emitting device*. *Adv. Funct. Mater.* **16**, 2231–2242 (2006).
- [84] C. W. Tang, S. A. VanSlyke, and C. H. Chen. *Electroluminescence of doped organic thin films*. *J. Appl. Phys.* **65**, 3610–3616 (1989).
- [85] S. Riechel, U. Lemmer, J. Feldmann, S. Berleb, A. G. Mückl, W. Brütting, A. Gombert, and V. Wittwer. *Very compact tunable solid-state laser utilizing a thin-film organic semiconductor*. *Opt. Lett.* **26**, 593–595 (2001).
- [86] M. A. Baldo, S. Lamansky, P. E. Burrows, M. E. Thompson, and S. R. Forrest. *Very high-efficiency green organic light-emitting devices based on electrophosphorescence*. *Appl. Phys. Lett.* **75**, 4–6 (1999).

-
- [87] Y. Kawamura, K. Goushi, J. Brooks, J. J. Brown, H. Sasabe, and C. Adachi. *100% phosphorescence quantum efficiency of Ir(III) complexes in organic semiconductor films*. Appl. Phys. Lett. **86**, 071104 (2005).
- [88] H. Matsushima, S. Naka, H. Okada, and H. Onnagawa. *Organic electrophosphorescent devices with mixed hole transport material as emission layer*. Curr. Appl. Phys. **5**, 305–308 (2005).
- [89] C. Adachi, M. E. Thompson, and S. R. Forrest. *Architectures for efficient electrophosphorescent organic light-emitting devices*. IEEE J. Sel. Topics in Quantum Electron. **8**, 372–377 (2002).
- [90] L.-W. Chong, Y.-N. Chou, Y.-L. Lee, T.-C. Wen, and T.-F. Guo. *Hole-injection enhancement of top-emissive polymer light-emitting diodes by P3HT/FNAB modification of Ag anode*. Org. Electron. **10**, 1141–1145 (2009).
- [91] J. Y. Lee. *Pure color emission in transparent organic light-emitting diodes*. Thin Solid Films **515**, 6997–7000 (2007).
- [92] D. F. O’Brien, M. A. Baldo, M. E. Thompson, and S. R. Forrest. *Improved energy transfer in electrophosphorescent devices*. Appl. Phys. Lett. **74**, 442–444 (1999).
- [93] S. Han, X. Feng, Z. H. Lu, D. Johnson, and R. Wood. *Transparent-cathode for top-emission organic light-emitting diodes*. Appl. Phys. Lett. **82**, 2715–2717 (2003).
- [94] Y. Sun and S. R. Forrest. *Organic light emitting devices with enhanced outcoupling via microlenses fabricated by imprint lithography*. J. Appl. Phys. **100**, 073106 (2006).
- [95] P. Yeh. *Optical Waves in Layered Media*. John Wiley & Sons (1988).
- [96] W. Nolting. *Grundkurs Theoretische Physik 3: Elektrodynamik*. Springer (2004).
- [97] S. A. Maier. *Plasmonics: Fundamentals and Applications*. Springer (2007).
- [98] T. Fließbach. *Elektrodynamik. Lehrbuch zur Theoretischen Physik II*. Spektrum Akademischer Verlag (2008).
- [99] G. A. Reider. *Photonik: Eine Einführung in die Grundlagen*. Springer (2005).
- [100] J. R. Sambles, G. W. Bradbery, and F. Yang. *Optical excitation of surface plasmons: An introduction*. Contemp. Phys. **32**, 173–183 (1991).
- [101] H. Kogelnik. *Theory of Optical Waveguides*. In T. Tamir, editor, *Guided-Waves Optoelectronics*. Springer-Verlag (1990).
- [102] W. Demtröder. *Experimentalphysik 2. Elektrizität und Optik*. Springer (2006).

- [103] A. Penzkofer, W. Holzer, H. Tillmann, and H. H. Hörhold. *Leaky-mode emission of luminescent thin films on transparent substrates*. *Opt. Commun.* **229**, 279–290 (2004).
- [104] H. Raether. *Surface Plasmons on Smooth and Rough Surfaces and on Gratings*. Springer (1988).
- [105] R. P. Van Duyne. *Molecular plasmonics*. *Science* **306**, 985–986 (2004).
- [106] S. A. Maier and H. A. Atwater. *Plasmonics: Localization and guiding of electromagnetic energy in metal/dielectric structures*. *J. Appl. Phys.* **98**, 011101 (2005).
- [107] H. A. Atwater. *Der Zauber der Plasmonik*. *Spektrum der Wissenschaft* **6**, 58–65 (2007).
- [108] J. M. Pitarke, V. M. Silkin, E. V. Chulkov, and P. M. Echenique. *Theory of surface plasmons and surface-plasmon polaritons*. *Rep. Prog. Phys.* **70**, 1–87 (2007).
- [109] G. W. Ford and W. H. Weber. *Electromagnetic interactions of molecules with metal surfaces*. *Phys. Rep.* **113**, 195–287 (1984).
- [110] U. Schröter and D. Heitmann. *Grating couplers for surface plasmons excited on thin metal films in the Kretschmann-Raether configuration*. *Phys. Rev. B* **60**, 4992–4999 (1999).
- [111] E. Kretschmann. *Die Bestimmung optischer Konstanten von Metallen durch Anregung von Oberflächenplasmaschwingungen*. *Z. Physik* **241**, 313–324 (1971).
- [112] A. Otto. *Excitation of nonradiative surface plasma waves in silver by the method of frustrated total reflection*. *Z. Physik* **216**, 398–410 (1968).
- [113] P. T. Worthing and W. L. Barnes. *Coupling efficiency of surface plasmon polaritons to radiation using a corrugated surface; angular dependence*. *J. Mod. Opt.* **49**, 1453–1462 (2002).
- [114] M. Leitz. *RSim program – Reflectivity simulation of a multilayer system*. <http://www.boptics.de/rsim.html>.
- [115] E. Ozbay. *Plasmonics: Merging photonics and electronics at nanoscale dimensions*. *Science* **311**, 189–193 (2006).
- [116] J. Frischeisen, C. Mayr, N. A. Reinke, S. Nowy, and W. Brütting. *Surface plasmon resonance sensor utilizing an integrated organic light emitting diode*. *Opt. Express* **16**, 18426–18436 (2008).

-
- [117] J. Frischeisen, N. Reinke, C. Ostermayr, J. Neumann, S. Nowy, and W. Brütting. *Surface plasmon resonance sensor based on a planar polychromatic OLED light source*. Proc. of SPIE **7003**, 70031B (2008).
- [118] J. Frischeisen, N. A. Reinke, and W. Brütting. *OLEDs enable integrated surface-plasmon-resonance sensor*. Laser Focus World **45**, 57–60 (2009).
- [119] N. A. Reinke, J. Neumann, and W. Brütting. *Vorrichtung für die Oberflächenplasmonen-Resonanzspektroskopie*. Patent application DE102007021563A1 (2007).
- [120] J. Homola, S. S. Yee, and G. Gauglitz. *Surface plasmon resonance sensors: review*. Sens. Actuators, B **54**, 3–15 (1999).
- [121] K. A. Peterlinz and R. Georgiadis. *Two-color approach for determination of thickness and dielectric constant of thin films using surface plasmon resonance spectroscopy*. Opt. Commun. **130**, 260–266 (1996).
- [122] J. Homola. *Present and future of surface plasmon resonance biosensors*. Anal. Bioanal. Chem. **377**, 528–539 (2003).
- [123] V. Lirtsman, M. Golosovsky, and D. Davidov. *Infrared surface plasmon resonance technique for biological studies*. J. Appl. Phys. **103**, 014702 (2008).
- [124] R. C. Weast, editor. *CRC Handbook of Chemistry and Physics*. CRC Press, Inc., 64th edition (1983).
- [125] P. Schiebener, J. Straub, J. M. H. L. Sengers, and J. S. Gallagher. *Refractive index of water and steam as function of wavelength, temperature and density*. J. Phys. Chem. Ref. Data **19**, 677–717 (1990).
- [126] A. H. Harvey, J. S. Gallagher, and J. M. H. L. Sengers. *Revised formulation for the refractive index of water and steam as a function of wavelength, temperature and density*. J. Phys. Chem. Ref. Data **27**, 761–774 (1998).
- [127] J. Homola and S. S. Yee. *Surface plasmon resonance sensor based on planar light pipe: theoretical optimization analysis*. Sens. Actuators, B **37**, 145–150 (1996).
- [128] A. Sommerfeld. *Über die Ausbreitung der Wellen in der drahtlosen Telegraphie*. Ann. Phys. **333**, 665–736 (1909).
- [129] H. Kuhn. *Classical aspects of energy transfer in molecular systems*. J. Chem. Phys. **53**, 101–108 (1970).
- [130] N. Reinke. *Photophysikalische Prozesse und Lichtextraktion in organischen Leuchtdioden*. Ph.D. thesis, University of Augsburg, Germany (2008).

- [131] S. Nowy. *Understanding losses in OLEDs: optical device simulation and electrical characterization using impedance spectroscopy*. Ph.D. thesis, University of Augsburg, Germany (2010).
- [132] C.-L. Lin, T.-Y. Cho, C.-H. Chang, and C.-C. Wu. *Enhancing light outcoupling of organic light-emitting devices by locating emitters around the second antinode of the reflective metal electrode*. Appl. Phys. Lett. **88**, 081114 (2006).
- [133] W. Brütting, S. Berleb, and A. G. Mückl. *Device physics of organic light-emitting diodes based on molecular materials*. Org. Electron. **2**, 1–36 (2001).
- [134] R. M. Amos and W. L. Barnes. *Modification of the spontaneous emission rate of Eu^{3+} ions close to a thin metal mirror*. Phys. Rev. B **55**, 7249–7254 (1997).
- [135] J. M. Ziebarth and M. D. McGehee. *A theoretical and experimental investigation of light extraction from polymer light-emitting diodes*. J. Appl. Phys. **97**, 064502 (2005).
- [136] B. Krummacher, M. K. Mathai, V.-E. Choong, S. A. Choulis, F. So, and A. Winnacker. *Influence of charge balance and microcavity effects on resultant efficiency of organic-light emitting devices*. Org. Electron. **7**, 313–318 (2006).
- [137] J.-S. Kim, P. K. H. Ho, N. C. Greenham, and R. H. Friend. *Electroluminescence emission pattern of organic light-emitting diodes: Implications for device efficiency calculations*. J. Appl. Phys. **88**, 1073–1081 (2000).
- [138] K. Saxena, V. Jain, and D. S. Mehta. *A review on the light extraction techniques in organic electroluminescent devices*. Opt. Mater. **32**, 221–233 (2009).
- [139] K. Meerholz and D. C. Müller. *Outsmarting waveguide losses in thin-film light-emitting diodes*. Adv. Funct. Mater. **11**, 251–253 (2001).
- [140] B. W. D’Andrade and J. J. Brown. *Organic light-emitting device luminaire for illumination applications*. Appl. Phys. Lett. **88**, 192908 (2006).
- [141] C. F. Madigan, M.-H. Lu, and J. C. Sturm. *Improvement of output coupling efficiency of organic light-emitting diodes by backside substrate modification*. Appl. Phys. Lett. **76**, 1650–1652 (2000).
- [142] M.-K. Wei and I.-L. Su. *Method to evaluate the enhancement of luminance efficiency in planar OLED light emitting devices for microlens array*. Opt. Express **12**, 5777–5782 (2004).
- [143] S. Möller and S. R. Forrest. *Improved light out-coupling in organic light emitting diodes employing ordered microlens arrays*. J. Appl. Phys. **91**, 3324–3327 (2002).

-
- [144] E. P. Chan and A. J. Crosby. *Fabricating microlens arrays by surface wrinkling*. *Adv. Mater.* **18**, 3238–3242 (2006).
- [145] G. Gaertner and H. Greiner. *Light extraction from OLEDs with (high) index matched glass substrates*. *Proc. of SPIE* **6999**, 69992T (2008).
- [146] L. Lin, T. K. Shia, and C.-J. Chiu. *Silicon-processed plastic micropyramids for brightness enhancement applications*. *J. Micromech. Microeng.* **10**, 395–400 (2000).
- [147] F. Li, X. Li, J. Zhang, and B. Yang. *Enhanced light extraction from organic light-emitting devices by using microcontact printed silica colloidal crystals*. *Org. Electron.* **8**, 635–639 (2007).
- [148] T. Yamasaki, K. Sumioka, and T. Tsutsui. *Organic light-emitting device with an ordered monolayer of silica microspheres as a scattering medium*. *Appl. Phys. Lett.* **76**, 1243–1245 (2000).
- [149] J. J. Shiang, T. J. Faircloth, and A. R. Duggal. *Experimental demonstration of increased organic light emitting device output via volumetric light scattering*. *J. Appl. Phys.* **95**, 2889–2895 (2004).
- [150] R. Bathelt, D. Buchhauser, C. Gärditz, R. Paetzold, and P. Wellmann. *Light extraction from OLEDs for lighting applications through light scattering*. *Org. Electron.* **8**, 293–299 (2007).
- [151] S. Chen and H. S. Kwok. *Light extraction from organic light-emitting diodes for lighting applications by sand-blasting substrates*. *Opt. Express* **18**, 37–42 (2010).
- [152] H. Yokogawa, K. Kawano, M. Yokoyama, T. Tsutsui, M. Yahiro, and Y. Shigesato. *L-5: Late-news paper: Silica aerogel thin film substrate for OLED*. *SID 01 Digest* **32**, 405–407 (2001).
- [153] T. Tsutsui, M. Yahiro, H. Yokogawa, K. Kawano, and M. Yokoyama. *Doubling coupling-out efficiency in organic light-emitting devices using a thin silica aerogel layer*. *Adv. Mater.* **13**, 1149–1152 (2001).
- [154] L. H. Smith and W. L. Barnes. *Using a low-index host layer to increase emission from organic light-emitting diode structures*. *Org. Electron.* **7**, 490–494 (2006).
- [155] M.-H. Lu and J. C. Sturm. *External coupling efficiency in planar organic light-emitting devices*. *Appl. Phys. Lett.* **78**, 1927–1929 (2001).
- [156] B. J. Matterson, J. M. Lupton, A. F. Safonov, M. G. Salt, W. L. Barnes, and I. D. W. Samuel. *Increased efficiency and controlled light output from a microstructured light-emitting diode*. *Adv. Mater.* **13**, 123–127 (2001).

- [157] J. M. Ziebarth, A. K. Saafir, S. Fan, and M. D. McGehee. *Extracting light from polymer light-emitting diodes using stamped Bragg gratings*. *Adv. Funct. Mater.* **14**, 451–456 (2004).
- [158] J. M. Lupton, B. J. Matterson, I. D. W. Samuel, M. J. Jory, and W. L. Barnes. *Bragg scattering from periodically microstructured light emitting diodes*. *Appl. Phys. Lett.* **77**, 3340–3342 (2000).
- [159] D. Stegall, S. Lamansky, J. Anim-Addo, M. Gardiner, E. Hao, L. Kreilich, F. B. McCormick, H. Le, Y. Lu, T. L. Smith, D. Wang, and J.-Y. Zhang. *OLED light extraction with roll-to-roll nanostructured films*. *Proc. of SPIE* **7415**, 74150S (2009).
- [160] U. Geyer, J. Hauss, B. Riedel, S. Gleiss, U. Lemmer, and M. Gerken. *Large-scale patterning of indium tin oxide electrodes for guided mode extraction from organic light-emitting diodes*. *J. Appl. Phys.* **104**, 093111 (2008).
- [161] Y.-J. Lee, S.-H. Kim, J. Huh, G.-H. Kim, Y.-H. Lee, S.-H. Cho, Y.-C. Kim, and Y. R. Do. *A high-extraction-efficiency nanopatterned organic light-emitting diode*. *Appl. Phys. Lett.* **82**, 3779–3781 (2003).
- [162] Y. R. Do, Y. C. Kim, Y.-W. Song, C.-O. Cho, H. Jeon, Y.-J. Lee, S.-H. Kim, and Y.-H. Lee. *Enhanced light extraction from organic light-emitting diodes with 2D SiO₂/SiN_x photonic crystals*. *Adv. Mater.* **15**, 1214–1218 (2003).
- [163] T. H. Park, Y. M. Kim, Y. W. Park, J. H. Choi, J.-W. Jeong, K. C. Choi, and B.-K. Ju. *Self-assembled microarray of organic light-emitting diodes using a self-assembled monolayer by microcontact printing*. *Appl. Phys. Lett.* **95**, 113310 (2009).
- [164] K. Neyts and A. U. Nieto. *Importance of scattering and absorption for the outcoupling efficiency in organic light-emitting devices*. *J. Opt. Soc. Am. A* **23**, 1201–1206 (2006).
- [165] N. Nakamura, N. Fukumoto, F. Sinapi, N. Wada, Y. Aoki, and K. Maeda. *40.4: Glass substrates for OLED lighting with high out-coupling efficiency*. *SID 09 Digest* **40**, 603–606 (2009).
- [166] H.-W. Lin, C.-L. Lin, H.-H. Chang, Y.-T. Lin, C.-C. Wu, Y.-M. Chen, R.-T. Chen, Y.-Y. Chien, and K.-T. Wong. *Anisotropic optical properties and molecular orientation in vacuum-deposited ter(9,9-diarylfuorene)s thin films using spectroscopic ellipsometry*. *J. Appl. Phys.* **95**, 881–886 (2004).
- [167] D. Yokoyama, A. Sakaguchi, M. Suzuki, and C. Adachi. *Horizontal molecular orientation in vacuum-deposited organic amorphous films of hole and electron transport materials*. *Appl. Phys. Lett.* **93**, 173302 (2008).

- [168] D. Yokoyama, A. Sakaguchi, M. Suzuki, and C. Adachi. *Horizontal orientation of linear-shaped organic molecules having bulky substituents in neat and doped vacuum-deposited amorphous films*. *Org. Electron.* **10**, 127–137 (2009).
- [169] P. Andrew and W. L. Barnes. *Energy transfer across a metal film mediated by surface plasmon polaritons*. *Science* **306**, 1002–1005 (2004).
- [170] G. Winter and W. L. Barnes. *Emission of light through thin silver films via near-field coupling to surface plasmon polaritons*. *Appl. Phys. Lett.* **88**, 051109 (2006).
- [171] H. Riel, S. Karg, T. Beierlein, W. Riess, and K. Neyts. *Tuning the emission characteristics of top-emitting organic light-emitting devices by means of a dielectric capping layer: An experimental and theoretical study*. *J. Appl. Phys.* **94**, 5290–5296 (2003).
- [172] H. Riel, S. Karg, T. Beierlein, B. Ruhstaller, and W. Rieß. *Phosphorescent top-emitting organic light-emitting devices with improved light outcoupling*. *Appl. Phys. Lett.* **82**, 466–468 (2003).
- [173] X.-W. Zhang, X.-Y. Jiang, M. A. Khan, J. Li, L. Zhang, J. Cao, W.-Q. Zhu, and Z.-L. Zhang. *Colour tunability of blue top-emitting organic light-emitting devices with single-mode resonance and improved performance by using C₆₀ capping layer and dual emission layer*. *J. Phys. D: Appl. Phys.* **42**, 145106 (2009).
- [174] C.-L. Lin, H.-W. Lin, and C.-C. Wu. *Examining microcavity organic light-emitting devices having two metal mirrors*. *Appl. Phys. Lett.* **87**, 021101 (2005).
- [175] C.-W. Chen, P.-Y. Hsieh, H.-H. Chiang, C.-L. Lin, H.-M. Wu, and C.-C. Wu. *Top-emitting organic light-emitting devices using surface-modified Ag anode*. *Appl. Phys. Lett.* **83**, 5127–5129 (2003).
- [176] G. Z. Ran, W. Q. Zhao, G. L. Ma, L. Dai, and G. G. Qin. *Role of the dielectric capping layer in enhancement of light outcoupling for semitransparent metal-cathode organic light-emitting devices*. *J. Opt. A: Pure Appl. Opt.* **8**, 733–736 (2006).
- [177] H. Yokoyama. *Physics and device applications of optical microcavities*. *Science* **256**, 66–70 (1992).
- [178] R. Meerheim, R. Nitsche, and K. Leo. *High-efficiency monochrome organic light emitting diodes employing enhanced microcavities*. *Appl. Phys. Lett.* **93**, 043310 (2008).
- [179] N. Takada, T. Tsutsui, and S. Saito. *Control of emission characteristics in organic thin-film electroluminescent diodes using an optical-microcavity structure*. *Appl. Phys. Lett.* **63**, 2032–2034 (1993).

- [180] N. A. Reinke, C. Ackermann, and W. Brütting. *Light extraction via leaky modes in organic light emitting devices*. Opt. Commun. **266**, 191–197 (2006).
- [181] W. C. H. Choy and C. Y. Ho. *Improving the viewing angle properties of microcavity OLEDs by using dispersive gratings*. Opt. Express **15**, 13288–13294 (2007).
- [182] Q. Huang, K. Walzer, M. Pfeiffer, K. Leo, M. Hofmann, and T. Stübinger. *Performance improvement of top-emitting organic light-emitting diodes by an organic capping layer: An experimental study*. J. Appl. Phys. **100**, 064507 (2006).
- [183] J. Meyer, T. Winkler, S. Hamwi, S. Schmale, H.-H. Johannes, T. Weimann, P. Hinze, W. Kowalsky, and T. Riedl. *Transparent inverted organic light-emitting diodes with a tungsten oxide buffer layer*. Adv. Mater. **20**, 3839–3843 (2008).
- [184] J. Frischeisen, B. J. Scholz, B. J. Arndt, T. D. Schmidt, R. Gehlhaar, C. Adachi, and W. Brütting. *Strategies for light extraction from surface plasmons in organic light-emitting diodes*. J. Photon. Energy **1**, 011004 (2011).
- [185] J. Frischeisen, S. Nowy, N. Reinke, W. Brütting, B. C. Krummacher, and F. Schindler. *Strahlungsemitterendes Bauelement*. Patent application DE102008-022830A1 (2008).
- [186] S. Wedge, I. R. Hooper, I. Sage, and W. L. Barnes. *Light emission through a corrugated metal film: The role of cross-coupled surface plasmon polaritons*. Phys. Rev. B **69**, 245418 (2004).
- [187] S. Wedge, A. Giannattasio, and W. L. Barnes. *Surface plasmon-polariton mediated emission of light from top-emitting organic light-emitting diode type structures*. Org. Electron. **8**, 136–147 (2007).
- [188] S. Wedge and W. L. Barnes. *Surface plasmon-polariton mediated light emission through thin metal films*. Opt. Express **12**, 3673–3685 (2004).
- [189] K.-C. Tien, M.-S. Lin, Y.-H. Lin, C.-H. Tsai, M.-H. Shiu, M.-C. Wei, H.-C. Cheng, C.-L. Lin, H.-W. Lin, and C.-C. Wu. *Utilizing surface plasmon polariton mediated energy transfer for tunable double-emitting organic light-emitting devices*. Org. Electron. **11**, 397–406 (2010).
- [190] J. Feng, T. Okamoto, R. Naraoka, and S. Kawata. *Enhancement of surface plasmon-mediated radiative energy transfer through a corrugated metal cathode in organic light-emitting devices*. Appl. Phys. Lett. **93**, 051106 (2008).
- [191] K. Celebi, T. D. Heidel, and M. A. Baldo. *Simplified calculation of dipole energy transport in a multilayer stack using dyadic Green’s functions*. Opt. Express **15**, 1762–1772 (2007).

-
- [192] A. Giannattasio, I. R. Hooper, and W. L. Barnes. *Transmission of light through thin silver films via surface plasmon-polaritons*. *Opt. Express* **12**, 5881–5886 (2004).
- [193] A. Giannattasio, S. Wedge, and W. L. Barnes. *Role of surface profiles in surface plasmon-polariton-mediated emission of light through a thin metal film*. *J. Mod. Opt.* **53**, 429–436 (2006).
- [194] H. F. Ghaemi, T. Thio, D. E. Grupp, T. W. Ebbesen, and H. J. Lezec. *Surface plasmons enhance optical transmission through subwavelength holes*. *Phys. Rev. B* **58**, 6779–6782 (1998).
- [195] C. Liu, V. Kamaev, and Z. V. Vardeny. *Efficiency enhancement of an organic light-emitting diode with a cathode forming two-dimensional periodic hole array*. *Appl. Phys. Lett.* **86**, 143501 (2005).
- [196] J. Frischeisen, Q. Niu, A. Abdellah, J. B. Kinzel, R. Gehlhaar, G. Scarpa, C. Adachi, P. Lugli, and W. Brütting. *Light extraction from surface plasmons and waveguide modes in an organic light-emitting layer by nanoimprinted gratings*. *Opt. Express* **19**, A7–A19 (2011).
- [197] P. T. Worthing and W. L. Barnes. *Efficient coupling of surface plasmon polaritons to radiation using a bi-grating*. *Appl. Phys. Lett.* **79**, 3035–3037 (2001).
- [198] S. Y. Chou, P. R. Krauss, and P. J. Renstrom. *Imprint lithography with 25-nanometer resolution*. *Science* **272**, 85–87 (1996).
- [199] S. Harrer, S. Strobel, G. Scarpa, G. Abstreiter, M. Tornow, and P. Lugli. *Room temperature nanoimprint lithography using molds fabricated by molecular beam epitaxy*. *IEEE T. Nanotechnol.* **7**, 363–370 (2008).
- [200] G. Lévêque and O. J. F. Martin. *Optimization of finite diffraction gratings for the excitation of surface plasmons*. *J. Appl. Phys.* **100**, 124301 (2006).
- [201] J. Feng, T. Okamoto, and S. Kawata. *Highly directional emission via coupled surface-plasmon tunneling from electroluminescence in organic light-emitting devices*. *Appl. Phys. Lett.* **87**, 241109 (2005).
- [202] T. Okamoto, J. Simonen, and S. Kawata. *Plasmonic band gaps of structured metallic thin films evaluated for a surface plasmon laser using the coupled-wave approach*. *Phys. Rev. B* **77**, 115425 (2008).
- [203] J. Hauss, B. Riedel, S. Gleiss, U. Geyer, U. Lemmer, and M. Gerken. *Periodic nanostructuring for guided mode extraction in organic light-emitting diodes*. *J. Photon. Energy* **1**, 011012 (2011).

- [204] W. L. Barnes, T. W. Preist, S. C. Kitson, and J. R. Sambles. *Physical origin of photonic energy gaps in the propagation of surface plasmons on gratings*. Phys. Rev. B **54**, 6227–6244 (1996).
- [205] S. C. Kitson, W. L. Barnes, G. W. Bradberry, and J. R. Sambles. *Surface profile dependence of surface plasmon band gaps on metallic gratings*. J. Appl. Phys. **79**, 7383–7385 (1996).
- [206] S. C. Kitson, W. L. Barnes, and J. R. Sambles. *Surface-plasmon energy gaps and photoluminescence*. Phys. Rev. B **52**, 11441–11445 (1995).
- [207] K. A. S. Immink. *The digital versatile disc (DVD): System requirements and channel coding*. SMPTE J. **105**, 483–489 (1996).
- [208] J. Moreland, A. Adams, and P. K. Hansma. *Efficiency of light emission from surface plasmons*. Phys. Rev. B **25**, 2297–2300 (1982).
- [209] F. Burmeister, C. Schäfle, B. Keilhofer, C. Bechinger, J. Boneberg, and P. Leiderer. *From mesoscopic to nanoscopic surface structures: Lithography with colloid monolayers*. Adv. Mater. **10**, 495–497 (1998).
- [210] H. W. Deckman and J. H. Dunsmuir. *Natural lithography*. Appl. Phys. Lett. **41**, 377–379 (1982).
- [211] T. Yamasaki and T. Tsutsui. *Fabrication and optical properties of two-dimensional ordered arrays of silica microspheres*. Jpn. J. Appl. Phys. **38**, 5916–5921 (1999).
- [212] W. Kandulski. *Shadow nanosphere lithography*. Ph.D. thesis, University of Bonn, Germany (2007).
- [213] S. Hayashi, Y. Yamada, A. Maekawa, and M. Fujii. *Surface plasmon-mediated light emission from dye layer in reverse attenuated total reflection geometry*. Jpn. J. Appl. Phys. **47**, 1152–1157 (2008).
- [214] L. Luan, P. R. Sievert, W. Mu, Z. Hong, and J. B. Ketterson. *Highly directional fluorescence emission from dye molecules embedded in a dielectric layer adjacent to a silver film*. New J. Phys. **10**, 073012 (2008).
- [215] J. Frischeisen, S. Nowy, and W. Brütting. *Organische Leuchtdiode / Organic light-emitting diode*. Patent application DE102009037185A1 (2009) / WO2010136537A1 (2010).
- [216] R. D. Shannon, R. C. Shannon, O. Medenbach, and R. X. Fischer. *Refractive index and dispersion of fluorides and oxides*. J. Phys. Chem. Ref. Data **31**, 931–970 (2002).

- [217] J. Meyer, P. Görrn, F. Bertram, S. Hamwi, T. Winkler, H.-H. Johannes, T. Weimann, P. Hinze, T. Riedl, and W. Kowalsky. *Al₂O₃/ZrO₂ nanolaminates as ultrahigh gas-diffusion barriers – a strategy for reliable encapsulation of organic electronics*. *Adv. Mater.* **21**, 1845–1849 (2009).
- [218] J. Meyer, D. Schneidenbach, T. Winkler, S. Hamwi, T. Weimann, P. Hinze, S. Ammermann, H.-H. Johannes, T. Riedl, and W. Kowalsky. *Reliable thin film encapsulation for organic light emitting diodes grown by low-temperature atomic layer deposition*. *Appl. Phys. Lett.* **94**, 233305 (2009).
- [219] K. Kukli, J. Ihanus, M. Ritala, and M. Leskela. *Tailoring the dielectric properties of HfO₂-Ta₂O₅ nanolaminates*. *Appl. Phys. Lett.* **68**, 3737–3739 (1996).
- [220] H. Kattelus, M. Ylilammi, J. Saarilahti, J. Antson, and S. Lindfors. *Layered tantalum-aluminum oxide films deposited by atomic layer epitaxy*. *Thin Solid Films* **225**, 296–298 (1993).
- [221] J. L. H. Chau, Y.-M. Lin, A.-K. Li, W.-F. Su, K.-S. Chang, S. L.-C. Hsu, and T.-L. Li. *Transparent high refractive index nanocomposite thin films*. *Mater. Lett.* **61**, 2908–2910 (2007).
- [222] F. W. Mont, J. K. Kim, M. F. Schubert, E. F. Schubert, and R. W. Siegel. *High-refractive-index TiO₂-nanoparticle-loaded encapsulants for light-emitting diodes*. *J. Appl. Phys.* **103**, 083120 (2008).
- [223] S. Hofmann, M. Thomschke, P. Freitag, M. Furno, B. Lüssem, and K. Leo. *Top-emitting organic light-emitting diodes: Influence of cavity design*. *Appl. Phys. Lett.* **97**, 253308 (2010).
- [224] J. Frischeisen, D. Yokoyama, C. Adachi, and W. Brütting. *Determination of molecular dipole orientation in doped fluorescent organic thin films by photoluminescence measurements*. *Appl. Phys. Lett.* **96**, 073302 (2010).
- [225] J. Frischeisen, D. Yokoyama, A. Endo, C. Adachi, and W. Brütting. *Increased light outcoupling efficiency in dye-doped small molecule organic light-emitting diodes with horizontally oriented emitters*. *Org. Electron.* **12**, 809–817 (2011).
- [226] A. Köhler and J. Wilson. *Phosphorescence and spin-dependent exciton formation in conjugated polymers*. *Org. Electron.* **4**, 179–189 (2003).
- [227] S. L. M. van Mensfoort, M. Carvelli, M. Megens, D. Wehenkel, M. Bartyzel, H. Greiner, R. A. J. Janssen, and R. Coehoorn. *Measuring the light emission profile in organic light-emitting diodes with nanometre spatial resolution*. *Nature Photon.* **4**, 329–335 (2010).

- [228] M. Flämmich, M. C. Gather, N. Danz, D. Michaelis, A. H. Bräuer, K. Meerholz, and A. Tünnermann. *Orientation of emissive dipoles in OLEDs: Quantitative in situ analysis*. *Org. Electron.* **11**, 1039–1046 (2010).
- [229] J. Frischeisen, D. Yokoyama, A. Endo, C. Adachi, and W. Brütting. *Increased light outcoupling efficiency in dye-doped small molecule organic light-emitting diodes with horizontally oriented emitters*. *Org. Electron.* **12**, 809–817 Supplementary information (2011).
- [230] W. H. Weber and C. F. Eagen. *Energy transfer from an excited dye molecule to the surface plasmons of an adjacent metal*. *Opt. Lett.* **4**, 236–238 (1979).
- [231] S. H. Garrett, J. A. E. Wasey, and W. L. Barnes. *Determining the orientation of the emissive dipole moment associated with dye molecules in microcavity structures*. *J. Mod. Opt.* **51**, 2287–2295 (2004).
- [232] Y. Cao, I. D. Parker, G. Yu, C. Zhang, and A. J. Heeger. *Improved quantum efficiency for electroluminescence in semiconducting polymers*. *Nature* **397**, 414–417 (1999).
- [233] D. Yokoyama, M. Moriwake, and C. Adachi. *Spectrally narrow emissions at cut-off wavelength from edges of optically and electrically pumped anisotropic organic films*. *J. Appl. Phys.* **103**, 123104 (2008).
- [234] H. M. Hiep, M. Fujii, and S. Hayashi. *Effects of molecular orientation on surface-plasmon-coupled emission patterns*. *Appl. Phys. Lett.* **91**, 183110 (2007).
- [235] H. S. Bang, S. Y. Seo, D. C. Choo, T. W. Kim, S. J. Lee, J. H. Seo, Y. K. Kim, C. Chu, and J. Ha. *Effect of doped emitting layer on electrical and optical properties in blue organic light-emitting devices*. *Thin Solid Films* **517**, 5314–5317 (2009).
- [236] T. Niimi and M. Umeda. *Electron transfer between a photoexcited azo pigment particle and an electron donor molecule in a solid system*. *J. Phys. Chem. B* **106**, 3657–3661 (2002).
- [237] M. Grell and D. D. C. Bradley. *Polarized luminescence from oriented molecular materials*. *Adv. Mater.* **11**, 895–905 (1999).
- [238] F. A. M. Ghazali, M. Fujii, and S. Hayashi. *Anisotropic propagation of surface plasmon polaritons caused by oriented molecular overlayer*. *Appl. Phys. Lett.* **95**, 033303 (2009).
- [239] M. Jandke, P. Strohriegl, J. Gmeiner, W. Brütting, and M. Schworer. *Polarized electroluminescence from rubbing-aligned poly(p-phenylenevinylene)*. *Adv. Mater.* **11**, 1518–1521 (1999).

- [240] K. S. Whitehead, M. Grell, D. D. C. Bradley, M. Jandke, and P. Strohriegel. *Highly polarized blue electroluminescence from homogeneously aligned films of poly(9,9-dioctylfluorene)*. Appl. Phys. Lett. **76**, 2946–2948 (2000).
- [241] Y. Yoshida, N. Tanigaki, K. Yase, and S. Hotta. *Color-tunable highly polarized emissions from uniaxially aligned thin films of thiophene/phenylene co-oligomers*. Adv. Mater. **12**, 1587–1591 (2000).
- [242] J. C. Wittmann and P. Smith. *Highly oriented thin films of poly(tetrafluoroethylene) as a substrate for oriented growth of materials*. Nature **352**, 414–417 (1991).
- [243] X. L. Chen, Z. Bao, B. J. Sapjeta, A. J. Lovinger, and B. Crone. *Polarized electroluminescence from aligned chromophores by the friction transfer method*. Adv. Mater. **12**, 344–347 (2000).
- [244] C. Mayr. *Einfluss der molekularen Orientierung in organischen Leuchtdioden*. Diploma thesis, University of Augsburg, Germany (2011).
- [245] The optical simulation program “Radiating Slabs” can take both birefringence and reflection effects at the encapsulation glass into account. For further information contact norbert.danz@iof.fraunhofer.de.
- [246] D. Yokoyama, A. Sakaguchi, M. Suzuki, and C. Adachi. *Enhancement of electron transport by horizontal molecular orientation of oxadiazole planar molecules in organic amorphous films*. Appl. Phys. Lett. **95**, 243303 (2009).
- [247] D. Yokoyama, Y. Setoguchi, A. Sakaguchi, M. Suzuki, and C. Adachi. *Orientation control of linear-shaped molecules in vacuum-deposited organic amorphous films and its effect on carrier mobilities*. Adv. Funct. Mater. **20**, 386–391 (2010).
- [248] M. Flämmich, J. Frischeisen, D. S. Setz, D. Michaelis, B. C. Krummacher, T. D. Schmidt, W. Brütting, and N. Danz. *Oriented phosphorescent emitters boost OLED efficiency*. Submitted.
- [249] T. Tsutsui and M. Terai. *Electric field-assisted bipolar charge spouting in organic thin-film diodes*. Appl. Phys. Lett. **84**, 440–442 (2004).
- [250] L. S. Liao, K. P. Klubek, and C. W. Tang. *High-efficiency tandem organic light-emitting diodes*. Appl. Phys. Lett. **84**, 167–169 (2004).
- [251] F. Guo and D. Ma. *White organic light-emitting diodes based on tandem structures*. Appl. Phys. Lett. **87**, 173510 (2005).
- [252] S. L. Lai, M. Y. Chan, M. K. Fung, C. S. Lee, and S. T. Lee. *Copper hexadecafluorophthalocyanine and copper phthalocyanine as a pure organic connecting unit in blue tandem organic light-emitting devices*. J. Appl. Phys. **101**, 014509 (2007).

- [253] F. Schwarz. *Ioneninduzierte Umwandlung von Polymerschichten zu diamantähnlichem Kohlenstoff mit darin enthaltenen Silber-Nanopartikeln*. Ph.D. thesis, University of Augsburg, Germany (2010).
- [254] E. Scheler and P. Strohriegl. *Synthesis of oligofluorenes by endcapping*. *Liq. Cryst.* **34**, 667–672 (2007).
- [255] E. Da Como, E. Scheler, P. Strohriegl, J. Lupton, and J. Feldmann. *Single molecule spectroscopy of oligofluorenes: how molecular length influences polymorphism*. *Appl. Phys. A* **95**, 61–66 (2009).

List of publications and patents

Publications

- S. Nowy, N. A. Reinke, J. Frischeisen, and W. Brütting. *Light extraction and optical loss mechanisms in organic light-emitting diodes*. Proc. SPIE **6999**, 69992V (2008).
- J. Frischeisen, N. A. Reinke, C. Ostermayr, J. Neumann, S. Nowy, and W. Brütting. *Surface plasmon resonance sensor based on a planar polychromatic OLED light source*. Proc. SPIE **7003**, 70031B (2008).
- J. Frischeisen, C. Mayr, N. A. Reinke, S. Nowy, and W. Brütting. *Surface plasmon resonance sensor utilizing an integrated organic light emitting diode*. Opt. Express **16**, 18426–18436 (2008).
- S. Nowy, B. C. Krummacher, J. Frischeisen, N. A. Reinke, and W. Brütting. *Light extraction and optical loss mechanisms in organic light-emitting diodes: Influence of the emitter quantum efficiency*. J. Appl. Phys. **104**, 123109 (2008).
- B. C. Krummacher, S. Nowy, J. Frischeisen, M. Klein, and W. Brütting. *Efficiency analysis of organic light-emitting diodes based on optical simulation*. Org. Electron. **10**, 478–485 (2009).
- J. Frischeisen, N. A. Reinke, and W. Brütting. *Organic emitters: OLEDs enable integrated surface-plasmon-resonance sensor*. Laser Focus World **45**, 57–61 (2009).
- S. Nowy, J. Frischeisen, and W. Brütting. *Simulation based optimization of light-outcoupling in organic light-emitting diodes*. Proc. SPIE **7415**, 74151C (2009).
- J. Frischeisen, D. Yokoyama, C. Adachi, and W. Brütting. *Determination of molecular dipole orientation in doped fluorescent organic thin films by photoluminescence measurements*. Appl. Phys. Lett. **96**, 073302 (2010).
- T. Wehlius, T. Körner, S. Nowy, J. Frischeisen, H. Karl, B. Stritzker, and W. Brütting. *Hybrid organic-inorganic materials for integrated optoelectronic devices*. phys. stat. sol. (a) **208**, 264–275 (2011).
- J. Frischeisen, Q. Niu, A. Abdellah, J. B. Kinzel, R. Gehlhaar, G. Scarpa, C. Adachi, P. Lugli, and W. Brütting. *Light extraction from surface plasmons and*

waveguide modes in an organic light-emitting layer by nanoimprinted gratings. Opt. Express **19**, A7–A19 (2011).

- J. Frischeisen, B. J. Scholz, B. J. Arndt, T. D. Schmidt, R. Gehlhaar, C. Adachi, and W. Brütting. *Strategies for light extraction from surface plasmons in organic light-emitting diodes.* J. Photon. Energy **1**, 011004 (2011).
- D. S. Setz, T. D. Schmidt, M. Flämmich, S. Nowy, J. Frischeisen, B. C. Krummacher, T. Dobbertin, K. Heuser, D. Michaelis, N. Danz, W. Brütting, and A. Winnacker. *Comprehensive efficiency analysis of organic light-emitting devices.* J. Photon. Energy **1**, 011006 (2011).
- J. Frischeisen, D. Yokoyama, A. Endo, C. Adachi, and W. Brütting. *Increased light outcoupling efficiency in dye-doped small molecule organic light-emitting diodes with horizontally oriented emitters.* Org. Electron. **12**, 809–817 (2011).
- W. Brütting, J. Frischeisen, B. J. Scholz, and T. D. Schmidt. *More light from organic light-emitting diodes.* In press.
- M. Flämmich, J. Frischeisen, D. S. Setz, D. Michaelis, B. C. Krummacher, T. D. Schmidt, W. Brütting, and N. Danz. *Oriented phosphorescent emitters boost OLED efficiency.* Submitted.

Patent applications

- J. Frischeisen, S. Nowy, N. Reinke, W. Brütting, B. C. Krummacher, and F. Schindler. *Strahlungsemitterendes Bauelement.* Patent application DE102008-022830A1 (2008).
- J. Frischeisen, S. Nowy, and W. Brütting. *Organische Leuchtdiode / Organic light-emitting diode.* Patent application DE102009037185A1 (2009) / WO2010-136537A1 (2010).

List of conference contributions and awards

International conference contributions and seminar talks (selection)

- *Surface plasmon resonance sensor based on a planar polychromatic OLED light source.* SPIE Europe / Photonics Europe, Strasbourg, France (2008).
- *OLEDs and Plasmons.* Center for Future Chemistry (CFC) seminar, Kyushu University, Japan (2008).
- *Novel surface plasmon resonance sensor based on a monolithically integrated OLED light source.* 7th International Conference on Electroluminescence of Molecular Materials and Related Phenomena (ICEL 7), Dresden, Germany (2008).
- *Influence of dipole orientation in organic light-emitting diodes.* Center for Future Chemistry (CFC) seminar, Kyushu University, Japan (2009).
- *Determination of dipole orientation in organic light-emitting diodes.* MRS Fall Meeting 2009, Boston, USA (2009).
- *Strategies for enhanced outcoupling efficiency in organic light-emitting diodes* (invited talk). SPIE Optics + Photonics 2010, San Diego, USA (2010).

Awards

- *Photonic Devices + Applications Best Student Paper Runner-Up Award* for the contribution “Strategies for enhanced outcoupling efficiency in organic light-emitting diodes”. SPIE Optics + Photonics 2010, San Diego, USA (2010).

Danksagung

An dieser Stelle möchte ich mich bei all jenen bedanken, die mich bei dieser Arbeit unterstützt und zu ihrem Gelingen beigetragen haben. Besonderer Dank gilt:

- **Prof. Dr. Wolfgang Brütting** für die freundliche Aufnahme in seine Arbeitsgruppe, die Hilfsbereitschaft bei allen auftretenden Problemen und die ergiebigen Diskussionen, das entgegengebrachte Vertrauen, die hervorragende fachliche Betreuung meiner Arbeit sowie für die sorgfältige Korrektur aller Manuskripte und Veröffentlichungen.
- **Prof. Dr. Achim Wixforth** für seine Betreuung als Co-Advisor im Rahmen des CompInt-Programms und für seine Bereitschaft, das Zweitgutachten zu dieser Arbeit zu erstellen.
- **Prof. Dr. Bernd Stritzker** für die Möglichkeit, meine Promotion an seinem Lehrstuhl durchführen zu können.
- den Studenten, die ich bei der Durchführung ihrer Diplom- oder Bachelorarbeit betreuen durfte: **Bert Scholz, Christian Mayr, Benedikt Arndt** und **Bettina Reisner**. Herzlichen Dank für euren Arbeitseinsatz und die exzellente Zusammenarbeit! Danke speziell auch an Bert Scholz fürs Korrekturlesen.
- meinen Kollegen von der Arbeitsgruppe Organische Halbleiter und vom Lehrstuhl für Experimentalphysik IV, vor allem **Mark Gruber, Dr. Stefan Gsell, Ulrich Hörmann, Daniel Kraus, Michael Kraus, Dr. Stefan Nowy, PD Dr. Andreas Opitz, Cornelia Ostermayr, Dr. Nils Reinke, Tobias Schmidt** (Danke auch fürs Korrekturlesen!), **Julia Wagner, Dr. Thomas Wehler** und **Michael Weigl** sowie dem Rest von EPIV, für die fantastische Atmosphäre, die gegenseitige Unterstützung und die tolle Zusammenarbeit.
- **Cornelia Ludescher** und **Maria Fuso** für die stete Hilfsbereitschaft bei Fragen zu Dienstreiseanträgen usw.
- **Wolfgang Reiber, Birgit Knoblich** und **Sybille Heidemeyer** für die Unterstützung bei technischen Problemen im Labor und bei Bestellungen.

- **Dr. Jürgen Neumann** und **Jörg Kinzel** vom Lehrstuhl EPI für die Zusammenarbeit beim SPR-Sensor bzw. bei den SEM-Messungen und für die Herstellung von Gittern mittels SEM.
- den Mitarbeitern der Festkörperchemie, vor allem **Dr. Jan Hanss** und **Andreas Kalytta-Mewes**, für die Hilfestellungen bei chemischen Fragen und die Nutzung der Räumlichkeiten für Versuche.
- der **Feinmechanischen Werkstatt** sowie der **Elektronik-Werkstatt** für die rasche Hilfe bei technischen Problemen sowie für die Herstellung diverser Bauteile für experimentelle Aufbauten.
- **Prof. Dr. Chihaya Adachi** (Kyushu University, Japan) for giving me the opportunity to work at the Center for Future Chemistry during two research visits. I also want to thank the members of his group, in particular **Dr. Robert Gehlhaar** and **Ayataka Endo**.
- **Assistant Prof. Dr. Daisuke Yokoyama** (Yamagata University, Japan) for the excellent collaboration regarding emitter orientation and for many fruitful discussions.
- **Prof. Dr. Paolo Lugli**, **PD Dr.-Ing. Giuseppe Scarpa**, **Alaa Abdellah** and **Quan Niu** (Lehrstuhl für Nanoelektronik, Technische Universität München) for the great collaboration and for the fabrication of DVD gratings.
- **Prof. Dr. Uli Lemmer** und **Klaus Huska** (Lichttechnisches Institut, Universität Karlsruhe) für die Herstellung von Gittern mittels Laserinterferenz-Lithographie.
- der OLED-Abteilung von OSRAM Opto Semiconductors GmbH in Regensburg für die langjährige hervorragende Zusammenarbeit in den gemeinsamen Projekten. Insbesondere möchte ich mich bei **Dr. Arndt Jaeger**, **Daniel Setz**, **Dr. Benjamin Krummacher**, **Dr. Thomas Dobbertin**, **Dr. Florian Schindler** und **Dr. Karsten Heuser** bedanken!
- **Michael Flämmich**, **Dr. Dirk Michaelis** und **Dr. Norbert Danz** (Fraunhofer-Institut für Angewandte Optik und Feinmechanik IOF in Jena) für die sehr gute Zusammenarbeit bei den gemeinsamen Publikationen.
- **Dr. Ulrich Niedermeier** für das sorgfältige Korrekturlesen meiner Doktorarbeit.
- den Geldgebern, insbesondere dem internationalen Graduiertenkolleg **Materials Science of Complex Interfaces** (CompInt) im Elitenetzwerk Bayern, sowie den BMBF geförderten Projekten **Organic Phosphorescent Area Light** (OPAL

2008, FKZ 13N8995) und **Tausend Lumen organische Phosphoreszenzbauelemente für Anwendungen in Licht-Systemen** (TOPAS 2012, FKZ 13N10474).

- **meinen Eltern** für die fortwährende Unterstützung während meines Studiums und meiner Promotion.
- und natürlich meiner Frau **Jessica** und meiner Tochter **Sophia** ... für alles!

Curriculum vitae

Personal data

Name: Jörg Frischeisen
Date of birth: October 7, 1979
Place of birth: Schwabmünchen
E-Mail: joerg.frischeisen@gmx.de
Marital status: married, one child

Education

10/2006 – 01/2011 **PhD thesis at University of Augsburg**
Institute of Physics
Advisor: Prof. Dr. Wolfgang Brütting
Topic: “Light extraction in organic light-emitting diodes”

10/2000 – 09/2006 **Studies of Physics at University of Regensburg**
Degree: Dipl.-Phys.
Diploma thesis:
“Injection of electrons through a tunneling barrier”

09/1990 – 07/1999 **Leonhard-Wagner-Gymnasium Schwabmünchen**
Degree: Abitur

Civilian service

09/1999 – 07/2000 **Municipal Hospital Schwabmünchen**

Experience abroad

10/2009 **Research visit at Kyushu University**
Adachi Laboratory, Center for Future Chemistry, (Japan)

10/2008 – 11/2008 **Research visit at Kyushu University**
Adachi Laboratory, Center for Future Chemistry, (Japan)

08/2003 – 05/2004 **Study abroad at University of Colorado**
Boulder, CO (USA)
